FIRST-PRINCIPLES QUANTUM MECHANICAL INSIGHTS INTO EMERGING 2D MATERIALS FOR FUTURISTIC ELECTRONICS AND ENERGY

Raihan Ahammed

A thesis submitted for the partial fulfillment of the degree of Doctor of Philosophy

Institute of Nano Science and Technology
Knowledge city, Sector-81, Mohali 140306, Punjab, India

Indian Institute of Science Education and Research Mohali
Knowledge city, Sector 81, Mohali 140306, Punjab, India.

April 2023

Dedicated to

My beloved Parents

and

brothers-Farid & Rijuyan

Declaration

The work presented in this thesis has been carried out by me under the guidance of **Prof. Abir De Sarkar** at the Institute of Nano Science and Technology, Mohali. This work has not been submitted in part or in full for a degree, a diploma, or a fellowship to any other university or institute. Whenever contributions of others are involved, every effort is made to indicate this clearly, with due acknowledgement of collaborative research and discussions. This thesis is a bonafide record of original work done by me and all sources listed within have been detailed in the bibliography.

Raihan Ahammed

(Candidate)

In my capacity as the supervisor of the candidate's thesis work, I certify that the above statements by the candidate are true to the best of my knowledge.

Prof. Abir De Sarkar
(Thesis Supervisor)

Acknowledgements

"The only reason for time is so that everything doesn't happen at once."

-Prof. Albert Einstein

This five-year journey of my Ph.D. research at INST Mohali in the research group of Prof. Abir De Sarkar has been a wonderful experience. I have enjoyed all the research works under the supervision of Prof. Abir De Sarkar. I am pleased to acknowledge the roles of several individuals who are instrumental in making this research journey beautiful.

First of all, I am extremely grateful to my Ph.D. supervisor, **Prof. Abir De Sarkar** for his valuable guidance, scholarly inputs and consistent inspiration I received throughout the research work. I would like to express my deepest gratitude to him for his invaluable advice, professional assistance and everlasting encouragement. It is my immense privilege and luck to have had the opportunity to work and learn from such an expert and enthusiast with great vision and a deep understanding of the research field. His tireless efforts and dedication towards research work have always inspired me. His positive and energetic attitude helped me a lot to stand strong and stay focused even during difficult times. His research command, clear vision and exciting ideas helped me overcome the hurdles that I encountered during my research and thesis work. It was always thought-provoking to me for preferring a new challenging research idea under his benign supervision. I honestly hope to carry forward his enthusiastic pursuit of science and incredible work ethic to shape my future endeavors.

I would like to thank the doctoral committee members, **Dr. Kiran Shankar Hazra** and **Dr. Ramendra Sundar Dey** for their constructive suggestions and criticism. I also want to thank **Dr. T. J. Dhilip Kumar** for evaluating my SRF presentation and providing useful suggestions to improve my work.

I have also been fortunate enough to work in collaboration with the research groups of **Dr. Ramendra Sundar Dey**, **Dr. Kiran Shankar Hazra**, **Prof. H. N. Ghosh & Prof. Amitava Patra.** They offered generous scientific help and insightful discussions on collaborative projects. I would like to extend my acknowledgement to them all. I also thank all our teachers who taught me during my coursework in INST and IISER Mohali.

I thank my fellow research group members, for the stimulating discussions. I am especially thankful to my seniors **Dr. Nityasagar Jena** and **Dr. Dimple** for their aspiring guidance, invaluably constructive criticism and friendly advice. I am also greatly thankful to **Dr. Ashima** and **Dr. Manish** for their immediate help, support and insightful scientific discussions. I extend my heartfelt thanks to **Pradip**, **Amal**, **Anu**, **Fathima**, **Harshita**, **Nilakantha**, **Arneet and Shivam** for being involved in many different insightful scientific aspects and their benign support towards this work. I never felt alone instead for being far away from home because of my research group members for sharing kind friendships. I want to sincerely acknowledge them all since I share a warm bond with them.

I thank all of my friends especially, **Estak**, **Aman**, **Sanjoy**, **Sourav**, **Varun**, **Rejaul**, **Manisha** and **Ritika** for motivating me to work harder towards my goal whenever I used to feel low and for sharing amazing companionship and beautiful memories. I always cherish the fun moments in INST. I want to thank all the table tennis and badminton community members, especially **Amal**, **Pradip**, **Ritika**, **Manvi**, **Anshu**, **Anamika**, **Sonu**, **Bharat**, **Rejaul**, **Sourav**, **Varun** and **Hari**.

I truly acknowledge financial support from the grant no. SR/NM/NS-1125/2016(G) from DST (Nanomission). The Ph.D. fellowship and the infrastructural support provided by the Department of Science and Technology (DST) and the Institute of Nano Science and Technology (INST) Mohali are gratefully acknowledged. My sincere thanks are extended to CDAC, Pune's supercomputing resources on PARAM YUVA II and INST, Mohali for inhouse supercomputing facility. The support and resources provided by the PARAM-Shivay Facility under the National Supercomputing Mission, Government of India, at the Indian Institute of Technology, Varanasi are gratefully acknowledged.

Last but not least, I would like to thank the **Almighty** and my beloved family: my Parents -**Mr. Nizamuddin Ahammed** & **Mrs. Mazera Khatun** and my brothers-**Farid** & **Rijuyan** for supporting me emotionally throughout the Ph.D. work and my life in general. I am deeply grateful for their constant unwavering love, unconditional support, and patience. This journey would not have been possible without them, and thus dedicate this milestone to them.

This work is never the work of an individual. It is more a combination of ideas, suggestions, reviews, contributions and efforts of many. I express my appreciation to all those, with whom I have worked, interacted, and whose thoughts and insights have helped me further my knowledge and understanding of the subject.

Date: ***Raihan Ahammed***

Abstract

This thesis encompasses a broad range of cutting-edge research areas extending from energy harvesting from renewable resources to futuristic electronic devices utilizing novel properties and different degrees of freedom of electrons which emerge in atomically thin two-dimensional (2D) semiconductors and their van der Waals heterostructures. Specifically, nanoelectromechanical energy conversion (piezoelectric effect), solar energy harvesting (photovoltaic effect) as well as spintronics and valleytronics based on 2D monolayers have been presented in the thesis. Atomic-scale insights into the electronic, optical, mechanical, piezoelectric, spintronic and valleytronic properties in selected 2D materials have been obtained through the lens of first-principles state-of-art density functional theory (DFT) based approaches. The significance of integrating their different properties in designing a multifunctional device for advanced applications has also been emphasized. The thesis is organized in the following way.

The first part of the thesis is concentrated on energy harvesting, particularly, on the generation of electricity from mechanical energy as well as spintronics device applications emanating from the Rashba effect. The simultaneous occurrence of gigantic piezoelectricity and Rashba effect in two-dimensional materials are unusually scarce. Inversion symmetry occurring in MX_3 (M= Ti, Zr, Hf; X= S, Se) monolayers is broken upon constructing their Janus monolayer structures MX_2Y ($X \neq Y$=S, Se), thereby inducing a large out-of-plane piezoelectric constant, d_{33} (~68 pm/V) in them. d_{33} can be further enhanced to a super high value of ~1000 pm/V upon applying vertical compressive strain in the van der Waals bilayers constituted by interfacing these Janus monolayers [1]. The 2D Janus transition metal trichalcogenide monolayers and their bilayers presented herewith in this Ph.D. work, straddle giant Rashba spin splitting and ultrahigh piezoelectricity, thereby making them immensely promising candidates in the next generation electronics, piezotronics and spintronics devices. A detailed theoretical investigation has been conducted for a quantitative study and in-depth understanding of the desired parameters.

Next, h-MN (M=Nb, Ta) monolayers have been investigated which are found to host valley physics together with Rashba effect due to the presence of strong spin-orbit coupling

and absence of inversion symmetry [2]. The search for new two-dimensional (2D) semiconductors with strong spin-orbit coupling, merging Rashba effect with valley physics, is essential for advancing the emerging fields of spintronics and valleytronics. Other than charge and spin degrees of freedom (DOF), valley DOF (+K, -K) of electron can be used for information storage in the domain of valleytronics. h-NbN (TaN) monolayers which exhibit a strong spin-orbit coupling leading to a large valley spin splitting (VSS) ~112 (406) meV at its conduction band edge has been investigated for its application in valleytronics. Valleytronic and spintronic properties in the studied monolayers are found to be superior to that in h-MoS_2 and Janus MoSSe monolayers and are therefore proposed for an effective coupling of spin and valley physics.

The final part of the thesis is focussed on energy harvesting, particularly, on the generation of electricity from solar radiation using two-dimensional vdW hetero-bilayers of ZrS_3/MS_2 and ZrS_3/MXY (M=Mo, W; X, Y=S, Se, Te; $X \neq Y$) [3]. Electronic, optical, and transport properties in these 2D vdW hetero-bilayers have been investigated in-depth for the purpose of exploring their prospects for applications in photovoltaics. The comprehensive study presented in this Ph.D. work illustrates a new avenue for an efficient solar energy conversion at the nanoscale based on ZrS_3/MS_2 and ZrS_3/MXY vdW hetero-bilayers in ultrathin, 2D excitonic solar cells.

The thesis emphasises the fundamental and technological significance of sustainable and alternative energy harvesting as well as next-generation electronic devices through efficient use and engineering of 2D materials. The approach implemented in the Ph.D. work involves in studying the several entangled properties in a multifunctional material, thereby enabling to draw a systematic correlation between them.

TABLE OF CONTENT

Content **Page No**
Declaration i
Acknowledgement iii
Abstract v
Table of content vii
List of Figures x
List of tables xvii
Abbreviations xix
Symbols xxi
Chapter 1 INTRODUCTION 1-14
1.1 An overall introduction to 2D materials and their vdWHs 3
1.2 Objective of thesis 5
    1.2.1 Piezoelectricity in 2D materials 5
    1.2.2 Spintronics in 2D materials 8
    1.2.3 Valleytronics in 2D materials 9
    1.2.4 Excitonic solar cells of 2D vdWHs 12
Chapter 2 Theoretical Methodology 15-44
2.1 Elementary many particles' physics 17
2.2 Density Functional Theory 20
    2.2.1 Hohenberg-Kohn theorem 22
    2.2.2 Kohn-Sham formalism 24
    2.2.3 Exchange-correlation functionals 27
        2.2.3.1 Local Density Approximations 27
        2.2.3.2 Generalized Gradient Approximations 28
        2.2.3.3 Meta-Generalized Gradient Approximations 29
        2.2.3.4 Hybrid functionals 29
        2.2.3.5 Correction of exchange-correlation error: van der Waals correction 31
    2.2.4 Methods for Electronic Structure Calculations 31

        2.2.4.1 Pseudopotential Approach 32
    2.2.5 Density-functional perturbation theory 33
        2.2.5.1 Perturbation in Kohn-Sham scheme 33
        2.2.5.2 Lattice dynamics approach 34
2.3 Vienna ab-initio simulation package (VASP) 35
2.4 Mechanical properties 37
2.5 Piezoelectric properties 38
2.6 Charge carrier mobility and Exciton binding energy 39
2.7 Optical properties 40
2.8 Power Conversion Efficiency of solar cell 41
2.9 Calculation details 42
Chapter 3 Piezoelectronic and spintronic properties of 2D Janus monolayers and bilayers of group-IV transition metal trichalcogenides 45-68
3.1 Introduction 47
3.2 Results and Discussion 50
    3.2.1 Crystal Structures and Symmetry 50
    3.2.2 Chemical Bonding Interactions 51
    3.2.3 Stability 53
    3.2.4 Elastic Properties 54
    3.2.5 Piezoelectric Properties 55
    3.2.6 Electronic Properties 61
    3.2.7 Rashba Properties 63
3.3 Conclusions 66
Chapter 4 Valley spin polarization in h-MN (M=Nb, Ta) monolayers 69-94
4.1 Introduction 71
4.2 Results and Discussion 73
    4.2.1 Crystal Symmetry and Electronic Property 73
    4.2.2 Rashba Effect 78
    4.2.3 Valley Physics of h-NbN monolayer 84
    4.2.4 Berry Curvature Modulation in h-NbN monolayer 89
    4.2.5 Response to Vertical Electric Field 93
4.3 Conclusions 94

Chapter 5 Electronic and optical properties of ZrS3/MS2 and ZrS3/MXY (M=Mo, W; X, Y=S, Se, Te; X≠Y) based type-II van der Waals heterostructure (vdWH) 95-122

5.1 Introduction 97

5.2 Results and Discussion 99

    5.2.1 Crystal structures of monolayer MoS_2, WS_2, their Janus structures MXY and ZrS_3/MS_2 vdW hetero-bilayers (M=Mo, W) 99

    5.2.2 Electronic properties 106

    5.2.3 Power Conversion Efficiency (PCE) 112

    5.2.4 Optical property 115

    5.2.5 Transport property 118

5.3 Conclusions 122

Chapter 6 Summary and Future Scope & Perspective 123-128

6.1 Summary 125

6.2 Future Scope & Perspective 127

List of Publications 129

Bibliography 133

Appendix Permissions for Content Reused 155

Vita 157

List of Figures

Figure 1.1 *Schematic representation of different kinds of energy conversion as well as futuristic electronics using different DOF of electrons (i.e., charge, spin and valley) investigated in the 2D materials*. **6**

Figure 1.2 *Schematic representation of the generation of piezoelectricity in monolayers; graphene (centrosymmetric) does not show piezoelectricity but h-BN exhibits due to broken inversion symmetry along in-plane and similarly out-of-plane polarization can be induced in Janus TMTC monolayers.* d_{11} *represents the in-plane piezoelectric coefficient and* d_{33} *represents the out-of-plane piezoelectric coefficient*. **6**

Figure 1.3 *Piezotronics and Spintronics in Janus TMTC monolayers. Schematic of next-generation spintronic device*. **8**

Figure 1.4 *Schematic of valley selective optical selection and valley hall effect. Valley-based information. Information can potentially be stored in "valley polarizations" of 2D semiconductors by polarizing carriers into −K and +K momentum space valleys. Here, a −K valley polarization of electrons and holes represents "0," and a +K valley polarization represents "1"* **10**

Figure 1.5 *Schematic of* ZrS_3/MS_2 *vdWHs based excitonic solar cell*. **13**

Figure 2.1 *Flow chart of the self-consistent procedure to solve Kohn-Sham equation*. . **26**

Figure 2.2 *Schematic of the workflow of VASP*. **37**

Figure 3.1 *(a) Crystal structure, (b) Top view, (c) Side view along a-axis and (d) Side view along b-axis of* MX_3 *monolayers. Similarly, for Janus* MX_2Y *monolayers (e) Crystal structure, (f) Top view, (g) Side view along a-axis and (h) Side view along b-axis*. **50**

Figure 3.2 *Chemical bond analysis: (a) Charge density distribution, (b) Charge transfer distribution and (c) Electron localization function (ELF) of* $ZrSe_3$ *monolayer (First part: 3D view and second part: projection on the (010) plane). Similarly, (d), (e), (f) for the Janus monolayer* $ZrSe_2S$. **52**

Figure 3.3 *Phonon frequency spectra of 2D Janus TMTC monolayers*. **53**

Figure 3.4 *Total energy fluctuation of the 2D Janus monolayer of (a)* TiS_2Se*, (b)* $TiSe_2S$*, (c)* ZrS_2Se *and (d)* $ZrSe_2S$ *with respect to time in AIMD simulation at 300 K. The inset shows the snapshot of the initial and final geometry depicting structural change in these monolayers in the AIMD simulation at 300 K*. **54**

Figure 3.5 Out-of-plane elastic constant (C_{33}), piezoelectric constant (e_{33}/d_{33}) and Universal anisotropy index, A_U of 2D Janus TMTC monolayers. **57**

Figure 3.6 Strain effects on in-plane and out-of-plane piezoelectric constants of 2D Janus $ZrSe_2S$ monolayer. **58**

Figure 3.7 Bilayer Janus structure of (a) Stacking-1 and (b) Stacking-2. Stacking-2 is designed by rotating 180 degree the top layer of stacking 1 with respect to z-axis. **58**

Figure 3.8 Variation in out-of-plane (a) piezoelectric stress constants (e_{33}), (b) elastic constant (C_{33}), (c) piezoelectric stain constants (d_{33}) and Universal Anisotropy Index (A_U) of bilayer $TiSe_2S$ with vertical compressive strain; h is the inter-layer distance in the bilayer, (d) schematic of the bilayer system under applied vertical compressive strain, (e) band structure in stacking-1 in bilayer $TiSe_2S$ under 0% and 8% vertical compressive strain, (f) variation in the band gap in stacking-1 in bilayer $TiSe_2S$ with vertical compressive strain. **59**

Figure 3.9 The initial and final geometry depicting structural change of bilayer Janus TiSe2S in AIMD simulation at 300 K. There is no noticeable distortion in the final geometry after 5 ps. **61**

Figure 3.10 Phonon frequency spectra of stacking-1 and stacking-2 of bilayer Janus $TiSe_2S$. **61**

Figure 3.11 Atomic layer and orbital projected bandstructure of (a) ZrS_3, (b) ZrS_2Se, (c) $ZrSe_3$, (d) $ZrSe_2S$ using HSE06 functional. (e) side view of crystal structure indicating layer number, (f) top view of crystal structure and (g) Reciprocal lattice vectors with shaded First Brillouin Zone (1BZ). **62**

Figure 3.12 (a) Planar average of electrostatic potential of 2D Janus TiS_2Se monolayer. The red arrow indicates the direction of the local electric field. (b) Band structure of 2D Janus TiS_2Se monolayer with and without spin-orbit coupling (SOC) using GGA-PBE functional. (c) Electronic band structure of monolayer Janus TiS_2Se with SOC using GGA_PBE functional with S_x spin projection. (d) Enlarged band structure as indicated in Figure 12c. Colour map represents the expectation value of S_x spin projection. (e) Spin structures of the Rashba split states for the spin projections S_x, S_y and S_z at an energy, $E = -0.17$ eV and $E_F = 0.0$ eV. **64**

Figure 3.13 Bandstructures of Janus TMTC monolayers near Fermi level with and without spin-orbit coupling (SOC) using GGA-PBE functional. Fermi level (EF) is set to zero. . **65**

Figure 3.14 Modulation of Rashba parameter, α_R of Janus TiS_2Se monolayer with application of strain along b-axis. **66**

Figure 4.1 (a) Top and side view of crystal structure of h-NbN, (b) 3D band structure near fermi level, (c) Energy contours of top valence band (VB), (d) Energy contours of bottom *conduction band (CB), (e) Band structure along high symmetry k-path. (f), (g) and (h) are enlarged view as in indicated in (e). Fermi level is set to zero. GGA-PBE functional is used to calculate electronic structure. (i) First Brillouin Zone (1BZ) of h-NbN monolayer. . . .***74**

Figure 4.2 Orbital projected band structure of h-NbN monolayer. **75**

Figure 4.3 *Phonon spectra of 2D monolayers of MX (M=V, Nb, Ta; X=N, P, As). . . . .* **76**

Figure 4.4 *Band structures of 2D monolayers of VN, NbN, NbP and TaN. . . . .* **77**

Figure 4.5 *Trend of band gap, SOC splitting and berry curvature in VN, NbN, NbP and TaN. . . . .* **78**

Figure 4.6 *Spin projected band structure of (a) S_x, (b) S_y and (c) S_z spin in monolayer h-NbN. Color map represents the spin expectation value. Fermi level is set to zero. ***78**

Figure 4.7 *Spin projected top two valence bands, i.e., (a) S_x, (b) S_y and (c) S_z in h-NbN. Corresponding contour plot (d, e, f) at $E=-0.5$ eV, $E_F=0$ eV: color map represents the expectation value of corresponding spin projection. Modulation of (g) energy offset, E_R, (h) momentum offset, k_R and (i) Rashba parameter, α_R with bi-axial strain. ***79**

Figure 4.8 *Spin-texture of top two valence bands of monolayer h-NbN, (b) Spin-texture around M-point as shown in Fig. (a). ***80**

Figure 4.9 *The Rashba parameter plotted as a function of different material descriptor: (a) electronegativity difference, (b) ionization energy difference, (c) Bader charges, (d) asymmetry in electric field, (e) Born effective charge (Z*) and (f) zz component of Z*. .***82**

Figure 4.10 *Distribution of electrostatic potential of NbN and NbP monolayers along z-direction. $\Delta\phi$ is the difference of work function, and the built-in electric field is from transition-metal atom to pnictide atom. Bader charge analysis shows that the inter-atomic charge transfer in NbN monolayer is 1.303 e. Two dashed vertical lines are the positions of transition-metal atom and pnictide atom. (b, d) Charge transfer distribution in NbN and NbP monolayers respectively. Isosurface value is set to 0.005 eV/Å^3. Cyan (yellow) colour represents the charge accumulation (depletion). . . . .* **83**

Figure 4.11 *Distribution of electrostatic potential of VN and TaN monolayers along z-direction. $\Delta\phi$ is the difference of work function, and the built-in electric field is from transition-metal atom to pnictide atom. Bader charge analysis shows that the inter-atomic charge transfer in NbN monolayer is 1.303 e. Two dashed vertical lines are the positions of transition-metal atom and pnictide atom. (b, d) Charge transfer distribution in VN and TaN monolayers respectively. Isosurface value is set to 0.005 eV/Å^3. Cyan (yellow) colour represents the spatial regions of charge accumulation (depletion). . . . .* **84**

Figure 4.12 *(a) Modulation of band structure of monolayer h-NbN with 5% compressive and tensile strain using GGA-PBE functional along with spin-orbit coupling (SOC). (b)* *and (c) are enlarged view of VB and CB as indicated in Fig. 4(a). Isoenergy contours of low energy valence bands of (d) 0% strain, (e) +5% and (f) -5% bi-axial strain respectively. Isoenergy contours of low energy conduction bands of (g) 0% strain, (h) +5% and (i) -5% bi-axial strain respectively.* **85**

Figure 4.13 *Bandgap modulation with bi-axial strain using GGA-PBE functional. (b) Tuning of SOC splitting of band edges with bi-axial strain using GGA-PBE + SOC functional.* **86**

Figure 4.14 *Spatial profile of Bloch wavefunctions for (a) VB and (b) CB edge states projected along the direction perpendicular to the basal plane of h-NbN monolayer. The atomic positions have been marked therein with dash vertical lines on Nb-N in the pristine (0%) system. Charge density of electronic states at the edges of VB hills and CB valleys for a 5% compressive strained (c, d), a strain-free (e, f) and a 5% tensile strained h-NbN monolayer. Isosurface value is set to 0.01 eV/Å^3.* **87**

Figure 4.15 *Variation in (a) elastic stiffness constants C_{11} and C_{12}. Variation in (b) Young's modulus, Y, and Poisson's ratio, v with bi-axial strain.* **89**

Figure 4.16 *(a) Contour map of Berry curvature distribution, Ω(k) of h-NbN monolayer in 2D k-space over all occupied Bloch bands of in units of Å^2. (b) Modulation of Berry curvature distribution along high symmetry k-line Γ-K-M-K-Γ with application of bi-axial strain, (c) Schematic of valley-selective excitation, (d) Circular dichroism polarization, $\eta(k)$.* **90**

Figure 4.17 *Vertical electric field modulation of (a) Rashba energy offset (ΔE_R), (b) momentum offset (Δk_R), (c) Rashba constant (α_R), (d) band gap (E_g), (e) CB SOC splitting (Δ_{SO}^{c}) and (f) VB SOC splitting (Δ_{SO}^{v}) in h-NbN monolayer.* **93**

Figure 5.1 *(a), (d), (g) and (j) are side views of MoS_2, MXY (M=Mo, W; X, Y=S, Se, Te; X≠Y), ZrS_3 monolayers and the ZrS_3/MoS_2 hetero-bilayer respectively in the first column. While (b), (e), (h) and (k) are the top views them respectively in the second column. (c), (f), (i) and (l) represent the electron localization function (ELF) in the third column. In Fig. (b), **a** and **b** form the primitive lattice vectors in the hexagonal unit cell, while the non-primitive lattice vectors $\mathbf{a_1}$ and $\mathbf{b_1}$ lie along the two mutually perpendicular directions in the rectangular unit cell. In-plane [100] direction is along x-axis, while [010] direction is along the y-axis. In Fig. (j), h is the inter-layer distance of the hetero-bilayer.* **100**

Figure 5.2 *Variation in binding energy per unit inter-facial area of ZrS_3/MS_2 hetero-bilayers with the interlayer distance of (a) case 1 (14 atoms in unit cell) and (b) case 2 (62 atoms in unit cell) using the GGA-PBE exchange correlation functional with DFT-D2 van der Waals correction.* **102**

Figure 5.3 *Variation in binding energy per unit inter-facial area of ZrS_3/MS_2 hetero-bilayers with the interlayer distance using the GGA-PBE exchange correlation functional with DFT-D2, DFT-D3, DFT-TS/HI for (a) case 1 and (b) case 2.* **103**

Figure 5.4 *(a) Band structure and (b) absorption coefficient (α) of ZrS_3/MoS_2 hetero-bilayer for case 1 using HSE06+DFT-D2, DFT-D3 and DFT-TS/HI. Fermi level is set to zero.* **104**

Figure 5.5 *Phonon frequency dispersion of ZrS_3/MS_2 hetero-bilayers (Case 1).* **105**

Figure 5.6 *Orbital projected electronic band structure of (a) MoS_2, (b) WS_2, (c) ZrS_3 monolayers HSE06 hybrid functional, (d) ZrS_3/MoS_2 and (e) ZrS_3/WS_2 hetero-bilayers (case 1) using HSE06 hybrid functional with DFT-D2 correction. Fermi level has been set to zero. Brillouin Zone of (f) hexagonal lattice of MS_2 and (g) rectangular lattice of ZrS_3 and ZrS_3/MS_2.* **107**

Figure 5.7 *Relaxed geometric structure of ZrS_3/MoS_2 hetero-bilayer in different stacking (a) S1, (b) S2, (c) S3. In Stacking-1, Mo atoms are placed above S atoms of ZrS_3 sheet. In Stacking-2, MoS_2 sheet is translated such that Mo atoms are placed on top of Zr atoms. In Stacking-3, MoS_2 sheet is rotated by 180 degree. (d, e) Band structures of ZrS_3/MoS_2 hetero-bilayer with different stacking. Band energy are plotted with respect to vacuum. (HSE06 + DFT-D2).* **108**

Figure 5.8 *Atomic layer projected band structure of (a) ZrS_3/MoS_2 and (b) ZrS_3/WS_2 vdW hetero- bilayers of case 1. Colour bar represents contribution of MS_2 layer. Fermi level is set to zero.The band decomposed charge density corresponding to the VBM and CBM of (c) ZrS_3/MoS_2 and (d) ZrS_3/WS_2 vdW hetero-bilayer with an isosurface value of 0.005 $e/Å^{-3}$. (HSE06+DFT-D2). The calculation of PCE has been discussed in section 5.2.3.* **110**

Figure 5.9 *Atomic layer projected band structure of (a) ZrS_3/MoS_2 and (b) ZrS_3/WS_2 vdW hetero- bilayers of case 2 using GGA-PBE with DFT-D2. Colour bar represents contribution of MS_2 layer. Fermi level is set to zero. (c,d) Energy of band edges (VBM and CBM) of the individual monolayers in the ZrS_3/MS_2 hetero-bilayer (case 2), as identified in (a) and (b) have been calculated further using HSE06 with DFT-D2 for a higher accuracy in PCE calculations. Energy of band edges are plotted with respect to vacuum level.* . **111**

Figure 5.10 *(a) Band edges of ZrS_3, MoS_2, MoSeTe, WS_2, WSSe, WSTe, WSeTe isolated monolayers calculated with respect to the absolute vacuum level using HSE06 functional. (b) Computed power conversion efficiency (PCE) contour as a function of donor bandgap and conduction band offset. The calculated PCE according to Anderson limit of possible type-II hetero-bilayers (Case 3) have been indicated by circles and stars.* **114**

Figure 5.11 *Absorption coefficient (α) of MoS_2, WS_2, ZrS_3 monolayers and ZrS_3/MS_2 hetero-bilayers for Case 2 using HSE06 + DFT-D2.* **115**

Figure 5.12 *Real (ε_1) and imaginary (ε_2) part of the dielectric function of (a) MoS_2, WS_2, ZrS_3 monolayers using hybrid HSE06 functional and (b) ZrS_3/MoS_2, ZrS_3/WS_2 hetero-bilayers (Case 1) using HSE06 with DFT-D2. (c) Extinction coefficient (κ) and (d) Absorption coefficient (α) as the function of wavelength.* **116**

Figure 5.13 *Deformation Potential of ZrS_3 monolayer. VBM_A and VBM_B represent the valence band minima when strain is applied along A-axis and B-axis respectively. A-axis & B-axis correspond to [100] and [010] directions respectively. Band edges are plotted with respect to vacuum. (GGA-PBE)* **117**

Figure 5.14 *Deformation Potential of (a) MoS_2 and (b) WS_2 monolayer. Band edges are plotted with respect to vacuum. (GGA-PBE).* **117**

Figure 5.15 *Deformation Potential of (a) ZrS_3/MoS_2 and ZrS_3/WS_2 hetero bilayers. Band edges are plotted with respect to vacuum. (GGA-PBE with DFT-D2).* **117**

Figure 5.16 *Deformation Potential of (a) ZrS_3/MoS_2 and ZrS_3/WS_2 hetero bilayers of case 2. Band edges are plotted with respect to vacuum. VBM_A and VBM_B represent the valence band minima when strain is applied along A-axis and B-axis respectively. A-axis & B-axis correspond to [100] and [010] directions respectively. (GGA-PBE + DFT-D2).* **118**

Figure 5.17 *Carrier mobility ratio (R) of monolayer MoS_2, WS_2, ZrS_3 and the ZrS_3/MS_2 hetero-bilayers (case 2) along (a) [100] and (b) [010] direction. (c) Exciton binding energies of these systems calculated using Mott-Wannier hydrogenic model.* **120**

List of Tables

Table 3.1 *Lattice constants [a, b (Å)], lattice angle [α, β, γ (º)], bond-lengths [d_1, d_2, d_3, d_4 (Å)], bond angles [θ_1, θ_2 (º)], cohesive energy per unit cell [E_c (eV)], charge transferred from metal atom [ΔQ_M(e)], dipole moment [μ (Debye)].* **51**

Table 3.2 *Elastic stiffness constants [C_{11} (N/m), C_{22} (N/m), C_{12} (N/m)], Young Modulus [Y_{11} (N/m), Y_{22} (N/m)] and Poisson Ratio [υ_{11}, υ_{22}] of TMTC monolayers MX_3 and their Janus derivatives MX_2Y.* **55**

Table 3.3 *Piezoelectric stress/strain constants (e/d) of Janus TMTC monolayers. The units of C, e, d is N/m, 10^{-10} C/m and pm/V respectively.* **56**

Table 3.4 *Out-of-plane piezoelectric constants (e_{33}/d_{33}) of bilayer Janus $TiSe_2S$ and $ZrSe_2S$ monolayers. The units of C_{33}, e_{33}, d_{33} are N/m, pC/m and pm/V respectively.* **58**

Table 3.5 *Bandgap of Janus TMTC monolayers. "M" stands for metallic state. "I" represents indirect band gap.* **62**

Table 3.6 *Orbital contribution of valence band of 2D Janus TiS_2Se monolayer at Γ and K' point as shown in without SOC band structure of Fig. 3.12(b).* **63**

Table 3.7 *Parameters characterizing Rashba splitting in Janus monolayers of TMTC.* **65**

Table 4.1 *Orbital contribution to VB edge of h-NbN monolayer.* **75**

Table 4.2 *Orbital contribution to CB edge of h-NbN monolayer.* **75**

Table 4.3 *Band gap, SOC splitting in valence band (VB) and conduction band (CB) and Berry curvature. Band gap has been calculated using Heyd–Scuseria–Ernzerhof (HSE) functional.* **77**

Table 4.4 *Orbital composition of the top valence band at M-point.* **80**

Table 4.5 *Rashba parameters.* **81**

Table 4.6 *The calculated mechanical stiffness constants C_{ij}, layer modulus (γ^{2D}), Young's modulus (Y), Poisson's ratio (ν), intrinsic strength (σ_{int}), bending modulus (D).* **88**

Table 5.1 *Optimized lattice constants, bond lengths in TMDC monolayers, their Janus structures, ZrS_3 monolayers and ZrS_3/MS_2 hetero-bilayers.* **101**

Table 5.2 *Lattice parameters (a, b), inter-layer distance (h) and binding energy (E_b) of ZrS_3/MoS_2 hetero-bilayer with different vdW-interactions.* **103**

Table 5.3 *Power Conversion Efficiency (PCE) of* ZrS_3/MoS_2 *hetero-bilayer for case 1 using HSE06+DFT-D2, DFT-D3 and DFT-TS/HI.* **105**

Table 5.4 *Power Conversion Efficiency (PCE) of* ZrS_3/MoS_2 *hetero-bilayer in different stacking.* **107**

Table 5.5 *Power Conversion Efficiency (PCE) of* ZrS_3/MoS_2 *hetero-bilayer in different case using HSE06 + DFT-D2.* **113**

Table 5.6 *Power Conversion Efficiency (PCE) of* ZrS_3/WS_2 *hetero-bilayer in different case using HSE06 + DFT-D2.* **113**

Table 5.7 *Elastic stiffness constant (*C_{2D}*), deformation potential (*E_{2D}*), effective mass (m*), carrier mobility (*μ_{2D}*), static dielectric constant (ε), exciton effective mass (*μ_{ex}*) and exciton binding energy (*E_b^{ex}*) of* MS_2*,* ZrS_3 *monolayers and* ZrS_3/MS_2 *hetero-bilayers (Case 1 and Case 2).* **119**

Table 5.8 *Exciton binding energy of the materials.* **121**

Abbreviations

2D	Two-dimensional
DFT	Density Functional Theory
DFPT	Density Functional Perturbation Theory
AIMD	Ab-Initio Molecular Dynamics
DOF	Degrees of Freedom
VSS	Valley Spin Splitting
vdWs	van der Waals
vdWHs	van der Waals heterostructures
VASP	Vienna ab-initio simulation package
TMDC	Transition-metal dichalcogenide
TMTC	Transition-metal trichalcogenide
SOC	Spin-Orbit Coupling
FET	Field Effect Transistor
SFET	Spin Field Effect Transistor
FM	Ferromagnet
VHE	Valley Hall Effect
XSC	Excitonic Solar Cell
PCE	Power Conversion Efficiency
HK	Hohenberg-Kohn
KS	Kohn-Sham
LDA	Local density approximation
GGA	Generalized gradient approximations
XC	Exchange-correlation
HF	Hartree-Fock
PBE	Perdew-Burke-Ernzerhof functional
HSE	Heyd–Scuseria–Ernzerhof
HOMO	Highest Occupied Molecular Orbital

LUMO	Lowest Unoccupied Molecular Orbital
CB	Conduction Band
VB	Valence Band
CBM	Conduction Band Minima
VBM	Valence Band Maxima
EQE	External Quantum Efficiency
FF	Fill Factor
DOS	Density of States
PFM	Piezoresponse force microscopy
AFM	Atomic force microscopy
ELF	Electron Localization Function
BZ	Brillouin Zone
BEC	Born Effective Charges
RHCP	Right-handed circularly polarized light
LHCP	Left-handed circularly polarized light
DP	Deformation Potential

Symbols

$\hbar$	Planck's constant
ρ	Charge density
Z_{ij}^{*}	Born effective charge tensor
T	Temperature in K
E_c	Cohesive energy per unit cell
m^{*}	Effective mass of electron/hole
σ_{ij}	Elastic stress tensor
ε_{kl}	Elastic strain tensor
C_{ijkl}	Total elastic stiffness tensor
P_i	Polarization vector
e_{ijk}	Piezoelectric stress coefficient
d_{ijk}	Piezoelectric strain coefficient
Y	Young's modulus
γ^{2D}	2D layer modulus
G	Shear modulus
D	Bending modulus
σ_{int}	Intrinsic strength
ν	Poisson ratio
ϵ_c	Buckling strain
κ	Extinction coefficient
α_{abs}	Absorption coefficient

Chapter 1

INTRODUCTION

1.1 An overall introduction to two-dimensional materials

A revolution in materials science has been accomplished through atomically thin two-dimensional (2D) materials. A rich set of electronic states can be found in 2D materials that differ substantially from those of their bulk counterparts due to quantum confinement and enhanced many-body effects [4]. The family of 2D materials, which started with graphene [5], has expanded quickly over the past few years and now includes insulators, semiconductors, semimetals, metals, and superconductors [6]. This development has stimulated an explosion in envisioned applications ranging from battery electrodes and catalysis to photovoltaics and electronics [7]. Despite the superior properties of graphene [8–10], the absence of a band gap limits its application in digital electronics. Hence, 2D semiconducting materials with considerable band gaps and high carrier mobilities have recently attracted tremendous attention [11]. In terms of materials, the most well-studied 2D systems beyond graphene, are the insulator hexagonal boron-nitride (hBN) [12,13], the anisotropic semiconductor phosphorene [14,15], and the semiconducting Mo- and W-based transition metal dichalcogenides (TMDCs) with the chemical formula MX_2 (M: transition metal; X: chalcogen) [16]. In addition to the Mo- and W-based compounds, about a dozen other semiconducting and metallic TMDCs have been synthesized in mono- or few-layer form. Apart from graphene (C) and phosphorene (P) a host of other elemental 2D materials, including borophene (B) [17], silicene (Si) [18,19], stanene (Sn) [20] and germanene (Ge) [21] have been realized on different substrates. Additionally, Group III–V compounds [22,23], transition metal carbides and -nitrides (MXenes) [24], transition metal oxides [25] and -halides [26], as well as organic-inorganic hybrid perovskites [27,28], represent new developing classes of 2D materials.

In the last 15 years, several electronic and optoelectronic applications have been investigated in 2D semiconducting materials. The advances in channel material treatment and device configuration ideally suit 2D channel-based FETs for nanoelectronics [29]. Unusual properties are exhibited by 2D systems according to their thickness or electrical and chemical environments. 2D devices were advanced by optimizing issues such as quality, dielectric environment, and contact resistance. Due to their exceptional properties, it is not only limited to conventional devices such as photodetectors, light emitters, and memory devices, but also novel applications such as flexible devices, tunnelling devices, and valley and spin electronics can be explored in 2D semiconductors. However, it still requires technological leaps and scientific study to realize their superior and novel properties in practical applications compared with conventional bulk materials [29].

Furthermore, the challenges are that all the above physical properties rely on high-quality materials, and the compatibility with integrated circuits and future commercialization requires large-scale synthetic techniques [30,31]. To address these challenges, continuous efforts have been devoted to exploring and investigating diverse synthetic methods of 2D materials. Basically, the synthetic strategies can be divided into two classes, i.e., top-down and bottom-up methods. In top-down methods, high-quality bulk crystals are first obtained by flux growth method [32,33], or chemical vapor transport (CVT) [34] and then the crystals are isolated into atomically thin flakes via various exfoliation technologies. Contrastingly, in bottom-up methods, vdW atomically thin flakes are prepared by assembling atoms on substrates directly, such as physical vapor deposition (PVD) or chemical vapor deposition (CVD) and molecular beam epitaxy (MBE). In both bottom-up and top-down methods, different flakes can be further stacked together [35,36], which provides an intriguing platform for achieving various heterostructures. In very recent years, great progress has been made in the field of synthesizing large-scale and high-quality 2D materials [37].

Even though 2D systems are fascinating in their own merit, much larger potential lies in the possibility of reassembling several dissimilar 2D materials into new layered compounds [30]. To achieve atomic interface design, energy band engineering and crystal symmetry regulation, heterostructures can be fabricated conveniently by stacking together various 2D materials. The stacking is very convenient as the surfaces of 2D materials are dangling-bond free. The fabrication of heterostructures with atomically sharp interfaces is possible due to the absence of chemical bonding between such different layers. These heterostructures are usually mentioned as van der Waals (vdW) heterostructures as the weak van der Waals interaction plays a role at the interface and is gaining more and more research attention from both fundamental and technological application perspectives [4].

The creation of a large variety of vdW heterostructures (vdWH) with free of lattice mismatching opens up an unprecedented opportunity for development of novel electronic, optoelectronic and spintronic devices with desirable functions and performance [38–41]. Many degrees of freedom are available for tuning electronic properties of vdWHs, such as material selections in stacking [42], twisted angle of component layers [43] etc. More interesting physics phenomena would emerge due to enhanced electron orbitals coupling in adjacent 2D materials when two individual 2D materials are stacked together [44]. For example, moire patterns can be created in the Gr/h-BN vdW heterostructure [45]. Gate-tunable Mott-like insulating and superconducting, as well as ferromagnetism behaviours, can be observed in the twisted bilayer electronic systems [46,47]. In the Gr/h-BN/Gr vertical vdW heterostructure, suitable alignment of crystallographic orientation in two graphene layers allows for realization of resonant tunnelling phenomenon [48,49].

The vdWH comprising of two different semiconductors can be generally classified into three categories according to the band alignment such as Type-I, Type-II and Type-III. For type-I vdWH, the electrons and holes will be accumulated in one semiconductor. Whereas for type-II band alignment, there is a spatial separation between electrons and holes i.e., electrons and holes will accumulate in two different semiconductors. Hence, the corresponding applications of type-I and type-II are very different. Type-I has very limited application, such as in LEDs, due to the fast recombination of charges in one layer [50]. In type-II band alignment, the recombination rate of the charge carriers decreases and thereby increases their lifetime, which is very beneficial for utilizing those photoexcited electrons and holes in high-performance nano and optoelectronic devices [51].

This Chapter provides a brief introduction to the Ph.D. work, while the details have been presented in the relevant Chapters.

1.2 Objective of the thesis

In energy-conversion systems and low-power electronics, there are many prospects towards 2D materials. For this reason, various research areas are now focused on exploring new materials to realize the desired properties. Fig. 1.1 shows the schematic representation of different kinds of energy conversion as well as futuristic electronics using different degrees of freedom (DOF) of electrons (i.e., charge, spin and valley) that have been investigated in the present thesis. A brief overview of the research topics that have been explored individually in the subsequent chapters is as follows.

1.2.1 Piezoelectricity in 2D monolayers

The non-centrosymmetric material having crystal symmetry not containing inversion symmetry [(x, y, z) → (-x, -y, -z)], is a prominent research area because of the coupling between the mechanical and electrical behaviours to allow efficient interconversion

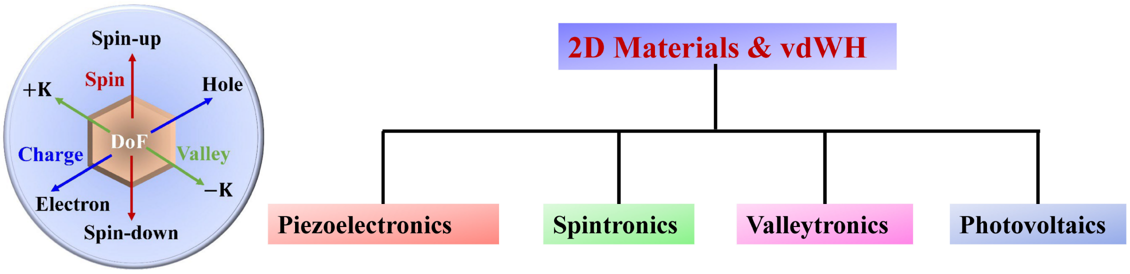
Spin-up
+K
Spin
Hole
Charge
DoF
Valley
Electron
−K
Spin-down
2D Materials & vdWH
Piezoelectronics
Spintronics
Valleytronics
Photovoltaics

Figure 1.1 *Schematic representation of different kinds of energy conversion as well as futuristic electronics using different DOF of electrons (i.e., charge, spin and valley) investigated in the 2D materials.*

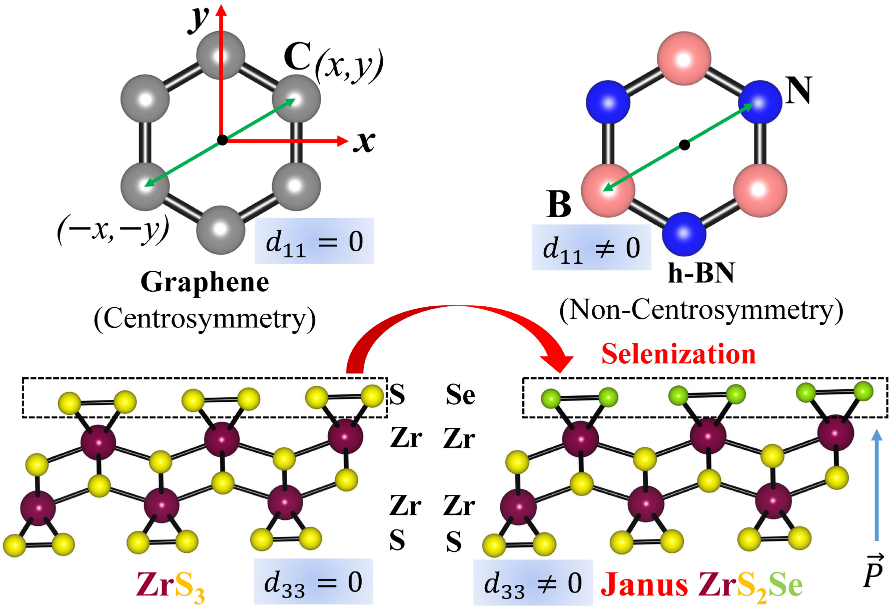
y
C(x,y)
x
(−x,−y)
d₁₁ = 0
Graphene
(Centrosymmetry)
N
B
d₁₁ ≠ 0
h-BN
(Non-Centrosymmetry)
Selenization
S
Se
Zr
Zr
Zr
Zr
S
S
ZrS₃
d₃₃ = 0
d₃₃ ≠ 0
Janus ZrS₂Se
P

Figure 1.2 *Schematic representation of the generation of piezoelectricity in monolayers; graphene (centrosymmetric) does not show piezoelectricity but h-BN exhibits due to broken inversion symmetry along in-plane and similarly out-of-plane polarization can be induced in Janus TMTC monolayers.* d_{11} *represents the in-plane piezoelectric coefficient and* d_{33} *represents the out-of-plane piezoelectric coefficient.*

between mechanical energy and electrical energy. Piezoelectricity describes the ability of a non-centrosymmetric solid to produce polarization charges in response to the externally applied mechanical stress. For piezoelectric materials, non-centrosymmetry analysis is a direct and effective method to estimate the existence of piezoelectricity. The piezoelectric effect was first observed in quartz crystals by the Curie brothers in 1880, and since then, plenty of materials, including crystals, polymer, and bi-molecules, have been reported to possess the piezoelectric responses for example GaN, BaTiO3, etc. and piezoelectric ceramics, such as lead zirconate titanate (PZT), which have been widely used in actuators, ultrasonics, transducers, sensors and energy harvesting systems [52,53]. The coupling of piezoelectricity and semiconductor materials has given rise to a new discipline named piezotronics. Compared with traditional bulk semiconductors, two-dimensional (2D) semiconductor materials not only exhibit excellent semiconducting characteristics but also have an outstanding mechanical performance [54]. Single-layer graphene having a hexagonal honeycomb structure presents central symmetry and has no piezoelectric properties. By contrast, monolayer h-BN exhibits piezoelectricity for inversion symmetry breaking [55,56], which has been illustrated in Fig. 1.2. However, h-BN is an intrinsic insulator with a bandgap of 5.5–6 eV (ultraviolet region), restricting its application in electronic devices. In 2012, based on DFT calculation, Duerloo et al. first predicted that monolayer TMDC materials are piezoelectric, unlike their bulk crystals [56]. Two years later, Wu et al. demonstrated this prediction using the flexible MoS_2 piezoelectric nanogenerator [57]. In 2014, Zhu et al. have proposed a novel device configuration for detecting the in-plane piezoelectricity in monolayer MoS_2 [58]. Their findings indicated that an odd number of layers of flakes would produce an in-plane piezoelectric response when mechanical strain or an electric field is applied, and the piezoelectric coefficient is comparable to that of the traditional bulk piezoelectric semiconductor. Compared with traditional piezoelectric semiconductors (like ZnO, GaN), 2D TMDCs have attracted much attention due to their exceptional mechanical and semiconducting properties [54].

For the application of atomically thin piezoelectric materials in practical device applications involves some critical issues because the piezoelectric current and voltage outputs are only about dozens of pA and mV, as found in monolayer MoS_2 [57]. Therefore, there is still a need to explore new 2D piezoelectric materials or new avenues to bring about a high magnitude of polarization and larger piezoelectric output signals together with long-term durability. For instance, in this Ph.D. work, inversion symmetry has been broken in the intrinsically centrosymmetric MX_3 (M=Ti, Zr, and Hf; X=S, Se) monolayers upon the

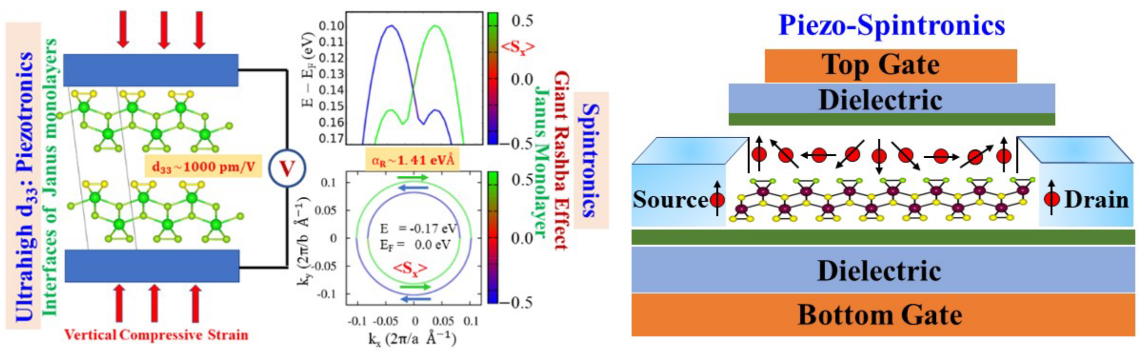
Ultrahigh d_{33}: Piezotronics
Interfaces of Janus monolayers
d_{33} ~1000 pm/V
V
Vertical Compressive Strain
$E - E_F$ (eV)
0.10
0.11
0.12
0.13
0.14
0.15
0.16
0.17
0.5
<S_x>
0.0
−0.5
α_R ~1.41 eVÅ
k_y (2π/b Å^{-1})
0.1
0.05
0
-0.05
-0.1
E = -0.17 eV
E_F = 0.0 eV
<S_x>
-0.1 -0.05 0 0.05 0.1
k_x (2π/a Å^{-1})
0.5
0.0
−0.5
Giant Rashba Effect
Janus Monolayer
Spintronics
Piezo-Spintronics
Top Gate
Dielectric
Source
Drain
Dielectric
Bottom Gate

Figure 1.3 *Piezotronics and Spintronics in Janus TMTC monolayers. Schematic of next-generation spintronic device.*

formation of their Janus structures as depicted in Fig. 1.2. As a result, a high level of piezoelectricity has been found to emerge in Janus Group TMTC monolayers along with giant Rashba effect, which has been discussed in detail in Chapter 3. The corresponding schematic has been presented in Fig. 1.3.

1.2.2 Spintronics in 2D monolayers

Spintronics which targets to exploit the spin degree of freedom (DOF) to counterpart the charge DOF of electrons as the information carrier, is one of the emerging fields for the next-generation nanoelectronic devices to reduce their power consumption and to increase their memory and processing capabilities [59]. Immediately after the discovery of giant magnetoresistance (GMR) in 1988, the research on spintronics has excelled outstanding advances in the development of information storage devices in the last few decades [60]. The physics behind the giant magnetoresistance (GMR) as observed in the metallic multilayers of ferromagnetic/nonmagnetic (FM/NM) where the resistance depends on the relative orientation of the ferromagnetic layers, has formed the foundation of spintronics and over past three decades the evolution of spin-transport experiments is advanced. Since Bychkov and Rashba suggested a simple relationship between charge and spin [61], Rashba spin–orbit coupling (SOC) has been a major topic of interest in the field of spintronics. Rashba SOC has led to a tremendous number of new discoveries and theories in physics, and to useful applications in electronics [62,63]. The essential feature of SOC is that a spin-polarized electron moving in an electric field experiences an effective magnetic field which drives the precession of the spin orientation even without an external magnetic field. Furthermore, the strength of the Rashba effective magnetic field can be modulated by an external gate voltage [64]. In 1990, Datta and Das proposed the idea of spin field effect transistor (spin FET), which relies on manipulation of the spins during transport in a semiconductor with an electric field [65]. After that, numerous investigations have been dedicated to electrical control of the spin current, which is key to realizing the device conception of spin transistor [66,67]. Due to the Rashba spin-orbit interaction (i.e., generation of an effective magnetic field by an electric field applied to the gate terminal), in the spin-transistor, the spin injected from the source FM contact travels towards the drain FM contact via Larmor precession. Spin-transistor is generally ON (i.e., depletion mode) because no precession at zero gate voltage leads to the spin direction parallel to the drain FM. Changing the gate voltage can then adjust the spin precession angle to result in a periodic modulation of the source-to-drain current. Even if, spin transistor assures performances of greater speed and energy-efficiency than conventional transistors [68], finding the optimal device structure employing the best-suited materials for each element still necessitates massive research ventures [60]. Enormous effort has been spent in injecting, detecting, and manipulating spin polarized electrons in metals and conventional semiconductors [69–72]. However, in spite of these efforts, an ideal candidate material for the spin channel is still needed. 2D materials, including graphene, the surface states of TIs, and TMDCs could be promising candidates due to their unusual spin dependent physical properties. No doubt, new prospects have been opened up due to the versatile crystal structures and functionalities of 2D materials and vdW heterostructures. The flexible piezo-spintronics devices of Janus TMTC monolayers, as illustrated in the schematic of Fig. 1.3, have been discussed in detail in Chapter 3.

1.2.3 Valleytronics in 2D monolayers

In crystalline materials, the electronic band structure establishes the correlation between the crystal momentum and energy of an electron. In intrinsic semiconductors, the electronic and optical properties are mainly governed by the two bands near about Fermi energy, one is the highest valence band (VB) below the Fermi energy and another is the lowest conduction band (CB) above the Fermi energy. The local minima in the CB or local maxima in the VB are referred to as “valleys”, which are stable points in the band structure where electrons or holes can reside.

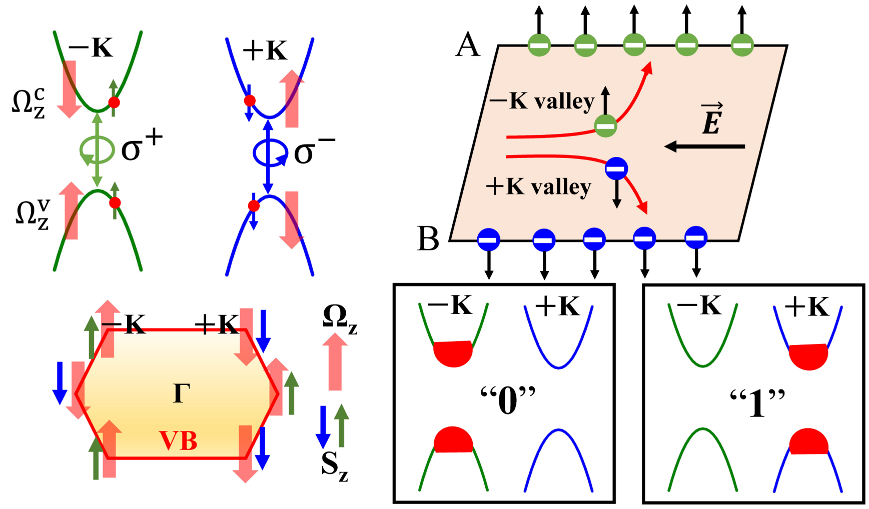

Figure 1.4 *Schematic of valley selective optical selection and valley hall effect. Valley-based information. Information can potentially be stored in "valley polarizations" of 2D semiconductors by polarizing carriers into −K and +K momentum space valleys. Here, a −K valley polarization of electrons and holes represents "0," and a +K valley polarization represents "1."*

So, in addition to charge and spin, electrons in a crystalline solid also have a valley degree of freedom (DOF) that controls the electron's position in crystal momentum space. The field of valleytronics is about using the electron's valley DOF to encode and process information, similar to charge in electronics or spin in spintronics [73–77]. An ideal valleytronic material system has a band structure composed of two (or more) degenerate but inequivalent valley 'states' (local energy extrema) that can be manipulated to encode, process and store information. The key drive of this field is to recognize valleytronic materials that can offer information storage and processing advantages that complement or surpass modern charge- and spin-based semiconductor technologies [78]. For example, a pure valley (or spin) current offers the possibility of carrying valley (or spin) information without the ohmic heating associated with a charge current. However, unlike charge that is easily manipulated by electric fields, it is more difficult to manipulate particles based on the valley degree of freedom. Moreover, compared with spintronic operations enabled by the various spin phenomena, the ability to exploit valley polarizations has been rather limited until the recent emergence of 2D materials with hexagonal honeycomb structures.

The electronic properties of 2D materials with hexagonal honeycomb structures, for example, graphene and TMDCs (e.g., MoS_2, WSe_2 etc.) are governed by the two inequivalent valleys of band edges that appear at the corners of the hexagonal Brillouin zone (i.e., +K and –K high-symmetry k-points). These valleys can be represented by a binary pseudospin that behaves like a spin-1/2 system; the electrons in the +K valley can be labelled as valley-pseudospin up, and the electrons in the –K valley can be labelled as valley-pseudospin down. Therefore, in a doped system, a carrier population distribution polarized in a +K or –K valley can store binary information. These systems are predicted to exhibit an anomalous Hall effect whose sign depends on the valley index, which is called the valley Hall effect (VHE) [77]. The valley Hall effect refers to the opposite Hall currents for carriers located in opposite valleys. It is the analogue of the spin Hall effect, which has been exploited for the electrical generation of spin polarization [79]. The schematic of valley selective optical selection, valley hall effect and valley-based binary information are illustrated in Fig. 1.4. Numerous manifestations of the valley Hall effect have been demonstrated in TMDC and graphene monolayers in the past decades. In hexagonal 2D materials with non-centrosymmetric crystal symmetry, the +K and –K valleys have opposite Berry curvatures [74,75], which show up as an effective magnetic field in momentum space to cause valley-contrasting Hall currents. To make use of graphene and bilayer graphene in valleytronic devices, external perturbations can be employed to break the inversion symmetry of centrosymmetric graphene and bilayer graphene, to produce a finite bandgap and valley-contrasting Berry curvature. The inversion symmetry of monolayer graphene can be broken by a superlattice potential caused by the hexagonal boron nitride (h-BN) substrate [80] while for bilayer graphene, an out-of-plane electric field is applied to break the inversion symmetry [81]. Using a 'Hall bar' geometry, the resultant valley Hall and its inverse effect together can manifest as a nonlocal resistance, as observed in both graphene/h-BN heterostructures and biased graphene bilayers [80–82].

The valley Hall effects have been exhibited in TMDC monolayers using optoelectronic measurements, in which valley-polarized electrons and holes have been extracted through optical excitation by exploiting the valley optical selection rules. Due to the population imbalance between the valleys, the valley Hall effect establishes as a charge Hall current that changes sign with the polarization of the excited light. Mak et al. [77] experimentally demonstrated that under the excitation of a circularly polarized light on the field-effect transistors, fabricated from MoS_2 monolayers where in plane electric field was applied between the source and the drain, a transverse voltage is developed, which changes sign when the helicity of the optical polarization is flipped. The experimental findings are in well concord with the theoretical prediction [75,83], even though the microscopic picture and the role of excitonic effects remain to be elucidated. Moreover, TMDCs show a small (large) valley spin splitting in the conduction (valence) bands. However, a large valley spin splitting in the conduction band is advantageous in valleytronics. Consequently, the circumstances necessitate extensive research into this nascent field. New 2D materials with large valley spin splitting in the conduction band showing valley properties complementary to that of TMDCs have been investigated in this Ph.D. thesis.

1.2.4 Excitonic Solar Cells of 2D vdWHs

Among the many energy resources, the conversion of solar radiation directly into electricity through solar cell technology has come out as one of the most promising sustainable alternatives to address the ever-growing energy crisis. The evolution of photovoltaic systems was initiated several years ago with the first practical silicon-based solar cells in 1954 [84]. Since then, photovoltaic materials with enhanced power conversion efficiency (PCE) have been continuously searched. According to the photoelectric conversion mechanism, solar cells can be categorized into two main classes, namely, conventional solar cells [85–87] and excitonic solar cells (XSCs) [88–91]. In conventional solar cells, the electron-hole pairs are directly generated in the bulk inorganic semiconductors such as Si, GaAS and CdTe etc. An excitonic solar cell (XSC) consists of a heterostructure formed by two different materials or phases, including organic solar cells (OSCs), dye-sensitized solar cells (DSSCs), molecular semiconductor solar cells, conducting polymer solar cells and two-dimensional (2D) heterojunction solar cells. In excitonic solar cell, a tightly bound electron-hole pair called exciton is formed by light absorption and dissociated simultaneously at the heterostructure interface due to the discontinuities of the electron affinity and ionization potential across the interface, producing free charge carriers and resulting in photoelectric conversion. Based on this heterointerface process, the photovoltaic performance is dominated by the interfacial effect over the bulk effect. Nano structuration of interfaces is a vital method toward highly efficient solar cell devices. 2D materials can form high-quality heterogeneous interfaces because of the absence of dangling bonds, promoting the research of vertical heterostructures.

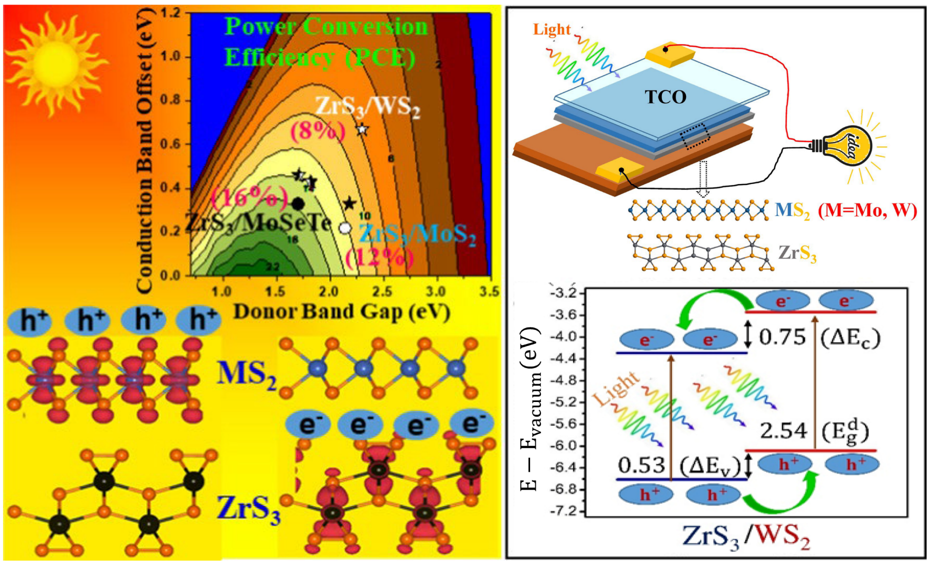
Power Conversion Efficiency (PCE)
Conduction Band Offset (eV)
Donor Band Gap (eV)
ZrS3/WS2 (8%)
(16%) ZrS3/MoSeTe
ZrS3/MoS2 (12%)
h+
MS2
e-
ZrS3
Light
TCO
MS2 (M=Mo, W)
ZrS3
E − Evacuum (eV)
e-
h+
0.75 (ΔEc)
2.54 (Egd)
0.53 (ΔEv)
Light
ZrS3/WS2

Figure 1.5 *Schematic of ZrS_3/MS_2 vdWHs based excitonic solar cell from ref. [3].*

Nowadays, atomically thin excitonic solar cells consisting of 2D vdW heterostructures [89,92,93] are found to be immensely promising for their superior interfacial effect as well as their high charge carrier separation abilities. Furthermore, many 2D materials possess exotic electronic and optoelectronic properties, making them attractive donor and acceptor materials for designing high-efficiency solar cells. In addition to the separation efficiency of excitons, the carrier mobility and the light-harvesting performance also play important roles in determining the PCE. Thus, searching for suitable 2D donor and acceptor materials with high carrier mobility and good light-harvesting performance is significant for the development of XSCs. The schematic of an excitation solar cell based on ZrS_3/MS_2 (M=Mo, W) vdWHs is presented in Fig. 1.5, where MoS_2 acts like a donor and ZrS_3 acts like acceptor, as discussed in Chapter 4.

Chapter 2

Theoretical methodology

In this chapter, we briefly describe the central theoretical foundations of computational methods that are pivotal to the calculation of results presented in this thesis by the use of different quantum simulation tools. The fundamental aspects of many-body Schrödinger equation, introductory density functional theory (DFT) methods, exchange-correlation functionals, and basis-sets essential to layout various *ab initio* calculations within the DFT have been presented in this chapter.

2.1 Elementary many particles' physics

The surrounding matter in our everyday experience, at the microscopic level, is comprised of a systematic collection of electrons that surround a few different kinds of nuclei. Basically, a solid is a collection of heavy positively charged particles (nuclei) and lighter, negatively charged particles (electrons). In a many-electron quantum system, the fundamental electrostatic interactions between electrons and nuclei are Coulombic in nature and governed by the many-particle Schrödinger equation, and mathematically described as,

$$\hat{H}\Psi_i(\vec{x}_1,\vec{x}_2,\ldots\ldots,\vec{x}_N,\vec{R}_1,\vec{R}_2,\ \ldots\ldots,\vec{R}_M) = \mathrm{E}_i\Psi_i\ (\vec{x}_1,\vec{x}_2,\ldots\ldots,\vec{x}_N,\vec{R}_1,\vec{R}_2,\ \ldots\ldots,\vec{R}_M) \quad (2.1)$$

Here, $\hat{H}$ is the Hamiltonian operator for an isolated N electron system consisting of M nuclei in the absence of any external perturbations, $\Psi_i(\vec{x}_1,\vec{x}_2,\ldots\ldots,\vec{x}_N,\vec{R}_1,\vec{R}_2,\ \ldots\ldots,\vec{R}_M)$ stands for the wave function of the i^{th} state, and E_i energy eigenvalues of a given quantum state described by Ψ_i.

We are interested in the energy corresponding to the ground-state of the system which dictates the various properties of the system. The Hamiltonian for a system of interacting electrons and ions in a solid can be written as

$$\hat{H} = \hat{H}_{el} + \hat{H}_{ion} + \hat{H}_{el-ion} \quad (2.2)$$

Each Hamiltonian operators (using the atomic units $\hbar = 1/4\pi\varepsilon_0 = m_0 = e = 1$) describing the total energy of a coupled electron-ion system are defined as

$$\hat{H}_{el} = -\frac{1}{2}\sum_{i=1}^{N}\nabla_i^2 + \sum_{i=1}^{N}\sum_{j>i}^{N}\frac{1}{r_{ij}} \quad (2.3)$$

$$\hat{H}_{ion} = -\frac{1}{2}\sum_{A=1}^{M}\frac{1}{M_A}\nabla_A^2 + \sum_{A=1}^{M}\sum_{B>A}^{M}\frac{Z_A Z_B}{R_{AB}} \tag{2.4}$$

$$\hat{H}_{el-ion} = -\sum_{i=1}^{N}\sum_{A=1}^{M}\frac{Z_A}{r_{iA}} \tag{2.5}$$

Here, *A* and *B* denotations are over the *M* nuclei present in the system, while *i,* and *j* run over the *N* electrons. The first two terms in the total energy operator are the kinetic energy of *N* electrons and *M* nuclei, respectively, where M_A is the mass of the nucleus in units of the electron mass. $\hat{H}_{ion}$ and $\hat{H}_{el}$ represents the ionic and electronic contribution to the Hamiltonian respectively and $\hat{H}_{el-ion}$ denotes the electron-ion interaction potential. This total Hamiltonian consists of both the electronic and ionic part. To make further progress, one needs to decouple the electronic part from the ionic part. The adiabatic or the Born-Oppenheimer (B-O) approximation provides a route for decoupling the ionic and electronic degrees of freedom (DOF).

***Born-Oppenheimer approximation*:**

The wave function $\Psi_i(\vec{x}_1, \vec{x}_2, \ldots\ldots, \vec{x}_N, \vec{R}_1, \vec{R}_2, \ldots\ldots, \vec{R}_M)$ of a many-particle quantum system contains essential information and central to describe all the desired physical properties of a given quantum system by various quantum operations. The Schrödinger equation (2.1), can further be simplified by considering the famous clamped-nuclei approximation for nuclear dynamics, comely referred to as *Born-Oppenheimer* approximation. The approximation takes advantage of differences in electron and proton (^{1}H) masses, which for the lightest nuclei (^{1}H), proton mass is 1800 times more than a single electron mass. Thus, the motion of nuclei is much slower as compared to the electron dynamics, and electronic motion happens within a fixed field of nuclear potential; therefore, the clamped-nuclei approximation is, in principle, an excellent approximation to simplify the problem by ceasing the nuclear dynamics. The kinetic energy term for the nuclear motion becomes zero under the *Born-Oppenheimer* approximation, and the rigid potential energy due to nucleus-nucleus repulsion becomes constant. The total energy operator can be rewritten under the *Born-Oppenheimer* approximation as the electronic Hamiltonian

$$\hat{H}_e = -\frac{1}{2}\sum_{i=1}^{N}\nabla_i^2 - \sum_{i=1}^{N}\sum_{A=1}^{M}\frac{Z_A}{r_{iA}} + \sum_{i=1}^{N}\sum_{j>i}^{N}\frac{1}{r_{ij}} = \hat{T} + \hat{V}_{Ne} + \hat{V}_{ee} \tag{2.6}$$

Where the first term $\hat{T}$ is the kinetic energy of *N* electrons in the system, the attractive potential acting on electrons due to the nuclei in the second term $\hat{V}_{Ne}$ is the nuclei-electron interaction potential and often termed as the external potential $V_{ext.}$ in density functional theory (DFT), while the last term $\hat{V}_{ee}$ represents the electron-electron interaction potentials. The solution of Schrödinger equation (2.1) for electronic Hamiltonian $\hat{H}_e$ is the electronic wave function Ψ_e and the corresponding electronic energy eigenvalues E_e. The electronic wave function Ψ_e explicitly dependent on electron coordinates only and the nuclear coordinates enter only parametrically, which do not appear explicitly in Ψ_e. Then the total energy E_T become the sum of electronic energy E_e part and constant nuclear repulsion term E_n, the electronic Schrödinger equation is expressed as

$$\hat{H}_e \, \Psi_e = \mathrm{E}_e \Psi_e \tag{2.7}$$

and

$$\mathrm{E}_T = \mathrm{E}_e + \mathrm{E}_n; \text{ where } \mathrm{E}_n = \sum_{A=1}^{M} \sum_{B>A}^{M} \frac{Z_A Z_B}{R_{AB}} \tag{2.8}$$

The above many-electron Schrödinger equation (2.7) for a given quantum system is essentially a simple story that describes everything about a system. The wave function itself is not an observable quantity in quantum mechanics and commonly interpreted by the probability density, which is the square of the wave function when multiplied with its complex conjugation. To solve the Schrödinger equation (2.7) for an arbitrarily chosen quantum system, first, the Hamilton operator for the target system needs to be set. The electronic Hamiltonian in equation (2.6) infers that the specific part of the total energy operator $\hat{H}$ that is relevant to an actual system depends only on the number of electrons in the system *N* and external potential $V_{ext.}$. The later is completely determined through the position and charge of all nuclei within the system, and the remaining parts of $\hat{H}$, such as kinetic energy or the electron-electron repulsion, are independent of the system under our consideration. Since the eigenfunctions Ψ_i is dependent on corresponding eigenvalues of $\hat{H}$, all properties of the system can be derived once the Ψ_i is fully determined. The operation of appropriate operators on the wave function can extract the desired physical properties of the system if and only if Ψ_i is fully described. However, these simple-sounding steps are hard in practice even for simple atomic and molecular systems due to the absence of adequate technique to solve the many-particle Schrödinger equation precisely by wave function determination method, which is a central quantity in this model.

Nonetheless, over the years this simplified description has traversed a long path in predicting and describing the structure-property relation of various real materials starting from the simple atomic and molecular structures to the solving of complex DNA structures, polymers, proteins, and solid crystals in the conventional electronic wave function minimization strategy to get the ground state wave functions and corresponding low energy states of material using variational methods, and Hartree-Fock approaches. These all-electron wave function minimization schemes are computationally way more expensive for a system containing a large number of electrons to be exactly solvable by the wave function minimization methods and often suffer for its computation volume of the problem.

The present-day computational approach in solving the many-electron Schrödinger equation takes a simple route via density functional theory (DFT) approach, where the consideration of electron density $\rho(\vec{r})$ of materials has simplified the enormity of solving the many-electron wave function Ψ_i for complex materials. In recent years, the use of sophisticated computational methods by clever algorithms has enabled the predictive accuracy of ground-state electronic properties of materials with near exactness.

In the following section, we present the basic foundations of modern-day density functional theory methods for a non-relativistic, interacting Coulomb system based on electron density and approximate functionals.

2.2 Density Functional Theory

The electronic part of the Hamiltonian as described in eq. 2.6 contains the difficult many body term and therefore cannot be solved without further approximation. One of the most efficient tools to solve this many electrons problem is the density functional theory (DFT) which offers a standard method to calculate the ground state properties of real materials. In DFT many electrons problem is mapped into single electron problem i.e., 3N DOF is transferred into 3 DOF embedded in the density $\rho(\vec{r})$. To compute the total energy and electronic structure of real materials using DFT, one basic variable, electronic charge density distribution $\rho(\vec{r})$ of the system is used rather than the many electrons wave function. Effectively it reduces the computational cost since density depends on three DOF whereas wavefunction based methods depend on 3N DOF. In the following we will show that the expectation value of energy corresponding to eq. 2.6 can be written as a functional of reduced density matrices. The density functional theory (DFT) or electron density theory reformulates the many-electron Schrödinger equation in terms of electron density $\rho(\vec{r})$ of materials that give a reliable computational measure and efficiency to solve the many-electron quantum system for various complex materials. The electron density or the probability density $\rho(\vec{r})$ of an *N* electron system is the central variable in DFT and defined as the integral over the spin coordinates of all *N* electrons within a volume element of $d^3\vec{r}$.

$$\rho(\vec{r}) = N \int \ldots \int |\Psi_i(\vec{x}_1, \vec{x}_2, \ldots, \vec{x}_N)|^2 d^3\vec{r} \tag{2.9}$$

The probability density $\rho(\vec{r})$ is a non-negative function of position variables of *N* electrons which vanishes when $\vec{r} \to \infty$ and integrates to the total number of electrons *N* present in the system. The electron density $\rho(\vec{r})$ is then used to calculate various material properties that are directly or indirectly related to the ground-state electron density and the corresponding total minimum energy of the system E_0. In principle, $\rho(\vec{r})$ is an observable quantity and can be experimentally measured by X-ray diffractions. The basic foundation of the density-based approach to describe the behavior of electrons in a quantum system was first theoretically demonstrated by Hohenberg and Kohn in their seminal work back in 1964 and Kohn-Sham in 1965, for which Walter Kohn was awarded the Nobel Prize in Chemistry in 1998. Their density-based approaches in solving the electronic structure of materials are still the most successful theoretical approach in density functional theory. However, the initial attempt to this simplified density-based approach to describe the properties of many-body quantum systems in terms of their electron density dates back to 1927 in Thomas-Fermi (TF) model of approximation, where the non-interacting kinetic energy functional of a many-electron system was approximated by the uniform electron gas with electron density $\rho(\vec{r})$.

$$T_{TF}[\rho[\vec{r}]] = \mathrm{A} \int d^3\vec{r}\, \rho^{5/3}(\vec{r}) \tag{2.10}$$

Where $\rho(\vec{r})$ is the electron density of homogeneous non-interacting electron gas, and A is a numerical constant $\frac{3}{10}(3\pi^2)^{2/3}$. The total energy of a system was determined by adding electrostatic energies using the classical expression for the nuclear-nuclear potential and the electron-electron potential.

$$E_{TF}[\rho[\vec{r}]] = A \int d^3r\ \rho^{5/3}[r] - \mathrm{Z} \int \frac{\rho[r]}{r}\, d^3r + \frac{1}{2} \iint \frac{\rho[r]\rho[r']}{|r - r'|} d^3r d^3r' \tag{2.11}$$

The first term in the above expression is the non-interacting kinetic energy density of a many-electron system, whereas the second term represents the energy of the ion-electron interaction energy or Coulombic term, and the third term is the classical Hartree energy.

The total energy of a many-electron system can be obtained by minimizing non-interacting wave function corresponding to a given electron density in some external potential, as given in equation (2.9), where the total electron number N in the system remains constant.

However, the description for total energy in the original Thomas-Fermi model overestimates the ground-state energy of many quantum systems because of an improper account of exchange-correlation energy, which is completely neglected in the Thomas-Fermi model which is expected to further lower the ground-state energies for interacting particles.

In summary, though the basic structure of a many-electron system based on Thomas-Fermi approximation provides a reasonable approximate result for non-interacting electronic systems with a few numbers of electrons, it fell short of predicting electrons in many real materials. Nonetheless, the use of electron density mapping over the conventional many-electron wave function method, without any additional information as a variable, established by the Thomas-Fermi model can describe divergent properties of materials and eventually gave birth to the foundation of modern density functional theory.

2.2.1 Hohenberg-Kohn theorem

The modern density functional theory methods that we use today was first established in 1964 by Hohenberg and Kohn. Hohenberg–Kohn (HK) stated, 'the ground state of any interacting many-electron system with a given fixed inter-particle interaction is a unique function of the electron density $\rho(\vec{r})$'; where the ground-state wave function Ψ_0 can be written as a unique functional of ground-state electron density ρ_0 as, $\Psi_0 = \Psi\,[\rho_0\,]$.

The equation (2.4) can now be rewritten in terms of the ground-state energy E_0 as a unique functional of ground-state electron density ρ_0, which enables one to establish a single physical quantity to describe all the properties of an interacting many-particle system.

$$E_0\big[\Psi\,[\rho_0]\big] = <\Psi\,[\rho_0]|\hat{T} + \hat{V}_{Ne} + \hat{V}_{ee}|\Psi\,[\rho_0]> \qquad (2.12)$$

***First HK theorem*:** In the first Hohenberg-Kohn (HK) theorem, they proved, the ground state electron density ρ_0 uniquely determines the Hamiltonian operator thereby can determine the number of electrons (*N*) and external potential $\mathrm{V}_{ext.}(\vec{r})$ to within a constant that fixes $\hat{H}$ for many-particle interacting ground states. There is a one-to-one correspondence between the ground-state density $\rho(\vec{r})$ of a many-electron system (atom, molecule, solid) and the external potential $\mathrm{V}_{ext.}$. An immediate consequence is that the ground-state expectation value of any observable $\hat{O}$ is a unique functional of the exact ground-state electron density:

$$< \Psi| \, \hat{O} \, |\Psi > = O[\rho] \tag{2.13}$$

***Second HK theorem*:** For $\hat{O}$ being the Hamiltonian $\hat{H}$, the ground-state total energy functional H $[\rho] \equiv \; E_{\mathrm{V}_{ext.}}[\rho]$ is of the form

$$E_{\mathrm{V}_{ext.}}[\rho] = < \Psi| \, \hat{T} + \hat{V} \, |\Psi > \; + < \Psi| \, \hat{V}_{ext} \, |\Psi > \tag{2.14}$$

$$= \; \mathrm{F_{HK}}[\rho] \; + \; \int \rho(\vec{r}) \, \mathrm{V_{ext}}(\vec{r}) d\vec{r} \tag{2.15}$$

Where the Hohenberg-Kohn density functional $\mathrm{F_{HK}}[\rho]$ is universal for any many-electron system. $E_{\mathrm{V}_{ext.}}[\rho]$ reaches its minimal value (equal to the ground-state total energy) for the ground-state density corresponding to $\mathrm{V_{ext}}$.

In the second Hohenberg-Kohn theorem, they proposed a universal functional: *Hohenberg-Kohn functional,* $F_{HK}[\tilde{\rho}]$ as a function of certain unknown ground state density $\tilde{\rho}$, where $F_{HK}[\tilde{\rho}] = T[\tilde{\rho}] + V_{ee}$ that exists completely independent of the choice of the system to be solved the many-electron Schrödinger equation (2.7), exactly! However, the explicit form of these functionals is still under mystery. The functional $F_{HK}[\tilde{\rho}]$ delivers the ground state energy of the system independent of the external potential into its lowest energy configuration if and only if the input electron density is close to the actual ground-state density ρ_0 of material. The second Hohenberg-Kohn theorem was the simplified version of the variational principle with a trial density $\tilde{\rho}$.

$$E_o \leq E[\tilde{\rho}] = \; \hat{T}[\tilde{\rho}] + \hat{V}_{Ne}[\tilde{\rho}] + \hat{V}_{ee}[\tilde{\rho}] \tag{2.16}$$

This trial density $\tilde{\rho}$ in Hohenberg-Kohn theorem satisfies the necessary boundary conditions, $\tilde{\rho}(\boldsymbol{\vec{r}}) \; \geq 0$, $\int \tilde{\rho}(\boldsymbol{\vec{r}}) \, d^3r = N$, and associate the external potential $V_{ext.}$ that give rise an upper bound to the true ground state energy $\boldsymbol{E_o}$ of a quantum system.

In summary, the Hohenberg-Kohn theorems have provided necessary methods to calculate all physical properties of a material as a unique functional of its ground-state density and some external potential $\mathrm{V}_{ext.}(\vec{r})$ in terms of a universal trial function $F_{HK}[\tilde{\rho}]$ through the variational procedure that associate to an unknown density $\tilde{\rho}$ to determine the true ground state density of electrons ρ_0. However, the application of the Hohenberg-Kohn theorem is only limited to the ground state material properties and intricate to generalize the method for the excited state problems due to challenges in Hohenberg-Kohn functional.

2.2.2 Kohn-Sham formalism

The second seminal contribution to the development of modern density functional theory was given by Kohn and Sham in 1965, a year after the Hohenberg-Kohn theorem (1964). The equations of Kohn and Sham, turn DFT into a practical tool. They are a practical procedure to evaluate the ground state density. Kohn-Sham introduced the concept of a non-interacting reference system built from a set of orbitals in a way such that the kinetic energy part of the universal Hohenberg-Kohn functional $F_{HK}[\tilde{\rho}]$ can be calculated with sufficient accuracy. The correlation energy is defined as this part of the total energy which is present in the exact solution, but absent in the Hartree-Fock solution. The total energy functionals $E_e[\rho]$ and $E_{HF}[\rho]$ corresponding to the exact and Hartree-Fock Hamiltonians respectively, are:

$$E_e = T + V \tag{2.17}$$

$$E_{HF} = T_0 + V = T_0 + V_H + V_x \tag{2.18}$$

Here T and V are the exact kinetic and electron-electron potential energy functionals, T_0 is the functional for the kinetic energy of a non-interacting electron gas, V_H stands for the Hartree contribution and V_x for the exchange contribution. For easier notation, the square brackets to represent functional have been dropped here.

The functional for the correlation contribution is expressed as:

$$V_c = E_{HF} - E_e = T - T_0 \tag{2.19}$$

The exchange contribution to the total energy is defined as the part which is present in the Hartree-Fock solution, but absent in the Hartree solution. The total energy of Hartree solution is given by

$$E_H = T_0 + V_H \tag{2.20}$$

Therefore, the exchange contribution can be defined as

$$V_x = V - V_H \tag{2.21}$$

Now, the Hohenberg-Kohn functional can be rewritten in the following way:

$$\begin{aligned} F_{HK} &= T + V + T_0 - T_0 \\ &= T_0 + V + (T - T_0) \\ &= T_0 + V + V_c + V_H - V_H \\ &= T_0 + V_H + V_c + (V - V_H) \\ &= T_0 + V_H + (V_c + V_x) \\ &= T_0 + V_H + V_{xc} \end{aligned} \tag{2.22}$$

Here V_{xc} is the exchange-correlation energy functional.

The Kohn-Sham Hamiltonian can be written as

$$\hat{H}_{KS} = \hat{T}_0 + \hat{V}_H + \hat{V}_{xc} + \hat{V}_{ext} \tag{2.23}$$

$$= -\frac{1}{2}\sum_{i=1}^{N} \nabla_i^2 + \int \frac{\rho(r')}{|r-r'|}\, d^3r' + V_{xc} + V_{ext} \tag{2.24}$$

Where the exchange-correlation potential is given by the functional derivative

$$\hat{V}_{xc} = \frac{\partial V_{xc}[\rho]}{\partial \rho} \tag{2.25}$$

The theorem of Kohn-Sham can now be formulated as:

The exact ground-state density $\rho(r)$ of an N-electron system is

$$\rho(r) = \sum_{i=1}^{N} |\phi_i(r)|^2 \tag{2.26}$$

Where the single-particle wave functions are the N lowest-energy solutions of the Kohn-Sham equation

$$\hat{H}_{KS}\, \phi_i = \varepsilon_i\, \phi_i \tag{2.27}$$

It should be noted that the single-particle wave functions ϕ_i are not the wave functions of electrons! They describe mathematical quasi-particles, without a direct physical meaning. Only the over-all density of these quasi-particles is guaranteed to be equal to the true electron density. Also, the single-particle energies ε_i are not single-electron energies.

Both the Hartree operator V_H and the exchange-correlation operator V_{xc} depend on the density $\rho(r)$, which in turn depends on the ϕ_i which are being searched. This means we are dealing with a self-consistency problem: the solutions (ϕ_i) determine the original equation (V_H and V_{xc} in H_{KS}), and the equation cannot be written down and solved before its solution is known. An iterative procedure is needed to escape from this paradox (see Fig. 2.1). Some starting density ρ_0 is guessed, and a hamiltonian H_{KS1} is constructed with it. The eigenvalue problem is solved, and results in a set of ϕ_1 from which a density ρ_1 can be derived. Most probably ρ_0 will differ from ρ_1. Now ρ_1 is used to construct H_{KS2}, which will yield a ρ_2, etc. The procedure can be set up in such a way that this series will converge to a density ρ_f which generates a H_{KSf} which yields as solution again ρ_f: this final density is then consistent with the Hamiltonian.

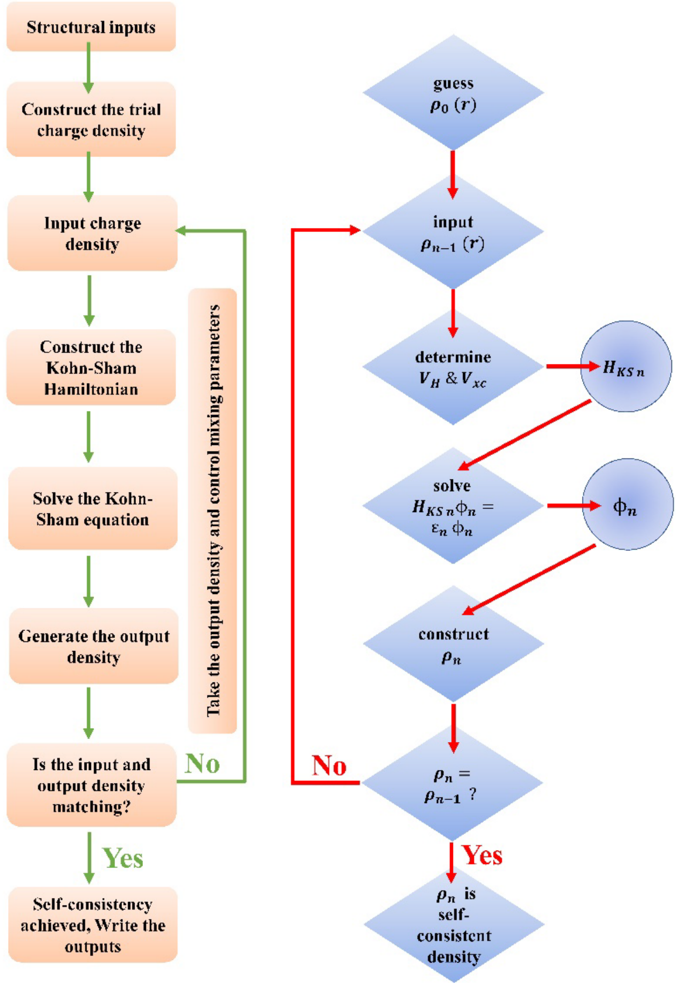
Structural inputs
Construct the trial charge density
Input charge density
Construct the Kohn-Sham Hamiltonian
Solve the Kohn-Sham equation
Generate the output density
Is the input and output density matching?
No
Yes
Self-consistency achieved, Write the outputs
Take the output density and control mixing parameters
guess $\rho_0(r)$
input $\rho_{n-1}(r)$
determine V_H & V_{xc}
H_{KSn}
solve $H_{KSn}\Phi_n = \varepsilon_n \Phi_n$
Φ_n
construct ρ_n
$\rho_n = \rho_{n-1}$?
No
Yes
ρ_n is self-consistent density

Figure 2.1 *Flow chart of the self-consistent procedure to solve Kohn-Sham equation.*

One should note here if the exact form of $V_{xc}(r)$ and $V_{KS}(r)$ is known to us, by using the Kohn-Sham strategy, one could get the exact ground-state electron density ρ_0 of a non-interacting real system when the density of reference system approaches to its real value in an effective Kohn-Sham potential.

Strictly speaking, in Kohn-Sham approach the exchange-correlation functional $V_{xc}[\rho(r)]$ is unknown, and the orbitals have no physical significance, except the highest occupied orbital (negative of exact ionization energy). To describe a real interacting quantum system, the description of accurate exchange-correlation functionals $V_{xc}[\rho(r)]$ is of utmost importance. Two widely studied approximate exchange-correlation functional $V_{xc}[\rho(r)]$ methods arise after the Kohn-Sham theory in the name of local density approximation (LDA) [94] and the generalized gradient approximations (GGA). [95]

2.2.3 Exchange-correlation functionals

2.2.3.1 Local Density Approximations

The LDA approximation for approximate exchange-correlation functionals is the general basis of all other density-based approximations. The LDA model is based on uniform electron gas where the motion of the electron is considered under a positive, ionic background charge distribution, with a total neutral charge ensemble of particles. In LDA, the exchange-correlation energy at a point r per particle remain the same in an ideal homogeneous electron gas with electron density $\rho(r)$. In this approximation the exchange-correlation functional $E_{XC}[\rho(r)]$] takes the following form

$$E_{XC}^{LDA}[\rho(r)] = \int \rho(r)\, \epsilon_{XC}^{hom}[\rho(r)]dr \tag{2.28}$$

$$= \int \rho(r)[\epsilon_{X}^{hom}(\rho(r)) + \epsilon_{C}^{hom}(\rho(r))]dr \tag{2.29}$$

$$= E_{X}^{LDA}[\rho(r)] + E_{C}^{LDA}[\rho(r)] \tag{2.30}$$

The exchange-correlation functional $E_{XC}[\rho(r)]$ in LDA assumption splits into two parts, the exchange part $E_{X}^{LDA}[\rho(r)]$ and the effective correlation contribution $E_{C}^{LDA}[\rho(r)]$.

By taking the derivative of the energy functional, the corresponding XC potential of the LDA is

$$V_{XC}^{LDA}[\rho(r)] = \frac{\partial E_{XC}^{LDA}[\rho(r)]}{\partial \rho(r)} \tag{2.31}$$

The moderate accuracy of *local density approximation (LDA)* is insufficient for most solids for practical applications in material science, it also failed miserably for heavy fermions, and systems that are primarily dominated by the electron-electron interactions.

2.2.3.2 Generalized Gradient Approximations

Since the exchange-correlation energy of a homogeneous electron distribution widely differs for a real material with non-local density variations, the first thoughtful step to go beyond the LDA formalism is the use of not only the information about the density $\rho(r)$ at a particular point r in space, but to supplement this uniform density with gradient correction of the charge density, $\nabla\rho(r)$ that accounts for the non-homogeneity of the actual electron density. Thus, the exchange-correlation energy in the generalized gradient approximation (GGA) becomes, [96]

$$E_{XC}^{GGA}[\rho(r)] = \int \rho(r)\, \epsilon_{XC}^{GGA}[\rho(r), \nabla\rho(r)]dr \tag{2.32}$$

The corresponding XC potential of the GGA is of the form

$$V_{XC}^{GGA}[\rho(r)] = \frac{\partial E_{XC}^{GGA}[\rho(r)]}{\partial\rho(r)} = \rho(r)\frac{\partial\epsilon_{XC}^{GGA}}{\partial\rho(r)} + \epsilon_{XC}^{GGA} \tag{2.33}$$

The GGA is found to work much better than the LDA in predicting material properties to their approximate real value in the Kohn-Sham method. The overcorrection of the local electronic density of uniform electron gas by gradient corrected density was hugely successful useful for semiconducting systems which largely reduce the ground state properties such as lattice constants were smaller by < 0.6% than an experiment, cohesive energy, dielectric function, elastic constants within 3% of its experimental value, and bandgap underestimation problem of LDA within 0.2 eV of its experimental value in GGA. [97,98]

Over the years many progress has been made in deriving the successful GGA functionals. [99,100] The most commonly used GGA formalism in DFT is Perdew-Wang (PW91) [101] and Perdew-Burke-Ernzerhof exchange-correlation energy for the GGA's [100]. In most of our DFT calculation results, we have used the Perdew-Burke-Ernzerhof variant of the generalized gradient approximation (GGA), which incorporates some inhomogeneity effects that are well suited for predicting the electronic properties of various semiconducting systems. The combination of GGA and PBE provides better accuracy than normal GGA's, results close to the experimental results for layered materials. [102]

2.2.3.3 Meta-Generalized Gradient Approximations

Meta-generalized gradient approximation (meta-GGA) exchange-correlation density functionals depend on the Kohn-Sham (KS) orbitals through the kinetic energy density. Consequently, there is a functional dependency on the electron density in the KS orbitals. Although the functional dependence of the KS orbitals is indirect and is not given by an explicit expression, the computation of analytic functional derivatives of meta-GGA functionals with respect to the density poses a challenge. The practical solution used in many computer implementations of meta-GGA density functionals for ground-state calculations is abstracted and generalized to a class of density functionals that is broader than meta-GGAs and to any order of functional differentiation. [103] A formal advantage of meta-GGAs is that they are able to recognize all types of orbital overlap, and thereby in principle represent all types of chemical bonds simultaneously. [104]

The most successful meta-GGA to date is the strongly constrained and appropriately normed (SCAN) functional. [105] Sun et al. proposed the first meta-GGA that is fully constrained, abiding by all 17 known exact constraints that a meta-GGA can. SCAN functional is also exact or nearly exact for a set of "appropriate norms," including rare-gas atoms and nonbonded interactions. This strongly constrained and appropriately normed meta-GGA achieves remarkable accuracy for systems where the exact exchange correlation hole is localized near its electron, and especially for lattice constants and weak interactions. [105] Compared to other nonempirical semilocal-density functionals, SCAN has been shown to yield a significantly more accurate representation of the bulk properties of many semiconducting solids, such as, bulk modulus, lattice parameter and volume [106], formation enthalpy [107], transition pressures [108], and reaction energies [109]. Furthermore, though SCAN produces accurate properties for strongly bound compounds [110] and ionic systems, it is moderately worse for weakly bound intermetallic compounds. [111,112]

2.2.3.4 Hybrid functionals

In a conventional local density approximation or gradient corrected density functional approximation, we have repeatedly seen that the exchange contribution E_X is usually much larger than the corresponding correlation E_C effects. Even the semilocal correction effects do not reproduce the reasonable bandgap in semiconductors due to self-interaction errors and missing derivative discontinuity in electron density. Hence, a reasonable accuracy of exchange functional is a prerequisite to get meaningful results in DFT. A straightforward way to get the most accurate exchange-correlation energy is the use of exact exchange energy in the Kohn–Sham density functional theory.

In hybrid density functionals, we include certain parts of the exact Hartree-Fock exchange energy to improve the results of our GGA calculations. However, the use of hybrid density functionals is computationally costly for most materials and very much dependent on the size of the system. In 1992, Axel D. Becke *et al.* [113] established a simple but rather powerful strategy to link the Hartree-Fock-based methods with the density functional theory calculation, the so-called "Hartree-Fock-Kohn-Sham" scheme by using an adiabatic connection to the nonlocal exchange potential in which the non-local Fock exchange operator replaces a part of the local exchange energy. [114]

The exchange-correlational energy in hybrid approximation,

$$E_{XC}^{hyb.} = aE_X^{KS} + (1-a)E_{XC}^{GGA} \tag{2.34}$$

where E_X^{KS} is the exchange energy of the exact Kohn-Sham wave function, E_{XC}^{GGA} approximate energy in GGA and a is a fitting parameter which determines the amount of non-local exchange part in the hybrid approximation, typically a ~ ¼ % of Hartree-Fock mixing.

The widely used hybrid functional in DFT is the **Heyd–Scuseria–Ernzerhof (HSE)** screened Coulomb potential were a part of short and long-range interaction of PBE exchange functional is replaced by the short-range non-local Hartree-Fork exchange interaction. [115,116]

The HSE functional can be expressed as:

$$E_{XC}^{HSE} = \frac{1}{4}E_X^{HF,SR}(\omega) + \frac{3}{4}E_X^{PBE,SR}(\omega) + E_X^{PBE,LR}(\omega) + E_C^{PBE} \tag{2.35}$$

where ω is the screening parameter.

In HSE, the spatial decay of the HF exchange interaction is accelerated by substitution of the full $\frac{1}{r}$ Coulomb potential with an error-function-screened Coulomb potential to calculate the exchange portion of the energy in order to improve computational efficiency. This enables a substantial lowering of the computational cost for calculations in extended systems. The HSE functional partitions the Coulomb potential for exchange into short-range (SR) and long-range (LR) components:

$$\frac{1}{r} = \frac{1 - \mathrm{erf}\,(\omega r)}{r} + \frac{\mathrm{erf}\,(\omega r)}{r}$$

Where the screening ω parameter defines the separation range. For $\omega = 0$, HSE reduces to the hybrid functional PBE0, and for $\omega \rightarrow \infty$, HSE becomes identical with PBE. HSE with a finite value of ω can be regarded as an interpolation between these two limits. [116]

The use of HSE functionals in DFT significantly improved the lattice parameters, bandgap, and elastic properties for many nonmetallic systems where the errors in the fundamental bandgap of semiconductors get reduce to 50% than the same calculated by using the GGA functionals alone. [117]

In a nutshell, the predictive potential of different functionals through incorporating various exchange-correlation parts to the density functional theory is progressively improving the accuracy of theoretical results close to the experimental values, where the accuracy in the bandgap: LDA < GGA < hybrid functional is scaling with the computing need of the problem. Using HSE functionals, the errors in ionization energy and affinity have reduced to ~ 0.2 eV for many semiconducting materials, including transition metal dichalcogenides. [118–121]

2.2.3.5 Correction of exchange-correlation error: van der Waals correction

Van der Waals force is the weak interaction that occurs among temporarily induced dipoles caused by the fluctuation in electron density and is present in every material. Since GGA is a semi-local functional and is not able to describe the long-range interaction, a correction due to van der Waals forces is needed. It can be corrected by two methods, using the empirical interatomic van der Waals parameter or the van der Waals functional. The first method contains the DFT+D2 method which corrects the interatomic interaction between the two atoms. [122] The DFT+D3 method adds an interatomic interaction among three atoms to the DFT+D2 method. [123]

2.2.4 Methods for Electronic Structure Calculations

For an infinite number of non-interacting electrons moving in the static potential of an infinite number of nuclei, electronic wave functions can extend spatially over the entire solid. Therefore, the wave function must be calculated for each of the infinite numbers of electrons in the system. These can be simplified by performing the calculations on a periodic system through the application of Bloch's theorem to the electronic wave function. The effective one- electron Kohn-Sham equations are iteratively solved by expressing the electronic wavefunctions through a linear combination of a set of basis functions. To describe the Kohn- Sham electronic wavefunctions, an accurate choice of a suitable set of simple basis functions is needed. Plane waves are the most common basis function which is suitable for a momentum space description of the material. The computational load can be reduced and optimized considerably by using various approximations such as pseudopotential approximation, projected-augmented wave method, etc.

2.2.4.1 Pseudopotential Approach

As its name suggests, it is not the actual potential but mimics the true characteristics of the actual potential. The key point of this approach is to reduce the number of electrons in a system by dividing electrons into two groups; freezing the nucleus and the core electrons together and pseudizing the remaining valence wave functions.

Core and Valence Electrons: The core electrons are generally tightly bound to their nucleus in a deep potential well, whereas the valence electrons lie far from their nuclei and high above in the potential well are relatively weakly bound. The valence electrons are active in forming chemical bonds, getting ionized, conducting electricity in metals, forming bands, and performing other atomic level activities.

Frozen-core Approximation: From the computational viewpoint, the core (nucleus plus core electrons) is frozen and deals with only the active valence electrons. This is called a frozen core approximation. The nuclear charge is largely screened by the core electrons and has much less effect on the valence electrons.

Projector-augmented wave (PAW) Potential

It may be classified as a frozen core all-electron (AE) potential. This is a generalized technique combining the pseudopotential with the linear augmented-plane-wave methods developed by Blöchl in 1994, which is well known as the projector augmented wave method (PAW). [124] Since valence wavefunctions oscillate near the ionic cores and are orthogonal to core states, many Fourier components are required to manage the orthogonality wiggles and in turn, describe the wavefunctions accurately. The PAW approach transforms these rapidly oscillating wavefunctions into smooth wavefunctions. It maps both core and parts of valence wave functions with two separate descriptions. The

ψ_{inter} of the valence part is represented via the PW expansion, whereas the ψ_{core} of the core part is projected on a radial grid at the atom center. After the additive augmentation of these two terms, the overlapping part ψ_{net} is trimmed off to make the final wave function ψ_{PAW} very close to the AE wave function:

$$\psi_{PAW} = \psi_{inter} + \psi_{core} - \psi_{net} \tag{2.36}$$

Basis set: The KS orbitals are approximated as a linear combination of known simple functions such as plane waves (PWs), the calculations become much easier.

Local basis set: A local basis set such as the Gaussian basis set is mainly localized and thus often used for atoms and molecules whose orbitals are highly localized around each atom.

Plane-wave basis set: Plane waves are nonlocal and span the whole space equally as

$$\phi_{PW} = Cexp(i\vec{\boldsymbol{k}}.\vec{\boldsymbol{r}}) \tag{2.37}$$

2.2.5 Density-functional perturbation theory

Many physical properties of a material are dependent on its response to an external perturbation in the form of lattice displacement or an applied external electric field. The lattice dynamics of crystalline solid can determine many such properties including the polarizability, elastic stiffness, phonon vibrational modes, thermal expansion of solids, specific heat, electron-phonon interactions, charge transport mechanism, superconducting properties, phonon dispersion, and thermal properties via *ab initio* density functional perturbation theory (DFPT) calculations. The determination of vibrational properties of materials from its crystal phonon is one of the astonishing successes of modern electronic structure theory. The density functional theory (DFT) deals with the electronic part of the system, while the DFPT is a linear response method to deal ionic part of the problem and the interaction among electron-phonon. The linear response properties in DFPT are calculated from the interatomic force constants for each atomic displacements, where a small perturbation is applied to the equilibrium lattice structure in terms of strain or electric field. [125]

2.2.5.1 Perturbation in Kohn-Sham scheme

The standard perturbation strategies in the form of small strain or electric field perturbations to the lattice displacement enter into the DFT scheme through an effective potential $V_{eff}(r)$ in the Kohn-Sham equation. [126] Moreover, a linear variation in perturbation will remain dependent on the ground state density of electrons. The effective potential under the Kohn-Sham scheme is defined as

$$\delta V_{eff}(r) = \delta V_{ext}(r) + \delta V_{scr}(r) = \delta V_{ext}(r) + \int d^3r' I(r,r')\, \delta\rho(r') \quad (2.38)$$

$$I(r,r') \equiv \frac{\delta V_{scr}(r)}{\delta\rho(r')} = \frac{\delta V_H(r)}{\delta\rho(r')} + \frac{\delta V_{XC}(r)}{\delta\rho(r')} \quad (2.39)$$

The perturbation induces the 1st-order variation in the single-particle wave function and defined as

$$\delta\psi_i = \sum_{j(\neq i)} \frac{< j|\delta V_{eff}|i >}{\epsilon_i - \epsilon_j} \psi_j(r) \quad (2.40)$$

Using a similar expression for $\psi_i{}^*(r)$ gives

$$\delta\rho(r) = \sum_{i\neq j} \frac{f_i - f_j}{\epsilon_i - \epsilon_j} < j|\delta V_{eff}|i > \psi_i{}^*(r)\psi_j(r) \quad (2.41)$$

An iterative solution to the equation (2.27) using (2.40) and (2.41) gives a 1st – order variation in density and corresponding total energy change of the system.

2.2.5.2 Lattice dynamics approach

The lattice dynamics under the Kohn-Sham perturbation scheme is the ionic displacement in solids. [126] Using the Hellmann-Feynman theorem, the potential corresponding to an applied perturbation is expressed in the Talyor expansion:

$$V_\lambda(r) = V_0(r) + \lambda\frac{\partial V}{\partial\lambda} + \lambda^2\frac{\partial^2 V}{\partial\lambda^2} + \cdots \quad (2.42)$$

The corresponding electron density ρ(r) and wave function ψ(r) under such perturbation

$$\rho_\lambda(r) = \rho_0(r) + \lambda\frac{\partial\rho}{\partial\lambda} + \lambda^2\frac{\partial^2\rho}{\partial\lambda^2} + \cdots \quad (2.43)$$

$$\psi_\lambda(r) = \psi_0(r) + \lambda\frac{\partial\psi}{\partial\lambda} + \lambda^2\frac{\partial^2\psi}{\partial\lambda^2} + \cdots \quad (2.44)$$

The 1st order solution to the equation (2.27) will be the 1st order Schrödinger equation under perturbation terms in equation (2.42) - (2.44) that leads to the Hellman-Feynman theorem to define the expectation value of the derivative of the Hamiltonian operator to get the eigenvalues of the system

$$\frac{\partial E}{\partial \lambda} = < \psi \left| \frac{\partial H}{\partial \lambda} \right| \psi > \qquad (2.45)$$

Using Hellman-Feynman theorem and 1st-order perturbation of electron density, the total energy expression of a perturbed system becomes:

$$E = E_0 + \sum_i \lambda_i \int \rho_0(r) \frac{\partial V(r)}{\partial \lambda} dr + \frac{1}{2} \sum_{i,j} \lambda_i \lambda_j \int \left(\frac{\partial \rho(r)}{\partial \lambda_i} \frac{\partial V(r)}{\partial \lambda_j} + \rho_0 \frac{\partial^2 V(r)}{\partial \lambda_i \lambda_j} \right) dr \qquad (2.46)$$

and Taylor series expansion of total energy

$$E = E_0 + \frac{1}{2} \sum_{L,L'} \sum_{i,j} u_i(R_L) u_j(R_{L'}) C_{i,j}(R_L, R_{L'}) \qquad (2.47)$$

2nd order term to the force constant becomes

$$C_{i,j}(R_L, R_{L'}) = \int \left(\frac{\partial \rho(r)}{\partial u_i(R_L)} \frac{\partial V(r)}{\partial u_j(R_{L'})} + \rho_0 \frac{\partial^2 V(r)}{\partial u_i(R_L) \partial u_j(R_{L'})} \right) dr \qquad (2.48)$$

In equation (2.43) a 1st order perturbation to the electron density is required to evaluate the 2nd order force constants. The matrix of interatomic force constants $C_{i,j}(R_L, R_{L'})$ is given by Hessian matrix $\frac{\partial^2 E(r)}{\partial u_i(R_L) \partial u_j(R_{L'})}$. The Hessian matrix contains the linear response term $\frac{\partial \rho(r)}{\partial u_i(R_L)}$ and is known as the electron-density response and is central to formulating the formalism known as the Density Functional Perturbation Theory. [127] This method is used to calculate the linear response properties, lattice dynamics studies. DFPT methods allow the calculations of corresponding properties such as phonon-dispersion spectra, elastic stiffness tensors, and dielectric polarization within the DFT framework.

2.3 Vienna *ab-initio* simulation package (VASP)

The calculation results presented in this thesis were carried out by the Vienna Ab-initio Simulation Package (VASP) [128–131]. VASP is a sophisticated quantum simulation tool to perform *ab initio* calculations within the density functional theory at zero Kelvin temperature. The interaction between ions and electrons is described by the projector-augmented wave (PAW) pseudopotential methods using a plane-wave basis set to solve the Kohn-Sham equations in DFT with kinetic energy cut off > 500 eV. The all-electron Kohn-Sham wave function is linearly transferred into a pseudo wave function in PAW for computational convenience implemented in VASP. For periodic solids, the use of a plane-wave basis set is advantageous over the other localized orbital basis, and the results produced are well endorsed by the computational material science community. The optimization of electronic wave functions leads to an instantaneous ground-state electron density by using efficient iterative matrix diagonalization schemes (RMM-DISS, and blocked Davidson) that allow a sufficient reduction in the number of plane-waves per atom, typically ~ 100 plane waves per atom in bulk solids. The Hellman-Feynman forces acting on various atomic species and a full stress matrix can be evaluated using VASP, whereas for each self-consistency cycle the minimum energy and corresponding stress matrix is determined, to minimize the same, with respect to the previous iteration till a reasonable accuracy is achieved in total energy change. The convergence in total energy is controlled by the cut off energy and k mesh sampling. The execution time in VASP scales with N^3, where N number of valence electrons in the system. VASP is useful for systems containing a number of valence electrons by up to 4000. The code also uses different symmetry reduction schemes for the efficient calculation of bulk properties of materials. Electronic smearing methods such as Fermi, Gaussian, and tetrahedron smearing are used in the integration of band structure energy in the Brillouin zone. The Blöchl's corrections for the semiconductors are used in our calculation to remove the quadratic errors in the linear tetrahedron smearing method that leads to faster convergence of energy. VASP runs well in many computing platforms, both in vector computers and parallel computers, at nearly the same speed.

The Vienna Ab-initio Simulation Package (VASP) consists of 4 input files for the calculation of various material properties: INCAR, POSCAR, POTCAR, and KPOINTS. Besides, an execution script is required to submit the VASP calculation in a high-performance computing platform. The schematic of work flow of VASP is provided in Fig. 2.2.

All the results presented in this thesis are obtained using the projected augmented-wave (PAW) method implemented in the Vienna Ab initio simulation package (VASP) to describe ion-electron interaction. The generalized gradient approximation at the level of

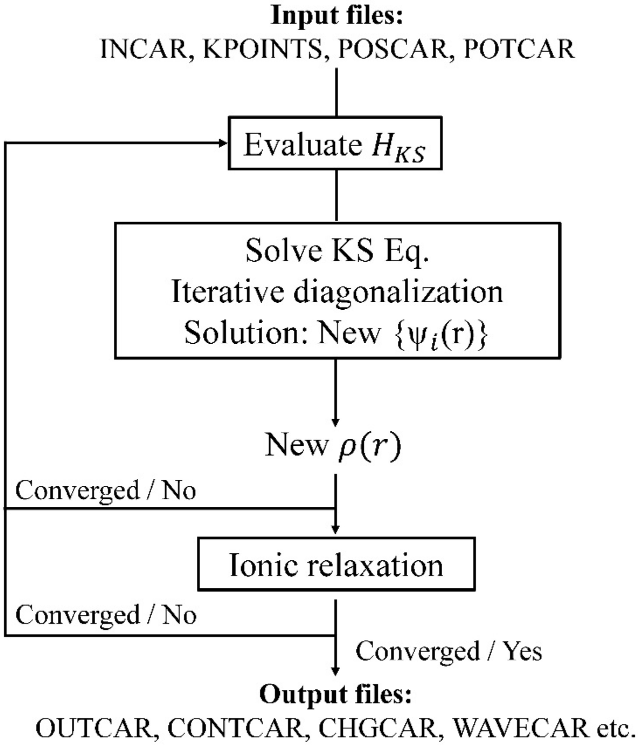
Input files:
INCAR, KPOINTS, POSCAR, POTCAR
Evaluate H_{KS}
Solve KS Eq.
Iterative diagonalization
Solution: New $\{\psi_i(r)\}$
New $\rho(r)$
Converged / No
Ionic relaxation
Converged / No
Converged / Yes
Output files:
OUTCAR, CONTCAR, CHGCAR, WAVECAR etc.

Figure 2.2 *Schematic of the workflow of VASP.*

Perdew, Burke, and Ernzerhof (GGA-PBE) [95] has been used in the description of the exchange-correlation functional. The hybrid HSE06 functional has been utilized for a more accurate band gap and band edges, which are usually underestimated in the GGA-PBE. [116] We have employed dispersion corrected density functional theory DFT-D2 [123] for van der Waals heterostructure. Kinetic energy cut-off of 500-550 eV has been used, while the sampling of Brillouin zone has been performed with a higher k-point grid of ~ (11×11×1) -(32×32×1). The PHONOPY [132] code was used to obtain the phonon dispersion curve through density functional perturbation theory (DFPT) using the supercell approach.

2.4 Mechanical properties

The elastic stiffness coefficients (C_{ijkl}) have been calculated by the formula

$$C_{ijkl} = C_{ijkl}^{ion} + C_{ijkl}^{el} = \frac{d\sigma_{ij}}{d\varepsilon_{kl}} \tag{2.49}$$

Where $\sigma_{ij}, \varepsilon_{kl}$ are the stress tensor and the strain tensor respectively. According to Voigt's notation, the subscripts i and j in σ_{ij} and ε_{ij} can be represented by $1 = xx, 2 = yy, 3 = zz, 4 = yz, 5 = zx, and\ 6 = xy$.

The 2D layer modulus, which indicates the resistance of a nanosheet to stretching, is defined by [133], [134];

$$\gamma^{2D} = \frac{1}{2}[C_{11} + C_{12}] \tag{2.50}$$

while Young's modulus (Y) $= \frac{C_{11}^2 - C_{12}^2}{C_{11}}$, (2.51)

Poisson ratio $(\nu) = C_{12}/C_{11}$, (2.52)

Shear modulus $(G) = C_{66}$. (2.53)

Moreover, intrinsic strength (σ_{int}) and bending modulus (D) of a nanosheet can be evaluated using

$$\sigma_{int} \sim \frac{\Upsilon}{9} \tag{2.54}$$

$$D = \frac{\Upsilon\Delta^2}{12(1-\nu^2)} \tag{2.55}$$

where Δ is the thickness of the nano-sheet.

The Born-Huang stability criteria:

$$\mathrm{C}_{11} > 0,\ \mathrm{C}_{22} > 0,\ \mathrm{C}_{11} - \mathrm{C}_{12} > 0,\ \mathrm{C}_{11}\mathrm{C}_{22} - \mathrm{C}_{12}^2 > 0 \tag{2.56}$$

The critical buckling strain (ϵ_c) of a 2D material can be evaluated using

$$\epsilon_c = -\frac{4\pi^2 D}{\Upsilon L^2} \tag{2.57}$$

where L is the length of the 2D nanosheet in the unit of Å.

2.5 Piezoelectric properties

The third rank linear piezoelectric stress and strain tensor components, e_{ijk} and d_{ijk}, that couple electronic polarization (P_i) or the macroscopic electric field (E_i) to the second-rank stress tensor (σ_{jk}) and the strain tensor (ε_{jk}) components is given by;

$$d_{ijk} = \left(\frac{\partial P_i}{\partial \sigma_{jk}}\right)_{E,T} = \left(\frac{\partial \varepsilon_{jk}}{\partial E_i}\right)_{\sigma,T} \tag{2.58}$$

$$e_{ijk} = \left(\frac{\partial P_i}{\partial \varepsilon_{jk}}\right)_{E,T} = -\left(\frac{\partial \sigma_{jk}}{\partial E_i}\right)_{\varepsilon,T} \tag{2.59}$$

Where i,j,k ∈ {1, 2 , 3}, 1, 2, 3 correspond to spatial x, y, z direction.

The piezoelectric strain constants d_{ijk} describes the change in polarization vector component P_i w.r.t stress components σ_{jk} keeping electric field constant or changes in strain components ε_{jk} with respect to electric field components E_i , keeping mechanical stress constant and similar for others. According to Voigt's notation, the tensor e_{ijk} of 3rd rank is reduced to a 2nd rank tensor e_{mn}, where m $\in \{1, 2, 3\}$ and n $\in \{1, 2, 3, 4, 5, 6\}$. Piezoelectric stress coefficient e_{mn}, is directly evaluated using DFPT as implemented in VASP. The piezoelectric strain coefficients, d_{mn} are calculated by solving the tensor relation,

$$e_{mn} = d_{mp}C_{pn} \tag{2.60}$$

where tensor sum runs through the p index, $p \in \{1, 2, 3, 4, 5, 6\}$ for example

$$e_{12} = d_{11}C_{12}+d_{12}C_{22}+d_{13}C_{32}+d_{14}C_{42}+d_{15}C_{52}+d_{16}C_{62} \tag{2.61}$$

2.6 Charge carrier mobility and Exciton binding energy

The charge carrier mobilities (μ_{2D}) of individual monolayers and their vdW hetero-bilayers have been computed using the acoustic phonon limited charge carrier mobility based on effective mass and deformation potential theory proposed by Bardeen and Shockley [135] using formula

$$\mu_{2D} = \frac{2e\hbar^3 C_{2D}}{3k_BT(m^*)^2E_i^2} \tag{2.62}$$

where C_{2D} is the elastic modulus of the material along the transport direction, E_i is the deformation potential which is defined as

$$E_i = \frac{\partial \mathrm{E}_{\text{band-edge}}}{\partial \varepsilon} \tag{2.63}$$

where $\mathrm{E}_{\text{band-edge}}$ is the energy of VBM or CBM.

m^* is the effective mass of the charge carrier along the transport direction and is calculated by

$$m^* = \hbar^2[\partial^2\mathrm{E(k)}/\partial k^2]^{-1} \tag{2.64}$$

For evaluating the intrinsic carrier mobility of 2D materials, the deformation potential approximation (DPA) as proposed by Shockley and Bardeen [135] has been widely used in first-principles method, where the scattering by longitudinal acoustic (LA) phonons are only taken into account. This approach is conceptually simple but has been extremely successful in calculating the intrinsic carrier mobility of 2D sheets or nanoribbons, such as graphene [136], α-graphyne [137], graphdiyne [138], silicene [139], germanene [140], transition metal dichalcogenide (TMD) [141], as well as perovskites [142]. DPA can overestimate the intrinsic room-temperature mobility because it only considers the longitudinal acoustic phonon scattering process. DPA fails when scatterings with ZA, TA or LO phonon modes dominate. [143,144]

The formulation of Lang et al. [145] (equation 2.65) has been employed, which is an improvement upon the acoustic phonon limited carrier mobility built upon the deformation potential theory and effective mass approximation originally proposed by Bardeen and Shockley [135]. The formulation of Lang et al. [145] incorporates the anisotropy in the elastic constant, carrier effective mass and deformation potential, and the carrier mobility according to this advanced cum robust formalism is given as;

$$\mu_{\alpha x} = \frac{e\hbar^{3}\left(\frac{5C_{x_{2D}}+3C_{y_{2D}}}{8}\right)}{k_B T (m_{\alpha x})^{\frac{3}{2}} (m_{\alpha y})^{\frac{1}{2}} \left(\frac{9E_{\alpha x}^{2}+7E_{\alpha x}E_{\alpha y}+4E_{\alpha y}^{2}}{20}\right)} \tag{2.65}$$

where $\alpha = e, h$ denotes the type of carriers (electrons or holes), the effective mass of carriers in the units of the rest mass of the electron, m_0 along the x and y directions are designated by $m_{\alpha x}$ and $m_{\alpha y}$ respectively , deformation potential of the carriers along the x and y directions are denoted by $E_{\alpha x}$ and $E_{\alpha y}$ respectively and 2D elastic stiffness coefficients along the x and y directions are designated by $C_{x_{2D}}$ and $C_{y_{2D}}$ respectively.

The separability of photo-generated charge carriers can be determined from exciton binding energies (E_b^{ex}), which is determined through Mott-Wannier hydrogenic model as expressed by

$$E_b^{ex} = \frac{4\times 13.6\mu_{ex}}{m_0 \varepsilon^2}\ (eV), \quad \frac{1}{\mu_{ex}} = \frac{1}{m_e} + \frac{1}{m_h} \tag{2.66}$$

where m_0 is the electron rest mass, μ_{ex} is the excitonic effective mass, ε is the macroscopic static dielectric constant.

$\varepsilon_{x(y)}$ is the macroscopic static dielectric constant along the x or y direction, while ε_z is the same along the z direction, $\varepsilon_{eff} = \sqrt{\varepsilon_{x(y)}.\varepsilon_z}$ is the effective macroscopic static dielectric constant.

E_B^{3D} is the 3D excitonic binding energy based on $\varepsilon_{x(y)}$, while $E_{B,eff}^{3D}$ is the same based on $\varepsilon_{eff} = \sqrt{\varepsilon_{x(y)}.\varepsilon_z}$, while $E_B^{2D} = 4 \text{ x } E_B^{3D}$ and $E_{B,eff}^{2D} = 4 \text{ x } E_{B,eff}^{3D}$

2.7 Optical properties

The linear response of a system to the incident electromagnetic (E.M.) radiation has been investigated based on the dielectric function which depends on the momentum transfer q in the photon-electron interaction and the energy ω. The optical properties are calculated from the complex dielectric function,

$$\varepsilon(\omega) = \varepsilon_1(\omega) + i\,\varepsilon_2(\omega) \tag{2.67}$$

where $\varepsilon_1(\omega)$ and $\varepsilon_2(\omega)$ correspond to real and imaginary parts.

The imaginary part is calculated in the long wavelength q→0 limit within the independent particle approximation,

$$\varepsilon_2(\omega) = \varepsilon_{\alpha\beta}^{(2)}(\omega) = \frac{4\pi^2 e^2}{\Omega} \lim_{q\to 0} \frac{1}{q^2} \sum_{c,v,k} 2w_k \delta(\epsilon_{ck} - \epsilon_{vk} - \omega) \times \langle u_{ck+e_\alpha q} | u_{vk} \rangle \langle u_{ck+e_\beta q} | u_{vk} \rangle^* \tag{2.68}$$

where Ω is the volume of the primitive cell, w_k are k-point weights and the factor 2 inside the summation accounts for the spin degeneracy. The $\epsilon_{ck}(\epsilon_{vk})$ are k-dependent conduction (valence) band energies; u_{vk}, u_{ck} are cell periodic part of the pseudo-wave function and $e_{\alpha,\beta}$ are the unit vectors along the Cartesian coordinate directions. The real part can then be calculated using the Kramers-Kronig transformation.

$$\varepsilon_1(\omega) = \varepsilon_{\alpha\beta}^{(1)}(\omega) = 1 + \frac{2}{\pi} P \int_0^\infty \frac{\varepsilon_{\alpha\beta}^{(2)}(\omega\prime)\omega\prime}{\omega'^2 - \omega^2 + i\eta} d\omega' \tag{2.69}$$

where P denotes the principle value and a small complex shift (η) of 0.1 has been used for slight smoothening of the real part of the dielectric function, which is acceptable for most of the calculations.

The optical parameters, such as extinction coefficient, absorption coefficient is based on ε_1 and ε_2. The complex refractive index is defined as

$$\mathrm{N}(\omega) = \mathrm{n}(\omega) + i\,\kappa(\omega) = \sqrt{\varepsilon(\omega)} \tag{2.70}$$

where n is the refractive index and κ is the extinction coefficient. The extinction coefficient (κ) is calculated using the following relation,

$$\kappa = \left(\sqrt{\varepsilon_1^2(\omega) + \varepsilon_2^2(\omega)} - \varepsilon_1(\omega)\right)^{1/2} / \sqrt{2} \tag{2.71}$$

The absorption coefficient (α_{abs}) is related to the extinction coefficient as

$$\alpha_{abs} = 4\pi\kappa/\lambda \tag{2.72}$$

where λ is the wavelength. If λ ~ nm, α reaches the order of 10^7 in cm^{-1} unit.

2.8 Power Conversion Efficiency of solar cell

Power conversion efficiency (PCE) in 2D excitonic solar cell constituted by vdW heterostructures with type-II band alignment is given by the formulation of Scharber et al. [146] as

$$\eta = \frac{J_{sc}V_{oc}\beta_{FF}}{P_{solar}} = \frac{0.65\left(E_g^d - \Delta E_c - 0.3\right)\int_{E_g^d}^{\infty}\frac{J_{ph}(\hbar\omega)}{\hbar\omega}d(\hbar\omega)}{\int_0^{\infty}J_{ph}(\hbar\omega)d(\hbar\omega)} \quad (2.73)$$

where J_{sc} is the short circuit current, V_{oc} is the open circuit voltage, β_{FF} is the fill factor (FF), and P_{solar} is incident solar energy power, J_{ph} (ħω) is the AM1.5 solar energy flux ($Wm^{-2}eV^{-1}$) at the photon energy ħω, and E_g^d is the energy bandgap of the donor materials.

In this calculation, the fill factor (β_{FF}) is assumed to be 0.65, as inferred from the Shockley-Queisser limit [147]. The maximum open circuit voltage V_{oc} (in eV units) is estimated as ($E_g^d - \Delta E_c - 0.3$) where the effective interface gap ($E_g^d - \Delta E_c$) is calculated as the energy difference between HOMO level of the donor and LUMO level of the acceptor and the value 0.3 in the V_{oc} term accounts for energy conversion kinetics.

In the equation, the integral in the numerator is the short circuit current, J_{sc}, which has been calculated using an upper bound of 100 % for external quantum efficiency (EQE), while the denominator is the integrated AM1.5 solar energy flux, which amounts to 1000 W/m^2. The efficiency, η is thus estimated as the product FF.V_{oc}.J_{sc} normalized by the incident energy flux, at the limit of 100% EQE.

2.9 Calculation details

In **Chapter 3**, the plane-wave basis has been treated explicitly 12 valence electrons ($p^6s^2d^4$) for transition metal atoms (Ti, Zr, Hf) and 6 valence electrons (s^2p^4) for chalcogen atoms (S, Se). We first carried out structural relaxation for all materials to get optimized geometry. Structural optimizations were continued until the forces on the atoms had converged to less than 0.01 eV/Å. A vacuum spacing larger than 20 Å along the z-direction has been used to decouple the adjacent periodic images to avoid spurious interactions. Brillouin-zone integrations were performed with a Gaussian broadening [148] of 0.1 eV during all structural optimizations. These calculations were carried out with a 5x7x1 Monkhorst-Pack **k**-point mesh [149] and an energy cut-off of 400 eV. To check the dynamical stability of the optimized structures, phonon calculations were carried out using the density-functional perturbation theory (DFPT) [150,151], as implemented in the VASP code along with the PHONOPY [152] package using a 4×4×1 supercell and a k-point mesh of 3×5×1. To ascertain the thermal stability, *ab initio* molecular dynamics (AIMD) has been performed at 300 K within 5 *ps* by the Nose-Hoover method. For electronic, elastic and piezoelectric calculations of the optimized materials, a kinetic energy cut-off of 500 eV was used, and the Brillouin zone was sampled with a 11×15×1 k-point grid of Monkhorst-Pack. The relaxed-ion stiffness coefficients C_{ijkl} including ionic relaxations have been calculated using finite difference method, as implemented in VASP code. The piezoelectric stress tensor e_{ij} have been calculated using DFPT as encoded in VASP using a 11×15×1 k-mesh. To achieve better accuracy of the electronic properties, the hybrid Heyd–Scuseria–Ernzerhof (HSE06) [115] functional was carried out in our present study. The HSE06 screening parameter [116] was set to a value of 0.2/Å. The atomic charge transfers are determined by Bader charge analysis using the bader-code [153–155] developed by Henkelman's group. Only to study Rashba-effect, we have considered spin-polarised and non-collinear calculation to incorporate spin-orbit coupling (SOC).

In **Chapter 4**, the interaction among electrons and nuclei is considered using the plane-wave projector augmented-wave (PAW) method. The exchange-correlation functional within generalized gradient approximation (GGA) is parameterized by the Perdew–Burke–Ernzerhof (PBE) formalism. We first performed structural relaxation for all materials to get optimized geometry by minimizing the forces on the atoms less than 0.01 eV/Å. A vacuum spacing larger than 15 Å along the z-direction has been used to avoid spurious interactions between the adjacent periodic images. These calculations were carried out with a Γ-centred 32 × 32 × 1 Monkhorst-Pack **k**-point mesh and an energy cut-off of 550 eV. To test the dynamical stability, phonon dispersion calculations have been performed using the density functional perturbation theory (DFPT) as implemented in the VASP code along with the PHONOPY [132] package. To plot spin-texture, we have considered spin-polarised and non-collinear calculation to incorporate spin-orbit coupling (SOC) using VASP package along with PYPROCAR [156] code. The elastic stiffness coefficients C_{ij} including ionic relaxations have been carried out using finite difference method, as implemented in VASP code.

In **Chapter 5**, the exchange-correlation functional used in this study lies within the ambit of generalized gradient approximation (GGA) parameterized by the Perdew–Burke–Ernzerhof (PBE) formalism. For the interlayer vdW interactions in the TMTC/TMDC hetero-bilayers, the DFT-D2 method of Grimme has been employed. The band structure, density of states (DOS) and optical properties of TMTC/TMDC hetero-bilayers have been computed using the HSE06 functional. The HSE06 screening parameter has been set to a value of 0.2/Å. The Brillouin Zone (BZ) of MoS_2 and WS_2 monolayer have been sampled using a Γ-centred 9x9x1 k-mesh. Whereas the Brillouin Zone (BZ) of ZrS_3 monolayer and ZrS_3/MS_2 hetero-bilayers have been sampled using a Γ-centred 7x5x1 k-mesh. The kinetic energy cut off has been set to 500 eV. Also, the total energy convergence criterion is chosen as 10^{-5} eV. The geometry optimizations have been performed based on the conjugate-gradient algorithm until the Hellmann-Feynman forces acting on individual atoms reached less than 0.01 eV/Å. Moreover, along the *c* axis, a vacuum slab of more than 14 Å has been used to decouple the periodic images of the hetero-bilayers to avoid spurious interaction arising from the non-local nature of the correlation energy. The density of states (DOS) has been calculated using tetrahedron smearing method [157] with Bloch correction and the optical properties have been computed via the frequency-dependent dielectric matrix. To check the dynamical stability, phonon calculations have been carried out using the density functional perturbation theory (DFPT) as implemented in the VASP code along with the PHONOPY package.

Chapter 3

Piezoelectronic and spintronic properties of 2D Janus monolayers and bilayers of group-IV transition metal trichalcogenides

This Chapter is based on the work published in:

Raihan Ahammed, Nityasagar Jena, Ashima Rawat, Manish K. Mohanta, Dimple, and **Abir De Sarkar***

"Ultrahigh Out-of-Plane Piezoelectricity Meets Giant Rashba Effect in 2D Janus Monolayers and Bilayers of Group IV Transition-Metal Trichalcogenides." ***The Journal of Physical Chemistry C*** 124, 21250 (2020)

3.1 Introduction

Piezoelectric materials are employed in various applications, for example, sensors, [158,159] actuators, [160,161] transducers, [162] energy harvesters [163,164] and at large, any function involving conversion between mechanical and electrical energy. [165] Nowadays, researchers are keenly interested in designing a new class of "nanopiezotronic" devices that make use of both their piezoelectric and semiconducting properties for their applications in nanogenerators, nanorobotics, field-effect transistors, piezoelectric diodes, and nanoelectromechanical systems. [166,167] The discovery of piezoelectricity in two-dimensional materials opens a new research avenue in the field of nano-piezoelectronics. [168–171] Two dimensional (2D) semiconducting materials can also show piezoelectric properties when inversion symmetry $(x, y, z) \rightarrow (-x, -y, -z)$ is broken or absent in these materials. For example, h-BN [172] and 2H-stacked transition-metal dichalcogenides (TMDCs), [173] such as MoS_2 and WS_2 monolayers, are centrosymmetric in bulk form and show no piezoelectricity; however, their monolayers lack inversion symmetry and show piezoelectricity. [58,174] Piezoelectricity in monolayer MoS_2 was first anticipated theoretically by means of first-principles calculations [56] and later perceived experimentally. [57] Nowadays, piezoelectricity at the atomic level is extensively investigated.

The conventional method to evaluate piezoelectricity in nanowires [175] consists in measuring the dipole moments induced by strain and this method has very recently been employed in MoS_2 supported on polymer substrate. [57] However, it is immensely challenging to determine the intrinsic piezoelectric properties quantitatively in such flexible 2D devices due to the interaction between the two-dimensional crystal and the substrate. The piezoelectric constant is quantitatively measurable by the state-of-art technique, the piezoresponse force microscopy (PFM). This method normally measures the deformations on a picometre scale with a spatial resolution of nanometres. [176] Recently, Zhu et al. [58] reported piezoelectricity in free standing monolayer MoS_2 using PFM; however, the conventional PFM technique was not applied, as the MoS_2 nanosheet is not coupled to the vertical electric field between the tip and substrate due to its mirror symmetry along the z-axis. A method combining a laterally applied electric field [177] and nanoindentation [178] in an atomic force microscope (AFM) was adopted to measure the piezoelectric stress arising at the membrane.

Huabing et al. [168] have reported extremely high piezoelectric values (d_{11} ~243.45 pm/V for α-SbAs) in the hexagonal phase of Group-V binary compounds. Large anisotropy in the piezoelectric constants in the nanosheets of Group-IV monochalcogenides, e.g., GeSe, have been predicted by Ruixiang et al. [179] Multifunctionality in these 2D materials can be attained synergistically via a systematic coupling of their semiconducting to the piezoelectric properties, which in turn may facilitate their applications in nanopiezotronics, piezophototronics, and piezophotocatalysis. Recently, Dimple et al. [180] have shown high in-plane piezoelectric coefficient (d_{22} =4.68-14.58 pm/V) in the Group IVB Janus TMDC (MXY, M=Zr, Hf, X, Y=S, Se Te) monolayers, which highly exceeds that in monolayer 1H-MoS_2 (d_{11}~3.0 pm/V) using first-principles calculations. However, Dong et al. [169] have previously predicted both strong in-plane (MoSeTe, d_{11}~5.3 pm/V) and much weaker out-of-plane (MoSeTe, d_{31}~0.03 pm/V) piezoelectric polarization. They have also found the out-of-plane piezoelectric coefficient d_{33} in multilayer MoSTe (5.7−13.5 pm/V) to be dependent on the stacking order. Moreover, it is significantly higher than the generally utilized three-dimensional bulk piezoelectric solids, such as wurtzite-AlN (d_{33} = 5.6 pm/V), [181] α-quartz (2.3 pm/V) [182] and wurtzite-GaN (d_{33}= 3.1 pm/V) [181]. Guo et al. [183] reported an enhanced piezoelectric effect in Janus group-III chalcogenide monolayers (Ga2STe, Ga2SeTe, In2STe, In2SeTe), where in-plane piezoelectric coefficients reached up to 8.47 pm/V and out-of-plane piezoelectric coefficient lain in the range of 0.07- 0.46 pm/V.

Monolayers of Group VI transition metal dichalcogenides (TMDCs), such as, MoS_2, WS_2, $MoSe_2$, WSe_2 etc. have been in the spotlight for their extraordinary mechanical flexibility and strength. As a result, they are capable of sustaining up to 10% of elastic strain, which enables a large dynamical tunability in their properties via strain engineering, thereby making them attractive for applications in ultrathin flexible electronics and optoelectronics. [184] Shen et al. [185] demonstrated strain induced tunability in band gap in TMDCs, where the three-terminal FET devices were fabricated on 500 μm thick polyimide (PI) flexible substrate and a cantilever sample holder was used to apply uniaxial tensile strain to the various multi-layer TMDC FETs. Shen et al. have shown that the band gap decreases between 50 and 75 meV per 1% strain, which is consistent with first-principles based DFT calculations40 and optical measurements carried out in experiments. [186]

Very recently, monolayers of Group-IV transition-metal trichalcogenides (TMTCs), [187,188] such as TiS_3, $TiSe_3$, ZrS_3, $ZrSe_3$, etc. have stimulated a great deal of research interest due to their exceptional photo-switching effect ($\tau \sim$ 50 s). They show outstanding spectral selectivity and demonstrate high capabilities for photodetection from visible to near Infra-Red (NIR) range (405 to 780 nm). [189] These 2D TMTC monolayers show immense prospects for their application in high-performance nanoscale optoelectronic devices. The Janus phase of TMDC monolayers, such as MoSSe have already been explored for their proficient photocatalytic and piezoelectric functionalities. Ang-Yu Lu et al. [190] have experimentally synthesized Janus structures of MoSSe, using home-made chemical vapor deposition and proposed that the key to the synthetic approach lies in controlling the reaction kinetics. S-Mo-Se Janus monolayer has also been synthesized experimentally by substituting the top layer of Se atoms in $MoSe_2$ by sulfur. [191] To date, there is no report on the experimental synthesis of Janus structures of TMTC monolayers. However, Janus structures of TMTC monolayers are envisioned to be synthesizable along with the footprints of the already synthesized Janus monolayers of TMDC. [190,191]

In the present chapter, the Janus structures of TMTC monolayers and their bilayers have been studied using the state-of-the-art density-functional theory (DFT). The absence of inversion symmetry in the Janus structures of these layered semiconducting nanosheets augments a different sphere to piezoelectricity. At present, research on piezoelectricity in 2D materials is at the rudimentary level. To overcome the disparities between the existing knowledge of piezoelectricity at the nanoscale and its envisioned practical applications, there is a strong need to gain an in-depth insight into the origin of piezoelectric properties in the 2D materials and its possible link-up with other features, such as Rashba effect. In our theoretical work, these Janus TMTC 2D nanosheets show enormous prospects in nanotechnology in the field of nanoelectronics, nanospintronics, and nanopiezotronics on account of their large Rashba spin splitting and superhigh out-of-plane piezoelectric constant. We have systematically shown the energetical, mechanical, and dynamical stability of these 2D nanosheets, which suggest a high degree of feasibility in the experimental realization of these Janus monolayers.

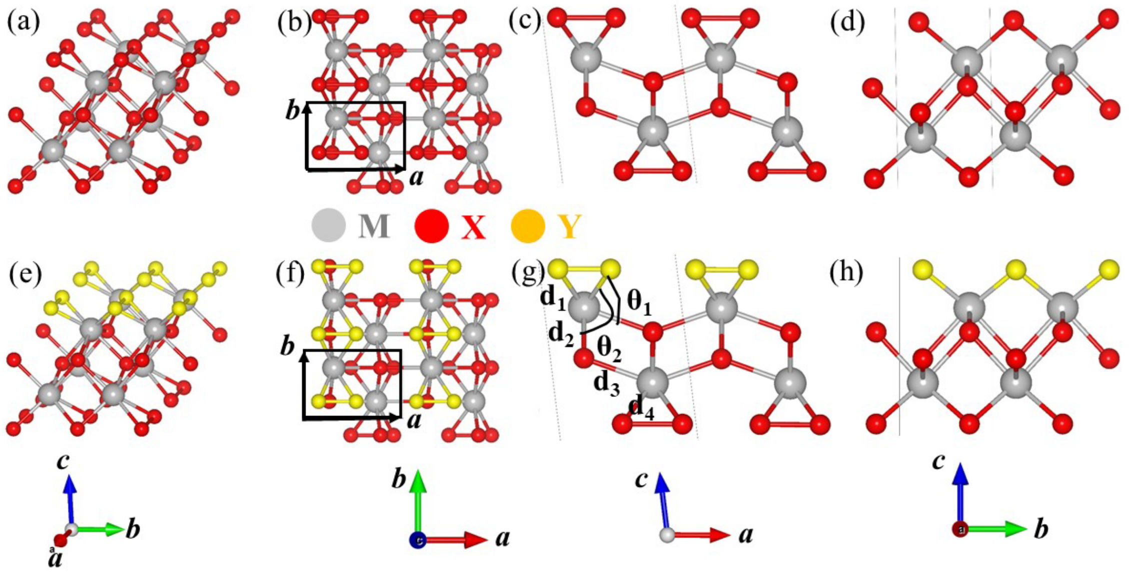

Figure 3.1 *(a) Crystal structure, (b) Top view, (c) Side view along a-axis and (d) Side view along b-axis of MX3 monolayers. Similarly, for Janus MX2Y monolayers (e) Crystal structure, (f) Top view, (g) Side view along a-axis and (h) Side view along b-axis.*

3.2 Results & Discussions

3.2.1 Crystal Structures and Symmetry

Structurally, monolayers of transition metal tri-chalcogenides, MX_3 (M=Ti, Zr, Hf; X = S, Se) belong to monoclinic crystal system. The unit cell comprises two basic structural units in which transition-metal atoms placed at the center of each prism while six chalcogen atoms lie at the corners, as displayed in Fig. 3.1(a−d). For preparing the Janus phase of MX_3 monolayer, the top layer of one type of chalcogen atoms (X) should be substituted by another Y chalcogen atoms, generating an asymmetric structure of chemical formula MX_2Y, as shown in Fig. 3.1(e−h). In this approach, six Janus monolayer structures, TiS_2Se, $TiSe_2S$, ZrS_2Se, $ZrSe_2S$, HfS_2Se, $HfSe_2S$, have been generated. Cohesive energy (E_c) calculations have been carried out to confirm the thermodynamic stability of these Janus monolayers (Table 3.1).

Table 3.1 *Lattice constants [a, b (Å)], lattice angle [α, β, γ (⁰)], bond-lengths [d_1, d_2, d_3, d_4 (Å)], bond angles [θ_1, θ_2 (⁰)], cohesive energy per unit cell [E_c (eV)], charge transferred from metal atom [ΔQ_M(e)], dipole moment [μ (Debye)].*

TMTC Materials	a	b	α, γ	β	d_1	d_2	d_3	d_4	θ_1	θ_2	E_c	ΔQ_M	μ_1	μ_2	μ_3
TiS_3	5.02	3.42	90	96.5	2.50	2.47	2.67	2.50	79.5	87.8	-5.67	3.34	0.0	0.0	0.0
$TiSe_3$	5.36	3.57	90	98.2	2.64	2.61	2.86	2.64	77.6	88.2	-5.05	3.07	0.0	0.0	0.0
ZrS_3	5.19	3.65	90	96.3	2.62	2.61	2.74	2.62	79.7	86.8	-6.09	4.00	0.0	0.0	0.0
$ZrSe_3$	5.48	3.78	90	97.2	2.76	2.75	2.91	2.76	78.0	87.6	-5.46	3.67	0.0	0.0	0.0
HfS_3	5.14	3.61	90	98.8	2.60	2.59	2.72	2.60	79.7	86.9	-6.05	4.06	0.0	0.0	0.0
$HfSe_3$	5.45	3.74	90	98.1	2.75	2.73	2.89	2.75	77.8	87.6	-5.40	3.74	0.0	0.0	0.0
TiS_2Se	5.15	3.46	90	97.1	2.68	2.46	2.91	2.50	79.8	90.3	-5.46	3.29	0.30	0.75	0.57
$TiSe_2S$	5.29	3.51	90	98.2	2.50	2.62	2.82	2.63	79.5	87.6	-5.25	3.12	0.10	0.69	-0.40
ZrS_2Se	5.27	3.69	90	96.4	2.77	2.61	2.78	2.63	77.8	87.8	-5.89	3.92	-0.13	-0.83	0.28
$ZrSe_2S$	5.45	3.74	90	97.3	2.63	2.75	2.89	2.76	79.6	86.6	-5.66	3.74	0.08	0.80	-0.27
HfS_2Se	5.21	3.65	90	102.3	2.77	2.59	2.75	2.75	79.9	89.3	-5.84	4.00	0.24	-0.84	0.37
$HfSe_2S$	5.41	3.70	90	99.3	2.61	2.72	2.87	2.74	79.4	86.6	-5.60	3.82	0.03	0.80	-0.48

The lattice constants, bond lengths, and bond angles are indicated in Fig. 3.1 and summarized in Table 3.1. The lattice constants (a, b) and bond lengths (d_1, d_2, d_2, d_3, d_4) of MS_3 monolayers are slightly smaller than the MSe_3 monolayers and similar trend is followed in their Janus derivatives MS_2Se and MSe_2S monolayers respectively. Janus MX_2Y monolayers possess monoclinic Pm (6) space group symmetry, which is non-centrosymmetric as the inversion symmetry $(x, y, z) \rightarrow (-x, -y, -z)$ is absent. In contrast, the parent structure has a centrosymmetric space group $P2_1/m$ (11) and contains inversion symmetry. As a result, parent TMTC structures do not show any intrinsic dipole moments, whereas their Janus derivatives show some finite intrinsic dipole moments as listed in Table 3.1.

3.2.2 Chemical Bonding Interactions

We have investigated the charge distribution to analyse the bonding interaction as depicted in Fig. 3.2(a) and 3.2(d). The character of charge distribution between the transition metal and chalcogen atom is directional, which indicates the existence of finite covalent bonding. To identify the nature of chemical bonding correctly, we have also calculated charge transfer distribution and electron localization function (ELF).

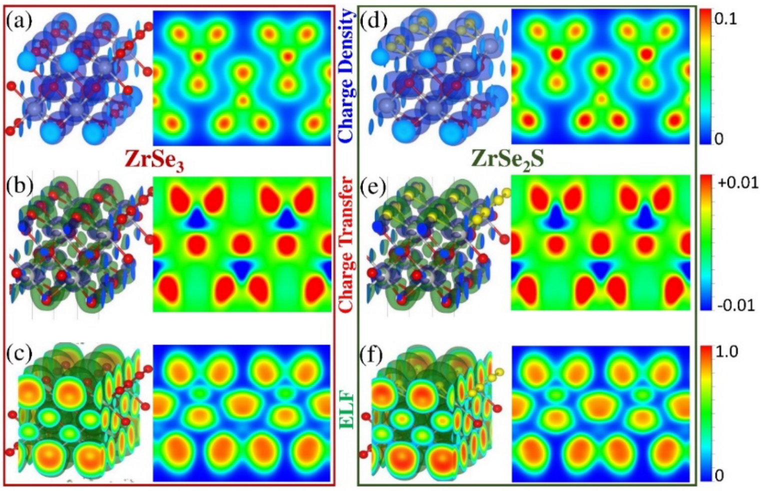

Figure 3.2 *Chemical bond analysis: (a) Charge density distribution, (b) Charge transfer distribution and (c) Electron localization function (ELF) of* $ZrSe_3$ *monolayer (First part: 3D view and second part: projection on the (010) plane). Similarly, (d), (e), (f) for the Janus monolayer* $ZrSe_2S$.

The charge transfer distribution (as shown in Fig. 3.2(b, e) in the bonding states is determined by the difference between the valence charge density of the MX_3 or MX_2Y nanosheet and the non-interacting charge density evaluated from a superposition of the valence charge density of the free atoms. Green and blue colors in the 3D picture in Fig. 3.2(b) and 3.2(e) represent spatial regions of electronic charge accumulation and depletion, respectively. Projection of charge transfer distribution on (010) plane (Fig. 3.2(b) and 3.2(e)) clearly shows the charge transfer from transition metals to chalcogen atoms consistent with ionic picture. Pure ionic bonding interaction between transition metals and chalcogen atoms could be expected if there is isotropic charge transfer distribution. The anisotropic charge transfer distribution indicates finite covalent bonding. Moreover, a finite electronic charge builds up around the center of the bond between the transition metal and chalcogen atom, confirming the covalent nature of the chemical bond. It indicates the existence of mixed bonding nature in these monolayers. Chemical bonding interaction between the transition metal and chalcogen atom (M-X or M-Y) shows both covalent and ionic bonding character. This kind of bonding nature is also supported by ELF calculation, as shown in Fig. 3.2(c) and 3.2(f). Probability of finding an electron at a specific region are measured by ELF. The complete localization of electrons is specified by red color in the ELF plots corresponding to the maximum value 1. Electron localization at chalcogen atoms and delocalization at transition metal atoms reiterate charge-transfer interaction. Finite ELF between transition metal and chalcogen atom, as represented by green color, indicates the hybridization interaction. Our results of charge-density, charge-transfer, and ELF analysis ascertain that the bonding interaction between transition metal and chalcogen atom show mixed ionic-covalent character. The strength of mixed ionic-covalent bond is weak which cause lower Young's Modulus in these materials. The nature of charge-density, charge-transfer, and ELF for both MX_3 TMTC monolayers and their Janus MX_2Y monolayers are the same only difference is the amount of charge transfer which reflects in their dipole moments as listed in Table 3.1.

3.2.3 Stability

To investigate the stability of the 2D Janus TMTC monolayers, we first perform phonon dispersion calculations. Phonon frequency spectra, which are widely used to validate the dynamical stability of materials, have been carried out with a 3x3x1 supercell using density-functional perturbation theory (DFPT), as depicted in Fig. 3.3. There is no imaginary frequency in the phonon band dispersion, which indicates its dynamical stability. Ab-initio molecular dynamics (AIMD) simulation with a canonical (NVT) ensemble has been performed to establish its thermal stability at room temperature (300K).

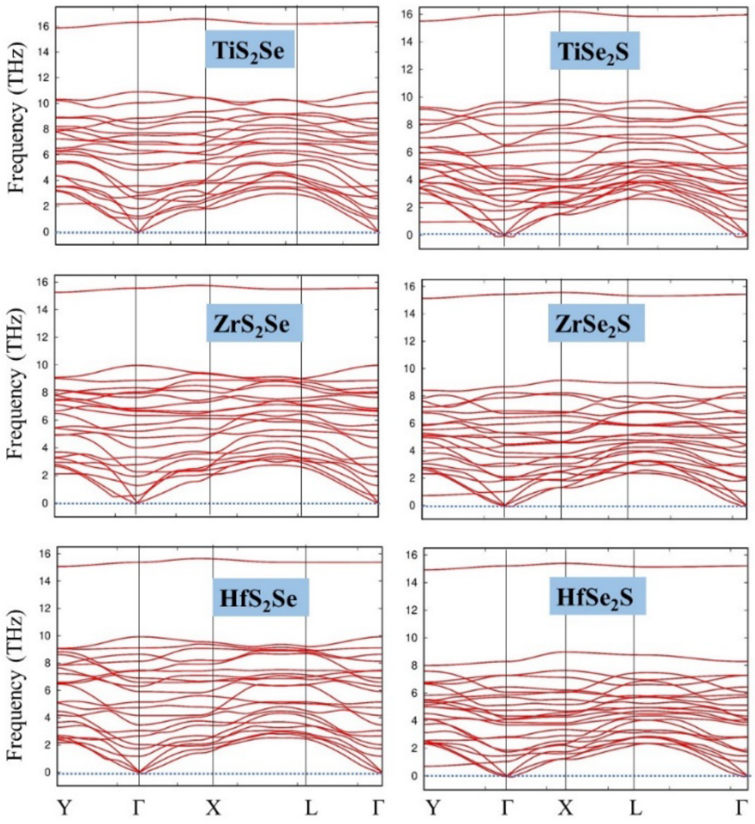

Figure 3.3 *Phonon frequency spectra of 2D Janus TMTC monolayers.*

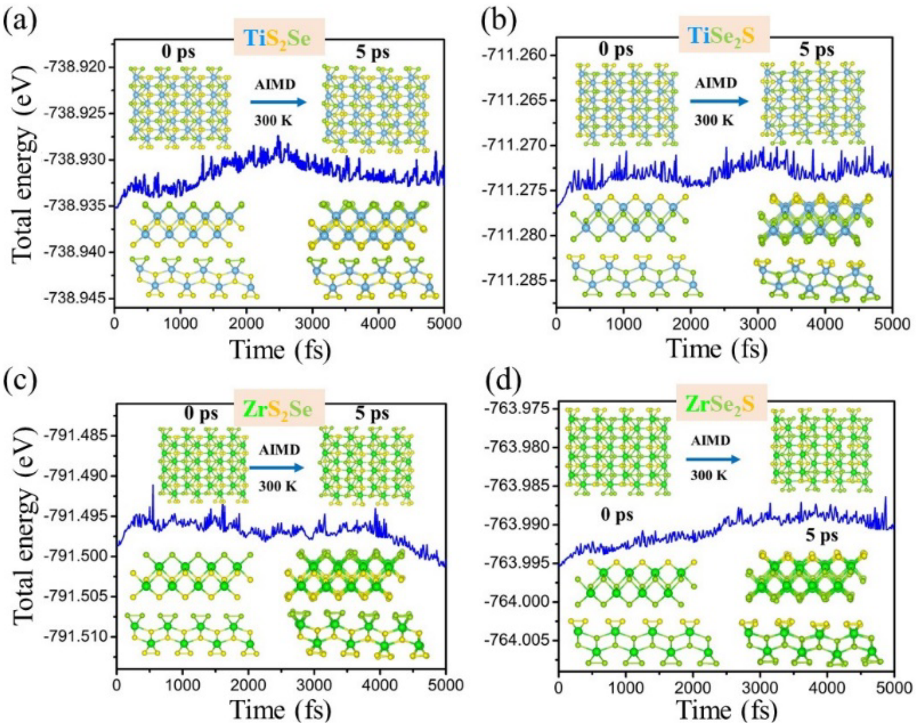

Figure 3.4 *Total energy fluctuation of the 2D Janus monolayer of (a) TiS_2Se, (b) $TiSe_2S$, (c) ZrS_2Se and (d) $ZrSe_2S$ with respect to time in AIMD simulation at 300 K. The inset shows the snapshot of the initial and final geometry depicting structural change in these monolayers in the AIMD simulation at 300 K.*

The simulations are implemented with a Nose-Hoover thermostat at 300 K up to 5 ps with a time step of 1 fs. For reducing the periodicity caused limitation, a 4x4x1supercell has been used for the 2D Janus structure to carry out the AIMD simulation. As illustrated in Fig. 3.4, the total energy fluctuation with simulation time is very negligible. From the final geometric structures in Figure 4, we cannot find any noticeable distortion after 5000 steps of AIMD simulation. Our findings confirm that these Janus TMTC monolayers are thermally stable at room temperature. Besides, the thermodynamic stability of these structures has been checked by calculating the cohesive energy as depicted in Table 3.1. The mechanical stability has also been verified by evaluating the elastic stiffness constants, Young’s Modulus, and Poisson’s ratio.

3.2.4 Elastic Properties

The calculated elastic constants of TMTC monolayers and their Janus derivatives are found to be positive as listed in Table 3.2 and satisfy the Born-Huang stability criteria, which indicate their mechanical stability.

***Table 3.2** Elastic stiffness constants [C_{11} (N/m), C_{22} (N/m), C_{12} (N/m)], Young Modulus [Y_{11} (N/m), Y_{22} (N/m)] and Poisson Ratio [υ_{11}, υ_{22}] of TMTC monolayers MX_3 and their Janus derivatives MX_2Y.*

TMTC Materials	**C_{11}**	**C_{22}**	**C_{12}**	**Y_{11}**	**Y_{22}**	**ν_{11}**	**ν_{22}**
TiS_3	87.87	134.55	16.38	131.50	85.88	0.19	0.12
$TiSe_3$	80.49	106.02	12.87	103.96	78.93	0.16	0.12
ZrS_3	81.06	124.20	16.48	120.85	78.87	0.20	0.13
$ZrSe_3$	79.04	107.86	14.02	105.64	77.41	0.17	0.12
HfS_3	90.64	134.48	17.92	130.94	88.25	0.20	0.13
$HfSe_3$	85.70	116.87	14.14	114.53	83.99	0.16	0.12
TiS_2Se	71.44	128.85	15.55	125.46	69.56	0.22	0.12
$TiSe_2S$	73.40	92.80	7.30	92.08	73.42	0.10	0.08
ZrS_2Se	91.52	123.44	15.44	119.53	89.59	0.17	0.12
$ZrSe_2S$	73.60	111.66	14.24	108.90	71.48	0.19	0.13
HfS_2Se	89.36	133.04	20.18	128.48	83.60	0.23	0.15
$HfSe_2S$	80.20	121.08	15.08	118.24	78.32	0.19	0.12

2D Young's modulus (Y) and Poisson's ratio (υ) can be determined using the following relations:

$$Y_{11} = \frac{C_{11}^2 - C_{12}^2}{C_{11}},\ Y_{22} = \frac{C_{22}^2 - C_{12}^2}{C_{22}},\ \upsilon_{11} = \frac{C_{12}}{C_{11}},\ \upsilon_{22} = \frac{C_{12}}{C_{22}}$$

All the TMTC monolayers and their Janus derivatives are elastically anisotropic. Young modulus along x-axis (Y_{11}) is larger than the y-axis (Y_{22}) for all the studied materials and have value less than 132 N/m. All these monolayers are more flexible than other two-dimensional nanosheets, for example graphene (Y=341 N/m), monolayer h-BN (Y=276 N/m) [70] and monolayer TMDCs (MoS_2, Y=134 N/m). [71] The elastic constants and Young's modulus of the Janus TMTC configurations are lesser than their parent TMTC structures. This suggests that MX_2Y monolayers are more flexible than MX_3 monolayers. The lower Young's modulus is because of the weaker M-X/Y bond strength. In-plane strain engineering at a significant scale will play a great role to tune their physical properties, for instance, band gap and piezoelectric properties.

3.2.5 Piezoelectric Properties

When mechanical stress or strain is applied on a non-centrosymmetric material, electric dipole moments are generated which produce an electrical voltage across the material. This phenomenon is called direct piezoelectric effect. On the other hand, the inverse piezoelectric effect is that the same material develops mechanical stress or strain when an electric field is applied. The responses of a piezoelectric solid are governed through various piezoelectric constants, for instance, piezoelectric stress tensor, $e_{ijk} = e_{ijk}^{ion} + e_{ijk}^{el} = (\frac{\mathrm{dP_i}}{\mathrm{d\varepsilon_{jk}}})_{\mathrm{E,T}}$, i,j,k $\in \{1, 2, 3\}$, 1, 2, 3 correspond to spatial x, y, z direction. Where $\mathrm{P_i}$ is the electric polarisation vector, ε_{jk} is the strain tensor, E is the macroscopic electric field and T is the temperature. According to Voigt's notation, the tensor e_{ijk} of 3rd rank is reduced to a 2nd rank tensor e_{mn}, where m $\in \{1, 2, 3\}$ and n $\in \{1, 2, 3, 4, 5, 6\}$. Piezoelectric stress coefficient e_{mn}, is directly evaluated using DFPT as implemented in VASP. The piezoelectric strain coefficients, d_{mn} are calculated by solving the tensor relation, $e_{mn} = d_{mp}C_{pn}$, where tensor sum runs through the p index, $p \in \{1, 2, 3, 4, 5, 6\}$ for example, $e_{12} = d_{11}C_{12}+d_{12}C_{22}+d_{13}C_{32}+d_{14}C_{42}+d_{15}C_{52}+d_{16}C_{62}$. In experiment, the piezoelectric strain constants (d_{mn}) are directly measured and it represent the mechano-electrical transduction efficiency of the material. The piezoelectric stress constants are converted to piezoelectric strain constants in order to compare experimental piezoelectric response (Table 3.3). The out-of-plane piezoelectric coefficients in these Janus monolayers have a significantly high value, as listed in Table 3.3. The out-of-plane piezoelectric coefficients in these Janus monolayers have a significantly high value. The piezoelectric strain coefficient d_{33} is found to be as high as 68.7 pm/V in Janus monolayer of $ZrSe_2S$ which is considerably larger than those of generally utilized three-dimensional bulk piezoelectric solids such as α-quartz (2.3 pm/V) [182] and AlN (5.6 pm/V) [181] suggesting the significance of out-of-plane piezoelectric properties in such Janus monolayers.

Table 3.3 *Piezoelectric stress/strain constants (e/d) of Janus TMTC monolayers. The units of C, e, d is N/m, 10^{-10} C/m and pm/V respectively.*

Janus TMTC	C_{11}	C_{22}	C_{33}	e_{11}	e_{22}	e_{33}	d_{11}	d_{22}	d_{33}
TiS_2Se	71.44	128.85	1.47	4.3329	0.0915	0.4358	5.66	0.08	0.49
$TiSe_2S$	73.40	92.80	0.90	0.0003	0.0130	0.4358	0.69	0.03	49.10
ZrS_2Se	91.52	123.44	0.89	0.0211	0.0310	0.1843	0.08	0.03	21.11
$ZrSe_2S$	73.60	111.66	0.32	0.0132	0.0313	0.2206	0.06	0.02	68.72
HfS_2Se	83.96	133.04	3.12	6.6902	0.0253	0.0896	8.19	0.02	4.08
$HfSe_2S$	80.20	121.08	2.98	0.0235	0.0269	0.1052	0.20	0.02	4.94

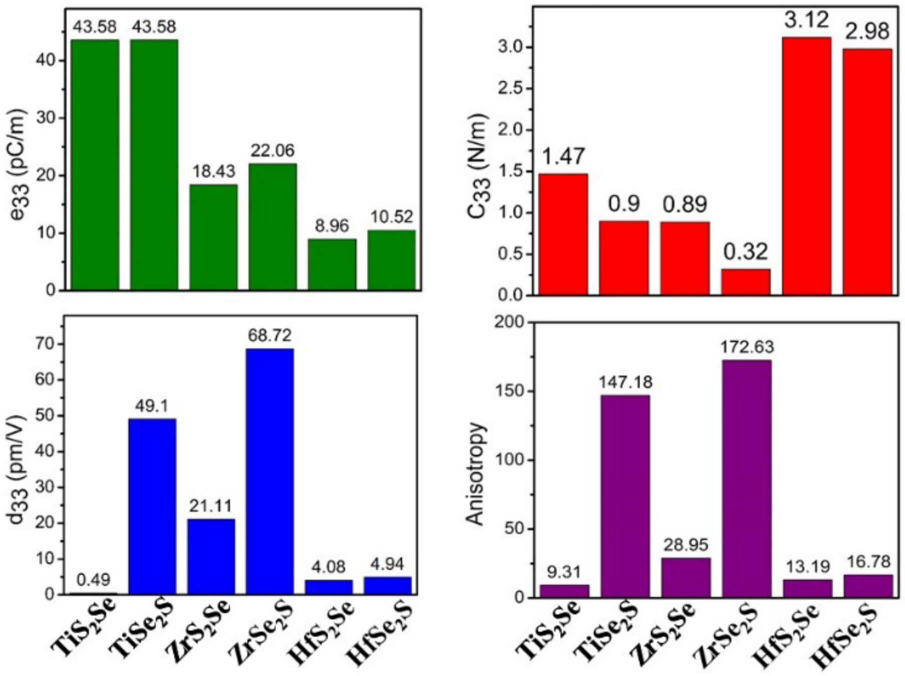

Figure 3.5 *Out-of-plane elastic constant (C_{33}), piezoelectric constant (e_{33}/d_{33}) and Universal anisotropy index, A_U of 2D Janus TMTC monolayers.*

These Janus TMTC monolayers show outstandingly large out-of-plane piezoelectric constants (Table 3.3) and prospective utilizations in nanoscale technologies. The out-of-plane piezoelectric stress/strain constant (e_{33}/d_{33}), elastic stiffness constant, C_{33} and anisotropy in elastic constant (A_U) have been plotted in the bar graph as shown in Fig. 3.5. It is found that $ZrSe_2S$ monolayer shows the highest anisotropy as well as highest d_{33} value. Whereas, TiS_2Se monolayer shows the lowest anisotropy in the elastic constant and lowest d_{33} value. We have calculated the universal anisotropy index [192] as defined by $A_U = 5G_V/G_R+K_V/K_R-6$, Where G and K are shear and bulk modulus respectively, subscript V denotes the Voigt bound and R denotes the Reuss bound. In plane, uniaxial and bi-axial strain have been applied in $ZrSe_2S$ monolayer to improve upon out-of-plane piezoelectric constant (e_{33}/d_{33}), but no significant improvement has been found as shown in Fig. 3.6. We also have investigated the piezoelectric properties of bilayer structure of Janus $TiSe_2S$ and $ZrSe_2S$ monolayers with two different stacking, as shown in Fig. 3.7. It is found that the out-of-plane piezoelectric constant d_{33} has been enhanced remarkably as of 541pm/V and 386 pm/V for stacking-1 and stacking-2 of $TiSe_2S$ bilayer as shown in Table 3. 4, which is larger than the highly efficient piezoelectric material of bulk ceramic PZT (d_{33}~268 pm/V). [193] In the $TiSe_2S$ bilayer of stacking-1, d_{33} component exceeds more than 50 times that of recently theoretically reported multi-layered structure of Janus MoSTe

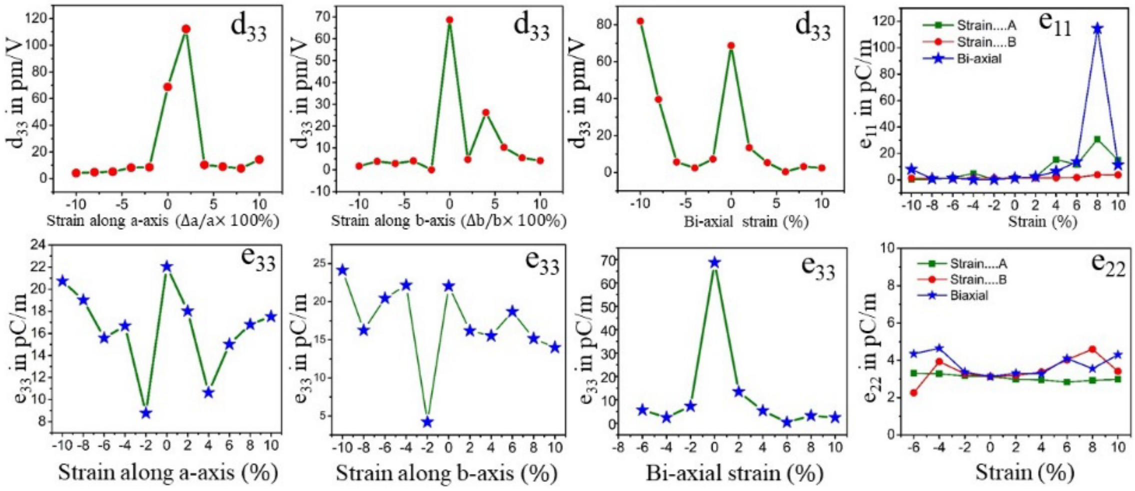

Figure 3.6 *Strain effects on in-plane and out-of-plane piezoelectric constants of 2D Janus* $ZrSe_2S$ *monolayer.*

Table 3.4 *Out-of-plane piezoelectric constants* (e_{33}/d_{33}) *of bilayer Janus* $TiSe_2S$ *and* $ZrSe_2S$ *monolayers. The units of* C_{33}, e_{33}, d_{33} *are N/m, pC/m and pm/V respectively.*

Bilayer Structure	Stacking Sequence	C_{33}	e_{33}	d_{33}
$TiSe_2S$	Stacking-1	14.03	7355.83	541.29
	Stacking-2	15.61	5643.54	386.13
$ZrSe_2S$	Stacking-1	2.75	75.41	23.95
	Stacking-2	0.69	44.90	56.92

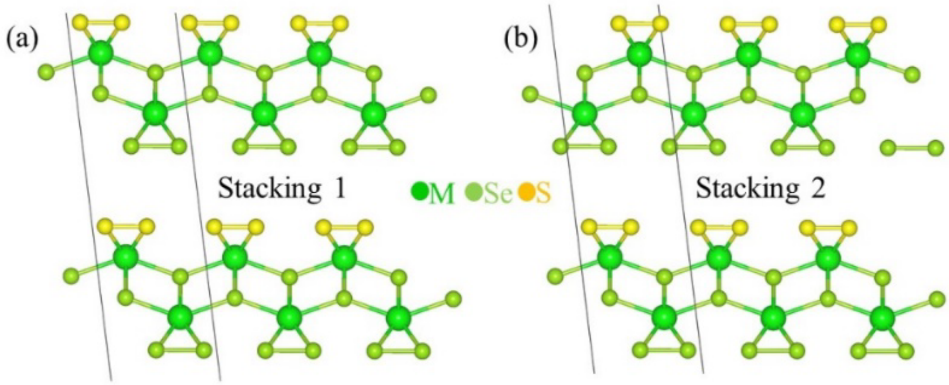

Figure 3.7 *Bilayer Janus structure of (a) Stacking-1 and (b) Stacking-2. Stacking-2 is designed by rotating 180 degree the top layer of stacking 1 with respect to z-axis.*

structure (d_{33}~10.57 pm/V) [169]. But in bilayer $ZrSe_2S$, d_{33} component is found to be decreased. It is evident that piezoelectric constant is highly dependent on the stacking sequence. To study the inter-layer coupling effect on the elastic and piezoelectric properties of bilayer $TiSe_2S$ of stacking-1, we decreased the inter-layer distance (h).

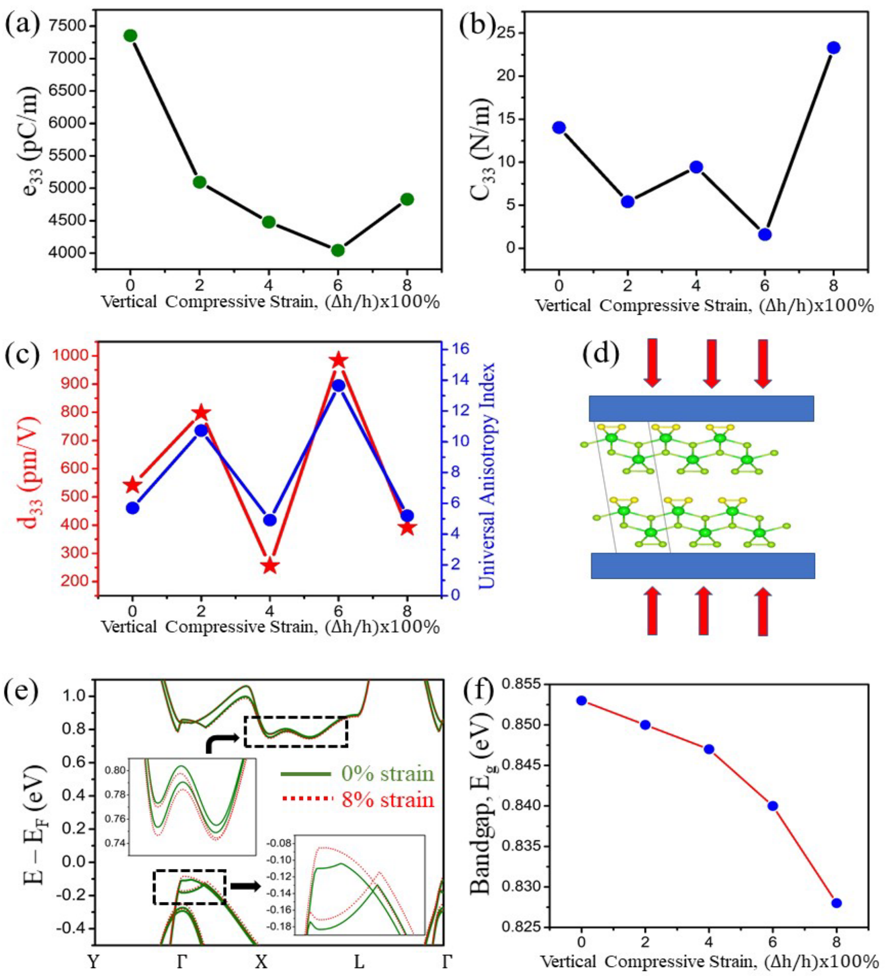

***Figure 3.8** Variation in out-of-plane (a) piezoelectric stress constants (e_{33}), (b) elastic constant (C_{33}), (c) piezoelectric stain constants (d_{33}) and Universal Anisotropy Index (A_U) of bilayer $TiSe_2S$ with vertical compressive strain; h is the inter-layer distance in the bilayer, (d) schematic of the bilayer system under applied vertical compressive strain, (e) band structure in stacking-1 in bilayer $TiSe_2S$ under 0% and 8% vertical compressive strain, (f) variation in the band gap in stacking-1 in bilayer $TiSe_2S$ with vertical compressive strain.*

The elastic and piezoelectric properties are found to be tunable upon the application of vertical compressive strain as shown in Fig. 3.8. It is found that the piezoelectric strain constant, d_{33} is enhanced by two-fold and reaches the value as high as 984 pm/V at 6% compressive strain. At 6% compressive strain, piezoelectric stress constant, e_{33} is lowest as well as elastic constant C_{33}. Lowering the C_{33} value is the main reason for enhancing the d_{33} value. The variation of anisotropy index, A_U follows the opposite trend as C_{33}. We find that the variation of d_{33} with vertical compressive strain is directly/inversely correlated with the variation of universal anisotropy index/C_{33} as shown in Figs. 3.8(b) and 3.8(c). The variation in e_{33} with strain differs from that of C_{33}, as shown in Figs. 3.8(a) and 3.8(b). In van der Waals crystals and heterostructures, $d_{33} \approx e_{33}/C_{33}$ and therefore, the simultaneous variation in both e_{33} and C_{33} with the application of vertical compressive strain results in the M-shaped trend. It mainly arises due to the zig-zag nature in the variation in C_{33} with the application of vertical compressive strain found in Fig. 3.8(b), although e_{33} decreases monotonically up to 6% strain. Similar behaviour is observed in hetero-bilayer [194] comprising of boron monophosphide (BP) and MoS_2, where e_{33} shows a steady trend with the application of vertical compressive strain, while C_{33} is found to be relatively oscillatory. Encouragingly, the nature of variation in d_{33} is found to be consistent with that of the Universal anisotropy index, as shown in Fig. 3.8(c). Crystalline phase of bilayer Janus TMTC remains the same upon the application of vertical compressive strain, as testified by the occurrence and retention of space group Pm in both unstrained and strained systems. The band gap is found to decrease very slowly with the application of vertical compressive strain. Stacking-1 and Stacking-2 of bilayer Janus $TiSe_2S$ are found to show all round stability. Thermodynamic stability has been confirmed from the exothermicity in the interlayer binding energy calculated in this work. The interlayer binding energy in stacking-1 (-16 meV/Å^2) and stacking-2 (-14 meV/Å^2) in bilayer Janus $TiSe_2S$ are comparable to typical vdW crystals like graphite (-12.0 meV/ Å^2) [195] and bilayer transition metal dichalcogenides (~ -19 meV/Å^2) [196]. Thermal and dynamical stability of the Janus bilayer structures in both the stacking order have been confirmed by performing ab-initio molecular dynamics (AIMD) simulation at 300 K (room temperature) and phonon dispersion calculations respectively. Absence of noticeable structural distortion in both Stacking-1 and Stacking-2 noted after 5 ps of AIMD simulation in Fig. 3.9 clearly confirms the thermal stability in them. Besides, lattice dynamical stability has been confirmed from the absence of imaginary frequencies in the phonon dispersion calculated and plotted in Fig. 3.10.

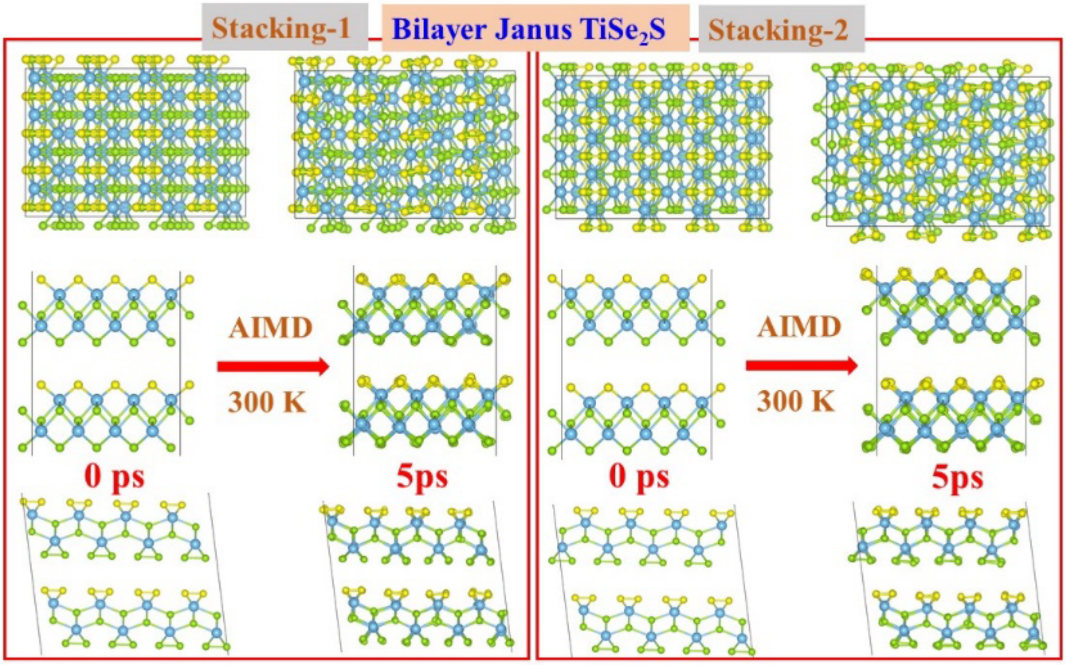

Figure 3.9 *The initial and final geometry depicting structural change of bilayer Janus TiSe2S in AIMD simulation at 300 K. There is no noticeable distortion in the final geometry after 5 ps.*

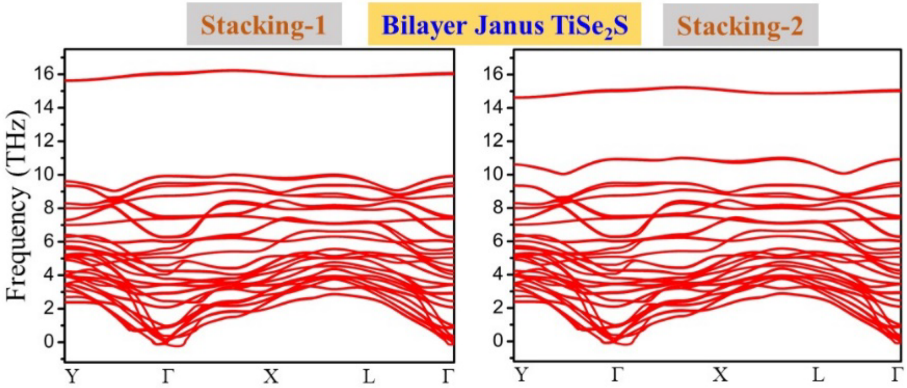

Figure 3.10 *Phonon frequency spectra of stacking-1 and stacking-2 of bilayer Janus* $TiSe_2S$.

3.2.6 Electronic Properties

The atomic layer and orbital contribution weighed electronic band structures of ZrS_3, $ZrSe_3$, and Janus ZrS_2Se, ZrS_2Se monolayers are shown in Fig. 3.11. As the band gap is underestimated using DFT with GGA-PBE functional, HSE06 functional has been used to calculate a more precise band gap. Hybrid functionals, which mix a fraction of Hartree-Fock (HF) exchange with local or semilocal exchange, have become increasingly popular in quantum chemistry and Computational Materials Science due to the description of more precise or accurate electronic band gap, which reaches closer to experimentally measured band gaps. Flores et al. [197] assessed the accuracy of the Heyd-Scuseria-Ernzerhof (HSE) hybrid functional to describe many-electron interactions and charge localization in semiconductors. They have found the HSE functional to accurately describe many-electron interactions with moderate correlations.

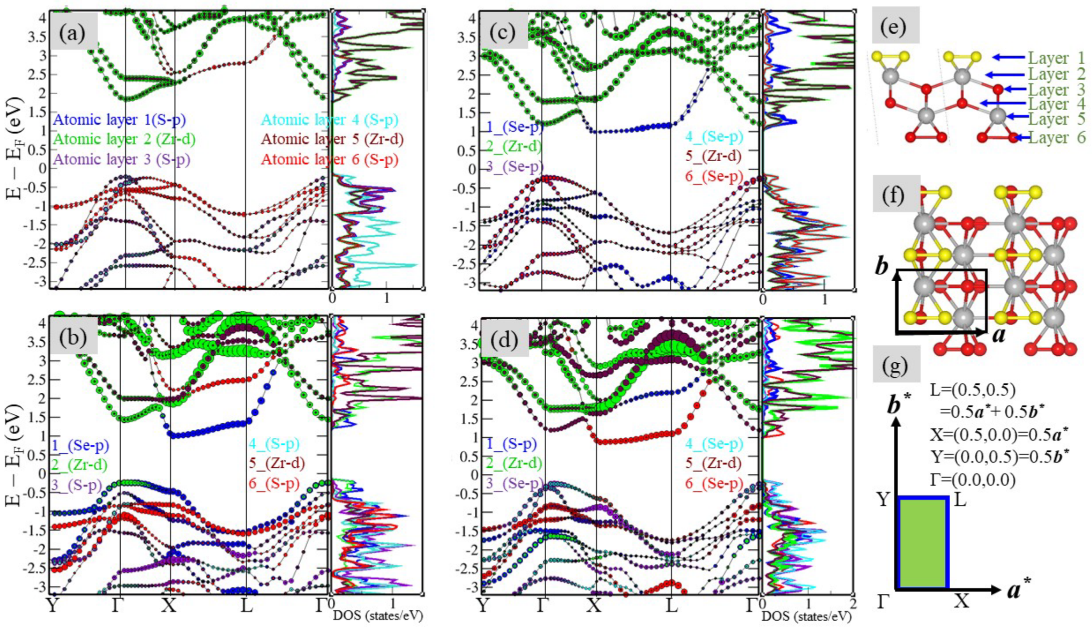

Figure 3.11 *Atomic layer and orbital projected bandstructure of (a) ZrS_3, (b) ZrS_2Se, (c) $ZrSe_3$, (d) $ZrSe_2S$ using HSE06 functional. (e) side view of crystal structure indicating layer number, (f) top view of crystal structure and (g) Reciprocal lattice vectors with shaded First Brillouin Zone (1BZ).*

Table 3.5 *Bandgap of Janus TMTC monolayers. "M" stands for metallic state. "I" represents indirect band gap.*

Bandgap (eV)	**TiS_2Se**	**$TiSe_2S$**	**ZrS_2Se**	**$ZrSe_2S$**	**HfS_2Se**	**$HfSe_2S$**
GGA-PBE	0.18 (I)	M	0.55 (I)	0.41 (I)	0.34 (I)	0.29 (I)
HSE06	0.75 (I)	0.42 (I)	1.24 (I)	1.11 (I)	1.11 (I)	0.98 (I)

It is observed that band gaps in all Janus TMTC monolayers are indirect and have a value ranging from 0.42–1.24 eV as listed in Table 3.5. The conduction band minimum (CBM) lies at the high-symmetric point, X [(0.5, 0.0, 0.0)2π/*a*] however valence band maximum (VBM) lies around Γ point of Brillouin zone (BZ). To gain insight about VBM and CBM state, atomic orbital contributions have been investigated. For ZrS_2Se ($ZrSe_2S$) monolayer, the valence band maximum state is hybridized with ~64% (86%) p-orbitals of chalcogen atoms and ~36% (14%) d-orbitals of metal atoms. However, conduction band minima state is hybridized with ~85% (85%) p-orbitals of chalcogen atoms and ~15% (15%) d-orbitals of transition metal atoms. The orbital contribution of the valence band around the Γ point plays a vital role in the Rashba spin-band splitting of the VB around the Γ point, which will be discussed in the next section in detail.

Table 3.6 *Orbital contribution of valence band of 2D Janus TiS_2Se monolayer at Γ and K' point as shown in without SOC band structure of Fig. 3.12(b).*

Atomic Orbital Contribution	p_z(S)	p_z(Se)	p_x(S)	p_x(Se)	p_y(S)	p_y(Se)	d_{xy}(Ti)	d_{xz}(Ti)	d_{z2}(Ti)
Γ point	0.021	0.048	0.374	0.0	0.0	0.135	0.201	0.317	0.0
K′ point	0.017	0.039	0.301	0.0	0.0	0.173	0.199	0.259	0.012

3.2.7 Rashba Properties

Significantly, the absence of in-plane mirror symmetry (x, y, z) → (x, y, −z) combined with spin-orbit coupling (SOC) effect in the 2D Janus TMTC monolayers cause Rashba-like spin-band splitting. The S_x-spin projected electronic bands in the monolayer of TiS_2Se Janus structure using GGA-PBE functional, including SOC have been depicted in Figs. 3.12(c) and 3.12(d). The contour of spin-resolved energy ($E= -0.17$ eV and $E_F= 0.0$ eV) in Fig. 3.12(e) demonstrates an exact circular shape for both outer and inner parts of the spin split valence band. We have observed in-plane spin orientation, as shown in Fig. 3.12(e), which is the signature of the Rashba effect as predicted in the 2D electron gas model. [61] There is no spin contribution from S_z. S_x mainly contributes in the in-plane spin contribution. There is a small S_y spin contribution only around $k_y = 0$. It is found that SOC incorporation breaks spin degeneracy of valence band (VB) around the high-symmetry Γ point. VB undergoes noticeable spin-band splitting. Consequently, in-plane spin polarization is observed as the energy bands shift in the momentum space. To know the source of spin splitting in the TiS_2Se Janus structure, we have to know the atomic orbital distributions of valence band around Γ point, as listed in Table 3.6. It is found that VBM of TiS_2Se monolayer at the low-symmetric K' point shows the major contribution from S-p_x (30.1%), Se-p_y (17.3%), Ti-d_{xy} (19.9%), and Ti-d_{xz} (25.9%) orbitals. Therefore, these

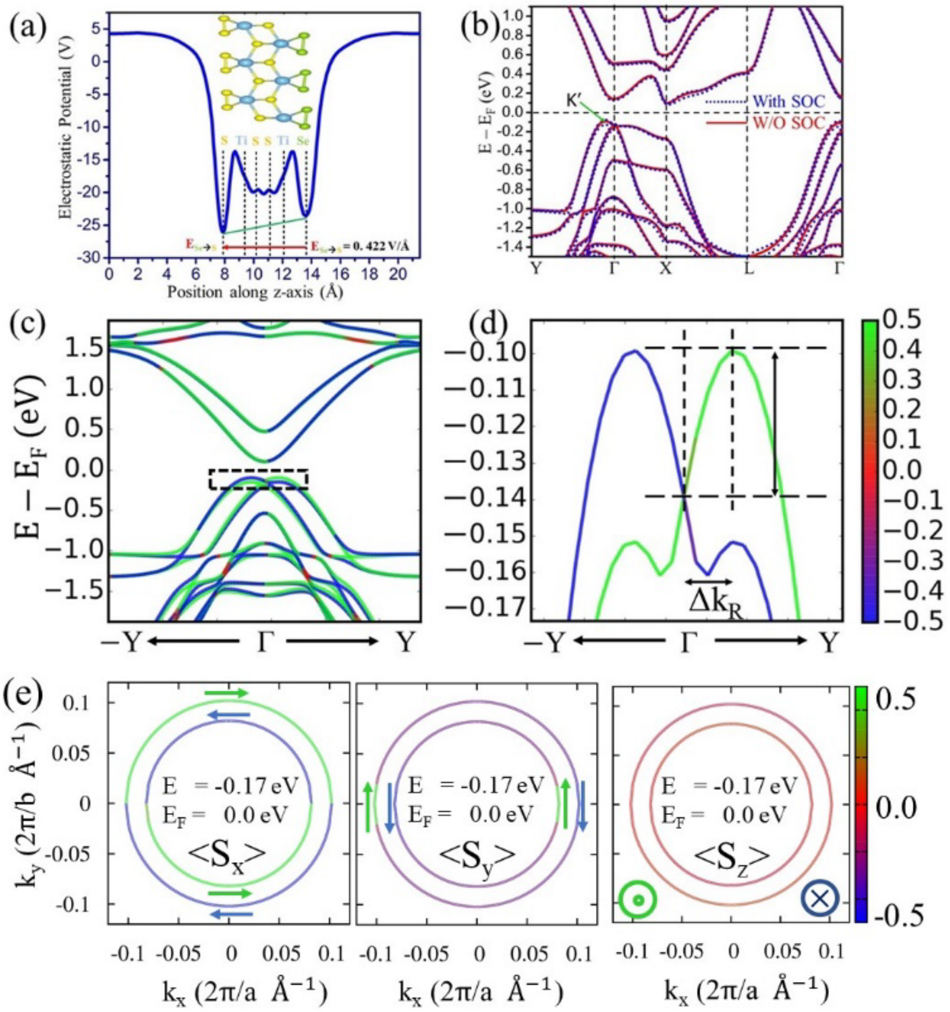

Figure 3.12 *(a) Planar average of electrostatic potential of 2D Janus TiS$_2$Se monolayer. The red arrow indicates the direction of the local electric field. (b) Band structure of 2D Janus TiS$_2$Se monolayer with and without spin-orbit coupling (SOC) using GGA-PBE functional. (c) Electronic band structure of monolayer Janus TiS$_2$Se with SOC using GGA_PBE functional with S$_x$ spin projection. (d) Enlarged band structure as indicated in Figure 12c. Colour map represents the expectation value of S$_x$ spin projection. (e) Spin structures of the Rashba split states for the spin projections S$_x$, S$_y$ and S$_z$ at an energy, E$= -0.17$ eV and E$_F$$=$ 0.0 eV.*

orbitals mainly contribute to Rashba spin splitting. Specifically, transition-metal d$_{xy}$ orbital plays a crucial role in the Rashba spin splitting. There is no transition-metal d$_{xy}$ contribution in the valence band around Γ-point in MSe$_3$ based Janus monolayers consequently Rashba spin splitting in the valence band has not been observed in these monolayers, as shown in Fig. 3.13. Mainly, Rashba effect has been observed in the Janus structures derived from the MS$_3$ monolayers, as depicted in Fig. 3.13. According to linear Rashba model, the SOC-included spin splitting is described by the well-defined Rashba parameter (α_R) as $\alpha_R = \frac{2\Delta E_R}{\Delta k_R}$, where ΔE_R and Δk_R are the Rashba energy splitting and the momentum shift, respectively, as indicated in Fig. 3.12(d). The parameters characterizing Rashba effect are listed in Table 3.7. The parameters of ΔE_R and Δk_R of Janus TiS_2Se monolayer are 40 meV and 0.074 $Å^{-1}$, respectively, thus α_R is calculated to be 1.081 eVÅ. The value of Rashba parameter is much higher than the conventional semiconducting heterostructure of InGaAs/InAlAs (α_R~0.07 eVÅ), [198] metallic surface state of Au(111) surface (α_R~0.33 eVÅ) [199] and Bi(111) surface (α_R~0.55 eVÅ) [200]. Although this value is much smaller than that previously reported in the Bi/Ag (111) surface alloy (α_R~3.05 eVÅ), [201] it is still much larger than that in the Janus tellurene (Te_2Se) monolayer (α_R~0.39 eVÅ), [202] Janus MoSSe monolayer (α_R~0.53 eVÅ) [203] and $GaSe/MoSe_2$ heterostructure (α_R~0.49 eVÅ), [204] indicating its potential applications in spintronic devices at the nanoscale.

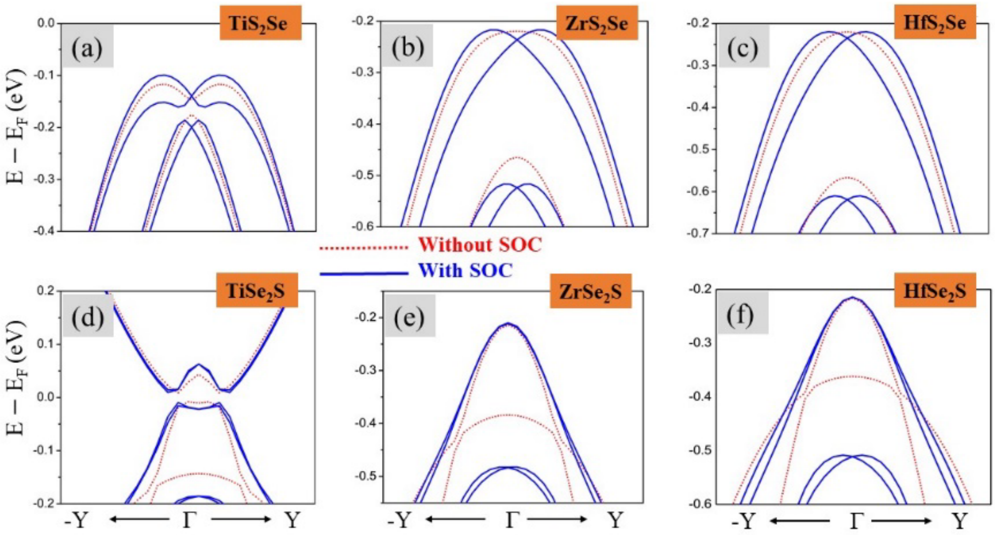

Figure 3.13 *Bandstructures of Janus TMTC monolayers near Fermi level with and without spin-orbit coupling (SOC) using GGA-PBE functional. Fermi level (EF) is set to zero.*

Table 3.7 *Parameters characterizing Rashba splitting in Janus monolayers of TMTC.*

Janus TMTC	ΔE_R (meV)	Δk_R ($Å^{-1}$)	α_R (eVÅ)
TiS_2Se	40	0.074	1.081
$TiSe_2S$	0	0.0	0.0
ZrS_2Se	19	0.053	0.717
$ZrSe_2S$	0	0.0	0.0
HfS_2Se	15	0.053	0.566
$HfSe_2S$	0	0.0	0.0

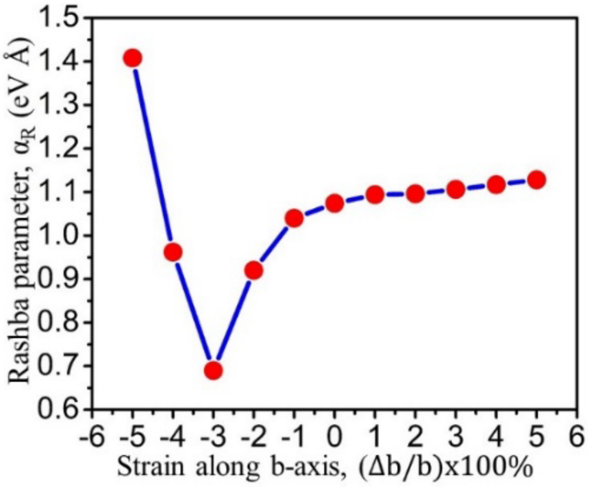

Figure 3.14 *Modulation of Rashba parameter, α_R of Janus TiS_2Se monolayer with application of strain along b-axis.*

The decreasing trend of Rashba parameter, α_R as TiS_2Se>ZrS_2Se >HfS_2Se is due to the decreasing inherent out-of-plane electric field (0.422, 0.326, 0.16 $VÅ^{-1}$). The Rashba parameter, α_R is directly proportional to the in-built electric field. The magnitude of the in-built electric field is determined by the slope of the planar-average electrostatic potential between two outermost atom minima (see the green line in Fig. 3.12a). As the Rashba effect is occurring along high symmetry Y-Γ-Y path, we have studied uniaxial strain effect along b-axis as depicted in Fig. 3.14. The momentum offset, Δk_R is slightly decreasing with tensile strain and increasing with compressive strain. As the Rashba energy splitting, ΔE_R is invariant under strain from -1% to 5%, Rashba parameter, α_R is increasing from 1.04 eVÅ to 1.23 eVÅ. At -5% strain, Rashba energy splitting, ΔE_R is strongly enhanced which causes a large Rashba parameter (α_R~1.41 eVÅ).

3.3 CONCLUSIONS

In this chapter, the stability, electronic, piezotronic and spintronic properties of the 2D Janus TMTC (MX_2Y) monolayers have been systematically examined by density-functional theory. The Janus structures of transition metal trichalcogenide (TMTC) monolayers have been predicted, which show superhigh out-of-plane piezoelectricity and giant Rashba spin-band splitting. These 2D Janus monolayers are found to be thermally, energetically, mechanically, and dynamically stable, which suggests the experimental feasibility in synthesizing these Janus monolayer structures. The electronic structure calculations show indirect bandgap in them, ranging from 0.5 eV to 1.5 eV. The absence of horizontal mirror symmetry and presence of strong spin-orbit coupling cause Rashba spin splitting in the electronic bands with high Rashba parameter (α_R ~ 1.08 eVÅ), which is much larger than the Janus MoSSe monolayer (α_R~0.53 eVÅ) and GaSe/$MoSe_2$ heterostructure (α_R~0.49 eVÅ). It rises to 1.408 eVÅ by applying a 5% uniaxial compressive strain along the y-direction. The breaking of structural and inversion symmetry together with mechanical flexibility leads to a large out-of-plane piezoelectric constant in these 2D Janus TMTC monolayers. The out-of-plane piezoelectric constant, d_{33} has been obtained as large as 68.7 pm/V in Janus $ZrSe_2S$ monolayer, which is very much higher than generally utilized three-dimensional bulk piezoelectric solids - wurtzite-AlN (d_{33} = 5.6 pm/V), wurtzite-GaN (d_{33} = 3.1 pm/V), α-quartz (d_{11} = 2.3 pm/V) in industry. By designing bilayer structures of these Janus TMTC monolayers, the d_{33} has been found to be enhanced. Moreover, d_{33} can be increased to an enormously high value (~1000 pm/V) by applying a vertical compressive strain in their bilayer structures, which is more than four times that of bulk ceramic PZT material (~268 pm/V). Our study reveals the immense potential of these 2D Janus TMTC monolayers and their bilayers in nanoscale energy harvesting through nano-piezo-electronics and spintronics.

Chapter 4

Valley spin polarization in h-MN (M=Nb, Ta) monolayers

This Chapter is based on the work published in:

Raihan Ahammed and **Abir De Sarkar**. "Valley spin polarization in two-dimensional h− M N (M= Nb, Ta) monolayers: Merger of valleytronics with spintronics." **Phys. Rev. B 105, 045426 (2022).**

4.1 Introduction

Nowadays, an extra valley degree of freedom (DOF), which is distinct and different from that of electronic charge and spin, has been stimulating intense interest in two-dimensional (2D) materials, offering a novel avenue in device design at the nanoscale. [74,75] The valley DOF occurs from multiply degenerate energy extrema of the valence band (VB) and conduction band (CB) in momentum space. So far, the valley DOF has drawn a great deal of attention in a large number of emergent quantum phenomena, such as, valley Hall effect [77] and valley-dependent orbital magnetic moment [205]. Valleytronics is aimed at actively controlling and manipulating the valley DOF in semiconductor devices analogous to the charge DOF in electronics and spin DOF in spintronics. [78] Several materials have been proposed as candidates for valleytronic materials, such as silicon [206], bismuth thin films [207], graphene [73,208], and transition-metal dichalcogenide (TMDC) [75,209] monolayers.

To exploit the valley DOF, it is essential to produce valley polarization via controllable techniques. Thus, various methodologies have been implemented to control valley polarization, such as, optical pumping [76,210], magnetic substrate proximity effect [209,211] and magnetic doping [212]. Charge carriers with suitable combinations of spin and valley indices, are selectively excited by the dynamic process of optical pumping using frequency-specific circular polarizations. Therefore, valley DOF can be utilized to encode information. As the nonequilibrium distribution of carriers of K/K′ valley with transient carrier lifetimes [213] will be generated by the dynamical valley polarization upon optical pumping, a rapid transfer of photogenerated carriers is needed to reduce the recombination.

When in-plane electric field is applied, photo-generated electrons and holes by optical excitation at the same K, will move along opposite directions under the effect of the Berry curvature, which is nothing but the effective magnetic field in momentum space. But the Berry curvature vanishes in inversion symmetric or centrosymmetric materials. Hence, broken inversion symmetry is compulsory for valleytronics. The two quantities, berry curvature ($\Omega_n(k)$) and orbital magnetic moment ($m(k)$) are fundamental quantities in valleytronics.

The presence of strong spin-orbit coupling (SOC) in inversion asymmetric materials induces Rashba-type spin splitting in the electronic band structure, which can be harnessed effectively in spintronics. The Rashba electronic states reveal unique band dispersion with spin-momentum locking, which can be explained by the Hamiltonian $\mathrm{H_R} = \alpha_\mathrm{R}\hat{\boldsymbol{\sigma}}.(\hat{\mathbf{k}}_{||} \times \hat{\mathbf{e}}_\mathbf{z})$ as proposed by Rashba et al. to describe 2D electron gas [61], where is α_R the Rashba constant, $\hat{\boldsymbol{\sigma}}$ is the vector of the Pauli matrices, $\hat{\mathbf{k}}_{||} = (\mathrm{k_x}, \mathrm{k_y}, 0)$ is the in-plane momentum of the electrons, and $\hat{\mathbf{e}}_\mathbf{z}$ is the out-of-plane unit vector indicating a direction of the local electric field induced by the asymmetric crystal potential. In heterostructures and at surfaces, the Rashba SOC field plays a crucial role for the electronic states as the structural asymmetry produces an out-of-plane electric field. [204] The Rashba SOC generated linear k-dependent spin-splitting of bands enables the control of electron current by steering the spin precession, which is the fundamental principle of action for spin field effect transistors (SFETs). [65] An essential factor in constructing such a device requires the channel length $\mathrm{L} = \pi\hbar^2/2\mathrm{m}^*\alpha_\mathrm{R}$ over which the spin precesses by π (180°); thus, shorter channel lengths need larger α_R. [214]

The Rashba effect in 2D materials has been garnering increasing scientific attention due to its remarkable capability in SFETs. [66] Charge carriers in materials with Rashba SO coupling experience a momentum-dependent effective magnetic field, a spin-dependent velocity correction resulting from the SO coupling. [62] These features are particularly attractive for the realization of device concepts [215] in which spin polarization is generated from charge current, manipulated by electric field. Rashba effect has been noticed experimentally in semiconductor quantum wells [216], polar semiconductors like BiTeI [217] and surfaces of heavy metals [218]. Several 2D materials have been predicted theoretically, such as graphene [219], Janus TMDC monolayers [220], and Janus transition metal trichalcogenide (TMTC) monolayers [1] and the $\mathrm{MoS_2}$/Bi (111) heterostructure [221].

The coupling of valley physics arising from spin-valley locking to the Rashba spin-band splitting caused by strong spin-orbit coupling is being increasingly sought after as the key ingredient in the flourishing field of valleytronics and spintronics. Yet, the paucity of 2D materials showing an appreciable spin-valley polarization along with Rashba effect holds back their implementation in next-generation electronics, such as, spin-valleytronics. Recently, Anand et al. [222] theoretically predicted the 2D nanosheets of single-layered niobium nitride, s-NbN, and h-NbN using ab-initio calculations. Anand et al. [222] reported that s-NbN is metallic and preserves the superconducting features of bulk NbN at low temperature, while h-NbN is a semiconductor exhibiting piezoelectric properties. Superconducting properties of high-quality NbN thin films [223,224] have been widely studied experimentally. The dynamical stability of monolayer h-NbN also suggests that it could be synthesized experimentally. [222] Chanana et al. [225] demonstrated a strange ferroelectric property in a strained 2D h-NbN monolayer that emanates from its electrons together with phonons, with out-of-plane spontaneous polarization linked with strain and electric field using first-principles DFT calculations. They also demonstrate electric field driven polarization switching in h-NbN at 5% bi-axial strain and present a simple model to capture the physics of its strongly coupled electronic and phononic ferroelectricity. Yet, Rashba effect and valley physics was overlooked in h-NbN. In this chapter, h-MN ($\mathrm{M} = \mathrm{Nb}, \mathrm{Ta}$) monolayers using first-principles calculations have been investigated. The presence of time-reversal symmetry and absence of inversion symmetry along with Zeeman-type valley and Rashba-type spin splitting are found to bring about a substantial coupling between the spin and valley degrees of freedom, which will facilitate seamless amalgamation of the evolving field of 2D spintronics with valleytronics.

4.2 Results & Discussions

4.2.1 Crystal symmetry and electronic property

Monolayer h-NbN has buckled trigonal lattice structure having space group P3m1 (156) as depicted in Fig. 4.1(a). Inversion symmetry [(x, y, z) → (−x, −y, −z)] is broken in this structure. The optimized lattice constant of the relaxed crystal structure is found to be |a|=|b|=3.16 Å, which is in very close agreement with other theoretical [37] result. The buckling height (Δ) is 0.78 Å. The direct lattice vectors are $\boldsymbol{a} = 3.16\, \boldsymbol{e_x}$, $b = -1.58\, \boldsymbol{e_x} + 2.74\, \boldsymbol{e_y}$. The corresponding reciprocal lattice vectors as shown in Fig. 4.1(i) are $\boldsymbol{a^*} = 0.32\, \boldsymbol{e_x} + 0.18\, \boldsymbol{e_y}$, $\boldsymbol{b^*} = 0.36\, \boldsymbol{e_y}$. The high symmetry k-points as indicated in the Brillouin zone are Γ (0.0,0.0), M (0.0,0.5$\boldsymbol{b^*}$), K (0.333$\boldsymbol{a^*}$, 0.333$\boldsymbol{b^*}$). 3D view of the valence band (VB) and conduction band (CB) about the Fermi level containing the energy extrema (VBM, CBM) is represented in Fig. 4.1(b). To clearly visualize these two bands, isoenergetic contours are plotted in 2D k-space as shown in Figs. 4.1(c) and 4.1(d). It is found that the isoenergetic contours near about the valence band edges are triangularly warped (TW) similar to monolayer TMDC [226] such as MoS_2. On the other hand, the isoenergetic contours near about the conduction band edges are elliptically warped. The electronic band structure with and without SOC, as shown in Fig. 4.1(e), has been calculated using GGA-PBE functional. Electronic structure of h-NbN exhibits an indirect band gap of 0.72 eV (without SOC) with VBM and CBM located at wave vectors in between high symmetric

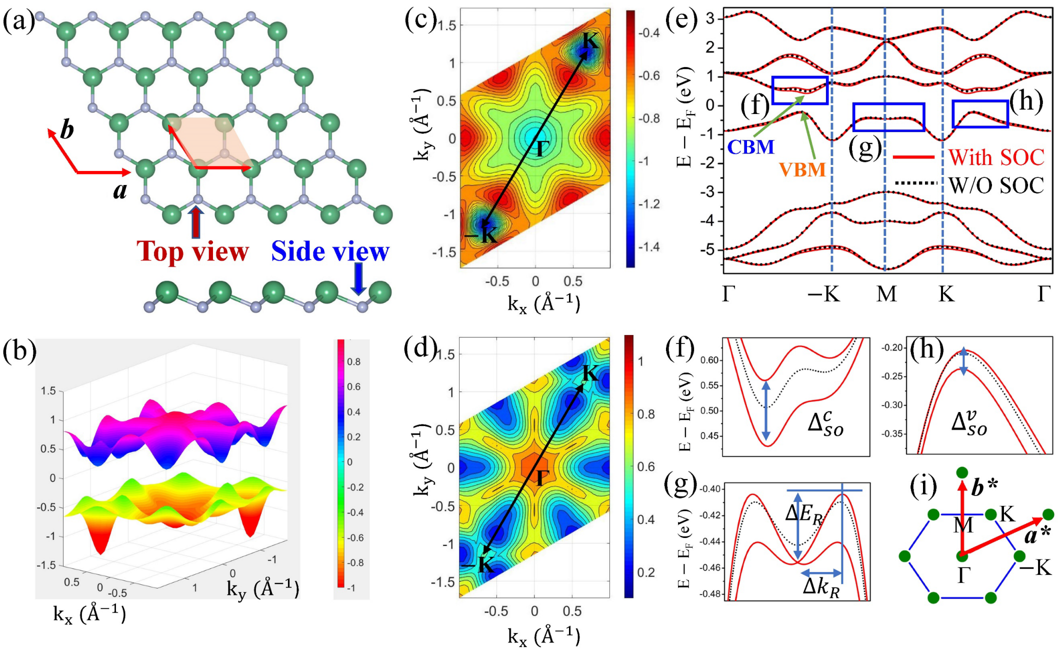

Figure 4.1 *(a) Top and side view of crystal structure of h-NbN, (b) 3D band structure near fermi level, (c) Energy contours of top valence band (VB), (d) Energy contours of bottom conduction band (CB), (e) Band structure along high symmetry k-path. (f), (g) and (h) are enlarged view as in indicated in (e). Fermi level is set to zero. GGA-PBE functional is used to calculate electronic structure. (i) First Brillouin Zone (1BZ) of h-NbN monolayer.*

K→Γ k-path, which is in excellent agreement with other theoretical report (~0.77 eV) [222]. The presence of strong SOC and absence of inversion symmetry lifts the spin degeneracy of VB and CB, causing Zeeman type (see Figs. 4.1(f) and 4.1(h)) and Rashba type (see Fig. 4.1(g)) spin splitting, which has been discussed in detail in the following section. The Zeeman-type valley spin splitting (VSS) is found to be 130 meV in the CB ($\Delta^{\mathrm{c}}_{\mathrm{SO}}$), whereas VSS in the VB ($\Delta^{\mathrm{v}}_{\mathrm{SO}}$) is found to be very small (~ 32 meV) upon introducing the relativistic SOC effect, which is exactly opposite to that of group-VI TMDCs, where small (large) VSS is noticed at CB (VB). The observed Zeeman-type VSS in monolayer h-NbN ($\Delta^{c(v)}_{SO}$~ 130 (32) meV) is comparable to that of Janus monolayer TMDC MoSSe [227] ($\Delta^{c(v)}_{SO}$~ 13.7 (170) meV). The atomic orbital contributions of VB and CB edges which involve in the SOC splitting have been investigated as listed in Table 4.1-4.2 and depicted in orbital projected band structure as shown Fig. 4.2. VB (CB) edge mainly comprise of Nb-d orbitals with 85.19 % (77.91%) contribution and maximum contribution consists of Nb-d_{z^2} orbital with 34.20 % (40.86%) respectively.

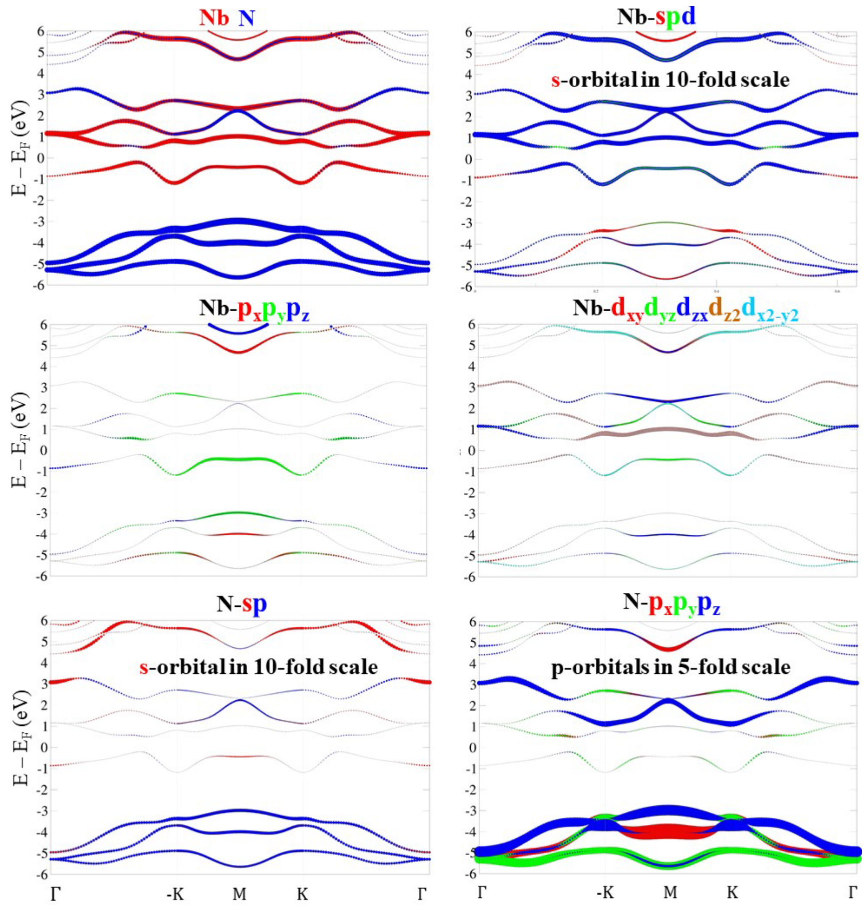

Figure 4.2 Orbital projected band structure of h-NbN monolayer.

Table 4.1 *Orbital contribution to VB edge of h-NbN monolayer.*

Orbital	s (%)	p_y (%)	p_z (%)	p_x (%)	d_{xy}(%)	d_{yz}(%)	d_{z^2}(%)	d_{xz}(%)	$d_{x^2-y^2}$(%)
Nb	1.98	1.07	0.30	0.76	11.14	9.62	34.20	12.06	18.17
N	0.0	4.43	3.82	2.45	0.0	0.0	0.0	0.0	0.0
NbN	1.98	5.50	4.12	3.21	11.14	9.62	34.20	12.06	18.17

Table 4.2 *Orbital contribution to CB edge of h-NbN monolayer.*

Orbital	s (%)	p_y (%)	p_z (%)	p_x (%)	d_{xy}(%)	d_{yz}(%)	d_{z^2}(%)	d_{xz}(%)	$d_{x^2-y^2}$(%)
Nb	0.36	3.80	1.27	1.45	1.0	25.54	40.86	9.42	1.09
N	0.54	4.17	2.71	7.79	0.0	0.0	0.0	0.0	0.0
NbN	0.90	7.97	3.98	9.24	1.0	25.54	40.86	9.42	1.09

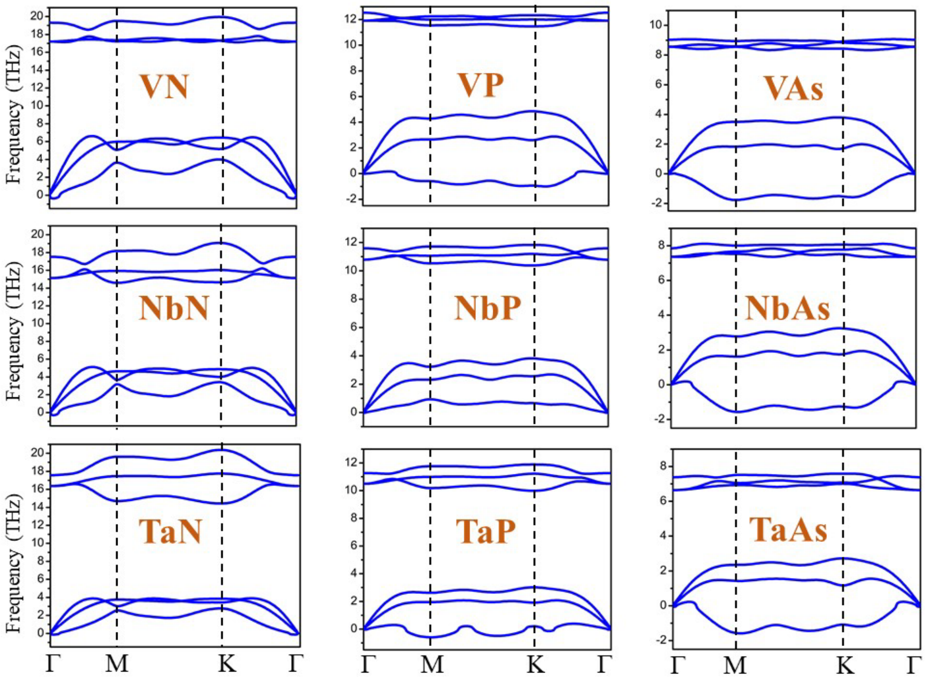

Figure 4.3 *Phonon spectra of 2D monolayers of MX (M=V, Nb, Ta; X=N, P, As).*

We have also investigated the other 2D monolayers with similar structure of h-NbN monolayer in the family of MX (M=V, Nb, Ta; X=N, P, As). Only the monolayers of VN, NbN, NbP and TaN show lattice dynamical stability, while the others show very large phonon instability in the out-of-plane flexural acoustic (ZA) phonon mode, as depicted in Fig. 4.3. Apart from a tiny pocket of negative frequency near the Γ point in the monolayer of h-VN (~0.17 THz), h-NbN (~0.16 THz) and h-TaN (~0.03 THz), no trace of imaginary frequency is found in the Brillouin zone. This tiny pocket is highly sensitive to the calculational details and it goes away completely in some cases. It just indicates the difficulty in getting numerical convergence for the flexural phonon mode, which commonly occurs in first-principles calculations on 2D materials. The tiny pockets of negative frequency (<0.3 THz or 10 cm^{-1}) around the Γ point originating from the flexural acoustic (ZA) modes have also been noticed in graphene, silicone, molybdenum disulphide and gallium chalcogenides. [228] This region of instability mainly depends on the simulation parameters, such as, supercell size and k-point sampling. Hence, these negative frequencies are understandably spurious.

We have studied the electronic properties of the stable structures and compared with NbN monolayer. It is noticed that the nature of band structures of VN and TaN monolayer are similar to NbN monolayer whereas the band structure of NbP monolayer is different from NbN monolayer as shown in Fig. 4.4. Spin polarized valley-spin splitting (VSS) in both

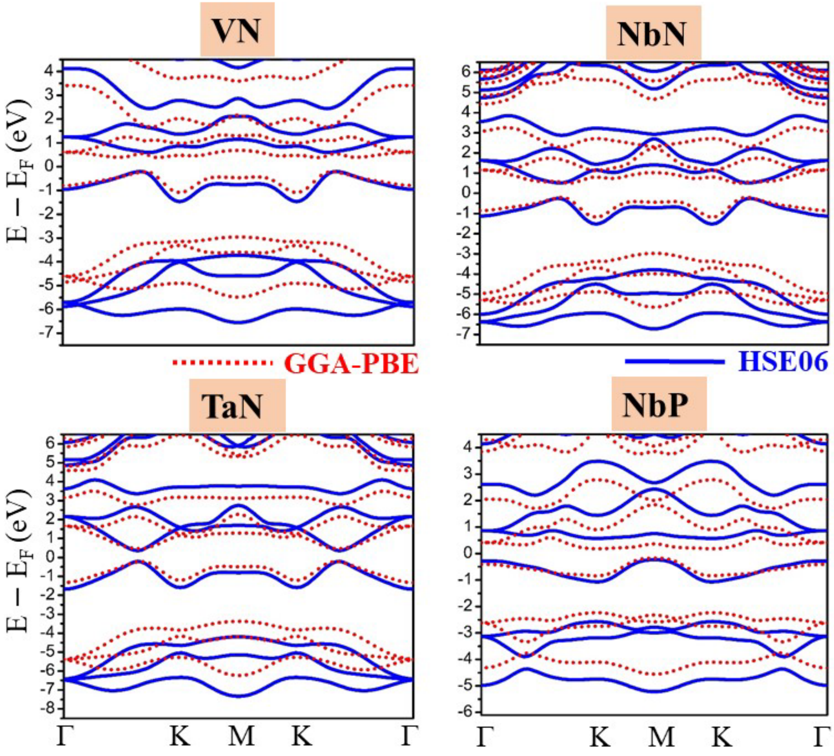

Figure 4.4 *Band structures of 2D monolayers of VN, NbN, NbP and TaN.*

valence and conduction bands are larger (smaller) in h-TaN (h-VN) monolayer relative to h-NbN on account of higher (lower) spin-orbit coupling arising from heavier (lighter) Ta (V) atoms. The value of band gap, SOC splitting in the VB(CB) and Berry-curvature are listed in Table 4.3. From Table 4.3 and Fig. 4.5, the trend in band gap is observed as VN > NbN > TaN and NbP > NbN; however, the trend in SOC splitting and Berry curvature is opposite to that in band gap as VN < NbN < TaN and NbP < NbN. It will be discussed in more detail in the context of Berry curvature and valley physics in the later section.

Table 4.3 *Band gap, SOC splitting in valence band (VB) and conduction band (CB) and Berry curvature. Band gap has been calculated using Heyd–Scuseria–Ernzerhof (HSE) functional.*

2D monolayer	E_g^{HSE} (eV)	Δ_{SO}^{v} (meV)	Δ_{SO}^{c} (meV)	Ω(Å^2)
VN	0.801	14	35	44
NbN	0.759	32	130	51
NbP	0.803	21	57	25
TaN	0.559	112	406	73

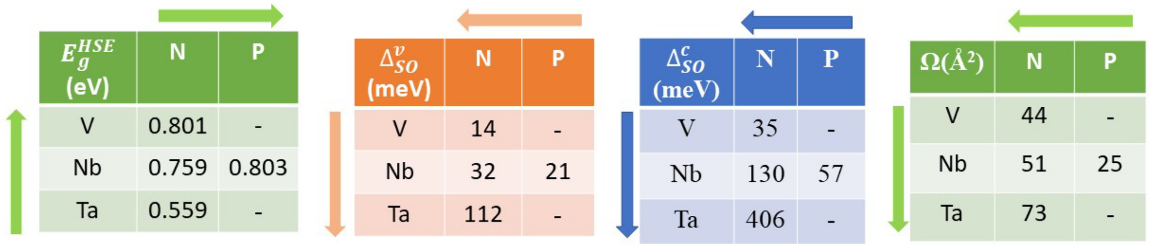

E_g^{HSE} (eV)	N	P
V	0.801	-
Nb	0.759	0.803
Ta	0.559	-

Δ_{SO}^{v} (meV)	N	P
V	14	-
Nb	32	21
Ta	112	-

Δ_{SO}^{c} (meV)	N	P
V	35	-
Nb	130	57
Ta	406	-

Ω(Å²)	N	P
V	44	-
Nb	51	25
Ta	73	-

***Figure 4.5** Trend of band gap, SOC splitting and berry curvature in VN, NbN, NbP and TaN.*

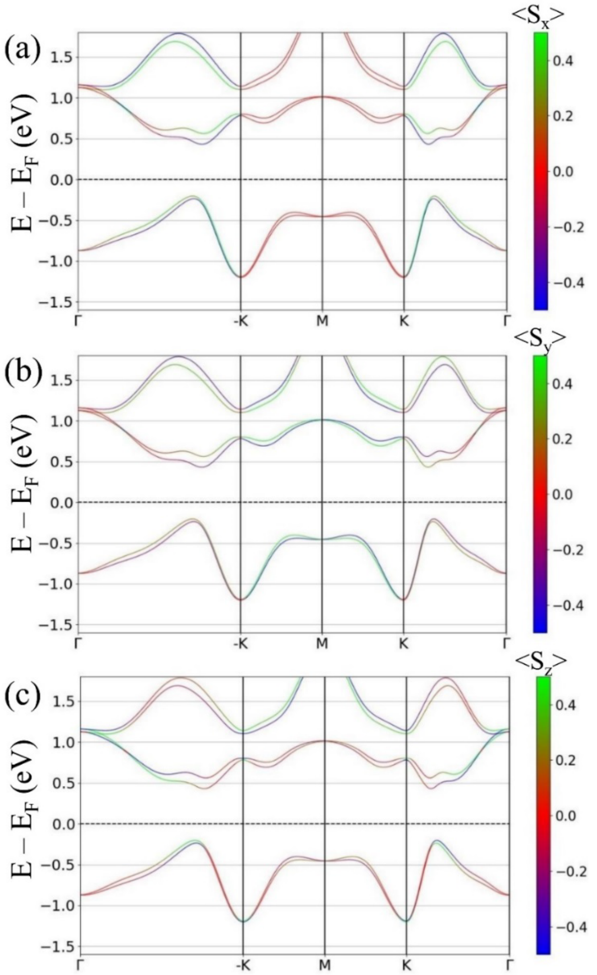

***Figure 4.6** Spin projected band structure of (a) S_x, (b) S_y and (c) S_z spin in monolayer h-NbN. Color map represents the spin expectation value. Fermi level is set to zero.*

4.2.2 Rashba effect

In monolayer h-NbN, the Zeeman-type spin splitting near the corners of the hexagonal 2D Brillouin zone occurs due to presence of strong SOC together with the breaking of inversion symmetry, (x, y, z) → (−x, −y, −z) as well as the Rashba-type spin splitting has been observed around the M-point because of the intrinsic out-of-plane electric field induced by mirror symmetry (x, y, z) → (x, y, −z) breaking along the z-direction. The spin projected electronic bands in the monolayer h-NbN using GGA-PBE functional with incorporation of SOC, have been shown in Figs. 4.6(a)-4.6(c) and top two valence bands as depicted in Figs. 4.7(a)-4.7(c) to study Rashba effect.

The spin-resolved isoenergy contours of the spin split top two valence bands (E= −0.5 eV and E_F= 0.0 eV) demonstrate in-plane spin distribution, as displayed in Figs. 4.7(d)-4.7(f), which is the signature of the Rashba effect, as observed in the 2D electron systems [61,229]. There is no spin distribution from S_z, while S_x and S_y mostly contribute to the in-plane spin distribution. S_y spin causes Rashba splitting only around M1 and M4 points along the high symmetry path Γ-M-K when $k_x = 0$. However, S_x spin causes Rashba splitting around M2, M3, M5 and M6 along the high symmetric path Γ-M-K. It is also clear from the spin-texture of top two valence bands as depicted in Fig. 4.8. We have observed that VB of NbN monolayer at the high-symmetric M-point shows the main contribution from Nb-p_y (9.72%), Nb-$d_{x^2-y^2}$ (15.49%), Nb-d_{yz} (60.91%), Nb-d_{z^2} (9.52) and N-s (3.93%) orbitals as listed in Table 4.4.

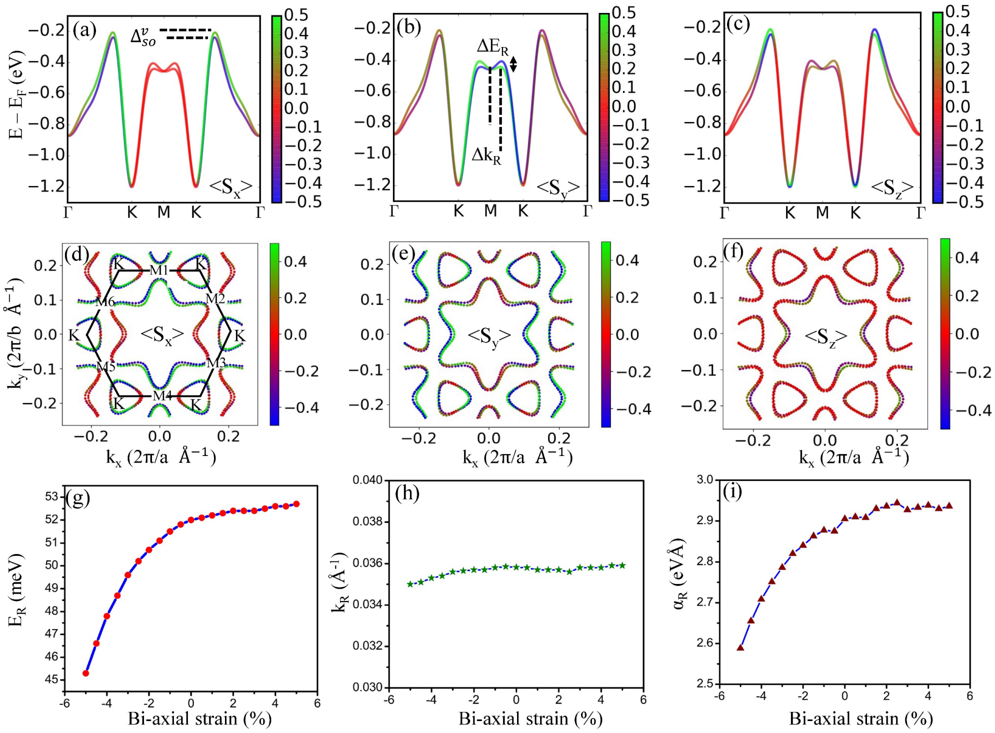

Figure 4.7 *Spin projected top two valence bands, i.e., (a) S_x, (b) S_y and (c) S_z in h-NbN. Corresponding contour plot (d, e, f) at E=−0.5 eV, E_F=0 eV: color map represents the expectation value of corresponding spin projection. Modulation of (g) energy offset, E_R, (h) momentum offset, k_R and (i) Rashba parameter, α_R with bi-axial strain.*

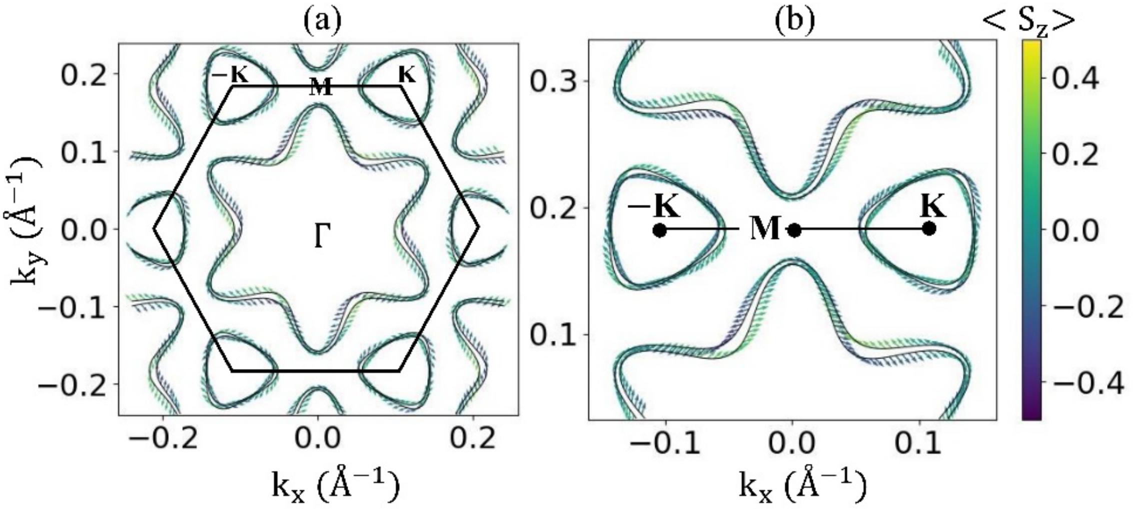

Figure 4.8 *Spin-texture of top two valence bands of monolayer h-NbN, (b) Spin-texture around M-point as shown in Fig. (a).*

Table 4.4 *Orbital composition of the top valence band at M-point.*

Orbital	s (%)	p_y (%)	p_z (%)	p_x (%)	d_{xy}(%)	d_{yz}(%)	d_{z^2}(%)	d_{xz}(%)	$d_{x^2-y^2}$(%)
Nb	0.0	9.72	0.20	0.0	0.0	60.91	9.52	0.0	15.49
N	3.37	0.20	0.59	0.0	0.0	0.0	0.0	0.0	0.0
NbN	3.37	9.92	0.79	0.0	0.0	60.91	9.52	0.0	15.49

Therefore, Rashba spin splitting occurs due to these orbitals mainly. According to linear Rashba model, the SOC-included spin splitting is described by the well-defined Rashba constant (α_R) as $\alpha_R = \frac{2\Delta E_R}{\Delta k_R}$, where ΔE_R and Δk_R are the Rashba energy splitting and the momentum shift, respectively. The parameters of ΔE_R and Δk_R of h-NbN monolayer are 52.0 meV and 0.0358 $Å^{-1}$, respectively, thus α_R is calculated to be 2.905 eVÅ. The value of Rashba constant is comparable to recently predicted 2D Rashba monolayers, such as, AlBi (2.77 eVÅ) [230], BiSb (2.3 eVÅ) [231] and much higher than the conventional semiconducting heterostructure of InGaAs/InAlAs (α_R~0.07 eVÅ) [198], metallic surface state of Au (111) surface (α_R~0.33 eVÅ) [199] and Bi (111) surface (α_R~0.55 eVÅ) [200], monolayer Janus MoSSe (α_R~0.077 eVÅ) [220], Janus WSeTe (α_R~0.514 eVÅ) [220]. Modulation of Rashba parameters has been investigated by applying in-plane bi-axial compressive and tensile strain up to 5%. It has been found that Rashba parameter, α_R is enhanced to 2.944 eVÅ at 2.5% tensile strain. In general, a large Rashba parameter implies significant SOC, which is desirable for suppressing the spin relaxation, controlling the spin precession, and the system's stability and robustness against all forms of spin independent scattering. [62] [232] As a consequence, structures with large Rashba-type splitting are sought after. We have also studied the changes in Rashba properties upon changing the cation and anion elements, as depicted in Table 4.5. The trend in Rashba parameter is observed as VN < NbN < TaN and NbP < NbN. TaN monolayer shows highest energy offset (ΔE_R ~74 meV) and Rashba parameter (α_R~4.229 eVÅ), as the spin-orbit coupling strength is larger in heavier atoms. A large Rashba parameter indicates that monolayer h-NbN and h-TaN could be realized as a promising candidate in spin field effect transistors.

Table 4.5 *Rashba parameters*

2D monolayer	ΔE_R (eV)	Δk_R (Å^{-1})	α_R (eVÅ)
VN	0.030	0.0376	1.618
NbN	0.052	0.0358	2.905
NbP	0.002	0.0057	0.548
TaN	0.074	0.0350	4.229

Several possible descriptors have been taken into consideration to deduce a relationship with Rashba parameters of different monolayers such as electronegativity, ionization energy, Bader charges, Born effective charges and out-of-plane electric field asymmetry as depicted in Figs. 4.9(a)-4.9(f). Asymmetry in crystal potential as well as electric field perpendicular to the 2D plane as shown in Figs. 4.10 and 4.11 is also responsible for Rashba effect. The out-of-plane electric field at the specific atom site is calculated from electrostatic potential using central difference method ($E = -\frac{dV}{dz}$). The strength of electric field asymmetry is evaluated as $|\vec{E}| = |\vec{E}_M - \vec{E}_X|$. It is observed that $|\vec{E}|$ does not correlate well with α_R as depicted in Fig. 4.9(d). Bader charges of individual atom as calculated using bader code [155] are also not found to be a good descriptor (Fig. 4.9(c)). Only Z^*_{zz}, is found to correlate well with α_R. Out-of-plane Born effective charges on each atom in these monolayers is found to be a proper descriptor to gauge strength of Rashba effect.

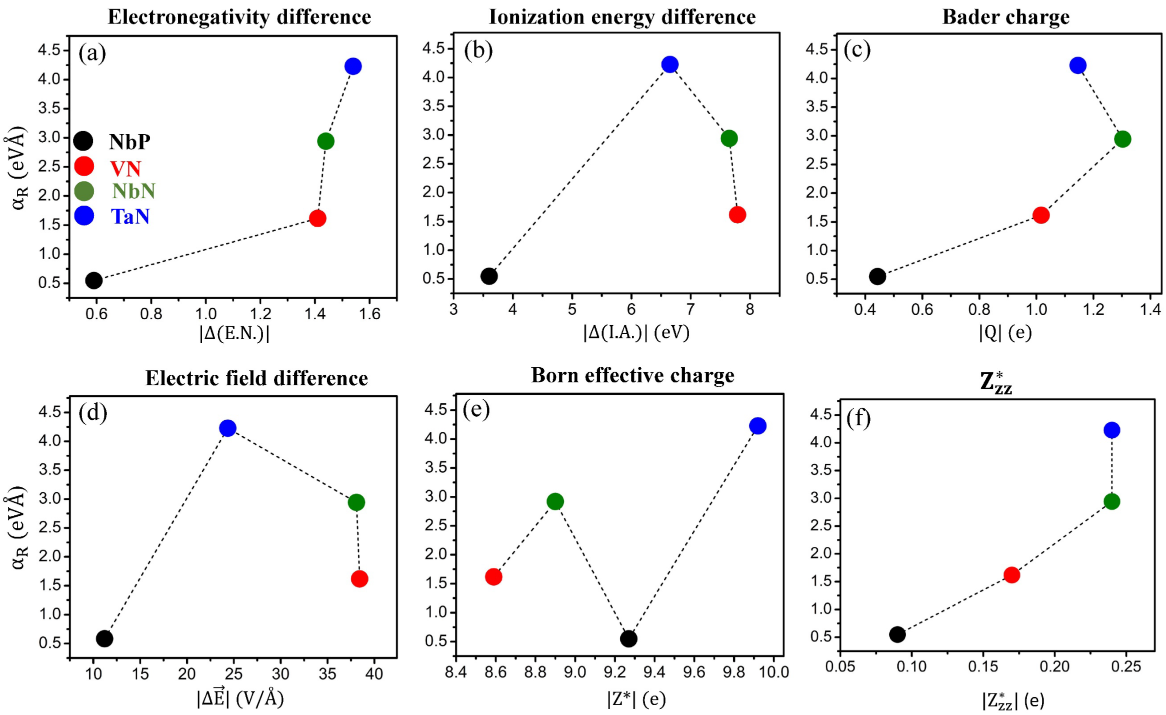

***Figure 4.9** The Rashba parameter plotted as a function of different material descriptor: (a) electronegativity difference, (b) ionization energy difference, (c) Bader charges, (d) asymmetry in electric field, (e) Born effective charge (Z*) and (f) zz component of Z*.*

Born effective charges (Z^*_{ij}, a tensor) on the ions is different from the formal static charge and corresponds to the amount of charge that effectively contributes to the polarization during external perturbation such as ionic displacement. The dynamical Born effective charge (BEC) is defined as $Z^*_{ij} = (\Omega/e)\,(\partial P_i/\partial u_j) = (1/e)\,(\partial F_i/\partial E_j)$; i, j=x, y and z, Ω is the unit cell volume, u is the strain, E is the electric field and F is the Hellmann-Feynman forces. The scalar charge on each atom Z* is given by $Tr(Z^*_{ij})$. Microscopically, Born effective charge (Z*) of the atoms is a sum of static charge (Z(u)) and anomalous contributions, $Z^*(u) = Z(u) + u.\partial Z(u)/\partial u$, u is the interatomic distance. The Born effective charge, *Z** is a fundamental quantity in the study of lattice dynamics, because it governs the amplitude of the long-range Coulomb interaction between nuclei, and the splitting between longitudinal optic (LO) and transverse optic (TO) phonon modes. The dynamical charge measures the macroscopic current flowing across the sample while the ions are adiabatically displaced. Such currents are responsible for building up spontaneous polarization.

The collective displacements of atoms participating in interatomic chemical bonds, hybridisation of orbitals and charge exchange depends on the Z* of atoms in the

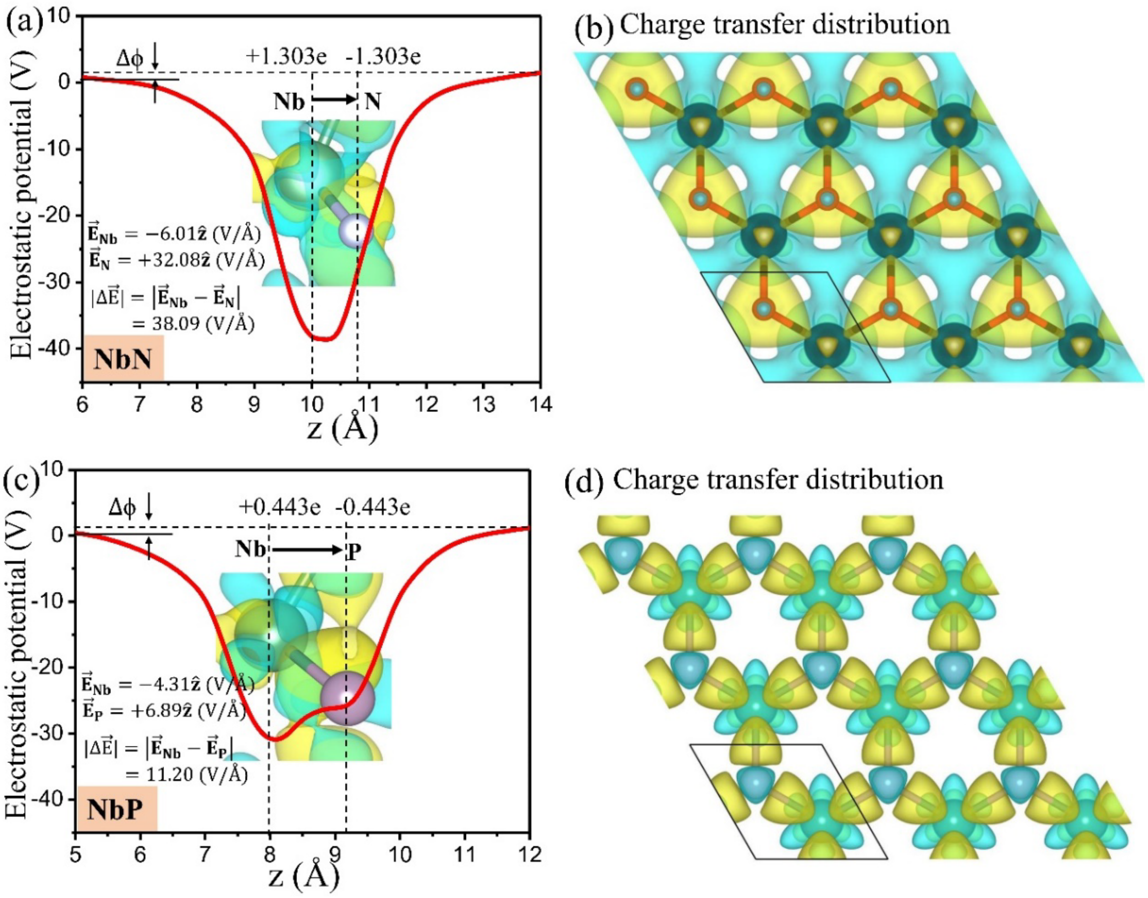

Figure 4.10 *Distribution of electrostatic potential of NbN and NbP monolayers along z-direction. $\Delta\phi$ is the difference of work function, and the built-in electric field is from transition-metal atom to pnictide atom. Bader charge analysis shows that the inter-atomic charge transfer in NbN monolayer is 1.303 e. Two dashed vertical lines are the positions of transition-metal atom and pnictide atom. (b, d) Charge transfer distribution in NbN and NbP monolayers respectively. Isosurface value is set to 0.005 $eV/Å^3$. Cyan (yellow) colour represents the charge accumulation (depletion).*

monolayers. Qualitatively, chemical bonding is understood to be influenced by the polarizability and dielectric constants of the materials, which are related to Z*. Although the total Z* is not a good descriptor for Rashba parameter of the studied material, only the zz component of Z* (Z^*_{zz}) shows good trend as depicted in Figs. 4.9(e) and 4.9(f).

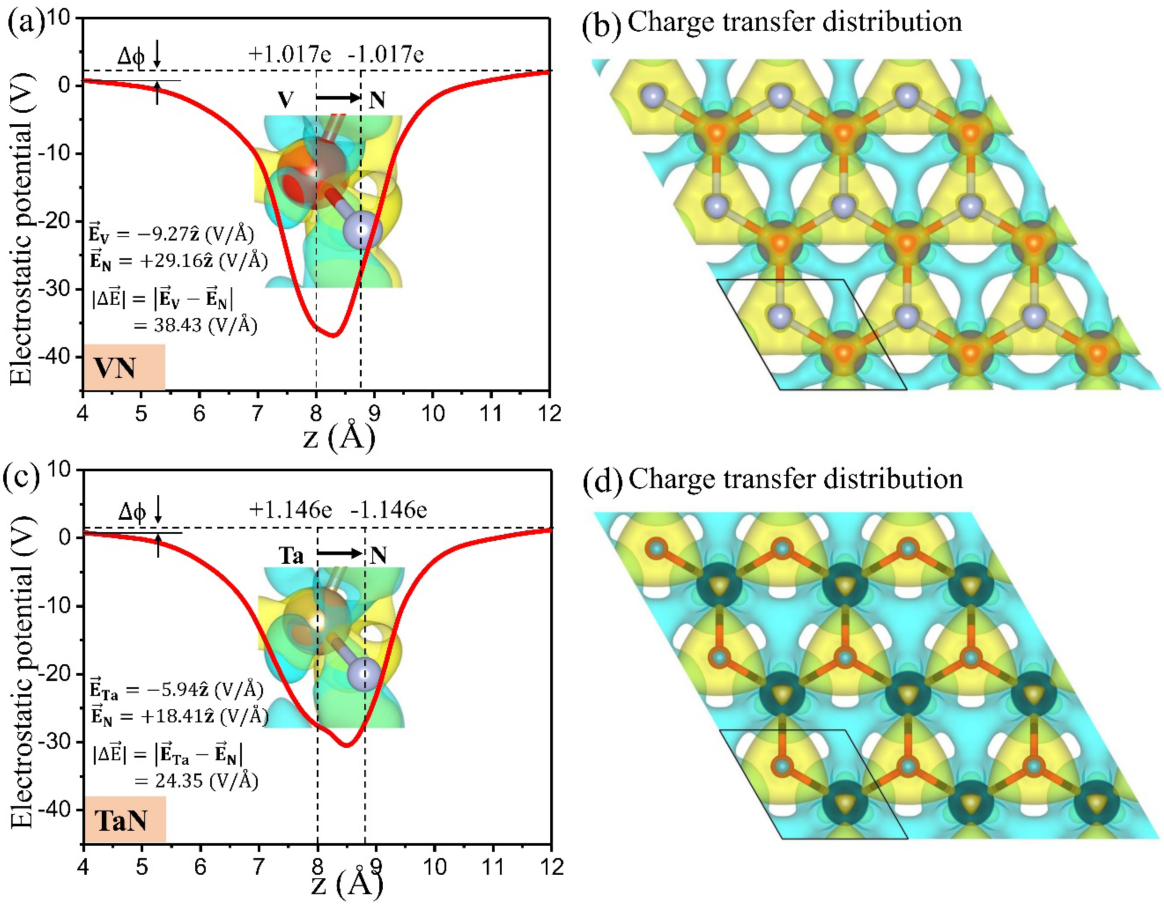

Figure 4.11 *Distribution of electrostatic potential of VN and TaN monolayers along z-direction. $\Delta\phi$ is the difference of work function, and the built-in electric field is from transition-metal atom to pnictide atom. Bader charge analysis shows that the inter-atomic charge transfer in NbN monolayer is 1.303 e. Two dashed vertical lines are the positions of transition-metal atom and pnictide atom. (b, d) Charge transfer distribution in VN and TaN monolayers respectively. Isosurface value is set to 0.005 eV/Å^3. Cyan (yellow) colour represents the spatial regions of charge accumulation (depletion).*

4.2.3 Valley physics of h-NbN monolayer

On account of the hexagonal honeycomb lattice structure and broken in-plane inversion symmetry in h-NbN monolayer, it shows valley physics or valleytronic properties, i.e., opposite spins are locked to the K and K’ valleys at the band edges. When h-NbN will be supported on a substrate to realize its practical applications, the lattice mismatch between the underlying support and h-NbN monolayer can induce a strain in h-NbN. Besides, even in van der Waals heterostructures, incommensurate lattices can bring about interfacial strain. Strain is therefore unavoidable in ultrathin, flexible 2D nanosheets. Therefore, it is

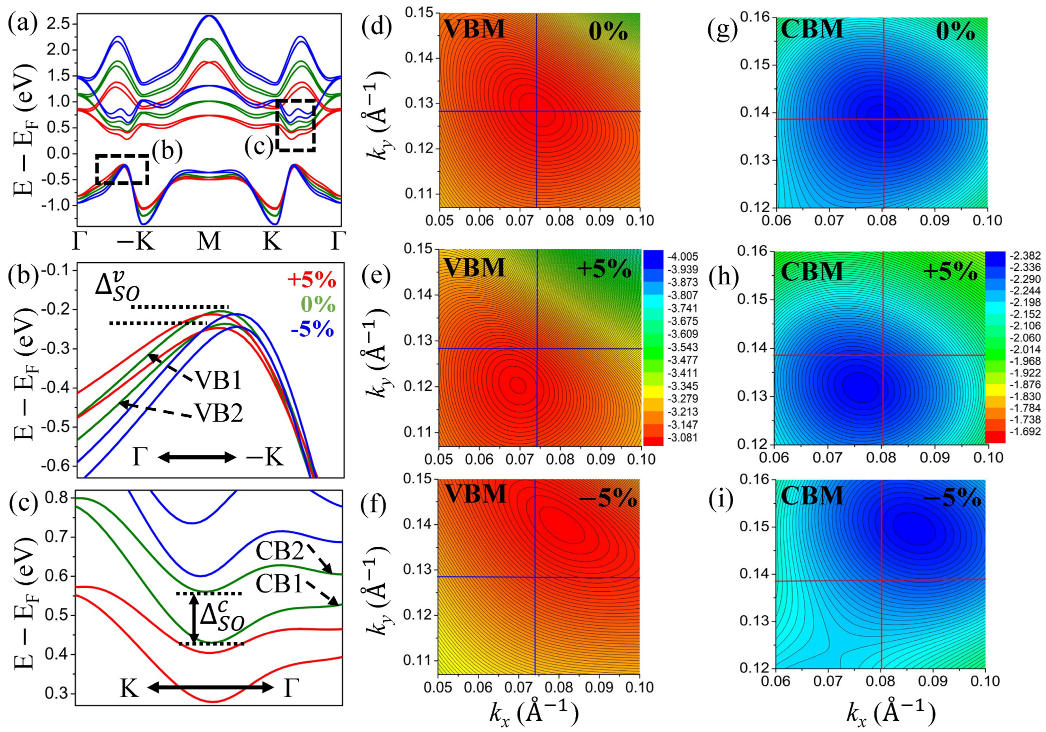

Figure 4.12 *(a) Modulation of band structure of monolayer h-NbN with 5% compressive and tensile strain using GGA-PBE functional along with spin-orbit coupling (SOC). (b) and (c) are enlarged view of VB and CB as indicated in Fig. 4(a). Isoenergy contours of low energy valence bands of (d) 0% strain, (e) +5% and (f) -5% bi-axial strain respectively. Isoenergy contours of low energy conduction bands of (g) 0% strain, (h) +5% and (i) -5% bi-axial strain respectively.*

instructive to investigate the effect of strain on various properties in 2D materials, including valleytronics. The role of strain has been addressed in this study. Bi-axial tensile and compressive strain in a dilation deformation range of 5% have been applied on monolayer h-NbN to investigate the evolution in the band edges with strain as shown in Figs. 4.12(a)-4.12(c). With the application of tensile (compressive) bi-axial strain, band gap is decreasing (increasing) while the Zeeman-type valley spin splitting (VSS) $\Delta_{\mathrm{SO}}^{\mathrm{v}}$ and $\Delta_{\mathrm{SO}}^{\mathrm{c}}$ are found to be almost invariant as displayed in Figs. 4.13(a) and 4.13(b). A robust strain-valley coupling between mechanical strain and low-energy Bloch bands around the band edges on either side of the Fermi level has been observed, where an applied elastic deformation by bi-axial strain substantially drifts the CB and VB edges (i.e., valleys and hills) far away from K/K'-points in the momentum-space, as depicted in Figs. 4.12(b) and 4.12(c). The isoenergetic contours of highest occupied valence band and lowest unoccupied conduction

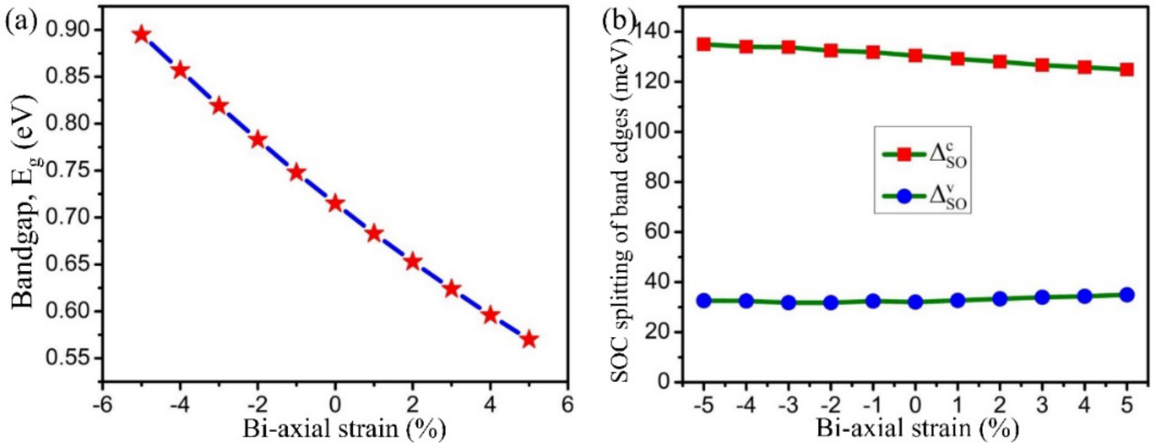

Figure 4.13 *Bandgap modulation with bi-axial strain using GGA-PBE functional. (b) Tuning of SOC splitting of band edges with bi-axial strain using GGA-PBE + SOC functional.*

band near about the band edges have been depicted in Figs. 4.12(d)-4.12(i) to shed further light into valley drift. Unlike graphene, the iso-energy contours of the band edges in a monolayer h-NbN are not isotropic in the close proximity of K1-point and an elliptical warping (EW) effect of energy bands can be seen in the isoenergy lines around the K1-point.

As shown in Figs. 4.12(g)-4.12(i), the lowermost spin-split conduction band edge ($CB1$) drifts off the K1-point at a rate (Δk/tensile strain) ~ 1.52 $\times 10^{-3}$Å^{-1}/1% when bi-axial tensile strain is applied, while it drifts off along the opposite direction at a rate (Δk/compressive strain) ~ 2.57 $\times 10^{-3}$ Å^{-1}/1% when bi-axial compressive strain is applied. We find the energy valley-drift in spin-split $CB1$ to be higher (> 1.6 times) upon compressive strain than the corresponding drift due to tensile strain which is attributable to the different kinds of variation in elastic constants, Young's modulus (Y) and Poisson ratio (υ) with tensile and compressive strain, as shown in Figs. 4.15(a) and 4.15(b). A similar valley drift for the uppermost spin-split valence band edge ($VB1$) is observed. The valence band edge drifts away from K1-point at a rate ~ 1.80 $\times 10^{-3}$ Å^{-1}/1% when bi-axial tensile strain is applied, while it drifts off along the opposite direction at a rate ~ 2.88$\times 10^{-3}$ Å^{-1}/1% when compressive strain is applied. The valley drift of holes is found to be higher than that of the electrons on account of higher in-plane d-orbital contribution of VB edge [d_{xy} (1.0%), $d_{x^2-y^2}$ (1.09%)] than that of CB edge [d_{xy} (11.14%), $d_{x^2-y^2}$ (18.17%)], which is clearly observed in Table 4.1-4.2. The plane-average squared wavefunctions ($|\psi|^2$) have been projected along the direction perpendicular to the basal plane of h-NbN monolayer for

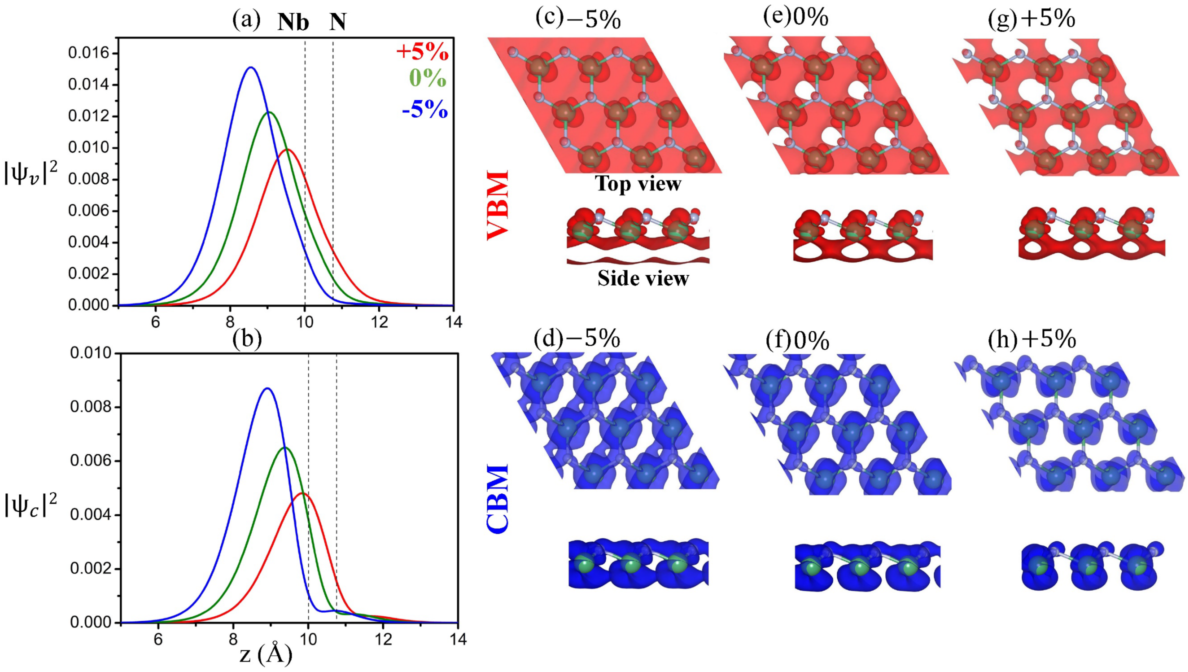

Figure 4.14 *Spatial profile of Bloch wavefunctions for (a) VB and (b) CB edge states projected along the direction perpendicular to the basal plane of h-NbN monolayer. The atomic positions have been marked therein with dash vertical lines on Nb-N in the pristine (0%) system. Charge density of electronic states at the edges of VB hills and CB valleys for a 5% compressive strained (c, d), a strain-free (e, f) and a 5% tensile strained h-NbN monolayer. Isosurface value is set to 0.01 eV/$Å^3$.*

pristine and strained system as depicted in Figs. 4.14(a) and 4.14(b). VB edge is found to be more delocalized than the CB edge, which is also evident from the corresponding charge density distribution originating from orbital wavefunctions of the specific band edges, as shown in Figs. 4.14(c)-4.14(h). Under compressive strain, the probability amplitude for both VB and CB edges increases, while for tensile strain it decreases. A similar valley drift response has been noticed in graphene [233] on account of its two-dimensional hexagonal structure. Although the drift is much enhanced in monolayer h-NbN; however, it is lower than that in monolayer MoS_2. Per percent of strain, the valley drift response is found to be nearly 0.6 (7.5)$\times10^{-3}$ $Å^{-1}$/1% in graphene (MoS_2) [233,234]. The valley drifts have immediate impacts on valleytronics performances, which is also applicable to the strong coupling between the spin and valley degrees of freedom. [234] As the valley degree of freedom is used to characterize the charge carriers [235], large valley shifts will induce decoherence and thus limit the performance of devices. In monolayer h-NbN, lesser valley shift is observed under tensile/compressive strain for both VBM and CBM than the monolayer MoS_2, which originates from its lower Young's modulus (~94.7 N/m) than that in MoS_2 (~124.1 N/m) monolayer.

The elastic deformation of materials plays a fundamental role in the electronic properties. Therefore, in modern electronics applications, it is crucial to get an in-depth understanding of elastic properties of the studied material. The elastic stiffness constants (C_{ij}) have been calculated with forward difference method using GGA-PBE functional as implemented in VASP and all the mechanical properties such as Young's modulus (Y), Poisson ratio (υ), critical buckling strain (ϵ_c), intrinsic strength (σ_{int}) have been systematically investigated. The elastic constants determined for the monolayer satisfy Born-Huang stability criteria and other mechanical properties are listed in Table 4.6.

Born-Huang stability criteria are statisfied:

$C_{11} > |C_{12}|$, $C_{22} > 0$, $C_{66} > 0$, $C_{11}C_{22} - C_{12}^2 > 0$

The critical buckling strain (ϵ_c) of a 2D material can be evaluated using $\epsilon_c = -\frac{4\pi^2 D}{YL^2}$, where *L* is the length of the 2D nanosheet in the unit of Å. For the same length L (in Å), the critical buckling strain for the h-NbN are found to be: $\epsilon_c = -\frac{2.11}{L^2}$ which is comparable to graphene ($-\frac{2.2}{L^2}$) [134]. The Young's modulus (~94.72 N/m) is found to be smaller than other 2D nanosheets such as graphene (~347.1 N/m) [134] and MoS_2 (~124.1 N/m) [134] which suggests that h-NbN monolayer will be more flexible than these monolayers. In Figs. 4.15(a) and 4.15(b), modulation of the elastic stiffness constants (C_{11}, C_{12}), Young's modulus (Y) and Poisson's ratio (ν) via bi-axial tensile and compressive strain have been investigated and the nature of variation in these elastic properties corroborates well the valley drift response to strain respectively.

***Table 4.6** The calculated mechanical stiffness constants C_{ij}, layer modulus (γ^{2D}), Young's modulus (Y), Poisson's ratio (ν), intrinsic strength (σ_{int}), bending modulus (D).*

System	C_{11} (N/m)	C_{12} (N/m)	C_{66} (N/m)	γ^{2D} (N/m)	Y (N/m)	ν	σ_{int} (N/m)	D (eV)
h-NbN	107.342	36.817	35.263	72.079	94.715	0.343	10.524	5.059

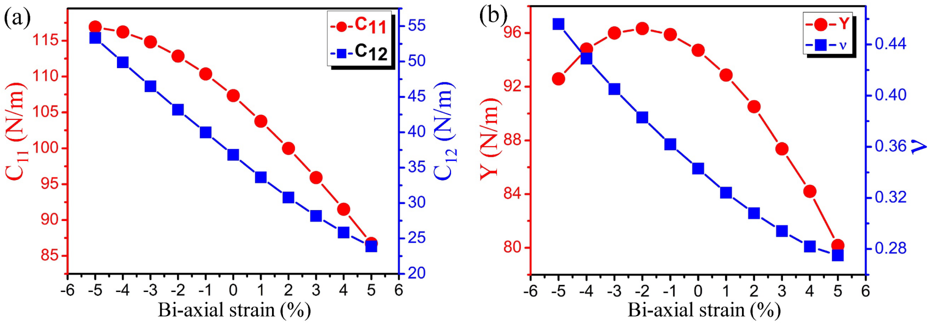

Figure 4.15 *Variation in (a) elastic stiffness constants C$_{11}$ and C$_{12}$. Variation in (b) Young's modulus, Y, and Poisson's ratio, v with bi-axial strain.*

4.2.4 Berry curvature modulation in h-NbN monolayer

It should be emphasized that the velocity of the carriers with a nonzero Berry curvature can be represented as $\hbar \boldsymbol{v}_n(\boldsymbol{k}) = \boldsymbol{v}_{\mathrm{g}} - \boldsymbol{v}_{\perp}$,where $\boldsymbol{v}_{\mathrm{g}}$ indicates the common group velocity, $\boldsymbol{v}_{\perp}$denotes the transverse velocity, while $\boldsymbol{v}_n(\boldsymbol{k})$ is derivable from the solution of the Boltzmann transport equation. Group velocity is defined as $\boldsymbol{v}_g(\boldsymbol{k}) = \boldsymbol{\nabla}_k \varepsilon_n(\boldsymbol{k})$, where ε_n corresponds to the energy of the n-th Bloch band. In addition, nonzero Berry curvature leads to an anomalous velocity, that is, the transverse velocity $\boldsymbol{v}_{\perp}$, which is indispensable for the valley Hall effect. The transverse velocity can be described as $\boldsymbol{v}_{\perp} = -\frac{e}{\hbar}\mathbf{E} \times \boldsymbol{\Omega}(\mathbf{k})$, where **E** is the in-plane electric field and $\boldsymbol{\Omega}(\mathbf{k})$ is the out-of-plane Berry curvature. [236] Actually, large $\boldsymbol{\Omega}(\mathbf{k})$ can amplify the transverse velocity, and the excited carriers moving in the direction perpendicular to **E** can therefore be transported faster and their recombination can be reduced. [232]

The Berry curvature $\Omega_n(k)$ of band n at **k** point is calculated from the first-principles wave function, using the Kubo formula [237,238] given by;

$$\Omega_n(k) \;= -2\mathrm{Im}\sum_{m\neq n} \frac{<\psi_{nk}|\hat{v}_x|\psi_{mk}><\psi_{mk}|\hat{v}_y|\psi_{nk}>}{(E_{nk}-E_{mk})^2} \tag{4.1}$$

where $\hat{v}_{x,y}$ are the velocity operators and the summation are over all the occupied states. $\Omega_n(-k) \;= -\Omega_n(k)$ as a consequence of time reversal symmetry.

The *k.p* Hamiltonian [75] to describe low energy electronic states of hexagonal system in the vicinity of band edges including spin-orbit coupling is given by;

$$H = at\left(\tau k_x\sigma_x + k_y\sigma_y\right) + \frac{\Delta}{2}\sigma_z - \lambda\tau\frac{\sigma_z - 1}{2}S_z \tag{4.2}$$

where a is the lattice spacing, t is the nearest-neighbor hopping integral, $\tau = \pm 1$ is the valley index, $\sigma_{x/y/z}$ is the Pauli matrix spanned by the conduction and valence states, S_z is the Pauli matrix for a spin, Δ is the band gap, λ is spin splitting. The k.p model is generally

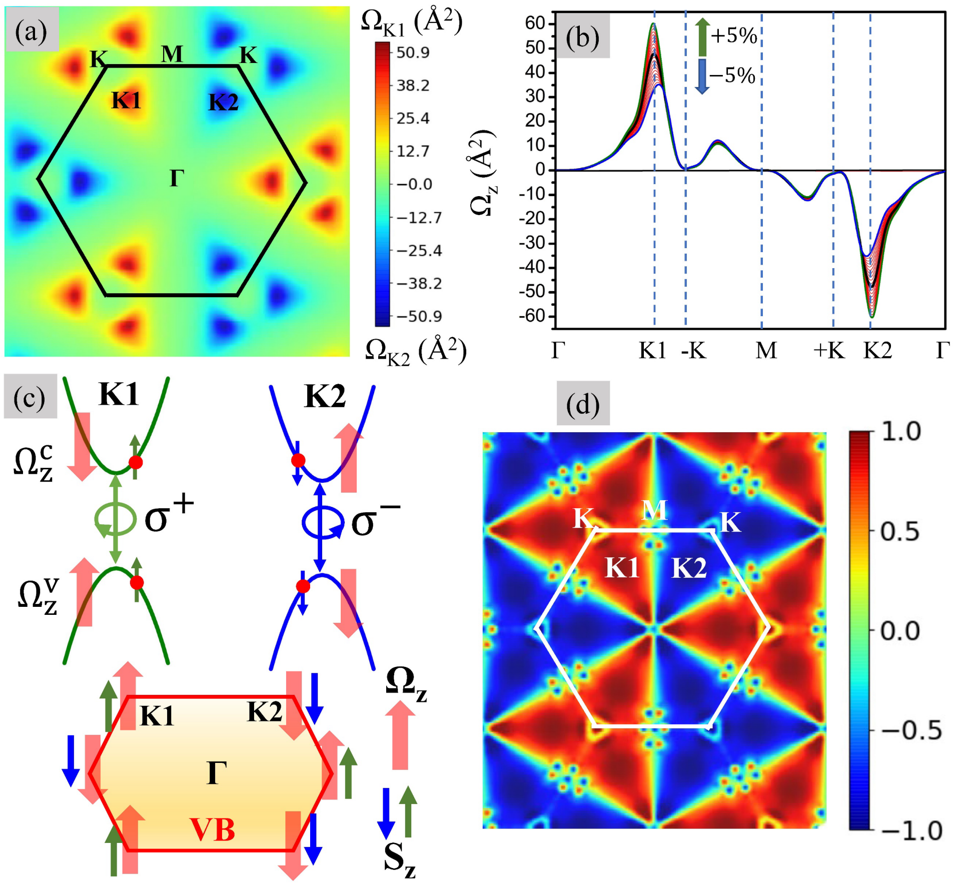

Figure 4.16 *(a) Contour map of Berry curvature distribution, Ω(k) of h-NbN monolayer in 2D k-space over all occupied Bloch bands of in units of Å^2. (b) Modulation of Berry curvature distribution along high symmetry k-line Γ-K-M-K-Γ with application of bi-axial strain, (c) Schematic of valley-selective excitation, (d) Circular dichroism polarization,* $\eta(k)$.

exploited in studying valleytronics in 2D materials. [239,240] The Berry curvature in the valence band is given by;

$$\Omega_v(k) = \tau \frac{2a^2t^2\Delta}{(4a^2t^2k^2+\Delta^2)^{\frac{3}{2}}} \tag{4.3}$$

Berry curvature in the conduction band is equal in magnitude but opposite in sign to that of the valence band, i.e., $\Omega_c(k) = -\Omega_v(k)$.

In the process of direct intervalley optical excitations through a circularly polarized light, only the orbital part of Bloch wavefunctions near the K/K' valleys of hexagonal monolayer TMDC couple to the optical field, although the spin component of carriers remains unchanged during this process. In ML-MoS$_2$, the electron/hole bands around K/K' are energetically degenerate. But the opposite nature of Berry curvature distributions, Ω (k) near the K/K' valleys helps to distinguish the valley carriers. The strength of Berry curvature distribution of valley carriers in ML-MoS_2, can be altered significantly by tuning the onsite electronic energy and orbital occupation factor of a given Bloch state with application of tensile or compressive strain. Similar behaviour of Berry-curvature can be found in the monolayer h-NbN. We have investigated the effect of bi-axial strain on the Ω (k) of electron/hole bands near K1–points lying along the high symmetry Γ-K path. Unlike ML-MoS_2, in monolayer h-NbN, the low energy valleys are not exactly around high symmetry K point. Due to 3-fold rotational C_3 symmetry, three similar and degenerate valleys of same Berry-curvature around the high symmetry K-point have been observed which is a very rare occurrence, thereby exhibiting great possibilities for spin-valley physics in this material. The Berry curvatures of a pristine (0% strain) and strained monolayer h-NbN for all the occupied bands below the Fermi energy along the high-symmetry line Γ-K-M-K- Γ has been shown in Fig. 4.16(b). The presence of strong spin-orbit interaction along with time-reversal symmetry and absence of lattice inversion symmetry allows charge carriers of alternate valleys to exhibit opposite Berry curvatures as well as opposite spin polarization, where the Berry curvature, Ω (k) is mostly confined around the K1/K2 valleys and found to be highest at both the K1 and K2 valleys in the BZ with opposite sign. While away from K1/K2, Ω (k) decays rapidly to almost zero at the K-point. In between, K-M path, a small peak arises and vanishes at M-point.

Equation (4.3) clearly shows that the Berry curvature varies inversely as the magnitude of wavevector (k) and band gap (Δ). As the wavevector (~0.147 $Å^{-1}$) and bandgap (~0.72 eV) in h-NbN monolayer is smaller than that in MoS_2 monolayer (~0.210 $Å^{-1}$, 1.69 eV), [241] Berry curvature in h-NbN monolayer (~51 $Å^2$) is found to be more than 4 times than the MoS_2 monolayer (~11 $Å^2$) [241]. Recently, Duo et al. [242] theoretically predicted strong spin-valley coupling in 2D monolayers of MN_2X_2 (M=Mo, W; X=F, H) and reported Berry-curvature ~19.3 $Å^2$ in monolayer WN_2F_2. To facilitate a reasonable functioning of the valleytronic device, it is essential to understand the physical mechanism underlying tunable Berry curvature in order to regulate the transverse transport velocity of carriers. In contrast to the previous strategies adopted to realize tunable Berry curvature, such as, constructing heterostructures of distinct 2D materials [204] and applying uniaxial strain (to such as monolayer MoS_2), [243] we have shown that biaxial strain engineering could also effectively tune the magnitude of the Berry curvature. $\mathbf{\Omega(k)}$ can be enhanced to the value of 60 $Å^2$ by applying 5% bi-axial tensile strain as depicted in Fig. 4.16(b). Application of biaxial strain reduces the band gap and the magnitude of the wave vector and hence, enhances the Berry curvature. Similarly, Wang et al. [232] investigated tunable Berry curvature in Janus TiXY ($X \neq Y$, X/Y=Cl, Br, I) monolayers and showed that Berry curvature, $\mathbf{\Omega}(\mathbf{k})$ of monolayer TiBrI can be enhanced to the value of 37.4 Å^2 by applying 2.5% bi-axial tensile strain from 29.7 Å^2 in pristine structure.

Similar to valley-contrasting Berry curvature $\Omega_n(k)$ at the K1 and K2 points in the BZ, it is expected to have valley-contrasted circular dichroism $\eta(k)$ as depicted in Fig. 4.16(d) allowing selective excitation in the two valleys by photons with different optical circular helicity permitting valley-dependent manipulation. Li et al. [244] have investigated valley dependent properties of monolayer MSi_2N_4 (M=Mo, W) and shown that valley fermions manifest spin-valley coupling and valley selective optical dichroism. The Berry curvature $\Omega(k)$ and optical circular dichroism $\eta(k)$ are related by;

$$\eta(k) = \frac{\Omega_n(k)\ .\hat{z}}{\mu_B^*(k)} \frac{e}{2\hbar} \Delta(k) \tag{4.4}$$

where $\mu_B^* = e\hbar/2m^*$ and $\Delta(k) = [\varepsilon_c(k) - \ \varepsilon_v(k)]$ is the transition energy, or band gap at k.

The optical polarization is defined as the difference between the absorption of the right- and left-handed circularly polarized lights (RHCP (σ^+)/LHCP (σ^-)), normalized by total absorption at each point in k-space, evaluated between the top of the valence bands (v) and the bottom of conduction bands (c). The k-resolved degree of optical polarization between the top of valence bands and bottom of conduction bands is called circular dichroism and it is calculated as, $\eta(k) = \frac{|P_+^{cv}|^2 - |P_-^{cv}|^2}{|P_+^{cv}|^2 + |P_-^{cv}|^2}$,

where the transition matrix element is $P_\pm^{cv}(\boldsymbol{k}) = \frac{1}{\sqrt{2}}(P_x^{cv}(\boldsymbol{k}) \pm iP_y^{cv}(\boldsymbol{k}))$.

The inter-band matrix elements, $P^{cv}(\boldsymbol{k}) = <\psi_{ck}| - i\hbar\nabla|\psi_{vk}>$ are evaluated from DFT calculations using GGA functional. Circular dichroism polarization due to the direct inter-band transition from the vicinity of the valence band edge to the vicinity of the conduction band edge can be clearly seen in Fig. 4.16(d). At the energetic minima at the K1 and K2 points, full selectivity occurs when $\eta(k) = \tau$. The inter-band transitions at K1 valley ($\tau = +1$) only couples to right-handed circularly polarized light (RHCP) (σ^+), whereas left-handed circularly polarized light (LHCP) (σ^-) is used to excite the carriers at K2 valley ($\tau = -1$), as pictorially shown in Fig. 4.16(c). A right-handed (left-handed) circularly polarized photon can be selectively absorbed around the K1(K2) valley, while a left-handed (right-handed) one is totally forbidden. Consequently, the nonequilibrium distribution of

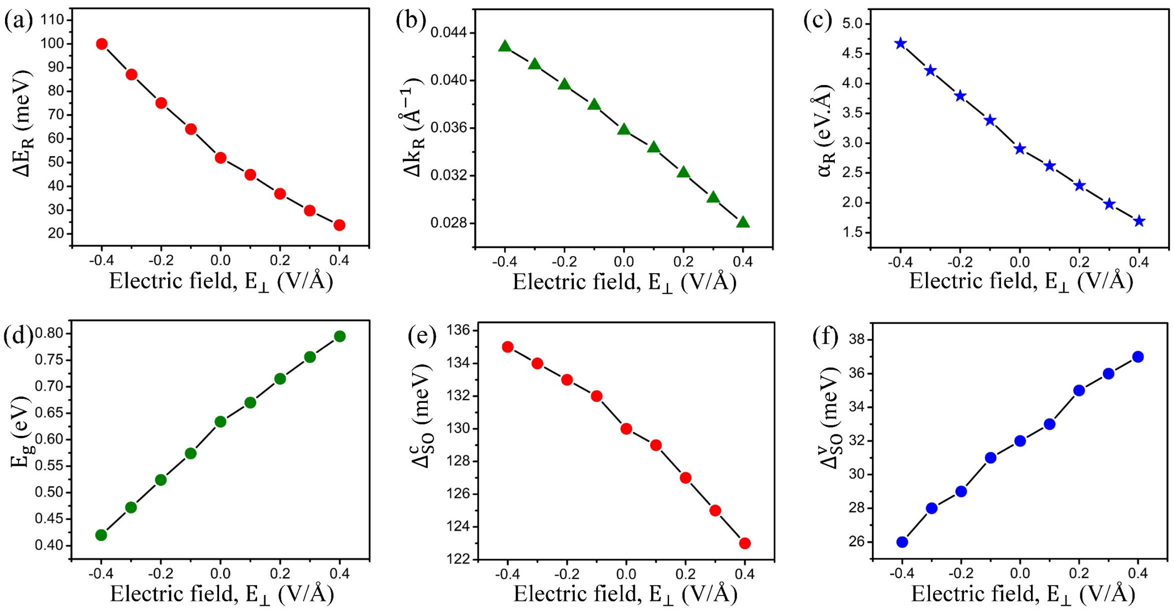

***Figure 4.17** Vertical electric field modulation of (a) Rashba energy offset (ΔE_R), (b) momentum offset (Δk_R), (c) Rashba constant (α_R), (d) band gap (E_g), (e) CB SOC splitting (Δ^c_{SO}) and (f) VB SOC splitting (Δ^v_{SO}) in h-NbN monolayer.*

charge carriers in two inequivalent valleys can be produced by selective optical pumping through circularly polarized light, which is essential for realizing valley Hall effects. [245]

4.2.5 Response to vertical electric field

As electric field control of Rashba SOC is of great significance in semiconductor spintronics, the application of an external electric field to the h-NbN monolayer has also been studied. In this section, a vertical electric field varying from −0.4 to +0.4 V/Å has been applied, and its response to Rashba splitting has been investigated. Rashba spin splitting and valley Zeeman splitting have been observed, as shown in Figs. 4.17(a)-4.17(f), which shows that the Rashba constant, α_R is linearly dependent on the strength of the electric field. Such a linear relationship between the electric field and the Rashba SOC strength will help a precise control of the spin precession in the spin-field-effect transistor. Under the application of a positive electric field, the value Rashba parameters are lowered, while the negative electric field increases the Rashba parameters. The value of α_R is found to be regulated from 1.693 to 4.673 eVÅ. Recently, similar modulation of Rashba constant via vertical electric field is reported in ZnTe monolayer, where it rises from 0.9 to 1.35 eVÅ [246]. Electric field response of CB SOC splitting (Δ^c_{SO}) and VB SOC splitting is found to be of opposite nature. With the application of positive (negative) electric field, $\Delta_{\mathrm{SO}}^{\mathrm{c}}$ decreases (increases), while $\Delta_{\mathrm{SO}}^{\mathrm{v}}$ is increases (decreases). $\Delta_{\mathrm{SO}}^{\mathrm{c}}(\Delta_{\mathrm{SO}}^{\mathrm{v}})$ can be modulated from 123 (26) to 135 (37) meV. Band gap is also linearly changed from 0.420 to 0.795 eV. Such great tunability in the Rashba and valley properties under the vertical electric field is very useful in designing spintronic and valleytronic devices.

4.3 CONCLUSIONS

In this chapter, h-NbN and TaN monolayers have been demonstrated to be promising 2D valleytronic and spintronic materials on account of large Zeeman-type valley spin splitting and Rashba-type spin splitting. Monolayer h-NbN (TaN) shows Zeeman-type valley spin splitting (VSS) of 32 (112) meV and 130 (406) meV in valence band (VB) and conduction band (CB) respectively. At the same time, it exhibits large Berry curvature ~50 (73) Å^2, which is more than four (six) times of monolayer MoS_2 (~11 Å^2). Inclusion of spin-orbit coupling yields the giant Rashba-type spin-splitting in the VB near the Fermi level. The Rashba energy and Rashba splitting constant of monolayer h-NbN (TaN) are found to be 52 (74) meV and 2.90 (4.23) eVÅ, respectively, which are competitive with the giant Rashba spin splitting parameters realized so far in 2D materials. The strength of Zeeman-type valley spin splitting and Rashba-type spin splitting is found to be substantially tweakable upon employing in-plane biaxial strain and out-of-plane electric field to the h-NbN monolayer, owing to the mechanical flexibility in this 2D material. Our results suggest that this theoretically predicted 2D material could serve as an ideal platform for studying valley physics, Rashba physics and for the integration of valleytronics with the spintronics. The true indicator of strength of Rashba constants is found to be the dynamical Born effective charge (Z_{zz}^{*}) along the out-of-plane z direction.

Chapter 5

Electronic and optical properties of ZrS_3/MS_2 and ZrS_3/MXY (M=Mo, W; X, Y=S, Se, Te; X≠Y) based type-II van der Waals heterostructure (vdWH)

This Chapter is based on the work published in:

Raihan Ahammed, Ashima Rawat, Nityasagar Jena, Dimple, Manish Kumar Mohanta, and **Abir De Sarkar**. "ZrS_3/MS_2 and ZrS_3/MXY (M=Mo, W; X, Y=S, Se, Te; X≠Y) type-II van der Waals hetero-bilayers: prospective candidates in 2D excitonic solar cells." ***Appl. Surf. Sci.*** **499, 143894 (2020)**.

5.1 Introduction

Ever since the discovery of graphene [247], interest in two-dimensional (2D) layered materials has ever been on the rise from both scientific and technological perspectives [248–251]. In the world of 2D materials, hexagonal boron nitride (h-BN) [172,252,253], the large family of transition-metal dichalcogenides (TMDCs) [173,254–256] and lately, transition-metal trichalcogenides (TMTCs) [187,188,257,258] have captured a great deal of scientific attention. Besides, the 2D materials show a wide range of properties, which include large band gap insulators [259,260], semiconductors [261,262] and semimetals [263,264]. Moreover, the atomically thin 2D monolayers offer themselves as essential building blocks in several devices owing to their superior electrical [265], optical [266] and thermal [267] properties, which do not exist in their corresponding bulk structures [268–273]. These 2D monolayers also exhibit excellent mechanical stability and can withstand mechanical deformation up to large extent due to strong in-plane covalent bonds [274], which brings about large elastic limit. On the other hand, weak interlayer van der Waals interaction enables a facile exfoliation of 2D monolayers from their bulk counterpart as well as restacking of the monolayers arbitrarily into vertical heterostructures. Hence, it opens up several research avenues based on vdW heterostructures [275–280]. Interestingly, 2D layered materials are devoid of dangling bonds and therefore, they can be readily stacked vertically to form vdW heterostructures, despite the differences in their crystal structures and lattice parameters [281]. Thus, it is possible to expand the choice of materials for emerging applications based on heterostructures of 2D materials, as it does away with the need for a lattice match. The semiconductor heterojunctions have been harnessed in many solid-state devices, such as solar cells [92], photodetectors [282], semiconductor lasers [283–285], and light-emitting diodes (LEDs) [286–288].

2D semiconducting TMDCs, such as, molybdenum disulfide (MoS_2) and tungsten disulfide (WS_2), exhibit high room-temperature carrier mobility (~ 300 $cm^2V^{-1}s^{-1}$), high current ON/OFF ratio (10^8) and excellent bendability which suit them for low power, high performance, flexible electronics [289–293]. The large carrier mobility and its ratio in these Group VI B transition-metal dichalcogenides (MX_2: M=Mo, W; X=S, Se, Te) may assist an efficient charge carrier separation, which is particularly useful in optoelectronic applications, e.g., photovoltaics [294–296], photocatalysis [297,298] and artificial photosynthesis [299,300]. In terms of optical absorbance, WS_2 monolayer is most suitable for photo-physical processes [301].

Janus phase (MXY: M=Mo, W; X=S, Se, Te; Y=S, Se, Te; X≠Y) [302] of TMDC is an important derivative which has become a research hot spot for their highly efficient photocatalytic properties [303]. By replacing one of the chalcogen layers of MX_2 with another type of chalcogen atoms, an asymmetric two-faced structure is formed. Ang-Yu Lu et al. [190] have demonstrated a state-of-the-art synthetic strategy in synthesizing Janus structures in transition-metal dichalcogenides and proposed that the key to the synthetic approach is to control the reaction by kinetics rather than thermodynamics.

In recent years, among the 2D materials, Group-IVB transition-metal trichalcogenides (MX_3: M =Ti, Zr and Hf; X=S, Se or Te) have been assuming utmost importance due to their diverse chemical and physical properties. TMTCs have a unique chain-like structure which imparts quasi-one-dimensional properties to these monolayers, such as, high anisotropy in carrier mobility and optical properties due to its high degree of in-plane lattice asymmetry along its mutually orthogonal crystallographic orientations [304–306]. Recently, a single layer ZrS_3, which has been successfully synthesized using liquid exfoliation technique, is found to be structurally and mechanically stable [307]. Its high spectral selectivity (405 to 780 nm) and excellent photo-switching effect (time period ~ 50 s) attest its strong abilities for photodetection from visible to NIR range of the electromagnetic spectrum, which in turn, highlights the enormous prospects for the application of ZrS_3 monolayers in high-performance nanoscale optoelectronic devices. [189]

Nowadays, atomically thin excitonic solar cell consisting of 2D vdW heterostructures [308–310] are found to be immensely promising for their high charge carrier separation abilities. Such solar cells contain an interface (junction) of two materials which conduct two different types of carriers (electron/hole). Efficient separation of photogenerated electron-hole pairs at the interface and their collection at the electrodes produces electricity. The interface constituted by Schottky or p-n junction using 2D materials in XSC is very thin [308]. The question arises whether it is practical to realize large enough solar energy conversion using such atomically thin layers. Theoretically, Bernardi and co-workers have reported the photovoltaic (PV) effects in 2D heterojunction formed from MoS_2/WS_2, including the Schottky barrier between MoS_2 and graphene [311]. Their theoretical findings demonstrate that in the atomically thin monolayer based solar cells, the power conversion efficiency (PCE) can reach up to ∼1%, while power density (~ 250 kW/kg) gets approximately three orders of magnitude higher than the best existing solar cells (GaAs ~ 54 kW/kg).

Recently, Furchi and co-workers have shown the PV effects in a hetero-interface made of n-type MoS_2 and p-type WSe_2 monolayers [310]. The 2D hetero-interface shows PCE of about 0.2% and the external quantum efficiency (EQE) is found to reach up to 1.5%.

MX_3/M'Y_3 and MX_2/M'Y_2 vdW hetero-bilayers have been studied by Q. Zhao *et al.* [312]. No studies on MX_3/M'X_2 and MX_3/M'Y_2 vdW hetero-bilayers have been reported till date. Our present work is the first attempt to address such hetero-bilayers constituted by transition metal dichalcogenides and trichalcogenides, which have significant lattice mismatch. The nature of the band edges in ZrS_3, and MS_2 monolayers induce high electron mobility and high hole mobility in these monolayers, respectively, which can be combined synergistically in the hetero-bilayers consisting of them. Additionally, effective mass, deformation potential, and carrier mobility have been studied in our work to substantiate the aforementioned synergistic effects arising in the hetero-bilayers.

In the present chapter, vdW hetero-bilayers have been designed by stacking a single-layer of transition-metal trichalcogenide, specifically, ZrS_3 on MS_2 and MXY (M=Mo, W; X, Y=S, Se, Te; X≠Y) monolayers. The electronic, optical and transport properties in vdW ZrS_3/MS_2 hetero-bilayers have been investigated in detail based on first-principles density functional theory (DFT) calculations. The cumulative effect of robust carrier mobility, high carrier mobility ratio, large photo-absorption coefficient ($\alpha \sim 10^5$ cm^{-1}) and high PCE in ZrS_3/MS_2 and ZrS_3/MXY hetero-bilayers makes them an excellent candidate in ultra-thin, 2D excitonic solar cells.

5.2 Results & Discussions

5.2.1 Crystal structures of monolayer MoS_2, WS_2, their Janus structures MXY and ZrS_3/MS_2 vdW hetero-bilayers

A single layer of MS_2 crystallizes in a hexagonal honeycomb structure with the space group $P\bar{6}m2$ which corresponds to the space group number 187, as shown in Figs. 5.1(a) and 5.1(b).

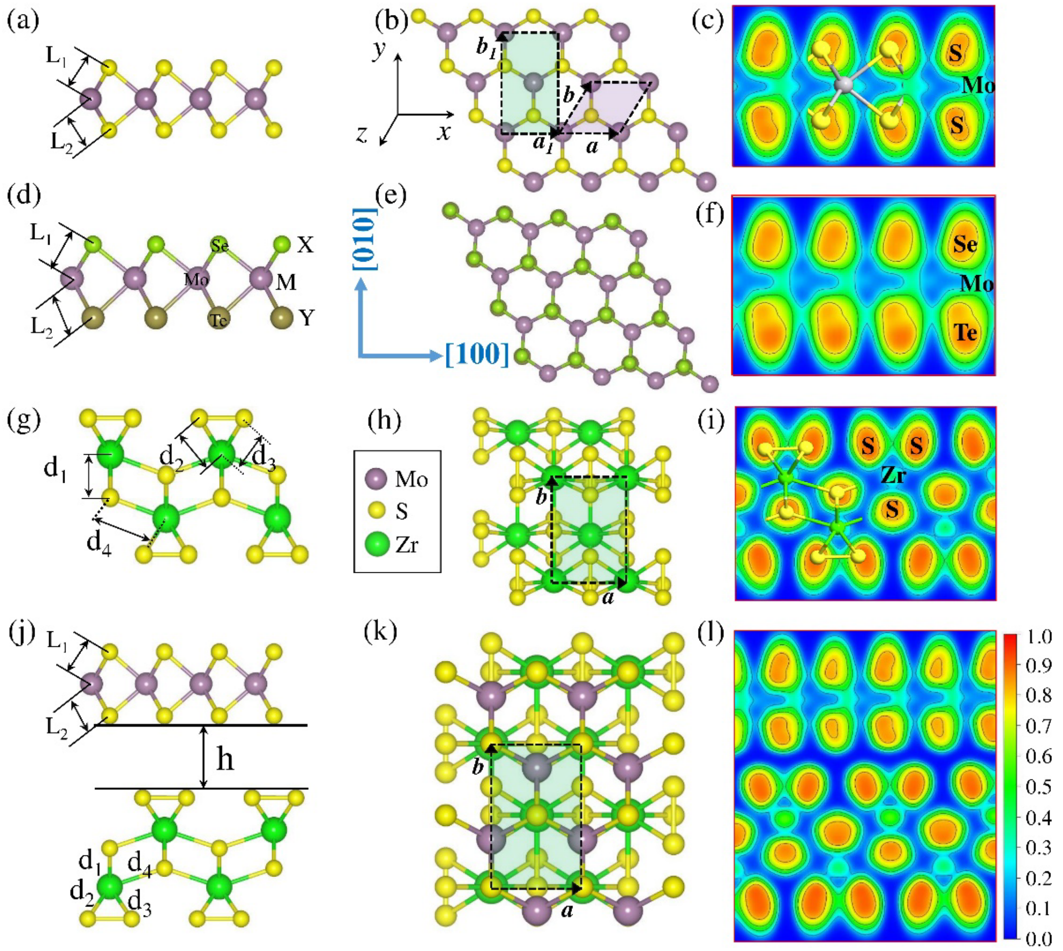
(a)
L1
L2
(b)
y
z
x
b1
b
a1
a
(c)
S
Mo
S
(d)
L1
L2
Se
Mo
Te
X
M
Y
(e)
[010]
[100]
(f)
Se
Mo
Te
(g)
d1
d2
d3
d4
(h)
Mo
S
Zr
b
a
(i)
S
S
Zr
S
(j)
L1
L2
h
d1
d4
d2
d3
(k)
b
a
(l)
1.0
0.9
0.8
0.7
0.6
0.5
0.4
0.3
0.2
0.1
0.0

Figure 5.1 *(a), (d), (g) and (j) are side views of MoS_2, MXY (M=Mo, W; X, Y=S, Se, Te; X≠Y), ZrS_3 monolayers and the ZrS_3/MoS_2 hetero-bilayer respectively in the first column. While (b), (e), (h) and (k) are the top views them respectively in the second column. (c), (f), (i) and (l) represent the electron localization function (ELF) in the third column. In Fig. (b),* ***a*** *and* ***b*** *form the primitive lattice vectors in the hexagonal unit cell, while the non-primitive lattice vectors* ***a₁*** *and* ***b₁*** *lie along the two mutually perpendicular directions in the rectangular unit cell. In-plane [100] direction is along x-axis, while [010] direction is along the y-axis. In Fig. (j), h is the inter-layer distance of the hetero-bilayer.*

The transition metal ions are sandwiched between two layers of S chalcogen ions. The optimized lattice parameter, both of MoS_2 and WS_2 is 3.18 Å, which is in good agreement with the previous studies [313–316]. Compared to the MS_2 monolayer, Janus group-VI chalcogenides MXY (X, Y=S, Se, Te; X≠Y) crystallizes in hexagonal lattice without horizontal mirror symmetry having space group P3m1. The monolayer of ZrS_3 has a unique one-dimensional chain-like structure, as depicted in Fig. 5.1(g). It crystallizes in the monoclinic structure with space group $P2_1/m$

having space group number 11. The unit cell contains two basic molecular units in which Zr atoms lie at the center of each prism where six S atoms are coordinated at the corners, as displayed in Figs. 5.1(g, h). The optimized lattice constants of monolayer ZrS_3 are found to be 3.65 Å and 5.19 Å along ***a*** and ***b***-axis respectively, which are consistent with other theoretical [16,98,100] and experimental [317] results. The lattice constants, bond lengths, and vertical interlayer distance, as shown in Fig. 5.1 are tabulated in Table 5.1. To investigate the bonding nature, electron localization function (ELF) analysis has been performed, as shown in Figs. 5.1(c), 5.1(f), 5.1(i) and 5.1(l) for MoS_2, MoSeTe, ZrS_3, and ZrS_3/MS_2 hetero-bilayers respectively. ELF measures the probability of finding an electron at a given position. The maximum value of 1 for ELF corresponds to the sound localization of electrons, which is indicated by red color in ELF plots. Green color corresponds to an ELF value of 0.5 which

Table 5.1 *Optimized lattice constants, bond lengths in TMDC monolayers, their Janus structures, ZrS_3 monolayers and ZrS_3/MS_2 hetero-bilayers.*

Materials	**Lattice Constants (Å)**	**Bond Lengths (Å)**	**Inter-layer distance (Å)**
MoS_2	$a=b=3.18$; $a_1=3.18$, $b_1=5.51$	$L_1=2.41$, $L_2=2.41$	
MoSeTe	$a=b=3.43$; $a_1=3.43$, $b_1=5.94$	$L_1=2.55$, $L_2=2.72$	
WS_2	$a=b=3.18$; $a_1=3.18$, $b_1=5.51$	$L_1=2.42$, $L_2=2.42$	
WSSe	$a=b=3.25$; $a_1=3.25$, $b_1=5.62$	$L_1=2.42$, $L_2=2.54$	
WSTe	$a=b=3.36$; $a_1=3.36$, $b_1=5.82$	$L_1=2.44$, $L_2=2.72$	
WSeTe	$a=b=3.43$; $a_1=3.43$, $b_1=5.94$	$L_1=2.56$, $L_2=2.72$	
ZrS_3	$a=3.65$, $b=5.19$	$d_1=2.61, d_2=d_3=2.62$, $d_4=2.74$	
ZrS_3/MoS_2 (Case 1)	$a=3.44$, $b=5.32$	$L_1=2.46, L_2=2.37$ $d_1=2.57, d_2=d_3=2.59, d_4=2.82$	3.20
ZrS_3/WS_2 (Case 1)	$a=3.44$, $b=5.33$	$L_1=2.46, L_2=2.38$ $d_1=2.57, d_2=d_3=2.59, d_4=2.78$	3.17
ZrS_3/MoS_2 (Case 2)	$a=15.27$, $b=5.43$	$L_1=2.40, L_2=2.39$ $d_1=2.63, d_2=d_3=2.66, d_4=2.83$	3.23
ZrS_3/WS_2 (Case 2)	$a=15.26$, $b=5.41$	$L_1=2.40, L_2=2.38$ $d_1=2.63, d_2=d_3=2.66, d_4=2.83$	3.27

means uniform distribution of electronic cloud, while ELF=0 corresponds to a blue color indicating zero probability of finding electrons in that region. It is found that the electronic cloud is localized on the chalcogenide atoms, as represented by the red color, whereas electronic cloud delocalization occurs on the transition metal atoms, as indicated by green color. It confirms the presence of mixed bonding nature in these systems. Both covalent and ionic bonding play a part in the M-X bond. The well-separated ELF with no overlap between the two constituent monolayers of ZrS_3/MS_2 hetero-bilayer, as shown in Fig. 5.1(l), implies that the two layers interact weakly via vdW forces.

To ascertain the thermodynamic stability, the interface binding energy of the hetero-bilayers has been calculated at different distances of separation between the individual, constituent monolayers, as shown in Fig. 5.2, using the following Equation (5.1),

$$E_b = E_{hetero.} - E_{ZrS_3} - E_{MS_2} \tag{5.1}$$

where $E_{hetero.}$, E_{ZrS_3} and E_{MS_2} are the total energies of the hetero-bilayer, ZrS_3 and MS_2 (M=Mo,W) monolayers respectively. The binding energy is calculated using the GGA-PBE exchange-correlation functional with DFT-D2 van der Waals correction.

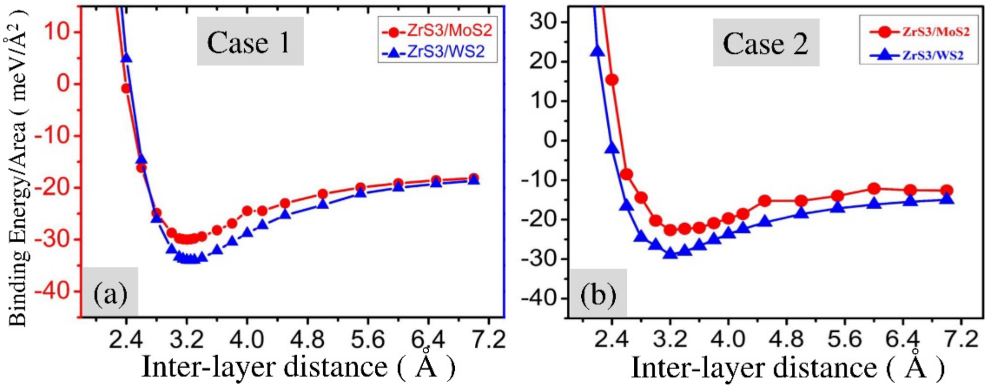

Figure 5.2 *Variation in binding energy per unit inter-facial area of ZrS_3/MS_2 hetero-bilayers with the interlayer distance of (a) case 1 (14 atoms in unit cell) and (b) case 2 (62 atoms in unit cell) using the GGA-PBE exchange correlation functional with DFT-D2 van der Waals correction.*

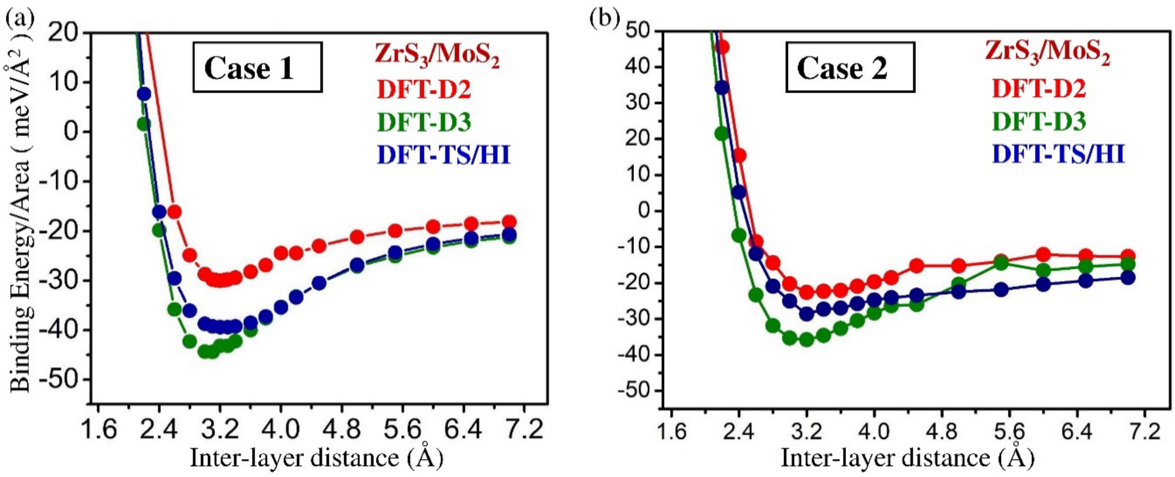

Figure 5.3 *Variation in binding energy per unit inter-facial area of ZrS_3/MS_2 hetero-bilayers with the interlayer distance using the GGA-PBE exchange correlation functional with DFT-D2, DFT-D3, DFT-TS/HI for (a) case 1 and (b) case 2.*

Table 5.2 *Lattice parameters (a, b), inter-layer distance (h) and binding energy (E_b) of ZrS_3/MoS_2 hetero-bilayer with different vdW-interactions.*

ZrS_3/MoS_2 (Case 1)	a	b	h	E_b (meV/Å^2)
DFT-D2	3.44	5.32	3.2	-30
DFT-D3	3.42	5.25	3.1	-42
DFT-TS/HI	3.45	5.27	3.2	-40

ZrS_3/MoS_2 (Case 2)	a	b	h	E_b (meV/Å^2)
DFT-D2	15.27	5.43	3.23	-23
DFT-D3	15.24	5.41	3.16	-36
DFT-TS/HI	15.26	5.43	3.2	-29

The variation in the binding energy with the interlayer distance is shown in Fig. 5.2, and the binding energies of ZrS_3/MoS_2 and ZrS_3/WS_2 bilayers for case 2 (case 1) are found to reach -23 (-30) meV/Å^2 and -29 (-34) meV/Å^2 respectively at the vdW minimum, implying that the process of hetero-bilayer formation is exothermic and exothermicity is higher in magnitude than the previously reported vdW hetero-bilayers, such as, GaSe/graphene (-18.4 meV/ Å^2) [318], g-C_3N_4/MoS_2 (-17.8 meV/ Å^2) [319]. Furthermore, this binding energy is also more than that of typical vdW crystals like graphite (-12.0 meV/ Å^2) [195] and bulk MoS_2 (-26.0 meV/ Å^2) [320]. Hence, the ZrS_3/MS_2 hetero-bilayers will be comparatively more stable. MoS_2 and WS_2 are piezoelectric materials. They polarize the electronic cloud on ZrS_3 and induce dipole moments in it. As a result, the vdW interaction or binding between ZrS_3 and MS_2 is strengthened. The effect of WS_2 is stronger owing to its higher piezoelectric coefficient and Bader charges on the S atoms.

For a systematic study, DFT-D2 results have been compared with two other DFT correction methods, such as DFT-D3 and DFT-TS/HI. Geometric structure, electronic, and optical properties are not found to vary much with the different vdW correction/dispersion as depicted in Figs. 5.3-5.4 and Table 5.2-5.3. The value of lattice parameters, interlayer distance, and interfacial binding energy are very close in different vdW corrections. For ZrS_3/MoS_2 hetero-bilayer of case 1, DFT-D3 and DFT-TS/HI give higher interfacial binding energy (-42, -40 meV/ $Å^2$) than DFT-D2 (- 30 meV/$Å^2$). The interfacial binding energy of ZrS_3/MoS_2 hetero-bilayer of case 2 are -23 and -36 meV/$Å^2$ for DFT-D2 and DFT-D3 respectively (see in Fig. 5.3 and Table 5.2). The variation in the Power Conversion Efficiency (PCE) in the ZrS_3/MoS_2 hetero-bilayer (case 1) with different types of vdW corrections are found to be in the range of 17-20% in Table 5.3. DFT-D2 is found to be the most optimum one in terms of giving out the lowest interlayer binding energies and highest PCE. The electronic and optical properties will be discussed in the following section in more details.

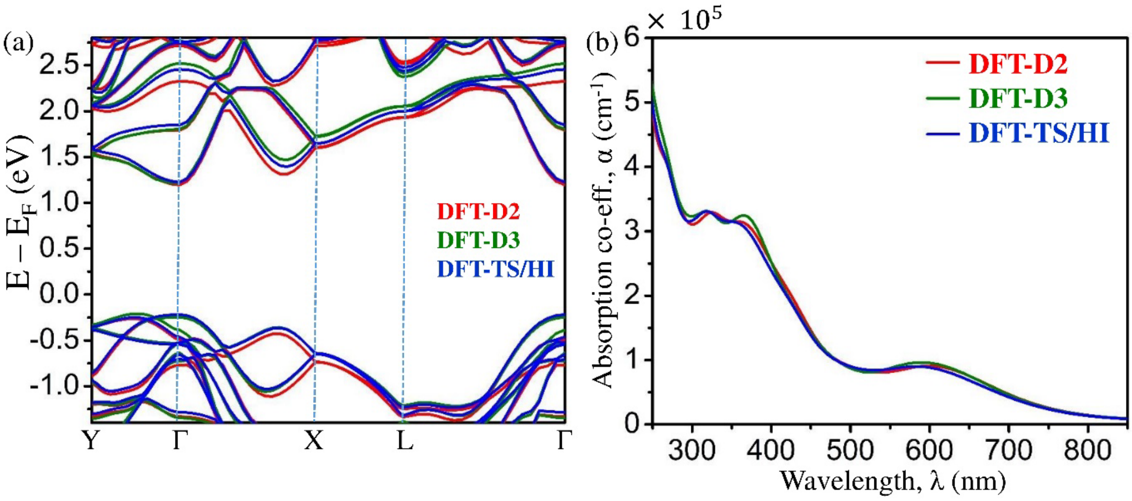

Figure 5.4 *(a) Band structure and (b) absorption coefficient (α) of* ZrS_3/MoS_2 *hetero-bilayer for case 1 using HSE06+DFT-D2, DFT-D3 and DFT-TS/HI. Fermi level is set to zero.*

Table 5.3 *Power Conversion Efficiency (PCE) of ZrS_3/MoS_2 hetero-bilayer for case 1 using HSE06+DFT-D2, DFT-D3 and DFT-TS/HI.*

vdW-interaction	Band gap (eV) of the hetero-bilayer	Donor (MoS_2) band gap (eV)	ΔE_c (eV)	PCE (%)
DFT-D2	1.41	1.52	0.11	20.4
DFT-D3	1.46	1.72	0.26	16.5
DFT-TS/HI	1.44	1.62	0.22	17.8

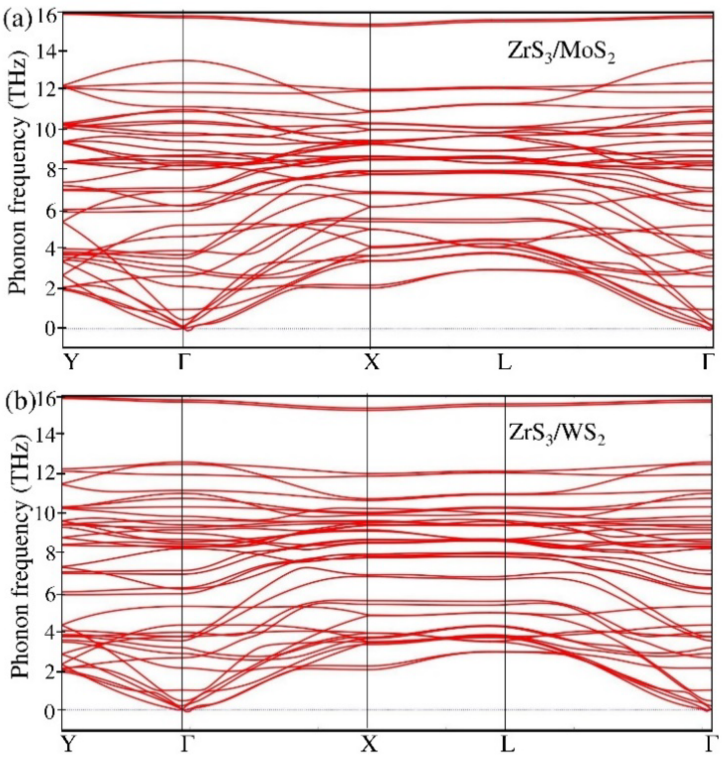

Figure 5.5 *Phonon frequency dispersion of ZrS_3/MS_2 hetero-bilayers (Case 1).*

Phonon dispersion calculations have been carried out to ascertain the dynamical stability. The phonon band dispersions of ZrS_3/MS_2 hetero-bilayers (case1) have been provided in Fig. 5.5. Except for a small pocket of negative frequency (-0.12 THz or -4.0 cm^{-1}) near the Γ point, no trace of imaginary frequency is observed in the Brillouin zone. This small pocket is extremely sensitive to the details of the calculations, and in some cases, it goes off altogether. It simply shows the difficulty in reaching numerical convergence for the flexural phonon mode, which happens to be a common issue in *ab-initio* calculations on 2D materials [228]. Small pockets of negative frequency around the Γ point arising from the flexural acoustic (ZA) modes have also been observed in graphene, silicone, molybdenum disulfide and gallium chalcogenides. This region of instability is particularly dependent on simulation parameters, such as supercell size and k-point sampling. For these reasons, these negative frequencies are understood to be spurious [228]. The hetero-bilayers are therefore found to be dynamically stable, despite large magnitude of strain in the unit cell of the hetero-bilayers. Moreover, the hetero-bilayers meet the Born-Huang stability criteria for mechanical stability.

5.2.2 Electronic properties

The electronic properties of these systems have been explored in detail via first-principles density functional theory. Hybrid HSE06 exchange-correlation functional has been used for a more accurate description of the electronic band structure of these systems. The orbital projected band structures of the hexagonal cell of monolayer MoS_2 and WS_2 have been depicted in Figs. 5.6(a) and 5.6(b) respectively which show direct band gap of 2.14 eV and 2.30 eV at the high symmetry K points. However, the band structure of monolayer ZrS_3, as displayed in Fig. 5.6 (c), shows an indirect bandgap of value 2.07 eV. Nonetheless, the hetero-bilayers (case 1) of ZrS_3/MS_2 are found to show a direct bandgap at the high symmetry Γ point, as depicted in Figs. 5.6 (d) and 5.6(e). The band gap in ZrS_3/MoS_2 and ZrS_3/WS_2 hetero-bilayers (case 1) have been calculated to be 1.41 and 1.17 eV respectively, which are suitable for photovoltaic applications. In case 1, individual monolayers are under significant level of strain, and the strain effects are apparent in the band structure in Fig. 5.7. Figs. 5.4 and 5.6 show that the band gap changes from 2.14 (2.28) eV to 1.52 (1.61) eV in MoS_2 (WS_2) monolayer, while in the ZrS_3 monolayer the same changes from 2.07 eV to 1.46 eV. As the donor band gap material MS_2 is under shear strain in case 1, its band gap decreases with respect to the pristine MS_2 and the band gap turns indirect while ZrS_3 monolayer remains indirect. The hetero-bilayers have been studied in a larger supercell, labeled as case 2, where the magnitude of strain is relatively small. MS_2 is subject to biaxial compressive strain in case 2, which raises its band gap while retaining the directness in the band gap as displayed in Figs. 5.9(a, b). Figs. 5.9(c,d) show energy of band edges (VBM and CBM) of the individual monolayers in the ZrS_3/MS_2 hetero-bilayer (case 2), as identified in Figs. 5.5(a) and 5.5(b) as calculated using HSE06 with DFT-D2 for a higher accuracy in PCE calculations. For case 2, the band gap changes from 2.14 (2.28) eV to 2.58 (2.54) eV in MoS_2 (WS_2) monolayer, while in the ZrS_3 monolayer the same changes from 2.07 eV to 2.39 (2.32) eV.

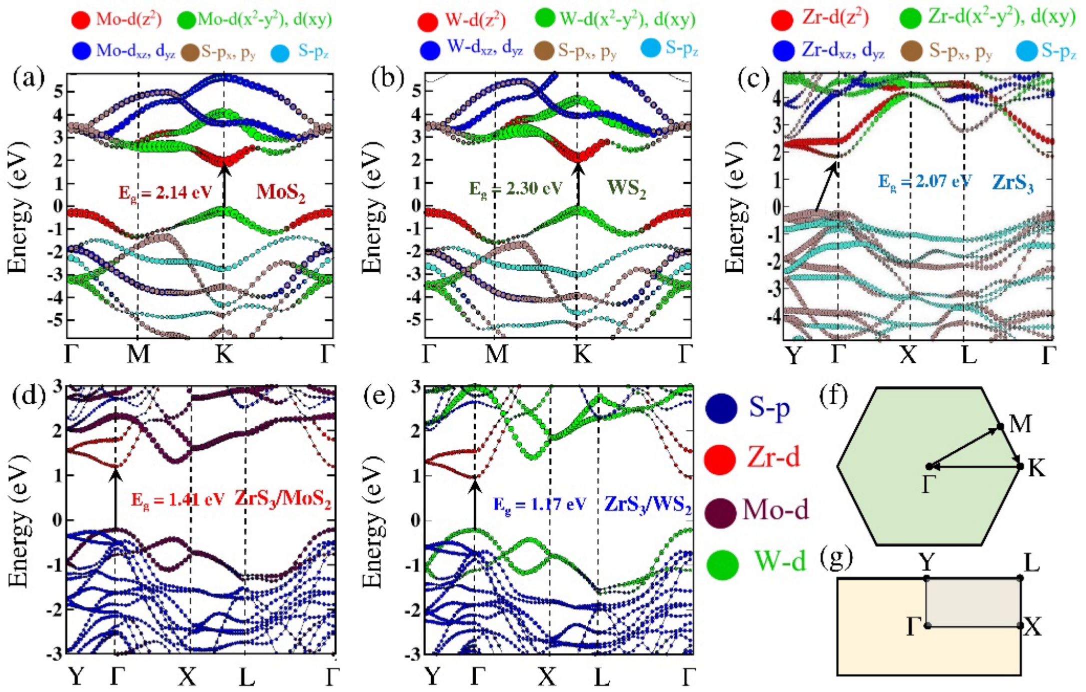

Figure 5.6 *Orbital projected electronic band structure of (a) MoS_2, (b) WS_2, (c) ZrS_3 monolayers HSE06 hybrid functional, (d) ZrS_3/MoS_2 and (e) ZrS_3/WS_2 hetero-bilayers (case 1) using HSE06 hybrid functional with DFT-D2 correction. Fermi level has been set to zero. Brillouin Zone of (f) hexagonal lattice of MS_2 and (g) rectangular lattice of ZrS_3 and ZrS_3/MS_2.*

Three stacking modes in case 1 have been studied in this work and the variation in the studied properties with the stacking order are found to be ignorable, as depicted in Fig. 5.7 and Table 5.4. The variation in Power Conversion Efficiency (PCE) with different stacking sequences is less than 1.1%. The calculation of PCE has been discussed in the following section.

Table 5.4 *Power Conversion Efficiency (PCE) of ZrS_3/MoS_2 hetero-bilayer in different stacking.*

Stacking	Band gap (eV) of the hetero-bilayer	Donor Bandgap (eV)	ΔE_c (eV)	PCE (%)
S1	1.41	1.52	0.11	20.4
S2	1.46	1.54	0.08	20.8
S3	1.45	1.57	0.12	19.8

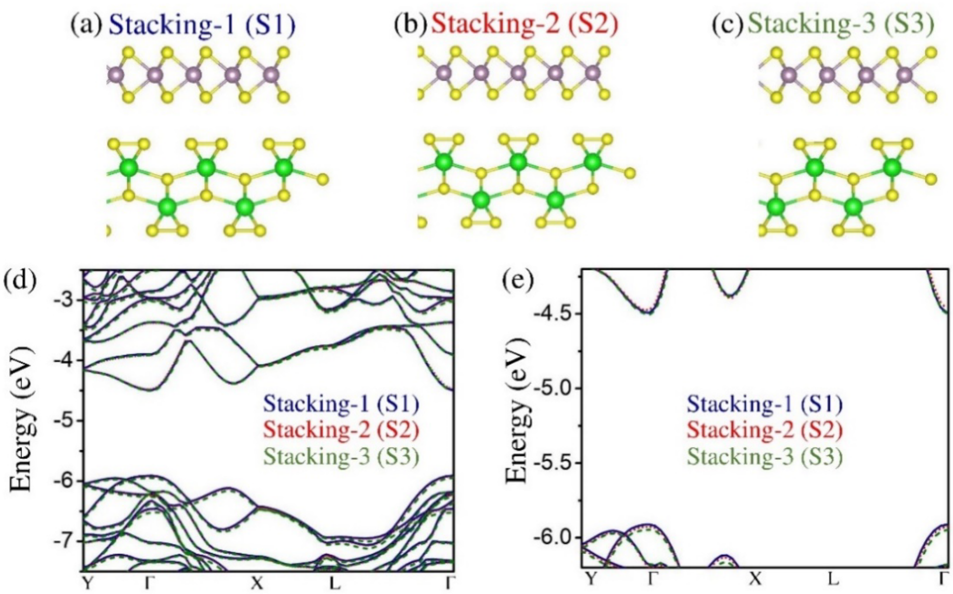

Figure 5.7 *Relaxed geometric structure of ZrS_3/MoS_2 hetero-bilayer in different stacking (a) S1, (b) S2, (c) S3. In Stacking-1, Mo atoms are placed above S atoms of ZrS_3 sheet. In Stacking-2, MoS_2 sheet is translated such that Mo atoms are placed on top of Zr atoms. In Stacking-3, MoS_2 sheet is rotated by 180 degree. (d, e) Band structures of ZrS_3/MoS_2 hetero-bilayer with different stacking. Band energy are plotted with respect to vacuum. (HSE06 + DFT-D2).*

Conduction band minimum (CBM) of MS_2 mainly comprise of M-$d(z^2)$ and S-p_x, p_y orbitals while valence band maximum (VBM) consists of M-$d(x^2-y^2)$, M-d_{xy} and S-p_x, p_y orbitals. For the case of MS_2, VBM and CBM correspond to bonding and anti-bonding states, as they arise from the hybridization between M-d and S-p orbitals. So, the VBM and CBM are, in a way, coupled. However, the CBM of ZrS_3 monolayer is mainly contributed by Zr-d orbitals while its VBM is chiefly composed of S-p orbitals. Therefore, the band edges are decoupled for ZrS_3 monolayer.

The effect of strain on coupled and decoupled band edges are opposite [321]. In MS_2 (ZrS_3) monolayers, the band gap decrease (increase) with the application of tensile strain [321]. It has important implications for the carrier deformation potential, which is an essential ingredient in the calculation of carrier mobility, as discussed in a later section. The detailed information on deformation potential of ZrS_3, MS_2 monolayer and their hetero-bilayers has been depicted in Figs. 5.13-5.16. The deformation potential for holes is lower than that of electrons for MS_2, which causes higher mobility for holes in MS_2. The underlying physical picture has been discussed in detail in an earlier work [301]. The kinetic energy of a state, say, VBM or CBM, is proportional to the square of the reciprocal lattice vector and therefore, kinetic energy both in CBM and VBM drop with the application of tensile strain. The potential energy of a state depends on band width. The width of the decoupled band edges (i.e., conduction and valence bands) in ZrS_3 monolayer narrows with the application of tensile strain as a consequence of localization of states [321], which in turn raises (lowers) the potential energy of CBM (VBM). The potential (kinetic) energy of CBM shifts up (down) under the application of tensile strain. The downshift in kinetic energy outweighs the upshift in potential energy and therefore, a resultant downshift in the CBM is observed. Thus, the change in total energy is small, giving rise to a low deformation potential for electrons in ZrS_3 monolayers. However, in the case of VBM, both the potential energy and its kinetic energy shift down with the application of tensile strain. As the change in total energy is substantial, it causes high deformation potential for holes. The resultant is high (low) mobility for electrons (holes) in ZrS_3 monolayer, which is precisely opposite to that of the MS_2 monolayers. The underlying physical picture or mechanism revealed herein can account for the low (high) deformation for electrons (holes), and the resultant high (low) mobility for electrons (holes) observed on TiS_3 monolayer [304], which belongs to the same family as ZrS_3.

The electronic properties have been investigated further via the atomic layer projected band structure, as depicted in Figs. 5.8(a, b) and Figs. 5.9(a, b). It is clearly shown that valence band maxima (VBM) originate from MS_2 layer and conduction band minima consist of ZrS_3 layer, confirming type-II band alignment of the vdW hetero-bilayers. So, these hetero-bilayers would be very effective in separating the electrons and holes on ZrS_3 and MS_2 monolayers respectively, upon photo-absorption, and thereby in minimizing the carrier recombination rate. The high electron (hole) mobility in ZrS_3 (MS_2) monolayers can be synergistically utilized in these type-II hetero-bilayers, as discussed in a subsequent section.

The type-II nature of these hetero-bilayers is also confirmed by the band decomposed charge density corresponding to the VBM and CBM, as shown in Figs. 5.8(c, d). It is found that the band decomposed charge density of the highest occupied molecular orbital (HOMO) or VBM lies on the MS_2 monolayer whereas the lowest unoccupied molecular orbital (LUMO) or CBM occurs on the ZrS_3 monolayer. In the photo-physical process, the MS_2 monolayer acts as the donor level while ZrS_3 monolayer serves as the acceptor level.

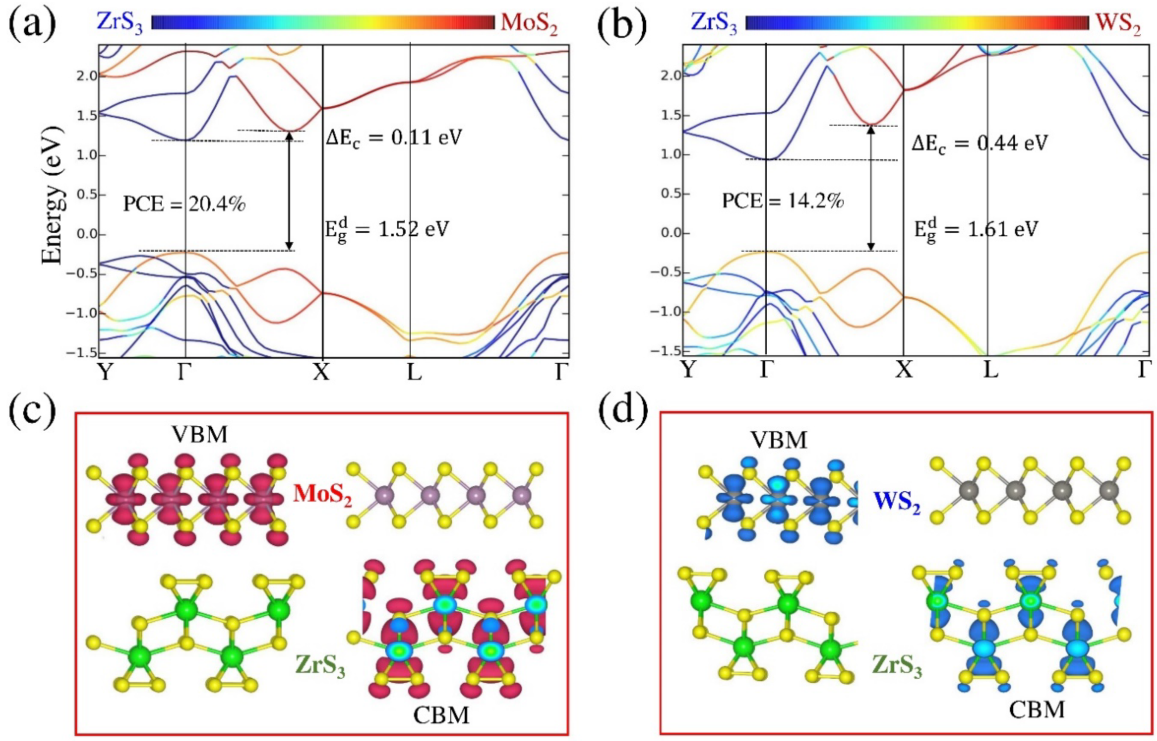

Figure 5.8 *Atomic layer projected band structure of (a) ZrS_3/MoS_2 and (b) ZrS_3/WS_2 vdW hetero- bilayers of case 1. Colour bar represents contribution of MS_2 layer. Fermi level is set to zero.The band decomposed charge density corresponding to the VBM and CBM of (c) ZrS_3/MoS_2 and (d) ZrS_3/WS_2 vdW hetero-bilayer with an isosurface value of 0.005 e/$Å^{-3}$. (HSE06+DFT-D2). The calculation of PCE has been discussed in section 5.2.3.*

The conduction band offset (CBO) in these two hetero-bilayers have been calculated by atomic layer projected band structure of the hetero-bilayers, as shown in Figs. 5.8(a, b) and Figs. 5.9(a, b). The CBOs in ZrS_3/MS_2 (M=Mo, W) are found to be 0.11 eV and 0.44 eV respectively. In several findings, including high throughput calculations [309], the CBO is routinely calculated, within the Anderson limit, from the difference in electron affinity between the isolated donor and acceptor, without addressing the actual heterostructure.

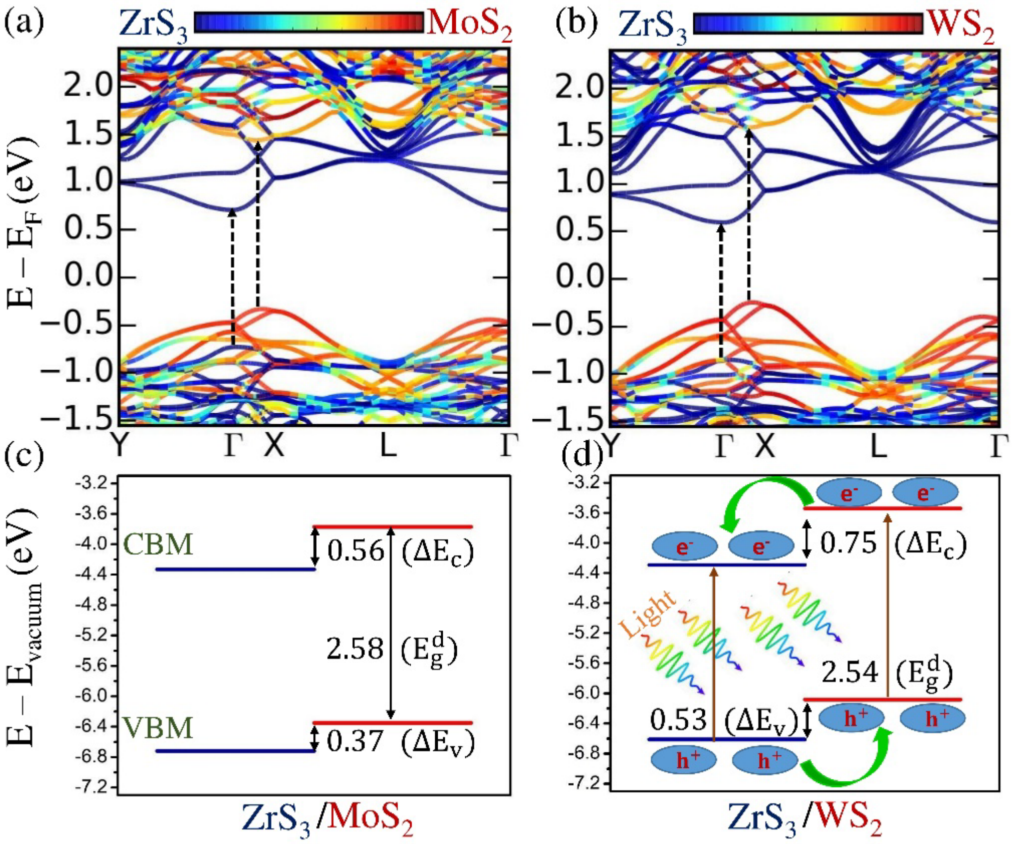

Figure 5.9 *Atomic layer projected band structure of (a) ZrS_3/MoS_2 and (b) ZrS_3/WS_2 vdW hetero- bilayers of case 2 using GGA-PBE with DFT-D2. Colour bar represents contribution of MS_2 layer. Fermi level is set to zero. (c,d) Energy of band edges (VBM and CBM) of the individual monolayers in the ZrS_3/MS_2 hetero-bilayer (case 2), as identified in (a) and (b) have been calculated further using HSE06 with DFT-D2 for a higher accuracy in PCE calculations. Energy of band edges are plotted with respect to vacuum level.*

The band gap of the individual and isolated donor goes into the calculation of PCE. Although PCE is calculable with reasonable accuracy from the differences in electron affinities; yet, many important properties of the heterostructures are not unveiled from this perspective. For instance, the changes in the band gap, optical absorbance, deformation potential and carrier mobility between the heterostructures and the individual components can be important.

5.2.3 Power Conversion Efficiency (PCE)

For these vdW hetero-bilayers, a practical upper limit to the power conversion efficiency has been estimated by employing the method introduced by Scharber et al. [322], which is commonly employed in efficiency calculations. The maximum PCE, η for such devices with type-II alignment can be calculated by Formula (5.2)

$$\eta = \frac{J_{sc}V_{oc}\beta_{FF}}{P_{solar}} = \frac{0.65\left(E_g^d - \Delta E_c - 0.3\right)\int_{E_g^d}^{\infty}\frac{J_{ph}(\hbar\omega)}{\hbar\omega}d(\hbar\omega)}{\int_0^{\infty}J_{ph}(\hbar\omega)d(\hbar\omega)} \tag{5.2}$$

where J_{sc} is the short circuit current, V_{oc} is the open circuit voltage, β_{FF} is the fill factor (FF), and P_{solar} is incident solar energy power, J_{ph} (ħω) is the AM1.5 solar energy flux ($Wm^{-2}eV^{-1}$) at the photon energy ħω, and E_g^d is the energy bandgap of the donor materials (MS_2 monolayers).

In this calculation, the fill factor (β_{FF}) is assumed to be 0.65, as inferred from the Shockley-Queisser limit [147]. The maximum open circuit voltage V_{oc} (in eV units) is estimated as (E_g^d - ΔE_c - 0.3) where the effective interface gap (E_g^d - ΔE_c) is calculated as the energy difference between HOMO level of the donor and LUMO level of the acceptor and the value 0.3 in the V_{oc} term accounts for energy conversion kinetics.

In the equation, the integral in the numerator is the short circuit current, J_{sc}, which has been calculated using an upper bound of 100 % for external quantum efficiency (EQE), while the denominator is the integrated AM1.5 solar energy flux, which amounts to 1000 W/m^2. The efficiency, η is thus estimated as the product FF.V_{oc}.J_{sc} normalized by the incident energy flux, at the limit of 100% EQE.

The band edges of isolated monolayers have been indicated in Fig. 5.10(a). As shown in Fig. 5.10(b), the PCEs in ZrS_3/MoS_2 and ZrS_3/WS_2 vdW hetero-bilayers, calculated within the Anderson limit (i.e., case 3), from the band edges of the isolated monolayers, in an absolute vacuum scale, reach 12% and 8% respectively. However, when hetero-bilayers of ZrS_3 monolayer and the different Janus monolayers are considered, the PCE is enhanced. ZrS_3/MoSTe, ZrS_3/WSTe ZrS_3/WSeTe hetero-bilayers show 16%, 14% and 14% PCE respectively in the Anderson limit. Conduction band offset is also found to be very sensitive to the application of strain. In case 1, it is 0.11 eV for ZrS_3/MoS_2 hetero-bilayer, while it is 0.56 eV in case 2, as tabulated in Table 5.5 and 5.6. Consequently, beyond the Anderson limit, the modeled hetero-bilayers of ZrS_3/MoS_2 show PCE of about 20% and 6% for case

Table 5.5 *Power Conversion Efficiency (PCE) of ZrS_3/MoS_2 hetero-bilayer in different case using HSE06 + DFT-D2.*

ZrS_3/MoS_2	Band gap (eV)	Donor Bandgap (eV)	ΔE_c (eV)	PCE (%)
S1(Case 1)	1.41	1.52	0.11	20.4
S1(Case 2)	2.02	2.58	0.56	5.9

Table 5.6 *Power Conversion Efficiency (PCE) of ZrS_3/WS_2 hetero-bilayer in different case using HSE06 + DFT-D2.*

ZrS_3/WS_2	Band gap (eV)	Donor Bandgap (eV)	ΔE_c (eV)	PCE (%)
S1(case 1)	1.17	1.61	0.44	14.2
S1(case 2)	1.79	2.54	0.75	5.3

1 and case 2 respectively. These PCE values are much larger than MoS_2/p-Si heterojunction solar cells (5.23%) [294] reported till now and are comparable to that of the theoretically proposed PCBM fullerene/BCN system (10−20%) [323] and g-SiC_2-based systems (12−20%) [324] and the recently predicted TiNF/TiNBr (18%), TiNCl/TiNBr (19%), TiNF/TiNCl (22%) bilayer solar cell systems [325]. Furthermore, our predicted systems are competitive with that of recently proposed hetero-bilayer of GeSe/SnS systems (~18%) [326], bilayer phosphorene/MoS_2 systems (16–18%) [327], and phosphorene/TMDC systems (4–12%) [328] for highly efficient solar cells.

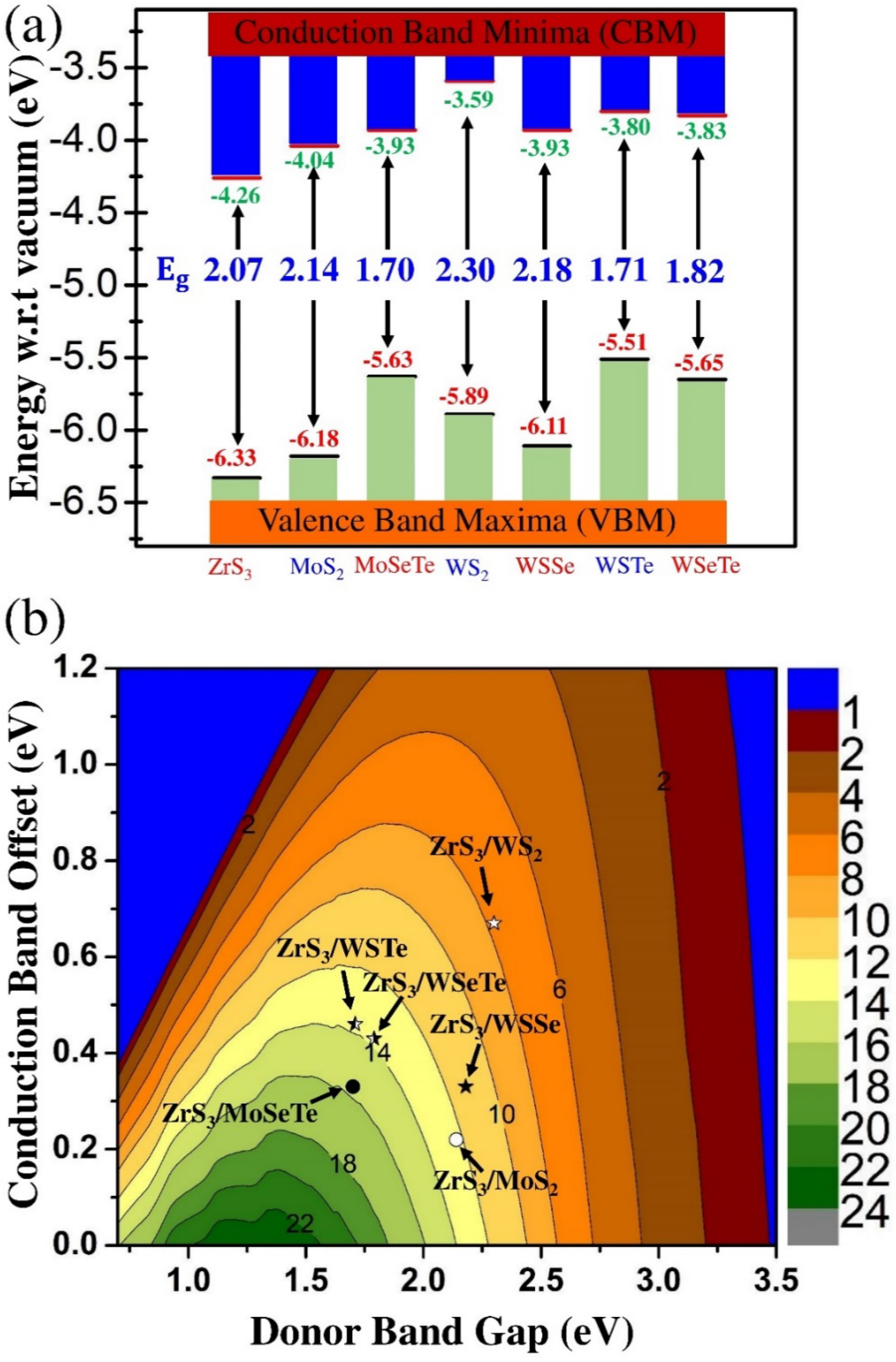

Figure 5.10 *(a) Band edges of ZrS_3, MoS_2, MoSeTe, WS_2, WSSe, WSTe, WSeTe isolated monolayers calculated with respect to the absolute vacuum level using HSE06 functional. (b) Computed power conversion efficiency (PCE) contour as a function of donor bandgap and conduction band offset. The calculated PCE according to Anderson limit of possible type-II hetero-bilayers (Case 3) have been indicated by circles and stars.*

5.2.4 Optical property

A good photovoltaic material should be able to absorb significant part of the visible light spectrum efficiently. Absorption coefficient determines most of the optical properties of a material. Materials with high absorption coefficient in the visible light wavelength range are therefore desirable. The absorption coefficient of a substance is related to the frequency-dependent dielectric function. The optical properties are calculated from the complex dielectric function, $\varepsilon(\omega) = \varepsilon_1(\omega) + i\,\varepsilon_2(\omega)$. The optical parameters, such as the extinction coefficient, absorption coefficient is based on ε_1 and ε_2. The computational methodological details on the calculation of optical properties, such as extinction coefficient (κ) and absorption coefficient (α) are provided in the computational details.

Fig. 5.11 shows the absorption coefficient as a function of wavelength. The maximum visible light absorption for MoS_2, WS_2, and ZrS_3 monolayers arises at 598 nm, 537 nm, and 459 nm respectively. These three peaks correspond to the transitions from VBM to CBM in the respective monolayers. The hetero-bilayers of ZrS_3/MoS_2 and ZrS_3/WS_2 for case 1 show peaks in the visible range at 623 nm and 590 nm respectively. The hetero-bilayers of ZrS_3/MoS_2 and ZrS_3/WS_2 for case 1 show peaks in the visible range at 623 nm and 590 nm respectively as depicted in Fig. 5.12. These peaks are red-shifted relative to the peaks of individual monolayers as the bandgaps of the individual monolayers are decreased. While for case 2 the peaks are blue shifted as the bandgaps of the individual monolayers are increased. The first peaks of the hetero-bilayers of ZrS_3/MoS_2 and ZrS_3/WS_2 for case 2 arise at 339 nm and 314 nm respective as shown in Fig. 5.11.

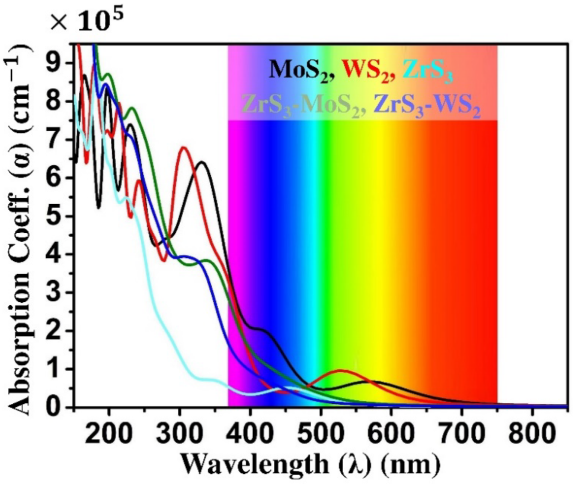

Figure 5.11 *Absorption coefficient (α) of MoS_2, WS_2, ZrS_3 monolayers and ZrS_3/MS_2 hetero-bilayers for Case 2 using HSE06 + DFT-D2.*

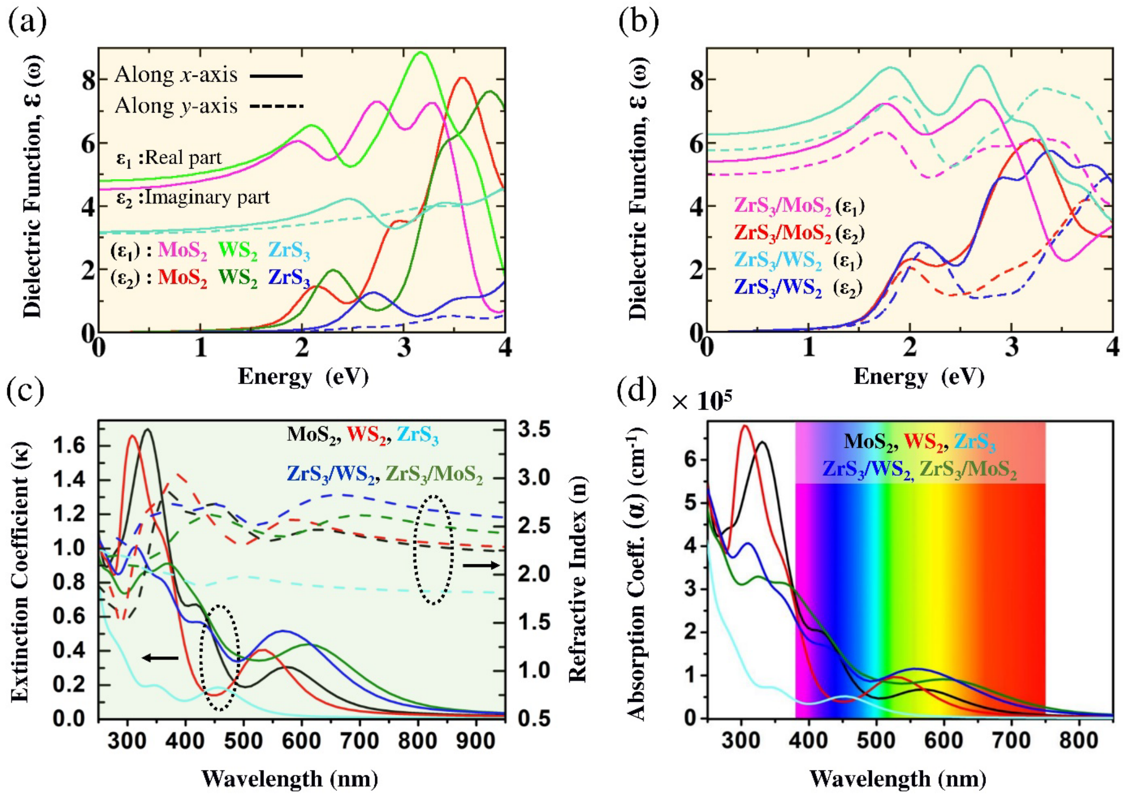

Figure 5.12 *Real (ε_1) and imaginary (ε_2) part of the dielectric function of (a) MoS_2, WS_2, ZrS_3 monolayers using hybrid HSE06 functional and (b) ZrS_3/MoS_2, ZrS_3/WS_2 hetero-bilayers (Case 1) using HSE06 with DFT-D2. (c) Extinction coefficient (κ) and (d) Absorption coefficient (α) as the function of wavelength.*

The calculated absorption spectra, as shown in Fig. 5.11, reveal photo-absorption in the visible region with a very high absorption coefficient, $(\alpha_{abs.}) \sim 10^5\ cm^{-1}$. Overall, the hetero-bilayer shows good absorbance over the entire spectrum of the visible wavelength (380-750 nm). Therefore, ZrS_3/MS_2 hetero-bilayers are confirmed to be efficient visible light harvesting photovoltaic materials.

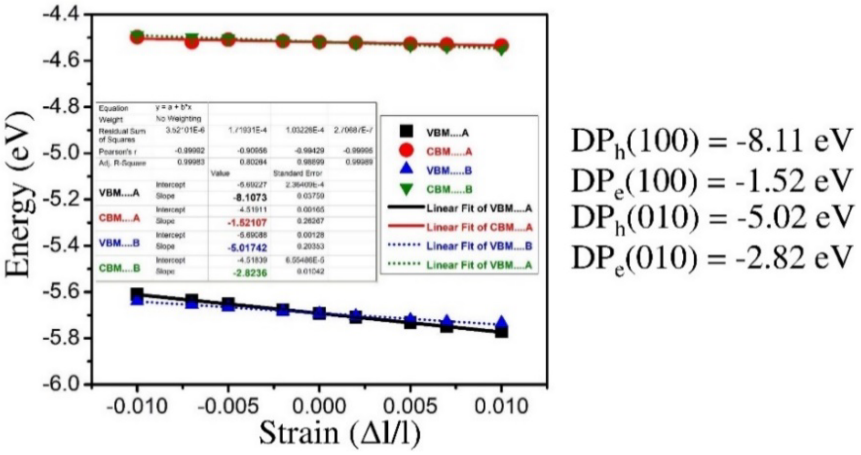

Figure 5.13 *Deformation Potential of ZrS_3 monolayer. VBM_A and VBM_B represent the valence band minima when strain is applied along A-axis and B-axis respectively. A-axis & B-axis correspond to [100] and [010] directions respectively. Band edges are plotted with respect to vacuum. (GGA-PBE)*

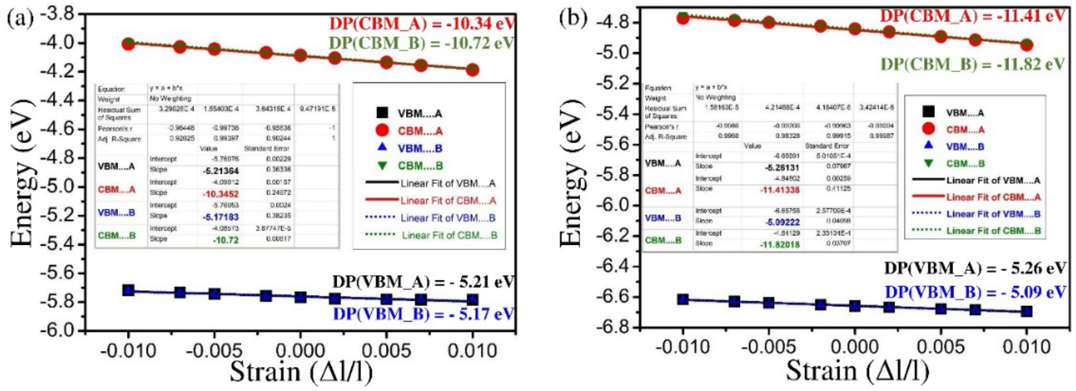

Figure 5.14 *Deformation Potential of (a) MoS_2 and (b) WS_2 monolayer. Band edges are plotted with respect to vacuum. (GGA-PBE).*

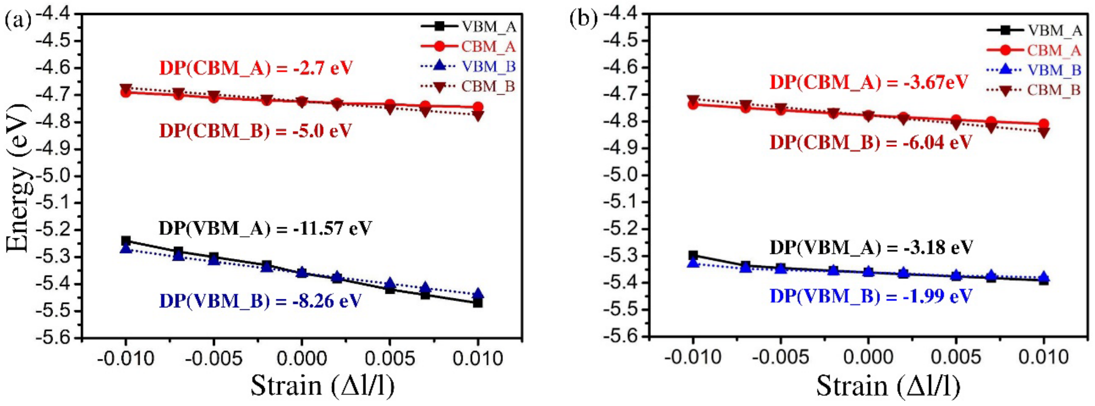

Figure 5.15 *Deformation Potential of (a) ZrS_3/MoS_2 and ZrS_3/WS_2 hetero bilayers. Band edges are plotted with respect to vacuum. (GGA-PBE with DFT-D2).*

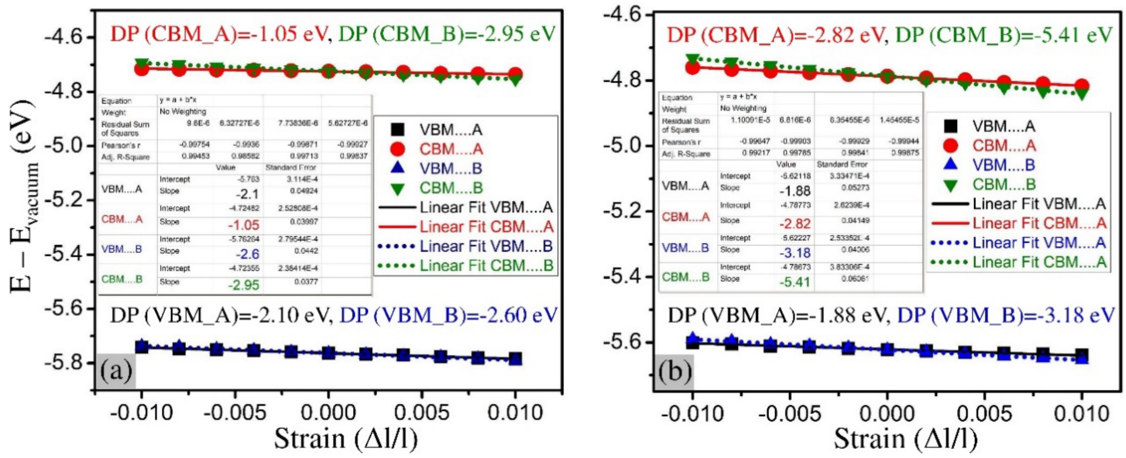

Figure 5.16 Deformation Potential of (a) ZrS_3/MoS_2 and ZrS_3/WS_2 hetero bilayers of case 2. Band edges are plotted with respect to vacuum. VBM_A and VBM_B represent the valence band minima when strain is applied along A-axis and B-axis respectively. A-axis & B-axis correspond to [100] and [010] directions respectively. (GGA-PBE + DFT-D2)

5.2.5 Transport property

Charge carrier mobility also plays a vital role in determining the photovoltaic activity of solar cell material. Higher carrier mobility along with large carrier mobility ratio is required to prolong the carrier lifetime or reduce the electron-hole recombination rate and in turn, facilitating the optimal utilization of the carriers in the photophysical processes. Moreover, lower the exciton binding energy, easier it would be to separate the electron-hole pairs.

The calculated values of the effective mass (m^*), exciton mass (μ_{ex}), macroscopic static dielectric constant (ε), the exciton binding energy(E_b^{ex}), elastic stiffness constant (C_{2D}), deformation potential (E_i), and carrier mobility (μ_{2D}) are summarized in Table 5.7. Acoustic phonon limited carrier mobility has been calculated based on the formulation of Bardeen and Shockley [135] and the most advanced cum robust one by Lang et al [145]. It is observed that in the monolayer of ZrS_3, the electron mobility is very high (~2500 $cm^2V^{-1}s^{-1}$) along the direction which is perpendicular to the chain-like structure. The electron mobility is altered in the hetero-bilayers of ZrS_3/MS_2 (M=Mo, W) of case 2 relative to the individual monolayers; however, the order of magnitude is retained with electron mobility reaching ~5124 and 1191 $cm^2V^{-1}s^{-1}$, respectively.

Table 5.7 *Elastic stiffness constant (C_{2D}), deformation potential (E_{2D}), effective mass (m^*), carrier mobility (μ_{2D}), static dielectric constant (ε), exciton effective mass (μ_{ex}) and exciton binding energy (E_b^{ex}) of MS_2, ZrS_3 monolayers and ZrS_3/MS_2 hetero-bilayers (Case 1 and Case 2). [a]Ref 116, [b]Ref 117.*

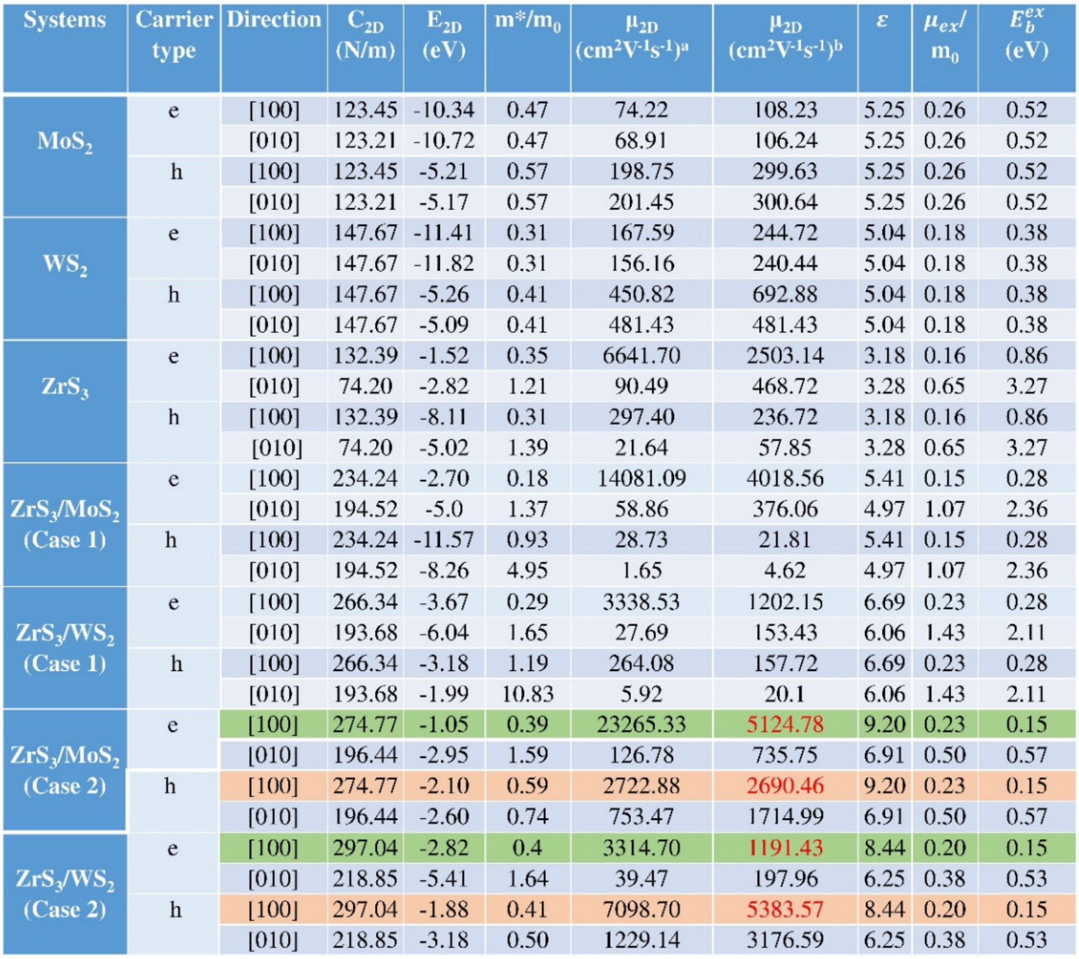

Systems	Carrier type	Direction	C_{2D} (N/m)	E_{2D} (eV)	m^*/m_0	μ_{2D} ($cm^2V^{-1}s^{-1}$)[a]	μ_{2D} ($cm^2V^{-1}s^{-1}$)[b]	ε	μ_{ex}/m_0	E_b^{ex} (eV)
MoS_2	e	[100]	123.45	-10.34	0.47	74.22	108.23	5.25	0.26	0.52
		[010]	123.21	-10.72	0.47	68.91	106.24	5.25	0.26	0.52
	h	[100]	123.45	-5.21	0.57	198.75	299.63	5.25	0.26	0.52
		[010]	123.21	-5.17	0.57	201.45	300.64	5.25	0.26	0.52
WS_2	e	[100]	147.67	-11.41	0.31	167.59	244.72	5.04	0.18	0.38
		[010]	147.67	-11.82	0.31	156.16	240.44	5.04	0.18	0.38
	h	[100]	147.67	-5.26	0.41	450.82	692.88	5.04	0.18	0.38
		[010]	147.67	-5.09	0.41	481.43	481.43	5.04	0.18	0.38
ZrS_3	e	[100]	132.39	-1.52	0.35	6641.70	2503.14	3.18	0.16	0.86
		[010]	74.20	-2.82	1.21	90.49	468.72	3.28	0.65	3.27
	h	[100]	132.39	-8.11	0.31	297.40	236.72	3.18	0.16	0.86
		[010]	74.20	-5.02	1.39	21.64	57.85	3.28	0.65	3.27
ZrS_3/MoS_2 (Case 1)	e	[100]	234.24	-2.70	0.18	14081.09	4018.56	5.41	0.15	0.28
		[010]	194.52	-5.0	1.37	58.86	376.06	4.97	1.07	2.36
	h	[100]	234.24	-11.57	0.93	28.73	21.81	5.41	0.15	0.28
		[010]	194.52	-8.26	4.95	1.65	4.62	4.97	1.07	2.36
ZrS_3/WS_2 (Case 1)	e	[100]	266.34	-3.67	0.29	3338.53	1202.15	6.69	0.23	0.28
		[010]	193.68	-6.04	1.65	27.69	153.43	6.06	1.43	2.11
	h	[100]	266.34	-3.18	1.19	264.08	157.72	6.69	0.23	0.28
		[010]	193.68	-1.99	10.83	5.92	20.1	6.06	1.43	2.11
ZrS_3/MoS_2 (Case 2)	e	[100]	274.77	-1.05	0.39	23265.33	5124.78	9.20	0.23	0.15
		[010]	196.44	-2.95	1.59	126.78	735.75	6.91	0.50	0.57
	h	[100]	274.77	-2.10	0.59	2722.88	2690.46	9.20	0.23	0.15
		[010]	196.44	-2.60	0.74	753.47	1714.99	6.91	0.50	0.57
ZrS_3/WS_2 (Case 2)	e	[100]	297.04	-2.82	0.4	3314.70	1191.43	8.44	0.20	0.15
		[010]	218.85	-5.41	1.64	39.47	197.96	6.25	0.38	0.53
	h	[100]	297.04	-1.88	0.41	7098.70	5383.57	8.44	0.20	0.15
		[010]	218.85	-3.18	0.50	1229.14	3176.59	6.25	0.38	0.53

Likewise, the order of magnitude in the hole mobility in MS_2 monolayers is retained in this type-II vdW hetero-bilayers along the [100] direction, as tabulated in Table 5.7. Furthermore, the mobility ratio of the charge carriers has been evaluated using the following relation, $R_\alpha = \frac{\max(\mu_{e\_}\alpha, \mu_{h\_}\alpha)}{\min(\mu_{e\_}\alpha, \mu_{h\_}\alpha)}$, where α is either along [100] or [010] direction, as shown in Figs. 5.17(a) and 5.17(b).

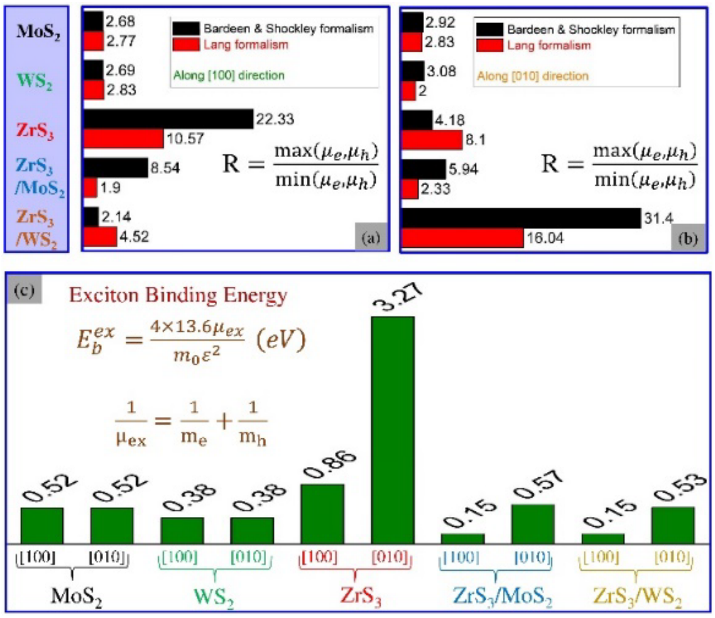

Figure 5.17 *Carrier mobility ratio (R) of monolayer MoS_2, WS_2, ZrS_3 and the ZrS_3/MS_2 hetero-bilayers (case 2) along (a) [100] and (b) [010] direction. (c) Exciton binding energies of these systems calculated using Mott-Wannier hydrogenic model.*

The carrier mobility ratio of ZrS_3/MS_2 hetero-bilayer (case 2) is found to be comparable to the individual monolayers. It is also found that the exciton binding energy of ZrS_3/MS_2 hetero-bilayer of case 2 along [100] direction is 0.15 eV which is much less than the value ~ 0.57 (0.53) eV along [010] direction, as depicted in Fig. 5.17(c). Not only that, exciton binding energy in the hetero-bilayer along the [100] direction is lowered with respect to the individual constituent monolayers on account of the higher macroscopic dielectric constant (or relative permittivity) in the hetero-bilayer. The exciton binding energy is also found to be strain sensitive. In case 2, the individual monolayers in the hetero-bilayers are under a relatively smaller strain than case 1. Smaller excitonic mass and larger macroscopic static dielectric constant, as tabulated in Table 5.7, causes a smaller excitonic binding energy as compared to case 1. Mott-Wannier hydrogenic model has been consistently used in this work to calculate the exciton binding energies based on two different considerations of the macroscopic static dielectric constants, as shown in Table 5.8. Generally, exitonic binding energy is calculated using GW-BSE theory for a higher accuracy. Rasmussen and Thygesen have benchmarked the Mott-Wannier hydrogenic model against the complete GW-BSE calculations and have found the exciton binding energies to vary by less than 0.1 eV [321] for 2H-MoS_2 and 2H-WS_2. It is known that Mott-Wannier exciton binding energies are generally smaller than the ones obtained using GW methods. However, once the Mott-Wannier model is adapted to the 2D systems [329,330], i.e. $E_b^{2D} = 4\,\mathrm{x}\,E_b^{3D} = 4\mathrm{x}\frac{13.6\ \mathrm{x}\ \mu_{ex}}{m_0\varepsilon^2}$ (eV), where $\frac{1}{\mu_{\mathrm{ex}}} = \frac{1}{\mathrm{m_e}} + \frac{1}{\mathrm{m_h}}$, the Mott-Wannier exciton binding energy reaches closer to experiments [331] and the GW values [330]. A. Ramasubramaniam [330] has calculated exciton binding energy using the Mott-Wannier model based on the effective macroscopic static dielectric constant ($\varepsilon_{eff} = \sqrt{\varepsilon_{x(y)}.\varepsilon_z}$) and have found the excitonic binding energy of monolayer MoS_2 to be 0.85 eV, which is very close to our calculated value (0.96 eV), tabulated in Table 5.8. Exciton binding energy calculated via G_0W_0-BSE is 1.04 eV [330]. Advantageously, the carrier mobility and their ratio are high along the [100] direction where the exciton binding energy is low (~0.15 eV), thereby easing the separation of electron-hole pairs along the [100] direction and enhancing their utility in photovoltaics. These results indicate that current needs to be collected along the [100] direction in the photovoltaic set up for optimum efficiency.

Table 5.8 *Exciton binding energy of the materials.*

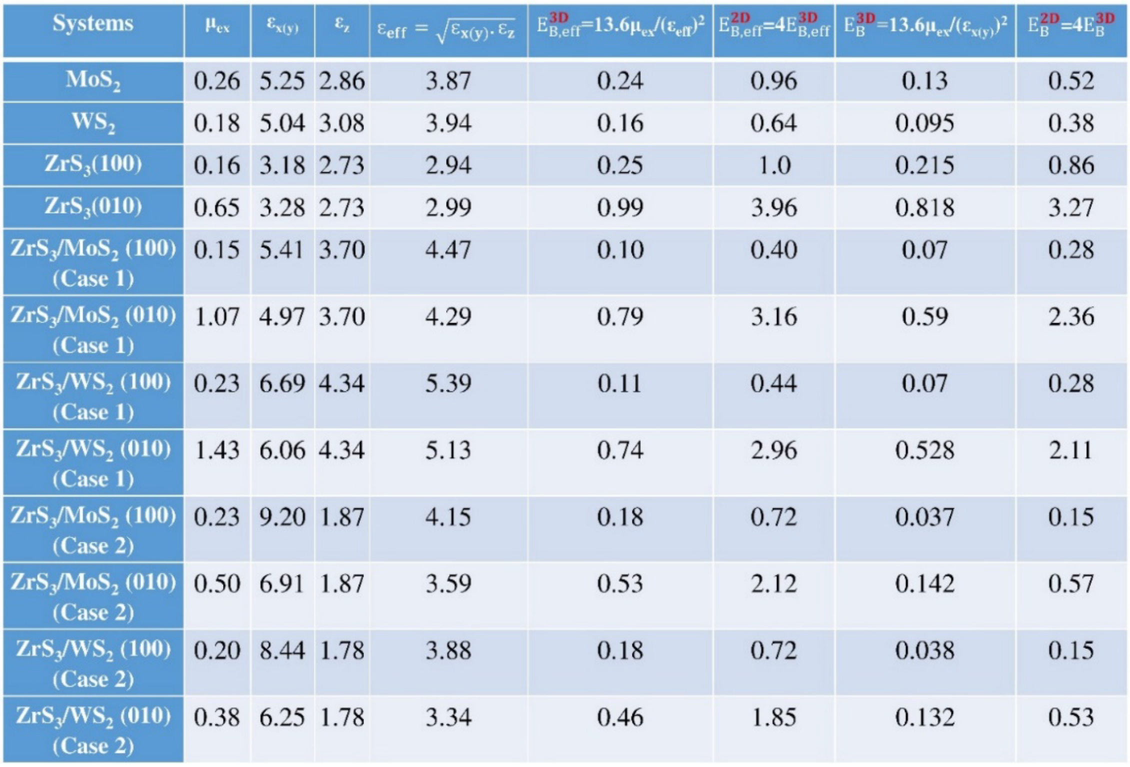

Systems	μ_{ex}	$\varepsilon_{x(y)}$	ε_z	$\varepsilon_{eff} = \sqrt{\varepsilon_{x(y)}\cdot\varepsilon_z}$	$E_{B,eff}^{3D}=13.6\mu_{ex}/(\varepsilon_{eff})^2$	$E_{B,eff}^{2D}=4E_{B,eff}^{3D}$	$E_B^{3D}=13.6\mu_{ex}/(\varepsilon_{x(y)})^2$	$E_B^{2D}=4E_B^{3D}$
MoS_2	0.26	5.25	2.86	3.87	0.24	0.96	0.13	0.52
WS_2	0.18	5.04	3.08	3.94	0.16	0.64	0.095	0.38
ZrS_3(100)	0.16	3.18	2.73	2.94	0.25	1.0	0.215	0.86
ZrS_3(010)	0.65	3.28	2.73	2.99	0.99	3.96	0.818	3.27
ZrS_3/MoS_2 (100) (Case 1)	0.15	5.41	3.70	4.47	0.10	0.40	0.07	0.28
ZrS_3/MoS_2 (010) (Case 1)	1.07	4.97	3.70	4.29	0.79	3.16	0.59	2.36
ZrS_3/WS_2 (100) (Case 1)	0.23	6.69	4.34	5.39	0.11	0.44	0.07	0.28
ZrS_3/WS_2 (010) (Case 1)	1.43	6.06	4.34	5.13	0.74	2.96	0.528	2.11
ZrS_3/MoS_2 (100) (Case 2)	0.23	9.20	1.87	4.15	0.18	0.72	0.037	0.15
ZrS_3/MoS_2 (010) (Case 2)	0.50	6.91	1.87	3.59	0.53	2.12	0.142	0.57
ZrS_3/WS_2 (100) (Case 2)	0.20	8.44	1.78	3.88	0.18	0.72	0.038	0.15
ZrS_3/WS_2 (010) (Case 2)	0.38	6.25	1.78	3.34	0.46	1.85	0.132	0.53

5.3 CONCLUSIONS

In this chapter, electronic, optical, and transport properties in two-dimensional vdW hetero-bilayers of ZrS_3/MS_2 and ZrS_3/MXY (M=Mo, W; X, Y=S, Se, Te; X≠Y) have been investigated in-depth for the purpose of exploring their prospects for applications in photovoltaics using first-principles calculations. These vdW hetero-bilayers exhibit type-II band alignment except in ZrS_3/MoSSe and ZrS_3/MoSTe heterobilayers. The higher energy of the conduction band edge in transition metal dichalcogenide (TMDC) monolayers with respect to that of transition metal trichalcogenide (TMTC) monolayers makes the former and latter, donor and acceptor materials, respectively, in solar energy conversion. Synergy is attained in ZrS_3/MS_2 hetero-bilayers via the realization of robust carrier mobility ($\mu_{electron}$~5124, 1191 $cm^2V^{-1}s^{-1}$, μ_{hole}~2690, 5383 $cm^2V^{-1}s^{-1}$) along the [100] direction. Besides, exciton binding energy is found to be encouragingly small (~0.15 eV) along the [100] direction, where the carrier mobility and the carrier mobility ratio are substantially high, thereby facilitating an efficient separation of electron-hole pairs along this direction. These results suggest that electrical current needs to be collected along the [100] direction in the actual photovoltaic set up for an optimum efficiency. Moreover, photo-absorbance is found to reach the order of 10^5 cm^{-1}. Overall, it necessitates a more detailed study on the optoelectronic and transport properties in the hetero-bilayers comprising of Janus TMDC monolayers and ZrS_3 monolayer, such as, ZrS_3/MoSeTe, ZrS_3/WSTe and ZrS_3/WSeTe. The Power Conversion Efficiency in these three heterobilayers are found to reach as high as 16%, 14%, and 14% respectively. The comprehensive study reported herewith illustrates a new avenue for an efficient solar energy conversion at the nanoscale based on ZrS_3/MS_2 and ZrS_3/MXY vdW hetero-bilayers in ultrathin, 2D excitonic solar cells.

Chapter 6

Summary and Future Scope & Perspective

6.1 Summary

In this final chapter, the important findings of this Ph.D. research work, illustrated in the form of various chapters in this thesis, have been summarized. The fundamental goal of this thesis is to first comprehend the intrinsic properties of 2D monolayers from first-principles quantum mechanical calculations and then, propose them for their applications in futuristic electronic devices and nano-energy harvesting systems. This thesis reflects a broad range of cutting-edge research areas extending from energy harvesting from renewable resources to next-generation devices utilizing novel properties and different degrees of freedom of electrons which emerge in atomically thin 2D semiconductors and their van der Waals heterostructures and offers atomic-scale insights through the lens of first-principles calculations based on the state-of-art density functional theory. The approach implemented in the Ph.D. work involves in studying the several entangled properties in a multifunctional material, thereby enabling to draw a systematic correlation between them. A summary of the strategies used and results obtained have been provided below:

Chapter 1 provides a broad overview of the necessity and significance of 2D materials in futuristic electronic devices and different energy harvesting systems. The chapter underlines the applications of the 2D materials in the areas of piezotronics, spintronics, valleytronics, and solar cells.

Chapter 2 illustrates an overview of the density functional theory and computational methodologies that have been used to determine properties provided in various chapters.

Chapter 3 highlights the piezoelectric and Rashba properties of 2D Janus transition metal trichalcogenide monolayers and their bilayers. The simultaneous occurrence of gigantic piezoelectricity and Rashba effect in two-dimensional materials are unusually scarce. Inversion symmetry occurring in MX_3 (M= Ti, Zr, Hf; X= S, Se) monolayers is broken upon constructing their Janus monolayer structures MX_2Y ($X \neq Y$=S, Se), thereby inducing a large out-of-plane piezoelectric constant, d_{33} (~68 pm/V) in them. d_{33} can be further enhanced to a super high value of ~1000 pm/V upon applying vertical compressive strain in the van der Waals bilayers constituted by interfacing these Janus monolayers. Moreover, the absence of horizontal mirror symmetry and presence of strong spin-orbit coupling cause Rashba spin splitting in the electronic bands with high Rashba parameter ($\alpha_R \sim 1.08$ eVÅ), which is much larger than the Janus MoSSe monolayer (α_R~0.53 eVÅ) and GaSe/MoSe$_2$ heterostructure (α_R~0.49 eVÅ). It rises to 1.408 eVÅ by applying a 5% uniaxial compressive strain. These 2D systems straddle giant Rashba spin splitting and ultrahigh piezoelectricity, thereby making them immensely promising candidates in the next generation electronics, piezotronics and spintronics devices.

In **Chapter 4**, valley spin polarization in 2D h-NbN and h-TaN monolayers has been demonstrated. Due to the presence of strong spin-orbit coupling and absence of inversion symmetry breaking, these 2D materials are found to host valley physics together with Rashba effect which is essential for advancing the emerging fields of spintronics and valleytronics. Monolayer h-NbN (TaN) shows Zeeman-type valley spin splitting (VSS) of 32 (112) meV and 130 (406) meV in valence band (VB) and conduction band (CB) respectively which are exceptional and complementary electronic properties with respect to the well-known MoS$_2$ monolayer. At the same time, it exhibits large Berry curvature ~50 (73) Å^2, which is more than four (six) times of monolayer MoS$_2$ (~11 Å^2). Moreover, the Rashba energy and Rashba splitting constant of monolayer h-NbN (TaN) are found to be 52 (74) meV and 2.90 (4.23) eVÅ, respectively, which are competitive with the giant Rashba spin splitting parameters realized so far in 2D materials. Valleytronic and spintronic properties in the studied monolayers are found to be superior to that in h-MoS$_2$ and Janus MoSSe monolayers and are therefore proposed for an effective coupling of spin and valley physics.

Chapter 5 deals with energy harvesting, particularly, on the generation of electricity from solar radiation using two-dimensional vdW hetero-bilayers of ZrS$_3$/MS$_2$ and ZrS$_3$/MXY (M=Mo, W; X, Y=S, Se, Te; $X \neq Y$). Electronic, optical, and transport properties in these 2D vdW hetero-bilayers have been investigated in-depth for the purpose of exploring their prospects for applications in photovoltaics. The Power Conversion Efficiency (PCE) in ZrS$_3$/MoS$_2$, ZrS$_3$/WS$_2$, ZrS$_3$/MoSeTe, ZrS$_3$/WSTe, and ZrS$_3$/WSeTe hetero-bilayers, calculated within the Anderson-limit, are found to reach as high as ~12%, 8%, 16%, 14%, and 14% respectively. Chapter 5 illustrates a new avenue for an efficient solar energy conversion at the nanoscale based on ZrS$_3$/MS$_2$ and ZrS$_3$/MXY vdW hetero-bilayers in ultrathin, 2D excitonic solar cells.

6.2 Future Scope & Perspectives

As reported in Chapter 3, Janus transition metal trichalcogenide, MX_2Y (M= Ti, Zr, Hf; X≠Y=S, Se) monolayers show large out-of-plane piezoelectric response along with high Rashba constant which may exhibit ferroelectric properties as most of the ferroelectric materials show Rashba properties. Therefore, there is a scope for a detailed theoretical study of ferroelectric properties in these systems. Particularly, the thesis strongly urges the experimentalists to synthesize the TiS_2Se and ZrS_2Se monolayers for their exceptional piezotronics and spintronic properties. Chapter 4 showcases the occurrence of valley-spin polarization in the conduction band of h-NbN and h-TaN monolayers which show exceptional and complementary electronic properties with respect to the well-known MoS_2 monolayer. There is an immense scope for constructing vdWHs out of these monolayers with TMDC monolayers to get the valley spin splitting at both conduction band and valence band. Chapter 5 highlights the occurrence of 2D excitonic solar cell effect in vdWH and thereby hints at the immense scope for development in this field through the applications of vdWH. Exploring new 2D semiconductors having exceptional properties will be of great interest from both theoretical and experimentalist perspectives.

List of Publications

Results published in the articles marked in blue below constitute my Ph.D. thesis.

Peer-Reviewed Publications during Ph.D.

(h-index 14, Citation 574, i10-index 16)

Source: Google Scholar (up to October 2022)

First Author:

1. Raihan Ahammed and Abir De Sarkar. "Valley spin polarization in two-dimensional h-MN (M= Nb, Ta) monolayers: Merger of valleytronics with spintronics." ***Phys. Rev. B*** 105, 045426 (2022).

2. Raihan Ahammed, Nityasagar Jena, Ashima Rawat, Manish K. Mohanta, Dimple, and Abir De Sarkar. "Ultrahigh Out-of-Plane Piezoelectricity Meets Giant Rashba Effect in 2D Janus Monolayers and Bilayers of Group IV Transition-Metal Trichalcogenides." ***J. Phys. Chem. C*** 124, 21250-21260 (2020).

3. Raihan Ahammed, Ashima Rawat, Nityasagar Jena, Dimple, Manish Kumar Mohanta, and Abir De Sarkar. "ZrS_3/MS_2 and ZrS_3/MXY (M=Mo, W; X, Y=S, Se, Te; X≠ Y) type-II van der Waals hetero-bilayers: prospective candidates in 2D excitonic solar cells." ***Appl. Surf. Sci.*** 499, 143894 (2020).

Co-Author:

4. Ashima Rawat, Dimple, **Raihan Ahammed**, and Abir De Sarkar. "Concurrence of negative in-plane piezoelectricity and photocatalytic properties in 2D ScAgP2S6 monolayers**."** ***J. Phys. Condens. Matt.*** 33, 375301 (2021).

5. Ashima Rawat, **Raihan Ahammed**, Dimple, Nityasagar Jena, Manish Kumar Mohanta, and Abir De Sarkar. "Solar energy harvesting in type II van der Waals heterostructures of semiconducting group III monochalcogenide monolayers." ***J. Phys. Chem. C*** *123, 12666-12675 (2019).*

6. Pradip Nandi, Ashima Rawat, **Raihan Ahammed**, Nityasagar Jena, and Abir De Sarkar. "Group-IV (A) Janus dichalcogenide monolayers and their interfaces straddle gigantic shear and in-plane piezoelectricity." ***Nanoscale*** *13, 5460-5478 (2021).*

7. Nityasagar Jena, Dimple, **Raihan Ahammed**, Ashima Rawat, Manish Kumar Mohanta, and Abir De Sarkar. "Valley drift and valley current modulation in strained monolayer MoS2." ***Phys. Rev. B*** 100, 165413 (2019).

8. Dimple, Manish Kumar Mohanta, Ashima Rawat, Nityasagar Jena, **Raihan Ahammed**, and Abir De Sarkar. "Ultra-low lattice thermal conductivity and giant phonon–electric field coupling in hafnium dichalcogenide monolayers." ***J. Phys. Condens. Matt.*** 32, 315301 (2020).

9. Manish Kumar Mohanta, Ashima Rawat, Nityasagar Jena, **Raihan Ahammed**, and Abir De Sarkar. "Superhigh flexibility and out-of-plane piezoelectricity together with strong anharmonic phonon scattering induced extremely low lattice thermal conductivity in hexagonal buckled CdX (X= S, Se) monolayers." ***J. Phys. Condens. Matt.*** 32, 355301 (2020).

10. Manish Kumar Mohanta, Dimple, Ashima Rawat, Nityasagar Jena, **Raihan Ahammed**, and Abir De Sarkar. "Ultra-low thermal conductivity and super-slow hot-carrier thermalization induced by a huge phononic gap in multifunctional nanoscale boron pnictides." ***Physica E: Low-dimensional Systems and Nanostructures*** 124, 114222 (2020).

11. Dimple, Nityasagar Jena, Ashima Rawat, **Raihan Ahammed**, Manish Kumar Mohanta, and Abir De Sarkar. "Emergence of high piezoelectricity along with robust electron mobility in Janus structures in semiconducting Group IVB dichalcogenide monolayers." ***J. Mater. Chem. A*** 6, 24885 (2018).

12. Mohanta, Manish Kumar, Ashima Rawat, Nityasagar Jena, Dimple, **Raihan Ahammed**, and Abir De Sarkar. "Interfacing boron monophosphide with molybdenum disulfide for an ultrahigh performance in thermoelectrics, two-dimensional excitonic solar cells, and nanopiezotronics." ***ACS Appl. Mater. Interfaces*** 12, 3114-3126 (2019).

13. Mohanta, Manish Kumar, Ashima Rawat, Dimple, Nityasagar Jena, **Raihan Ahammed**, and Abir De Sarkar. "Superhigh out-of-plane piezoelectricity, low thermal conductivity and photocatalytic abilities in ultrathin 2D van der Waals heterostructures of boron monophosphide and gallium nitride." ***Nanoscale*** 11, 21880-21890 (2019).

14. Ashima Rawat, Manish Kumar Mohanta, Nityasagar Jena, Dimple, **Raihan Ahammed**, and Abir De Sarkar. "Nanoscale interfaces of Janus monolayers of transition metal dichalcogenides for 2D photovoltaic and piezoelectric applications." ***J. Phys. Chem. C*** 124, 10385-10397 (2020).

Providing theoretical supports to corroborate the experimental findings:

15. Goutam Ghosh, Kritiman Marjit, Srijon Ghosh, Arnab Ghosh, **Raihan Ahammed**, Abir De Sarkar, and Amitava Patra. "Hot Hole Cooling and Transfer Dynamics from Lead Halide Perovskite Nanocrystals Using Porphyrin Molecules." ***J. Phys. Chem. C*** *125, 5859-5869 (2021).*

16. Taniya Purkait, **Raihan Ahammed**, Abir De Sarkar, and Ramendra Sundar Dey. "The role of exfoliating solvents for control synthesis of few-layer graphene-like nanosheets in energy storage applications: Theoretical and experimental investigation." ***Appl. Surf. Sci.*** 509, 145375 (2020).

17. Sachin R. Rondiya, Yogesh Jadhav, Nelson Y. Dzade, **Raihan Ahammed**, Tanmay Goswami, Abir De Sarkar, Sandesh Jadkar, Santosh Haram, and Hirendra N. Ghosh. "Experimental and Theoretical Study into Interface Structure and Band Alignment of the Cu2Zn1–x Cd x SnS4 Heterointerface for Photovoltaic Applications." ***ACS Applied Energy Materials*** 3, 5153-5162 (2020).

Bibliography

[1] R. Ahammed, N. Jena, A. Rawat, M. K. Mohanta, Dimple, and A. De Sarkar, *Ultrahigh Out-of-Plane Piezoelectricity Meets Giant Rashba Effect in 2D Janus Monolayers and Bilayers of Group IV Transition-Metal Trichalcogenides*, J. Phys. Chem. C **124**, 21250 (2020).

[2] R. Ahammed and A. De Sarkar, *Valley Spin Polarization in Two-Dimensional H− M N (M= Nb, Ta) Monolayers: Merger of Valleytronics with Spintronics*, Phys. Rev. B **105**, 45426 (2022).

[3] R. Ahammed, A. Rawat, N. Jena, Dimple, M. K. Mohanta, and A. De Sarkar, *ZrS3/MS2 and ZrS3/MXY (M=Mo, W; X, YS, Se, Te; X≠ Y) Type-II van Der Waals Hetero-Bilayers: Prospective Candidates in 2D Excitonic Solar Cells*, Appl. Surf. Sci. **499**, 143894 (2020).

[4] K. S. Thygesen, *Calculating Excitons, Plasmons, and Quasiparticles in 2D Materials and van Der Waals Heterostructures*, 2D Mater. **4**, 22004 (2017).

[5] K. S. Novoselov, A. K. Geim, S. V Morozov, D. Jiang, Y. Zhang, S. V Dubonos, I. V Grigorieva, and A. A. Firsov, *Electric Field Effect in Atomically Thin Carbon Films*, Science **306**, 666 (2004).

[6] G. R. Bhimanapati, Z. Lin, V. Meunier, Y. Jung, J. Cha, S. Das, D. Xiao, Y. Son, M. S. Strano, and V. R. Cooper, *Recent Advances in Two-Dimensional Materials beyond Graphene*, ACS Nano **9**, 11509 (2015).

[7] A. C. Ferrari, F. Bonaccorso, V. Fal'Ko, K. S. Novoselov, S. Roche, P. Bøggild, S. Borini, F. H. L. Koppens, V. Palermo, and N. Pugno, *Science and Technology Roadmap for Graphene, Related Two-Dimensional Crystals, and Hybrid Systems*, Nanoscale **7**, 4598 (2015).

[8] K. S. Novoselov, Z. Jiang, Y. Zhang, S. V Morozov, H. L. Stormer, U. Zeitler, J. C. Maan, G. S. Boebinger, P. Kim, and A. K. Geim, *Room-Temperature Quantum Hall Effect in Graphene*, Science **315**, 1379 (2007).

[9] Y. Zhang, Y.-W. Tan, H. L. Stormer, and P. Kim, *Experimental Observation of the Quantum Hall Effect and Berry's Phase in Graphene*, Nature **438**, 201 (2005).

[10] K. S. Novoselov, A. K. Geim, S. V. Morozov, D. Jiang, M. I. Katsnelson, Iv. Grigorieva, Sv. Dubonos, and andAA Firsov, *Two-Dimensional Gas of Massless Dirac Fermions in Graphene*, Nature **438**, 197 (2005).

[11] F. Xia, H. Wang, D. Xiao, M. Dubey, and A. Ramasubramaniam, *Two-Dimensional Material Nanophotonics*, Nat. Photonics **8**, 899 (2014).

[12] A. Nagashima, N. Tejima, Y. Gamou, T. Kawai, and C. Oshima, *Electronic States of Monolayer Hexagonal Boron Nitride Formed on the Metal Surfaces*, Surf. Sci. **357**, 307 (1996).

[13] L. Ci, L. Song, C. Jin, D. Jariwala, D. Wu, Y. Li, A. Srivastava, Z. F. Wang, K. Storr, and L. Balicas, *Atomic Layers of Hybridized Boron Nitride and Graphene Domains*, Nat. Mater. **9**, 430 (2010).

[14] H. Liu, A. T. Neal, Z. Zhu, Z. Luo, X. Xu, D. Tománek, and P. D. Ye, *Phosphorene:*

An Unexplored 2D Semiconductor with a High Hole Mobility, ACS Nano **8**, 4033 (2014).

[15] L. Li, Y. Yu, G. J. Ye, Q. Ge, X. Ou, H. Wu, D. Feng, X. H. Chen, and Y. Zhang, *Black Phosphorus Field-Effect Transistors*, Nat. Nanotechnol. **9**, 372 (2014).

[16] Q. H. Wang, K. Kalantar-Zadeh, A. Kis, J. N. Coleman, and M. S. Strano, *Electronics and Optoelectronics of Two-Dimensional Transition Metal Dichalcogenides*, Nat. Nanotechnol. **7**, 699 (2012).

[17] A. J. Mannix, X.-F. Zhou, B. Kiraly, J. D. Wood, D. Alducin, B. D. Myers, X. Liu, B. L. Fisher, U. Santiago, and J. R. Guest, *Synthesis of Borophenes: Anisotropic, Two-Dimensional Boron Polymorphs*, Science **350**, 1513 (2015).

[18] L. Tao, E. Cinquanta, D. Chiappe, C. Grazianetti, M. Fanciulli, M. Dubey, A. Molle, and D. Akinwande, *Silicene Field-Effect Transistors Operating at Room Temperature*, Nat. Nanotechnol. **10**, 227 (2015).

[19] B. Lalmi, H. Oughaddou, H. Enriquez, A. Kara, S. Vizzini, B. Ealet, and B. Aufray, *Epitaxial Growth of a Silicene Sheet*, Appl. Phys. Lett. **97**, 223109 (2010).

[20] F. Zhu, W. Chen, Y. Xu, C. Gao, D. Guan, C. Liu, D. Qian, S.-C. Zhang, and J. Jia, *Epitaxial Growth of Two-Dimensional Stanene*, Nat. Mater. **14**, 1020 (2015).

[21] M. E. Dávila, L. Xian, S. Cahangirov, A. Rubio, and G. Le Lay, *Germanene: A Novel Two-Dimensional Germanium Allotrope Akin to Graphene and Silicene*, New J. Phys. **16**, 95002 (2014).

[22] Z. Y. Al Balushi, K. Wang, R. K. Ghosh, R. A. Vilá, S. M. Eichfeld, J. D. Caldwell, X. Qin, Y.-C. Lin, P. A. DeSario, and G. Stone, *Two-Dimensional Gallium Nitride Realized via Graphene Encapsulation*, Nat. Mater. **15**, 1166 (2016).

[23] H. Şahin, S. Cahangirov, M. Topsakal, E. Bekaroglu, E. Akturk, R. T. Senger, and S. Ciraci, *Monolayer Honeycomb Structures of Group-IV Elements and III-V Binary Compounds: First-Principles Calculations*, Phys. Rev. B **80**, 155453 (2009).

[24] M. Naguib, O. Mashtalir, J. Carle, V. Presser, J. Lu, L. Hultman, Y. Gogotsi, and M. W. Barsoum, *Two-Dimensional Transition Metal Carbides*, ACS Nano **6**, 1322 (2012).

[25] Z. Sun, T. Liao, Y. Dou, S. M. Hwang, M.-S. Park, L. Jiang, J. H. Kim, and S. X. Dou, *Generalized Self-Assembly of Scalable Two-Dimensional Transition Metal Oxide Nanosheets*, Nat. Commun. **5**, 3813 (2014).

[26] S.-H. Lin and J.-L. Kuo, *Towards the Ionic Limit of Two-Dimensional Materials: Monolayer Alkaline Earth and Transition Metal Halides*, Phys. Chem. Chem. Phys. **16**, 20763 (2014).

[27] L. Dou, A. B. Wong, Y. Yu, M. Lai, N. Kornienko, S. W. Eaton, A. Fu, C. G. Bischak, J. Ma, and T. Ding, *Atomically Thin Two-Dimensional Organic-Inorganic Hybrid Perovskites*, Science **349**, 1518 (2015).

[28] M. Pandey, K. W. Jacobsen, and K. S. Thygesen, *Band Gap Tuning and Defect Tolerance of Atomically Thin Two-Dimensional Organic–Inorganic Halide Perovskites*, J. Phys. Chem. Lett. **7**, 4346 (2016).

[29] S. Kang, D. Lee, J. Kim, A. Capasso, H. S. Kang, J.-W. Park, C.-H. Lee, and G.-H. Lee, *2D Semiconducting Materials for Electronic and Optoelectronic Applications: Potential and Challenge*, 2D Mater. **7**, 22003 (2020).

[30] A. K. Geim and I. V Grigorieva, *Van Der Waals Heterostructures*, Nature **499**, 419 (2013).

[31] K. S. Novoselov, o A. Mishchenko, o A. Carvalho, and A. H. Castro Neto, *2D Materials and van Der Waals Heterostructures*, Science **353**, aac9439 (2016).

[32] J.-Q. Yan, B. C. Sales, M. A. Susner, and M. A. Mcguire, *Flux Growth in a Horizontal Configuration: An Analog to Vapor Transport Growth*, Phys. Rev. Mater. **1**, 23402 (2017).

[33] D. E. Bugaris and H. zur Loye, *Materials Discovery by Flux Crystal Growth: Quaternary and Higher Order Oxides*, Angew. Chemie Int. Ed. **51**, 3780 (2012).

[34] D. Wang, F. Luo, M. Lu, X. Xie, L. Huang, and W. Huang, *Chemical Vapor Transport Reactions for Synthesizing Layered Materials and Their 2D Counterparts*, Small **15**, 1804404 (2019).

[35] F. Liu, W. Wu, Y. Bai, S. H. Chae, Q. Li, J. Wang, J. Hone, and X.-Y. Zhu, *Disassembling 2D van Der Waals Crystals into Macroscopic Monolayers and Reassembling into Artificial Lattices*, Science **367**, 903 (2020).

[36] J. Li, P. Song, J. Zhao, K. Vaklinova, X. Zhao, Z. Li, Z. Qiu, Z. Wang, L. Lin, and M. Zhao, *Printable Two-Dimensional Superconducting Monolayers*, Nat. Mater. **20**, 181 (2021).

[37] R. Bian, C. Li, Q. Liu, G. Cao, Q. Fu, P. Meng, J. Zhou, F. Liu, and Z. Liu, *Recent Progress in the Synthesis of Novel Two-Dimensional van Der Waals Materials*, Natl. Sci. Rev. **9**, nwab164 (2022).

[38] D. Zhong, K. L. Seyler, X. Linpeng, R. Cheng, N. Sivadas, B. Huang, E. Schmidgall, T. Taniguchi, K. Watanabe, and M. A. McGuire, *Van Der Waals Engineering of Ferromagnetic Semiconductor Heterostructures for Spin and Valleytronics*, Sci. Adv. **3**, e1603113 (2017).

[39] D. Unuchek, A. Ciarrocchi, A. Avsar, K. Watanabe, T. Taniguchi, and A. Kis, *Room-Temperature Electrical Control of Exciton Flux in a van Der Waals Heterostructure*, Nature **560**, 340 (2018).

[40] Y. Wang, E. Liu, A. Gao, T. Cao, M. Long, C. Pan, L. Zhang, J. Zeng, C. Wang, and W. Hu, *Negative Photoconductance in van Der Waals Heterostructure-Based Floating Gate Phototransistor*, ACS Nano **12**, 9513 (2018).

[41] T. Song, X. Cai, M. W.-Y. Tu, X. Zhang, B. Huang, N. P. Wilson, K. L. Seyler, L. Zhu, T. Taniguchi, and K. Watanabe, *Giant Tunneling Magnetoresistance in Spin-Filter van Der Waals Heterostructures*, Science **360**, 1214 (2018).

[42] A. Frisk Kockum, A. Miranowicz, S. De Liberato, S. Savasta, and F. Nori, *Ultrastrong Coupling between Light and Matter*, Nat. Rev. Phys. **1**, 19 (2019).

[43] M. Liao, Z.-W. Wu, L. Du, T. Zhang, Z. Wei, J. Zhu, H. Yu, J. Tang, L. Gu, and Y. Xing, *Twist Angle-Dependent Conductivities across MoS2/Graphene Heterojunctions*, Nat. Commun. **9**, 4068 (2018).

[44] S. Liang, B. Cheng, X. Cui, and F. Miao, *Van Der Waals Heterostructures for High-performance Device Applications: Challenges and Opportunities*, Adv. Mater. **32**, 1903800 (2020).

[45] M. Orlita, D. M. Basko, M. S. Zholudev, F. Teppe, W. Knap, V. I. Gavrilenko, N. N. Mikhailov, S. A. Dvoretskii, P. Neugebauer, and C. Faugeras, *Observation of Three-Dimensional Massless Kane Fermions in a Zinc-Blende Crystal*, Nat. Phys. **10**, 233 (2014).

[46] Y. Cao, V. Fatemi, S. Fang, K. Watanabe, T. Taniguchi, E. Kaxiras, and P. Jarillo-Herrero, *Unconventional Superconductivity in Magic-Angle Graphene Superlattices*, Nature **556**, 43 (2018).

[47] L. A. Gonzalez-Arraga, J. L. Lado, F. Guinea, and P. San-Jose, *Electrically Controllable Magnetism in Twisted Bilayer Graphene*, Phys. Rev. Lett. **119**, 107201 (2017).

[48] A. Mishchenko, J. S. Tu, Y. Cao, R. V Gorbachev, J. R. Wallbank, M. T. Greenaway, V. E. Morozov, S. V Morozov, M. J. Zhu, and S. L. Wong, *Twist-Controlled Resonant Tunnelling in Graphene/Boron Nitride/Graphene Heterostructures*, Nat. Nanotechnol. **9**, 808 (2014).

[49] B. Fallahazad, K. Lee, S. Kang, J. Xue, S. Larentis, C. Corbet, K. Kim, H. C. P. Movva, T. Taniguchi, and K. Watanabe, *Gate-Tunable Resonant Tunneling in Double Bilayer Graphene Heterostructures*, Nano Lett. **15**, 428 (2015).

[50] M. Li, M. Z. Bellus, J. Dai, L. Ma, X. Li, H. Zhao, and X. C. Zeng, *A Type-I van Der Waals Heterobilayer of WSe2/MoTe2*, Nanotechnology **29**, 335203 (2018).

[51] X. Zhou, X. Hu, J. Yu, S. Liu, Z. Shu, Q. Zhang, H. Li, Y. Ma, H. Xu, and T. Zhai, *2D Layered Material-based van Der Waals Heterostructures for Optoelectronics*, Adv. Funct. Mater. **28**, 1706587 (2018).

[52] P. Muralt, *PZT Thin Films for Microsensors and Actuators: Where Do We Stand?*, IEEE Trans. Ultrason. Ferroelectr. Freq. Control **47**, 903 (2000).

[53] H. A. Sodano, G. Park, and D. J. Inman, *Estimation of Electric Charge Output for Piezoelectric Energy Harvesting*, Strain **40**, 49 (2004).

[54] J. Kou, Y. Liu, Y. Zhu, and J. Zhai, *Progress in Piezotronics of Transition-Metal Dichalcogenides*, J. Phys. D. Appl. Phys. **51**, 493002 (2018).

[55] K. H. Michel and B. Verberck, *Theory of Elastic and Piezoelectric Effects in Two-Dimensional Hexagonal Boron Nitride*, Phys. Rev. B **80**, 224301 (2009).

[56] K.-A. N. Duerloo, M. T. Ong, and E. J. Reed, *Intrinsic Piezoelectricity in Two-Dimensional Materials*, J. Phys. Chem. Lett. **3**, 2871 (2012).

[57] W. Wu, L. Wang, Y. Li, F. Zhang, L. Lin, S. Niu, D. Chenet, X. Zhang, Y. Hao, and T. F. Heinz, *Piezoelectricity of Single-Atomic-Layer MoS2 for Energy Conversion and Piezotronics*, Nature **514**, 470 (2014).

[58] H. Zhu, Y. Wang, J. Xiao, M. Liu, S. Xiong, Z. J. Wong, Z. Ye, Y. Ye, X. Yin, and X. Zhang, *Observation of Piezoelectricity in Free-Standing Monolayer MoS2*, Nat. Nanotechnol. **10**, 151 (2015).

[59] A. Avsar, H. Ochoa, F. Guinea, B. Ozyilmaz, B. J. Van Wees, and I. J. Vera-Marun, *Colloquium: Spintronics in Graphene and Other Two-Dimensional Materials*, Rev. Mod. Phys. **92**, 021003 (2020).

[60] E. C. Ahn, *2D Materials for Spintronic Devices*, Npj 2D Mater. Appl. **4**, 1 (2020).

[61] Y. A. Bychkov and É. I. Rashba, *Properties of a 2D Electron Gas with Lifted Spectral Degeneracy*, JETP Lett **39**, 78 (1984).

[62] A. Manchon, H. C. Koo, J. Nitta, S. M. Frolov, and R. A. Duine, *New Perspectives for Rashba Spin–Orbit Coupling*, Nat. Mater. **14**, 871 (2015).

[63] J. Fujimoto and G. Tatara, *Nonlocal Spin-Charge Conversion via Rashba Spin-Orbit Interaction*, Phys. Rev. B **99**, 54407 (2019).

[64] H. C. Koo, S. B. Kim, H. Kim, T. Park, J. W. Choi, K. Kim, G. Go, J. H. Oh, D. Lee, and E. Park, *Rashba Effect in Functional Spintronic Devices*, Adv. Mater. **32**, 2002117 (2020).

[65] S. Datta and B. Das, *Electronic Analog of the Electro-optic Modulator*, Appl. Phys. Lett. **56**, 665 (1990).

[66] P. Chuang, S.-C. Ho, L. W. Smith, F. Sfigakis, M. Pepper, C.-H. Chen, J.-C. Fan, J. P. Griffiths, I. Farrer, and H. E. Beere, *All-Electric All-Semiconductor Spin Field-Effect Transistors*, Nat. Nanotechnol. **10**, 35 (2015).

[67] H. C. Koo, J. H. Kwon, J. Eom, J. Chang, S. H. Han, and M. Johnson, *Control of Spin Precession in a Spin-Injected Field Effect Transistor*, Science **325**, 1515 (2009).

[68] S. Sugahara and J. Nitta, *Spin-Transistor Electronics: An Overview and Outlook*, Proc. IEEE **98**, 2124 (2010).

[69] T. Kimura and Y. Otani, *Large Spin Accumulation in a Permalloy-Silver Lateral Spin Valve*, Phys. Rev. Lett. **99**, 196604 (2007).

[70] F. J. Jedema, A. T. Filip, and B. J. Van Wees, *Electrical Spin Injection and Accumulation at Room Temperature in an All-Metal Mesoscopic Spin Valve*, Nature **410**, 345 (2001).

[71] B. T. Jonker, G. Kioseoglou, A. T. Hanbicki, C. H. Li, and P. E. Thompson, *Electrical Spin-Injection into Silicon from a Ferromagnetic Metal/Tunnel Barrier Contact*, Nat. Phys. **3**, 542 (2007).

[72] X. Lou, C. Adelmann, S. A. Crooker, E. S. Garlid, J. Zhang, K. S. Reddy, S. D. Flexner, C. J. Palmstrøm, and P. A. Crowell, *Electrical Detection of Spin Transport in Lateral Ferromagnet–Semiconductor Devices*, Nat. Phys. **3**, 197 (2007).

[73] A. Rycerz, J. Tworzydło, and C. W. J. Beenakker, *Valley Filter and Valley Valve in Graphene*, Nat. Phys. **3**, 172 (2007).

[74] D. Xiao, W. Yao, and Q. Niu, *Valley-Contrasting Physics in Graphene: Magnetic Moment and Topological Transport*, Phys. Rev. Lett. **99**, 236809 (2007).

[75] D. Xiao, G.-B. Liu, W. Feng, X. Xu, and W. Yao, *Coupled Spin and Valley Physics in Monolayers of MoS2 and Other Group-VI Dichalcogenides*, Phys. Rev. Lett. **108**, 196802 (2012).

[76] K. F. Mak, K. He, J. Shan, and T. F. Heinz, *Control of Valley Polarization in Monolayer MoS2 by Optical Helicity*, Nat. Nanotechnol. **7**, 494 (2012).

[77] K. F. Mak, K. L. McGill, J. Park, and P. L. McEuen, *The Valley Hall Effect in MoS2 Transistors*, Science **344**, 1489 (2014).

[78] J. R. Schaibley, H. Yu, G. Clark, P. Rivera, J. S. Ross, K. L. Seyler, W. Yao, and X. Xu, *Valleytronics in 2D Materials*, Nat. Rev. Mater. **1**, 16055 (2016).

[79] S. A. Wolf, D. D. Awschalom, R. A. Buhrman, J. M. Daughton, von S. von Molnár, M. L. Roukes, A. Y. Chtchelkanova, and D. M. Treger, *Spintronics: A Spin-Based Electronics Vision for the Future*, Science **294**, 1488 (2001).

[80] R. V Gorbachev, J. C. W. Song, G. L. Yu, A. V Kretinin, F. Withers, Y. Cao, A. Mishchenko, I. V Grigorieva, K. S. Novoselov, and L. S. Levitov, *Detecting Topological Currents in Graphene Superlattices*, Science **346**, 448 (2014).

[81] M. Sui, G. Chen, L. Ma, W.-Y. Shan, D. Tian, K. Watanabe, T. Taniguchi, X. Jin, W. Yao, and D. Xiao, *Gate-Tunable Topological Valley Transport in Bilayer Graphene*, Nat. Phys. **11**, 1027 (2015).

[82] Y. Shimazaki, M. Yamamoto, I. V Borzenets, K. Watanabe, T. Taniguchi, and S. Tarucha, *Generation and Detection of Pure Valley Current by Electrically Induced Berry Curvature in Bilayer Graphene*, Nat. Phys. **11**, 1032 (2015).

[83] W. Yao, D. Xiao, and Q. Niu, *Valley-Dependent Optoelectronics from Inversion Symmetry Breaking*, Phys. Rev. B **77**, 235406 (2008).

[84] D. M. Chapin, C. S. Fuller, and G. L. Pearson, *A New Silicon P-n Junction Photocell for Converting Solar Radiation into Electrical Power*, J. Appl. Phys. **25**, 676 (1954).

[85] X. Wu, *High-Efficiency Polycrystalline CdTe Thin-Film Solar Cells*, Sol. Energy **77**, 803 (2004).

[86] G. J. Bauhuis, P. Mulder, E. J. Haverkamp, J. Huijben, and J. J. Schermer, *26.1% Thin-Film GaAs Solar Cell Using Epitaxial Lift-Off*, Sol. Energy Mater. Sol. Cells **93**, 1488 (2009).

[87] C. Battaglia, A. Cuevas, and S. De Wolf, *High-Efficiency Crystalline Silicon Solar Cells: Status and Perspectives*, Energy Environ. Sci. **9**, 1552 (2016).

[88] W. Zhao, S. Li, H. Yao, S. Zhang, Y. Zhang, B. Yang, and J. Hou, *Molecular Optimization Enables over 13% Efficiency in Organic Solar Cells*, J. Am. Chem. Soc. **139**, 7148 (2017).

[89] J. Linghu, T. Yang, Y. Luo, M. Yang, J. Zhou, L. Shen, and Y. P. Feng, *High-Throughput Computational Screening of Vertical 2D van Der Waals Heterostructures for High-Efficiency Excitonic Solar Cells*, ACS Appl. Mater. Interfaces **10**, 32142 (2018).

[90] J. Gong, K. Sumathy, Q. Qiao, and Z. Zhou, *Review on Dye-Sensitized Solar Cells (DSSCs): Advanced Techniques and Research Trends*, Renew. Sustain. Energy Rev. **68**, 234 (2017).

[91] K. Wu, H. Ma, Y. Gao, W. Hu, and J. Yang, *Highly-Efficient Heterojunction Solar Cells Based on Two-Dimensional Tellurene and Transition Metal Dichalcogenides*,

J. Mater. Chem. A **7**, 7430 (2019).

[92] M. M. Furchi, A. Pospischil, F. Libisch, J. Burgdörfer, and T. Mueller, *Photovoltaic Effect in an Electrically Tunable van Der Waals Heterojunction*, Nano Lett. **14**, 4785 (2014).

[93] C.-H. Lee, G.-H. Lee, A. M. Van Der Zande, W. Chen, Y. Li, M. Han, X. Cui, G. Arefe, C. Nuckolls, and T. F. Heinz, *Atomically Thin p–n Junctions with van Der Waals Heterointerfaces*, Nat. Nanotechnol. **9**, 676 (2014).

[94] W. Kohn and L. J. Sham, *Self-Consistent Equations Including Exchange and Correlation Effects*, Phys. Rev. **140**, A1133 (1965).

[95] J. P. Perdew, K. Burke, and M. Ernzerhof, *Generalized Gradient Approximation Made Simple*, Phys. Rev. Lett. **77**, 3865 (1996).

[96] D. C. Langreth and M. J. Mehl, *Beyond the Local-Density Approximation in Calculations of Ground-State Electronic Properties*, Phys. Rev. B **28**, 1809 (1983).

[97] C. Filippi, D. J. Singh, and C. J. Umrigar, *All-Electron Local-Density and Generalized-Gradient Calculations of the Structural Properties of Semiconductors*, Phys. Rev. B **50**, 14947 (1994).

[98] M. Städele, M. Moukara, J. A. Majewski, P. Vogl, and A. Görling, *Exact Exchange Kohn-Sham Formalism Applied to Semiconductors*, Phys. Rev. B **59**, 10031 (1999).

[99] J. P. Perdew and W. Yue, *Accurate and Simple Density Functional for the Electronic Exchange Energy: Generalized Gradient Approximation*, Phys. Rev. B **33**, 8800 (1986).

[100] J. P. Perdew, K. Burke, and Y. Wang, *Generalized Gradient Approximation for the Exchange-Correlation Hole of a Many-Electron System*, Phys. Rev. B **54**, 16533 (1996).

[101] J. P. Perdew, P. Ziesche, and H. Eschrig, *Electronic Structure of Solids' 91*, Akademie Verlag Berlin (1991)

[102] H. Peng and J. P. Perdew, *Rehabilitation of the Perdew-Burke-Ernzerhof Generalized Gradient Approximation for Layered Materials*, Phys. Rev. B **95**, 81105 (2017).

[103] F. Zahariev, S. S. Leang, and M. S. Gordon, *Functional Derivatives of Meta-Generalized Gradient Approximation (Meta-GGA) Type Exchange-Correlation Density Functionals*, J. Chem. Phys. **138**, 244108 (2013).

[104] J. Sun, B. Xiao, Y. Fang, R. Haunschild, P. Hao, A. Ruzsinszky, G. I. Csonka, G. E. Scuseria, and J. P. Perdew, *Density Functionals That Recognize Covalent, Metallic, and Weak Bonds*, Phys. Rev. Lett. **111**, 106401 (2013).

[105] J. Sun, A. Ruzsinszky, and J. P. Perdew, *Strongly Constrained and Appropriately Normed Semilocal Density Functional*, Phys. Rev. Lett. **115**, 36402 (2015).

[106] G.-X. Zhang, A. M. Reilly, A. Tkatchenko, and M. Scheffler, *Performance of Various Density-Functional Approximations for Cohesive Properties of 64 Bulk Solids*, New J. Phys. **20**, 63020 (2018).

[107] Y. Zhang, D. A. Kitchaev, J. Yang, T. Chen, S. T. Dacek, R. A. Sarmiento-Pérez,

M. A. L. Marques, H. Peng, G. Ceder, and J. P. Perdew, *Efficient First-Principles Prediction of Solid Stability: Towards Chemical Accuracy*, Npj Comput. Mater. **4**, 9 (2018).

[108] C. Shahi, J. Sun, and J. P. Perdew, *Accurate Critical Pressures for Structural Phase Transitions of Group IV, III-V, and II-VI Compounds from the SCAN Density Functional*, Phys. Rev. B **97**, 94111 (2018).

[109] C. J. Bartel, A. W. Weimer, S. Lany, C. B. Musgrave, and A. M. Holder, *The Role of Decomposition Reactions in Assessing First-Principles Predictions of Solid Stability*, Npj Comput. Mater. **5**, 4 (2019).

[110] A. Chakraborty, M. Dixit, D. Aurbach, and D. T. Major, *Predicting Accurate Cathode Properties of Layered Oxide Materials Using the SCAN Meta-GGA Density Functional*, Npj Comput. Mater. **4**, 60 (2018).

[111] J. H. Yang, D. A. Kitchaev, and G. Ceder, *Rationalizing Accurate Structure Prediction in the Meta-GGA SCAN Functional*, Phys. Rev. B **100**, 35132 (2019).

[112] E. B. Isaacs and C. Wolverton, *Performance of the Strongly Constrained and Appropriately Normed Density Functional for Solid-State Materials*, Phys. Rev. Mater. **2**, 63801 (2018).

[113] A. D. Becke, *A New Mixing of Hartree–Fock and Local Density-functional Theories*, J. Chem. Phys. **98**, 1372 (1993).

[114] A. D. Becke, *Real-Space Post-Hartree–Fock Correlation Models*, J. Chem. Phys. **122**, 64101 (2005).

[115] J. Heyd, G. E. Scuseria, and M. Ernzerhof, *Hybrid Functionals Based on a Screened Coulomb Potential*, J. Chem. Phys. **118**, 8207 (2003).

[116] A. V. Krukau, O. A. Vydrov, A. F. Izmaylov, and G. E. Scuseria, *Influence of the Exchange Screening Parameter on the Performance of Screened Hybrid Functionals*, J. Chem. Phys. **125**, (2006).

[117] J. Heyd and G. E. Scuseria, *Efficient Hybrid Density Functional Calculations in Solids: Assessment of the Heyd-Scuseria-Ernzerhof Screened Coulomb Hybrid Functional*, J. Chem. Phys. **121**, 1187 (2004).

[118] A. Carvalho, S. Öberg, M. J. Rayson, and P. R. Briddon, *Electronic Properties, Doping, and Defects in Chlorinated Silicon Nanocrystals*, Phys. Rev. B **86**, 45308 (2012).

[119] T. M. Henderson, J. Paier, and G. E. Scuseria, *Accurate Treatment of Solids with the HSE Screened Hybrid*, Phys. Status Solidi **248**, 767 (2011).

[120] D. S. Koda, F. Bechstedt, M. Marques, and L. K. Teles, *Trends on Band Alignments: Validity of Anderson's Rule in SnS2 and SnSe2-Based van Der Waals Heterostructures*, Phys. Rev. B **97**, 165402 (2018).

[121] S. Bhattacharyya and A. K. Singh, *Semiconductor-Metal Transition in Semiconducting Bilayer Sheets of Transition-Metal Dichalcogenides*, Phys. Rev. B - Condens. Matter Mater. Phys. **86**, 075454 (2012).

[122] S. Grimme, *Accurate Description of van Der Waals Complexes by Density*

Functional Theory Including Empirical Corrections, J. Comput. Chem. **25**, 1463 (2004).

[123] S. Grimme, J. Antony, S. Ehrlich, and H. Krieg, *A Consistent and Accurate Ab Initio Parametrization of Density Functional Dispersion Correction (DFT-D) for the 94 Elements H-Pu*, J. Chem. Phys. **132**, 154104 (2010).

[124] P. E. Blöchl, *Projector Augmented-Wave Method*, Phys. Rev. B **50**, 17953 (1994).

[125] X. Wu, D. Vanderbilt, and D. R. Hamann, *Systematic Treatment of Displacements, Strains, and Electric Fields in Density-Functional Perturbation Theory*, Phys. Rev. B - Condens. Matter Mater. Phys. **72**, 035105 (2005).

[126] S. Baroni, S. De Gironcoli, A. D. Corso, S. Scuola, I. Superiore, I. Istituto, F. Materia, I.- Trieste, P. Giannozzi, S. De Gironcoli, A. Dal Corso, and P. Giannozzi, *Phonons and Related Crystal Properties from Density-Functional Perturbation Theory*, Rev. Mod. Phys. **73**, 515 (2001).

[127] P. Giannozzi and S. Baroni, *Density-Functional Perturbation Theory*, in *Handbook of Materials Modeling*, Springer, pp. 195–214 (2005).

[128] G. Kresse and J. Hafner, *Ab Initio Molecular Dynamics for Liquid Metals*, Phys. Rev. B **47**, 558 (1993).

[129] G. Kresse and J. Furthmüller, *Efficiency of Ab-Initio Total Energy Calculations for Metals and Semiconductors Using a Plane-Wave Basis Set*, Comput. Mater. Sci. **6**, 15 (1996).

[130] G. Kresse, J. Furthmüller, and J. Hafner, *Theory of the Crystal Structures of Selenium and Tellurium: The Effect of Generalized-Gradient Corrections to the Local-Density Approximation*, Phys. Rev. B **50**, 13181 (1994).

[131] G. Kresse and J. Furthmüller, *Efficient Iterative Schemes for Ab Initio Total-Energy Calculations Using a Plane-Wave Basis Set*, Phys. Rev. B **54**, 11169 (1996).

[132] A. Togo and I. Tanaka, *First Principles Phonon Calculations in Materials Science*, Scr. Mater. **108**, 1 (2015).

[133] M. K. Mohanta and A. De Sarkar, *Coupled Spin and Valley Polarization in Monolayer HfN2 and Valley-Contrasting Physics at the HfN2−WSe2 Interface*, Phys. Rev. B **102**, 125414 (2020).

[134] S. Singh, C. Espejo, and A. H. Romero, *Structural, Electronic, Vibrational, and Elastic Properties of Graphene/MoS2 Bilayer Heterostructures*, Phys. Rev. B **98**, 155309 (2018).

[135] J. Bardeen and W. Shockley, *Deformation Potentials and Mobilities in Non-Polar Crystals*, Phys. Rev. **80**, 72 (1950).

[136] J. Xi, M. Long, L. Tang, D. Wang, and Z. Shuai, *First-Principles Prediction of Charge Mobility in Carbon and Organic Nanomaterials*, Nanoscale **4**, 4348 (2012).

[137] J. Chen, J. Xi, D. Wang, and Z. Shuai, *Carrier Mobility in Graphyne Should Be Even Larger than That in Graphene: A Theoretical Prediction*, J. Phys. Chem. Lett. **4**, 1443 (2013).

[138] M. Long, L. Tang, D. Wang, Y. Li, and Z. Shuai, *Electronic Structure and Carrier*

Mobility in Graphdiyne Sheet and Nanoribbons: Theoretical Predictions, ACS Nano **5**, 2593 (2011).

[139] Z.-G. Shao, X.-S. Ye, L. Yang, and C.-L. Wang, *First-Principles Calculation of Intrinsic Carrier Mobility of Silicene*, J. Appl. Phys. **114**, 93712 (2013).

[140] X.-S. Ye, Z.-G. Shao, H. Zhao, L. Yang, and C.-L. Wang, *Intrinsic Carrier Mobility of Germanene Is Larger than Graphene's: First-Principle Calculations*, Rsc Adv. **4**, 21216 (2014).

[141] Y. Cai, G. Zhang, and Y.-W. Zhang, *Polarity-Reversed Robust Carrier Mobility in Monolayer MoS2 Nanoribbons*, J. Am. Chem. Soc. **136**, 6269 (2014).

[142] T. Zhao, W. Shi, J. Xi, D. Wang, and Z. Shuai, *Intrinsic and Extrinsic Charge Transport in CH3NH3PbI3 Perovskites Predicted from First-Principles*, Sci. Rep. **6**, 19968 (2016).

[143] G. Gaddemane, W. G. Vandenberghe, M. L. Van de Put, S. Chen, S. Tiwari, E. Chen, and M. V Fischetti, *Theoretical Studies of Electronic Transport in Monolayer and Bilayer Phosphorene: A Critical Overview*, Phys. Rev. B **98**, 115416 (2018).

[144] L. Cheng, C. Zhang, and Y. Liu, *Why Two-Dimensional Semiconductors Generally Have Low Electron Mobility*, Phys. Rev. Lett. **125**, 177701 (2020).

[145] H. Lang, S. Zhang, and Z. Liu, *Mobility Anisotropy of Two-Dimensional Semiconductors*, Phys. Rev. B **94**, 235306 (2016).

[146] M. C. Scharber, D. Mühlbacher, M. Koppe, P. Denk, C. Waldauf, A. J. Heeger, and C. J. Brabec, *Design Rules for Donors in Bulk-heterojunction Solar Cells—Towards 10% Energy-conversion Efficiency*, Adv. Mater. **18**, 789 (2006).

[147] W. Shockley and H. J. Queisser, *Detailed Balance Limit of Efficiency of P-n Junction Solar Cells*, J. Appl. Phys. **32**, 510 (1961).

[148] C. Elsässer, M. Fähnle, C. T. Chan, and K. M. Ho, *Density-Functional Energies and Forces with Gaussian-Broadened Fractional Occupations*, Phys. Rev. B **49**, 13975 (1994).

[149] J. D. Monkhorst, Hendrik J., Pack, *Special Points for Brillouin-Zone Integrations*, Phys. Rev. B **16**, 1748 (1977).

[150] X. Gonze, *DFPT: Adiabatic Density-Functional*, Phys. Rev. A **52**, 1096 (1995).

[151] A. Baroni, S., Giannozzi, P., & Testa, *Green's-Function Approach to Linear Response in Solids*, Phys. Rev. Lett. **58**, 1861 (1987).

[152] A. Togo, F. Oba, and I. Tanaka, *First-Principles Calculations of the Ferroelastic Transition between Rutile-Type and CaCl2-Type SiO2 at High Pressures*, Phys. Rev. B - Condens. Matter Mater. Phys. **78**, 134106 (2008).

[153] W. Tang, E. Sanville, and G. Henkelman, *A Grid-Based Bader Analysis Algorithm without Lattice Bias*, J. Phys. Condens. Matter **21**, 084204 (2009).

[154] A. Uhe, S. Kozuch, and S. Shaik, *Software News and Update Automatic Analysis of Computed Catalytic Cycles*, J. Comput. Chem. 32, 978 (2011).

[155] G. Henkelman, A. Arnaldsson, and H. Jónsson, *A Fast and Robust Algorithm for*

Bader Decomposition of Charge Density, Comput. Mater. Sci. **36**, 354 (2006).

[156] U. Herath, P. Tavadze, X. He, E. Bousquet, S. Singh, F. Muñoz, and A. H. Romero, *PyProcar: A Python Library for Electronic Structure Pre/Post-Processing*, Comput. Phys. Commun. **251**, 107080 (2020).

[157] P. E. Blöchl, O. Jepsen, and O. K. Andersen, *Improved Tetrahedron Method for Brillouin-Zone Integrations*, Phys. Rev. B **49**, 16223 (1994).

[158] H. Gullapalli, V. S. M. Vemuru, A. Kumar, A. Botello-Mendez, R. Vajtai, M. Terrones, S. Nagarajaiah, and P. M. Ajayan, *Flexible Piezoelectric ZnO–Paper Nanocomposite Strain Sensor*, Small **6**, 1641 (2010).

[159] X. Wang, J. Zhou, J. Song, J. Liu, N. Xu, and Z. L. Wang, *Piezoelectric Field Effect Transistor and Nanoforce Sensor Based on a Single ZnO Nanowire*, Nano Lett. **6**, 2768 (2006).

[160] J. C. Doll, A. W. Peng, A. J. Ricci, and B. L. Pruitt, *Faster than the Speed of Hearing: Nanomechanical Force Probes Enable the Electromechanical Observation of Cochlear Hair Cells*, Nano Lett. **12**, 6107 (2012).

[161] Y. Yun, V. Shanov, Y. Tu, M. J. Schulz, S. Yarmolenko, S. Neralla, J. Sankar, and S. Subramaniam, *A Multi-Wall Carbon Nanotube Tower Electrochemical Actuator*, Nano Lett. **6**, 689 (2006).

[162] A. Khan, Z. Abas, H. S. Kim, and I.-K. Oh, *Piezoelectric Thin Films: An Integrated Review of Transducers and Energy Harvesting*, Smart Mater. Struct. **25**, 53002 (2016).

[163] R. Araneo, F. Bini, A. Rinaldi, A. Notargiacomo, M. Pea, and S. Celozzi, *Thermal-Electric Model for Piezoelectric ZnO Nanowires*, Nanotechnology **26**, 265402 (2015).

[164] Z. L. Wang and J. Song, *Piezoelectric Nanogenerators Based on Zinc Oxide Nanowire Arrays*, Science **312**, 242 (2006).

[165] M. N. Blonsky, H. L. Zhuang, A. K. Singh, and R. G. Hennig, *Ab Initio Prediction of Piezoelectricity in Two-Dimensional Materials*, ACS Nano **9**, 9885 (2015).

[166] N. Jena, S. D. Behere, and A. De Sarkar, *Strain-Induced Optimization of Nanoelectromechanical Energy Harvesting and Nanopiezotronic Response in a MoS2 Monolayer Nanosheet*, J. Phys. Chem. C **121**, 9181 (2017).

[167] Y. Qi and M. C. McAlpine, *Nanotechnology-Enabled Flexible and Biocompatible Energy Harvesting*, Energy Environ. Sci. **3**, 1275 (2010).

[168] H. Yin, J. Gao, G.-P. Zheng, Y. Wang, and Y. Ma, *Giant Piezoelectric Effects in Monolayer Group-V Binary Compounds with Honeycomb Phases: A First-Principles Prediction*, J. Phys. Chem. C **121**, 25576 (2017).

[169] L. Dong, J. Lou, and V. B. Shenoy, *Large In-Plane and Vertical Piezoelectricity in Janus Transition Metal Dichalchogenides*, ACS Nano **11**, 8242 (2017).

[170] M. Zelisko, Y. Hanlumyuang, S. Yang, Y. Liu, C. Lei, J. Li, P. M. Ajayan, and P. Sharma, *Anomalous Piezoelectricity in Two-Dimensional Graphene Nitride Nanosheets*, Nat. Commun. **5**, 4284 (2014).

[171] J. Qi, Y.-W. Lan, A. Z. Stieg, J.-H. Chen, Y.-L. Zhong, L.-J. Li, C.-D. Chen, Y. Zhang, and K. L. Wang, *Piezoelectric Effect in Chemical Vapour Deposition-Grown Atomic-Monolayer Triangular Molybdenum Disulfide Piezotronics*, Nat. Commun. **6**, 7430 (2015).

[172] S. K. Singh, M. Neek-Amal, S. Costamagna, and F. M. Peeters, *Thermomechanical Properties of a Single Hexagonal Boron Nitride Sheet*, Phys. Rev. B **87**, 184106 (2013).

[173] S. Manzeli, D. Ovchinnikov, D. Pasquier, O. V. Yazyev, and A. Kis, *2D Transition Metal Dichalcogenides*, Nat. Rev. Mater. **2**, 17033 (2017).

[174] P. Ares, T. Cea, M. Holwill, Y. B. Wang, R. Roldán, F. Guinea, D. V Andreeva, L. Fumagalli, K. S. Novoselov, and C. R. Woods, *Piezoelectricity in Monolayer Hexagonal Boron Nitride*, Adv. Mater. **32**, 1905504 (2020).

[175] Z. Wang, J. Hu, A. P. Suryavanshi, K. Yum, and M.-F. Yu, *Voltage Generation from Individual BaTiO3 Nanowires under Periodic Tensile Mechanical Load*, Nano Lett. **7**, 2966 (2007).

[176] A. Gruverman, O. Auciello, and H. Tokumoto, *Nanoscale Investigation of Fatigue Effects in Pb (Zr, Ti) O3 Films*, Appl. Phys. Lett. **69**, 3191 (1996).

[177] M. Minary-Jolandan, R. A. Bernal, I. Kuljanishvili, V. Parpoil, and H. D. Espinosa, *Individual GaN Nanowires Exhibit Strong Piezoelectricity in 3D*, Nano Lett. **12**, 970 (2012).

[178] C. Lee, X. Wei, J. W. Kysar, and J. Hone, *Measurement of the Elastic Properties and Intrinsic Strength of Monolayer Graphene*, Science **321**, 385 (2008).

[179] R. Fei, W. Li, J. Li, and L. Yang, *Giant Piezoelectricity of Monolayer Group IV Monochalcogenides: SnSe, SnS, GeSe, and GeS*, Appl. Phys. Lett. **107**, 173104 (2015).

[180] N. Dimple, Jena, A. Rawat, R. Ahammed, M. K. Mohanta, and A. De Sarkar, *Emergence of High Piezoelectricity along with Robust Electron Mobility in Janus Structures in Semiconducting Group IVB Dichalcogenide Monolayers*, J. Mater. Chem. A **6**, 24885 (2018).

[181] I. Vurgaftman and J. R. n Meyer, *Band Parameters for Nitrogen-Containing Semiconductors*, J. Appl. Phys. **94**, 3675 (2003).

[182] V. E. Bottom, *Measurement of the Piezoelectric Coefficient of Quartz Using the Fabry-Perot Dilatometer*, J. Appl. Phys. **41**, 3941 (1970).

[183] Y. Guo, S. Zhou, Y. Bai, and J. Zhao, *Enhanced Piezoelectric Effect in Janus Group-III Chalcogenide Monolayers*, Appl. Phys. Lett. **110**, 163102 (2017).

[184] W. Li and J. Li, *Ferroelasticity and Domain Physics in Two-Dimensional Transition Metal Dichalcogenide Monolayers*, Nat. Commun. **7**, 10843 (2016).

[185] T. Shen, A. V Penumatcha, and J. Appenzeller, *Strain Engineering for Transition Metal Dichalcogenides Based Field Effect Transistors*, ACS Nano **10**, 4712 (2016).

[186] A. Azcatl, X. Qin, A. Prakash, C. Zhang, L. Cheng, Q. Wang, N. Lu, M. J. Kim, J. Kim, and K. Cho, *Covalent Nitrogen Doping and Compressive Strain in MoS2 by*

Remote N2 Plasma Exposure, Nano Lett. **16**, 5437 (2016).

[187] E. Flores, J. R. Ares, I. J. Ferrer, and C. Sánchez, *Synthesis and Characterization of a Family of Layered Trichalcogenides for Assisted Hydrogen Photogeneration*, Phys. Status Solidi - Rapid Res. Lett. **10**, 802 (2016).

[188] J. Dai, M. Li, and X. C. Zeng, *Group IVB Transition Metal Trichalcogenides: A New Class of 2D Layered Materials beyond Graphene*, Wiley Interdiscip. Rev. Comput. Mol. Sci. **6**, 211 (2016).

[189] Y. R. Tao, X. C. Wu, and W. W. Xiong, *Flexible Visible-Light Photodetectors with Broad Photoresponse Based on ZrS3nanobelt Films*, Small **10**, 4905 (2014).

[190] A.-Y. Lu, H. Zhu, J. Xiao, C.-P. Chuu, Y. Han, M.-H. Chiu, C.-C. Cheng, C.-W. Yang, K.-H. Wei, and Y. Yang, *Janus Monolayers of Transition Metal Dichalcogenides*, Nat. Nanotechnol. **12**, 744 (2017).

[191] J. Zhang, S. Jia, I. Kholmanov, L. Dong, D. Er, W. Chen, H. Guo, Z. Jin, V. B. Shenoy, and L. Shi, *Janus Monolayer Transition-Metal Dichalcogenides*, ACS Nano **11**, 8192 (2017).

[192] S. I. Ranganathan and M. Ostoja-Starzewski, *Universal Elastic Anisotropy Index*, Phys. Rev. Lett. **101**, 55504 (2008).

[193] A. J. Moulson and J. M. Herbert, *Electroceramics: Materials, Properties, Applications* (John Wiley & Sons, 2003).

[194] M. K. Mohanta, A. Rawat, N. Jena, Dimple, R. Ahammed, and A. De Sarkar, *Interfacing Boron Monophosphide with Molybdenum Disulfide for an Ultrahigh Performance in Thermoelectrics, Two-Dimensional Excitonic Solar Cells, and Nanopiezotronics*, ACS Appl. Mater. Interfaces **12**, 3114 (2019).

[195] Z. Liu, J. Z. Liu, Y. Cheng, Z. Li, L. Wang, and Q. Zheng, *Interlayer Binding Energy of Graphite: A Mesoscopic Determination from Deformation*, Phys. Rev. B - Condens. Matter Mater. Phys. **85**, 205418 (2012).

[196] J. He, K. Hummer, and C. Franchini, *Stacking Effects on the Electronic and Optical Properties of Bilayer Transition Metal Dichalcogenides MoS 2, MoSe 2, WS 2, and WSe2*, Phys. Rev. B **89**, 75409 (2014).

[197] M. A. Flores, W. Orellana, and E. Menéndez-Proupin, *Accuracy of the Heyd-Scuseria-Ernzerhof Hybrid Functional to Describe Many-Electron Interactions and Charge Localization in Semiconductors*, Phys. Rev. B **98**, 155131 (2018).

[198] J. Nitta, T. Akazaki, H. Takayanagi, and T. Enoki, *Gate Control of Spin-Orbit Interaction in an Inverted I n0.53Ga0.47As/In0.52Al0.48 as Heterostructure*, Phys. Rev. Lett. **78**, 1335 (1997).

[199] S. LaShell, Ba. McDougall, and E. Jensen, *Spin Splitting of an Au (111) Surface State Band Observed with Angle Resolved Photoelectron Spectroscopy*, Phys. Rev. Lett. **77**, 3419 (1996).

[200] Y. M. Koroteev, G. Bihlmayer, J. E. Gayone, E. V Chulkov, S. Blügel, P. M. Echenique, and P. Hofmann, *Strong Spin-Orbit Splitting on Bi Surfaces*, Phys. Rev. Lett. **93**, 46403 (2004).

[201] C. R. Ast, J. Henk, A. Ernst, L. Moreschini, M. C. Falub, D. Pacilé, P. Bruno, K. Kern, and M. Grioni, *Giant Spin Splitting through Surface Alloying*, Phys. Rev. Lett. **98**, 186807 (2007).

[202] Y. Chen, J. Liu, J. Yu, Y. Guo, and Q. Sun, *Symmetry-Breaking Induced Large Piezoelectricity in Janus Tellurene Materials*, Phys. Chem. Chem. Phys. **21**, 1207 (2019).

[203] F. Li, W. Wei, P. Zhao, B. Huang, and Y. Dai, *Electronic and Optical Properties of Pristine and Vertical and Lateral Heterostructures of Janus MoSSe and WSSe*, J. Phys. Chem. Lett. **8**, 5959 (2017).

[204] Q. Zhang and U. Schwingenschlögl, *Rashba Effect and Enriched Spin-Valley Coupling in GaX/MX2 (M=Mo, W; X=S, Se, Te) Heterostructures*, Phys. Rev. B **97**, 155415 (2018).

[205] J. Qi, X. Li, Q. Niu, and J. Feng, *Giant and Tunable Valley Degeneracy Splitting in MoTe 2*, Phys. Rev. B **92**, 121403 (2015).

[206] K. Takashina, Y. Ono, A. Fujiwara, Y. Takahashi, and Y. Hirayama, *Valley Polarization in Si (100) at Zero Magnetic Field*, Phys. Rev. Lett. **96**, 236801 (2006).

[207] Z. Zhu, A. Collaudin, B. Fauqué, W. Kang, and K. Behnia, *Field-Induced Polarization of Dirac Valleys in Bismuth*, Nat. Phys. **8**, 89 (2012).

[208] D. Gunlycke and C. T. White, *Graphene Valley Filter Using a Line Defect*, Phys. Rev. Lett. **106**, 136806 (2011).

[209] C. Zhao, T. Norden, P. Zhang, P. Zhao, Y. Cheng, F. Sun, J. P. Parry, P. Taheri, J. Wang, and Y. Yang, *Enhanced Valley Splitting in Monolayer WSe2 Due to Magnetic Exchange Field*, Nat. Nanotechnol. **12**, 757 (2017).

[210] H. Zeng, J. Dai, W. Yao, D. Xiao, and X. Cui, *Valley Polarization in MoS2 Monolayers by Optical Pumping*, Nat. Nanotechnol. **7**, 490 (2012).

[211] T. Norden, C. Zhao, P. Zhang, R. Sabirianov, A. Petrou, and H. Zeng, *Giant Valley Splitting in Monolayer WS2 by Magnetic Proximity Effect*, Nat. Commun. **10**, 4163 (2019).

[212] R. Peng, Y. Ma, S. Zhang, B. Huang, and Y. Dai, *Valley Polarization in Janus Single-Layer MoSSe via Magnetic Doping*, J. Phys. Chem. Lett. **9**, 3612 (2018).

[213] C. Mai, A. Barrette, Y. Yu, Y. G. Semenov, K. W. Kim, L. Cao, and K. Gundogdu, *Many-Body Effects in Valleytronics: Direct Measurement of Valley Lifetimes in Single-Layer MoS2*, Nano Lett. **14**, 202 (2014).

[214] S. Gupta and B. I. Yakobson, *What Dictates Rashba Splitting in 2D van Der Waals Heterobilayers*, J. Am. Chem. Soc. **143**, 3503 (2021).

[215] T. Jungwirth, J. Wunderlich, and K. Olejník, *Spin Hall Effect Devices*, Nat. Mater. **11**, 382 (2012).

[216] J. Luo, H. Munekata, F. F. Fang, and P. J. Stiles, *Effects of Inversion Asymmetry on Electron Energy Band Structures in GaSb/InAs/GaSb Quantum Wells*, Phys. Rev. B **41**, 7685 (1990).

[217] K. Ishizaka, M. S. Bahramy, H. Murakawa, M. Sakano, T. Shimojima, T. Sonobe,

K. Koizumi, S. Shin, H. Miyahara, and A. Kimura, *Giant Rashba-Type Spin Splitting in Bulk BiTeI*, Nat. Mater. **10**, 521 (2011).

[218] A. Kimura, E. E. Krasovskii, R. Nishimura, K. Miyamoto, T. Kadono, K. Kanomaru, E. V Chulkov, G. Bihlmayer, K. Shimada, and H. Namatame, *Strong Rashba-Type Spin Polarization of the Photocurrent from Bulk Continuum States: Experiment and Theory for Bi (111)*, Phys. Rev. Lett. **105**, 76804 (2010).

[219] H. Min, J. E. Hill, N. A. Sinitsyn, B. R. Sahu, L. Kleinman, and A. H. MacDonald, *Intrinsic and Rashba Spin-Orbit Interactions in Graphene Sheets*, Phys. Rev. B **74**, 165310 (2006).

[220] T. Hu, F. Jia, G. Zhao, J. Wu, A. Stroppa, and W. Ren, *Intrinsic and Anisotropic Rashba Spin Splitting in Janus Transition-Metal Dichalcogenide Monolayers*, Phys. Rev. B **97**, 235404 (2018).

[221] K. Lee, W. S. Yun, and J. D. Lee, *Giant Rashba-Type Splitting in Molybdenum-Driven Bands of MoS2/Bi (111) Heterostructure*, Phys. Rev. B **91**, 125420 (2015).

[222] S. Anand, K. Thekkepat, and U. V Waghmare, *Two-Dimensional Rectangular and Honeycomb Lattices of NbN: Emergence of Piezoelectric and Photocatalytic Properties at Nanoscale*, Nano Lett. **16**, 126 (2016).

[223] D. Hazra, N. Tsavdaris, S. Jebari, A. Grimm, F. Blanchet, F. Mercier, E. Blanquet, C. Chapelier, and M. Hofheinz, *Superconducting Properties of Very High Quality NbN Thin Films Grown by High Temperature Chemical Vapor Deposition*, Supercond. Sci. Technol. **29**, 105011 (2016).

[224] Y. F. Wu, A. B. Yu, L. B. Lei, C. Zhang, T. Wang, Y. H. Ma, Z. Huang, L. X. Chen, Y. S. Liu, and C. M. Schneider, *Superconducting NbN and CaFe0.88Co0.12 AsF Studied by Point-Contact Spectroscopy with a Nanoparticle Au Array*, Phys. Rev. B **101**, 174502 (2020).

[225] A. Chanana and U. V Waghmare, *Prediction of Coupled Electronic and Phononic Ferroelectricity in Strained 2D H-NbN: First-Principles Theoretical Analysis*, Phys. Rev. Lett. **123**, 37601 (2019).

[226] A. Kormányos, V. Zólyomi, N. D. Drummond, P. Rakyta, G. Burkard, and V. I. Fal'Ko, *Monolayer MoS2: Trigonal Warping, the Γ Valley, and Spin-Orbit Coupling Effects*, Phys. Rev. B **88**, 45416 (2013).

[227] H. U. Din, M. Idrees, A. Albar, M. Shafiq, I. Ahmad, C. V Nguyen, and B. Amin, *Rashba Spin Splitting and Photocatalytic Properties of GeC−MSSe (M= Mo, W) van Der Waals Heterostructures*, Phys. Rev. B **100**, 165425 (2019).

[228] V. Zólyomi, N. D. Drummond, and V. I. Fal'Ko, *Electrons and Phonons in Single Layers of Hexagonal Indium Chalcogenides from Ab Initio Calculations*, Phys. Rev. B **89**, 205416 (2014).

[229] S. V Eremeev, I. A. Nechaev, Y. M. Koroteev, P. M. Echenique, and E. V Chulkov, *Ideal Two-Dimensional Electron Systems with a Giant Rashba-Type Spin Splitting in Real Materials: Surfaces of Bismuth Tellurohalides*, Phys. Rev. Lett. **108**, 246802 (2012).

[230] K. Wu, J. Chen, H. Ma, L. Wan, W. Hu, and J. Yang, *Two-Dimensional Giant Tunable Rashba Semiconductors with Two-Atom-Thick Buckled Honeycomb*

Structure, Nano Lett. **21**, 740 (2020).

[231] S. Singh and A. H. Romero, *Giant Tunable Rashba Spin Splitting in a Two-Dimensional BiSb Monolayer and in BiSb/AlN Heterostructures*, Phys. Rev. B **95**, 165444 (2017).

[232] Y. Wang, W. Wei, H. Wang, N. Mao, F. Li, B. Huang, and Y. Dai, *Janus TiXY Monolayers with Tunable Berry Curvature*, J. Phys. Chem. Lett. **10**, 7426 (2019).

[233] M. Mohr, K. Papagelis, J. Maultzsch, and C. Thomsen, *Two-Dimensional Electronic and Vibrational Band Structure of Uniaxially Strained Graphene from Ab Initio Calculations*, Phys. Rev. B **80**, 205410 (2009).

[234] Q. Zhang, Y. Cheng, L.-Y. Gan, and U. Schwingenschlögl, *Giant Valley Drifts in Uniaxially Strained Monolayer MoS2*, Phys. Rev. B **88**, 245447 (2013).

[235] C. E. Nebel, *Electrons Dance in Diamond*, Nat. Mater. **12**, 690 (2013).

[236] D. Xiao, M.-C. Chang, and Q. Niu, *Berry Phase Effects on Electronic Properties*, Rev. Mod. Phys. **82**, 1959 (2010).

[237] D. J. Thouless, M. Kohmoto, M. P. Nightingale, and M. den Nijs, *Quantized Hall Conductance in a Two-Dimensional Periodic Potential*, Phys. Rev. Lett. **49**, 405 (1982).

[238] M. Gradhand, D. V Fedorov, F. Pientka, P. Zahn, I. Mertig, and B. L. Györffy, *First-Principle Calculations of the Berry Curvature of Bloch States for Charge and Spin Transport of Electrons*, J. Phys. Condens. Matter **24**, 213202 (2012).

[239] H. Hu, W.-Y. Tong, Y.-H. Shen, X. Wan, and C.-G. Duan, *Concepts of the Half-Valley-Metal and Quantum Anomalous Valley Hall Effect*, Npj Comput. Mater. **6**, 129 (2020).

[240] R. Peng, Z. He, Q. Wu, Y. Dai, B. Huang, and Y. Ma, *Spontaneous Valley Polarization in Two-Dimensional Organometallic Lattices*, Phys. Rev. B **104**, 174411 (2021).

[241] N. Jena, Dimple, R. Ahammed, A. Rawat, M. K. Mohanta, and A. De Sarkar, *Valley Drift and Valley Current Modulation in Strained Monolayer MoS2*, Phys. Rev. B **100**, (2019).

[242] K. Dou, Y. Ma, R. Peng, W. Du, B. Huang, and Y. Dai, *Promising Valleytronic Materials with Strong Spin-Valley Coupling in Two-Dimensional MN2X2 (M= Mo, W; X= F, H)*, Appl. Phys. Lett. **117**, 172405 (2020).

[243] J. Son, K.-H. Kim, Y. H. Ahn, H.-W. Lee, and J. Lee, *Strain Engineering of the Berry Curvature Dipole and Valley Magnetization in Monolayer MoS2*, Phys. Rev. Lett. **123**, 36806 (2019).

[244] S. Li, W. Wu, X. Feng, S. Guan, W. Feng, Y. Yao, and S. A. Yang, *Valley-Dependent Properties of Monolayer MoSi2N4, WSi2N4, and MoSi2As4*, Phys. Rev. B **102**, 235435 (2020).

[245] Z. Song, Z. Li, H. Wang, X. Bai, W. Wang, H. Du, S. Liu, C. Wang, J. Han, and Y. Yang, *Valley Pseudospin with a Widely Tunable Bandgap in Doped Honeycomb BN Monolayer*, Nano Lett. **17**, 2079 (2017).

[246] M. K. Mohanta, A. Kishore, and A. De Sarkar, *Spin-Current Modulation in Hexagonal Buckled ZnTe and CdTe Monolayers for Self-Powered Flexible-Piezo-Spintronic Devices*, ACS Appl. Mater. Interfaces **13**, 40872 (2021).

[247] A. A. Novoselov, K.S., Geim, A.K., Morozov, S.V., Jiang, D.A., Zhang, Y., Dubonos, S.V., Grigorieva, I.V. and Firsov, *Electric Field Effect in Atomically Thin Carbon Films*, Science **306**, 666 (2004).

[248] M. F. El-Kady, Y. Shao, and R. B. Kaner, *Graphene for Batteries, Supercapacitors and Beyond*, Nat. Rev. Mater. **1**, 16033 (2016).

[249] M. Allen, V. C. Tung, and R. B. Kaner, *Honeycomb Carbon -- A Review of Graphene*, Am. Chem. Soc. **110**, 132 (2009).

[250] E. P. Randviir, D. A. C. Brownson, and C. E. Banks, *A Decade of Graphene Research: Production, Applications and Outlook*, Mater. Today **17**, 426 (2014).

[251] A. W. Cummings, S. O. Valenzuela, F. Ortmann, and S. Roche, *Graphene Spintronics*, 2D Mater. Prop. Devices **9**, 197 (2017).

[252] A. Deepika, L. H. Li, A. M. Glushenkov, S. K. Hait, P. Hodgson, and Y. Chen, *High-Efficient Production of Boron Nitride Nanosheets via an Optimized Ball Milling Process for Lubrication in Oil*, Sci. Rep. **4**, 7288 (2014).

[253] S. Yuan, S. Linas, C. Journet, P. Steyer, V. Garnier, G. Bonnefont, A. Brioude, and B. Toury, *Pure & Crystallized 2D Boron Nitride Sheets Synthesized via a Novel Process Coupling Both PDCs and SPS Methods*, Sci. Rep. **6**, 20388 (2016).

[254] T. C. Berkelbach and D. R. Reichman, *Optical and Excitonic Properties of Atomically Thin Transition-Metal Dichalcogenides*, Annu. Rev. Condens. Matter Phys. **9**, 379 (2018).

[255] W. Choi, N. Choudhary, G. H. Han, J. Park, D. Akinwande, and Y. H. Lee, *Recent Development of Two-Dimensional Transition Metal Dichalcogenides and Their Applications*, Mater. Today **20**, 116 (2017).

[256] C. Tan and H. Zhang, *Two-Dimensional Transition Metal Dichalcogenide Nanosheet-Based Composites*, Chem. Soc. Rev. **44**, 2713 (2015).

[257] A. Lipatov, P. M. Wilson, M. Shekhirev, J. D. Teeter, R. Netusil, and A. Sinitskii, *Few-Layered Titanium Trisulfide (TiS_3) Field-Effect Transistors*, Nanoscale **7**, 12291 (2015).

[258] Y. Jin, X. Li, and J. Yang, *Single Layer of MX3 (M = Ti, Zr; X = S, Se, Te): A New Platform for Nano-Electronics and Optics*, Phys. Chem. Chem. Phys. **17**, 18665 (2015).

[259] K. K. Kim, A. Hsu, X. Jia, S. M. Kim, Y. Shi, M. Hofmann, D. Nezich, J. F. Rodriguez-Nieva, M. Dresselhaus, T. Palacios, and J. Kong, *Synthesis of Monolayer Hexagonal Boron Nitride on Cu Foil Using Chemical Vapor Deposition*, Nano Lett. **12**, 161 (2012).

[260] Y. Shi, C. Hamsen, X. Jia, K. K. Kim, A. Reina, M. Hofmann, A. L. Hsu, K. Zhang, H. Li, Z. Y. Juang, M. S. Dresselhaus, L. J. Li, and J. Kong, *Synthesis of Few-Layer Hexagonal Boron Nitride Thin Film by Chemical Vapor Deposition*, Nano Lett. **10**, 4134 (2010).

[261] C.-H. Chen, C.-L. Wu, J. Pu, M.-H. Chiu, P. Kumar, T. Takenobu, and L.-J. Li, *Hole Mobility Enhancement and P-Doping in Monolayer WSe2 by Gold Decoration*, 2D Mater. **1**, 34001 (2014).

[262] K.-K. Liu, W. Zhang, Y.-H. Lee, Y.-C. Lin, M.-T. Chang, C.-Y. Su, C.-S. Chang, H. Li, Y. Shi, and H. Zhang, *Growth of Large-Area and Highly Crystalline MoS2 Thin Layers on Insulating Substrates*, Nano Lett. **12**, 1538 (2012).

[263] S. M. Young and C. L. Kane, *Dirac Semimetals in Two Dimensions*, Phys. Rev. Lett. **115**, 126803 (2015).

[264] C. A. Downing and M. E. Portnoi, *Bielectron Vortices in Two-Dimensional Dirac Semimetals*, Nat. Commun. **8**, 897 (2017).

[265] Y. K. Hong, N. Liu, D. Yin, S. Hong, and D. H. Kim, *Recent Progress in High-Mobility Thin-Film Transistors Based on Multilayer 2D Materials*, J. Phys. D. Appl. Phys. **50**, 164001 (2017).

[266] H. L. Liu, C. C. Shen, S. H. Su, C. L. Hsu, M. Y. Li, and L. J. Li, *Optical Properties of Monolayer Transition Metal Dichalcogenides Probed by Spectroscopic Ellipsometry*, Appl. Phys. Lett. **105**, 201905 (2014).

[267] J. Judek, A. P. Gertych, M. Świniarski, A. Łapińska, A. Dużyńska, and M. Zdrojek, *High Accuracy Determination of the Thermal Properties of Supported 2D Materials*, Sci. Rep. **5**, 12422 (2015).

[268] G. Fiori, F. Bonaccorso, G. Iannaccone, T. Palacios, D. Neumaier, A. Seabaugh, S. K. Banerjee, and L. Colombo, *Electronics Based on Two-Dimensional Materials*, Nat. Nanotechnol. **9**, 768 (2014).

[269] F. H. L. Koppens, T. Mueller, P. Avouris, A. C. Ferrari, M. S. Vitiello, and M. Polini, *Photodetectors Based on Graphene, Other Two-Dimensional Materials and Hybrid Systems*, Nat. Nanotechnol. **9**, 780 (2014).

[270] M. G. Stanford, P. D. Rack, and D. Jariwala, *Emerging Nanofabrication and Quantum Confinement Techniques for 2D Materials beyond Graphene*, Npj 2D Mater. Appl. **2**, 20 (2018).

[271] C. Cui, F. Xue, W.-J. Hu, and L.-J. Li, *Two-Dimensional Materials with Piezoelectric and Ferroelectric Functionalities*, Npj 2D Mater. Appl. **2**, 18 (2018).

[272] O. V. Yazyev and Y. P. Chen, *Polycrystalline Graphene and Other Two-Dimensional Materials*, Nat. Nanotechnol. **9**, 755 (2014).

[273] M. Zeng, Y. Xiao, J. Liu, K. Yang, and L. Fu, *Exploring Two-Dimensional Materials toward the Next-Generation Circuits: From Monomer Design to Assembly Control*, Chem. Rev. **118**, 6236 (2018).

[274] D. Akinwande, C. J. Brennan, J. S. Bunch, P. Egberts, J. R. Felts, H. Gao, R. Huang, J. S. Kim, T. Li, Y. Li, K. M. Liechti, N. Lu, H. S. Park, E. J. Reed, P. Wang, B. I. Yakobson, T. Zhang, Y. W. Zhang, Y. Zhou, and Y. Zhu, *A Review on Mechanics and Mechanical Properties of 2D Materials—Graphene and Beyond*, Extrem. Mech. Lett. **13**, 42 (2017).

[275] Z. I. Alferov, *Nobel Lecture: The Double Heterostructure Concept and Its Applications in Physics, Electronics, and Technology*, Rev. Mod. Phys. **73**, 767

(2001).

[276] H. Wang, F. Liu, W. Fu, Z. Fang, W. Zhou, and Z. Liu, *Two-Dimensional Heterostructures: Fabrication, Characterization, and Application*, Nanoscale **6**, 12250 (2014).

[277] A. K. Geim and I. V. Grigorieva, *Van Der Waals Heterostructures*, Nature **499**, 419 (2013).

[278] M. Buscema, J. O. Island, D. J. Groenendijk, S. I. Blanter, G. A. Steele, H. S. J. Van Der Zant, and A. Castellanos-Gomez, *Photocurrent Generation with Two-Dimensional van Der Waals Semiconductors*, Chem. Soc. Rev. **44**, 3691 (2015).

[279] M. Y. Li, C. H. Chen, Y. Shi, and L. J. Li, *Heterostructures Based on Two-Dimensional Layered Materials and Their Potential Applications*, Mater. Today **19**, 322 (2016).

[280] H. Kroemer, *Nobel Lecture:Quasielectric Fields and Band Offsets: Teaching Electrons New Tricks*, Rev. Mod. Phys. **73**, 783 (2001).

[281] A. Koma, *Van Der Waals Epitaxy for Highly Lattice-Mismatched Systems*, J. Cryst. Growth **201**, 236 (1999).

[282] W. J. Yu, Y. Liu, H. Zhou, A. Yin, Z. Li, Y. Huang, and X. Duan, *Highly Efficient Gate-Tunable Photocurrent Generation in Vertical Heterostructures of Layered Materials*, Nat. Nanotechnol. **8**, 952 (2013).

[283] H. Nguyen-Van, A. N. Baranov, Z. Loghmari, L. Cerutti, J. B. Rodriguez, J. Tournet, G. Narcy, G. Boissier, G. Patriarche, M. Bahriz, E. Tournié, and R. Teissier, *Quantum Cascade Lasers Grown on Silicon*, Sci. Rep. **8**, 7206 (2018).

[284] Y. Ye, Z. J. Wong, X. Lu, X. Ni, H. Zhu, X. Chen, Y. Wang, and X. Zhang, *Monolayer Excitonic Laser*, Nat. Photonics **9**, 733 (2015).

[285] Y. Li, J. Zhang, D. Huang, H. Sun, F. Fan, J. Feng, Z. Wang, and C. Z. Ning, *Room-Temperature Continuous-Wave Lasing from Monolayer Molybdenum Ditelluride Integrated with a Silicon Nanobeam Cavity*, Nat. Nanotechnol. **12**, 987 (2017).

[286] F. Withers, O. Del Pozo-Zamudio, A. Mishchenko, A. P. Rooney, A. Gholinia, K. Watanabe, T. Taniguchi, S. J. Haigh, A. K. Geim, A. I. Tartakovskii, and K. S. Novoselov, *Light-Emitting Diodes by Band-Structure Engineering in van Der Waals Heterostructures*, Nat. Mater. **14**, 301 (2015).

[287] J. S. Ross, P. Klement, A. M. Jones, N. J. Ghimire, J. Yan, D. G. Mandrus, T. Taniguchi, K. Watanabe, K. Kitamura, W. Yao, D. H. Cobden, and X. Xu, *Electrically Tunable Excitonic Light-Emitting Diodes Based on Monolayer WSe2p-n Junctions*, Nat. Nanotechnol. **9**, 268 (2014).

[288] Z. Wang, Q. Jingjing, X. Wang, Z. Zhang, Y. Chen, X. Huang, and W. Huang, *Two-Dimensional Light-Emitting Materials: Preparation, Properties and Applications*, Chem. Soc. Rev. **47**, 6128 (2018).

[289] Q. He, Z. Zeng, Z. Yin, H. Li, S. Wu, X. Huang, and H. Zhang, *Fabrication of Flexible MoS2 Thin-Film Transistor Arrays for Practical Gas-Sensing Applications*, Small **8**, 2994 (2012).

[290] H. Fang, S. Chuang, T. C. Chang, K. Takei, T. Takahashi, and A. Javey, *High-Performance Single Layered WSe 2 p-FETs with Chemically Doped Contacts*, Nano Lett. **12**, 3788 (2012).

[291] J. Pu, Y. Yomogida, K. K. Liu, L. J. Li, Y. Iwasa, and T. Takenobu, *Highly Flexible MoS2 Thin-Film Transistors with Ion Gel Dielectrics*, Nano Lett. **12**, 4013 (2012).

[292] J. K. Huang, J. Pu, C. L. Hsu, M. H. Chiu, Z. Y. Juang, Y. H. Chang, W. H. Chang, Y. Iwasa, T. Takenobu, and L. J. Li, *Large-Area Synthesis of Highly Crystalline WSe2 Monolayers and Device Applications*, ACS Nano **8**, 923 (2014).

[293] B. Radisavljevic, A. Radenovic, J. Brivio, V. Giacometti, and A. Kis, *Single-Layer MoS2transistors*, Nat. Nanotechnol. **6**, 147 (2011).

[294] M.-L. Tsai, S.-H. Su, J.-K. Chang, D.-S. Tsai, C.-H. Chen, C.-I. Wu, L.-J. Li, L.-J. Chen, and J.-H. He, *Monolayer MoS_2 Heterojunction Solar Cells*, ACS Nano **8**, 8317 (2014).

[295] E. Singh, K. S. Kim, G. Y. Yeom, and H. S. Nalwa, *Atomically Thin-Layered Molybdenum Disulfide (MoS2) for Bulk-Heterojunction Solar Cells*, ACS Appl. Mater. Interfaces **9**, 3223 (2017).

[296] S. A. Svatek, E. Antolin, D. Y. Lin, R. Frisenda, C. Reuter, A. J. Molina-Mendoza, M. Muñoz, N. Agraït, T. S. Ko, D. P. De Lara, and A. Castellanos-Gomez, *Gate Tunable Photovoltaic Effect in MoS2 vertical P-n Homostructures*, J. Mater. Chem. C **5**, 854 (2017).

[297] E. Parzinger, B. Miller, B. Blaschke, J. A. Garrido, J. W. Ager, A. Holleitner, and U. Wurstbauer, *Photocatalytic Stability of Single- and Few-Layer MoS2*, ACS Nano **9**, 11302 (2015).

[298] S. S. Ding, W. Q. Huang, Y. C. Yang, B. X. Zhou, W. Y. Hu, M. Q. Long, P. Peng, and G. F. Huang, *Dual Role of Monolayer MoS2 in Enhanced Photocatalytic Performance of Hybrid MoS2/SnO2 Nanocomposite*, J. Appl. Phys. **119**, 205704 (2016).

[299] R. Kumar, D. Das, and A. K. Singh, *C2N/WS2 van Der Waals Type-II Heterostructure as a Promising Water Splitting Photocatalyst*, J. Catal. **359**, 143 (2018).

[300] Dimple, N. Jena, A. Rawat, and A. De Sarkar, *Strain and PH Facilitated Artificial Photosynthesis in Monolayer MoS2 Nanosheets*, J. Mater. Chem. A **5**, 22265 (2017).

[301] A. Rawat, N. Jena, Dimple, and A. De Sarkar, *A Comprehensive Study on Carrier Mobility and Artificial Photosynthetic Properties in Group VI B Transition Metal Dichalcogenide Monolayers*, J. Mater. Chem. A **6**, 8693 (2018).

[302] J. Wang, H. Shu, T. Zhao, P. Liang, N. Wang, D. Cao, and X. Chen, *Intriguing Electronic and Optical Properties of Two-Dimensional Janus Transition Metal Dichalcogenides*, Phys. Chem. Chem. Phys. **20**, 18571 (2018).

[303] C. Xia, W. Xiong, J. Du, T. Wang, Y. Peng, and J. Li, *Universality of Electronic Characteristics and Photocatalyst Applications in the Two-Dimensional Janus Transition Metal Dichalcogenides*, Phys. Rev. B **98**, 165424 (2018).

[304] J. Dai and X. C. Zeng, *Titanium Trisulfide Monolayer: Theoretical Prediction of a*

New Direct-Gap Semiconductor with High and Anisotropic Carrier Mobility, Angew. Chemie - Int. Ed. **54**, 7572 (2015).

[305] J. O. Island, R. Biele, M. Barawi, J. M. Clamagirand, J. R. Ares, C. Sánchez, H. S. J. Van Der Zant, I. J. Ferrer, R. D'Agosta, and A. Castellanos-Gomez, *Titanium Trisulfide (TiS3): A 2D Semiconductor with Quasi-1D Optical and Electronic Properties*, Sci. Rep. **6**, 22214 (2016).

[306] K. Osada, S. Bae, M. Tanaka, H. Raebiger, K. Shudo, and T. Suzuki, *Phonon Properties of Few-Layer Crystals of Quasi-One-Dimensional ZrS3and ZrSe3*, J. Phys. Chem. C **120**, 4653 (2016).

[307] J. Xie, R. Wang, J. Bao, X. Zhang, H. Zhang, S. Li, and Y. Xie, *Zirconium Trisulfide Ultrathin Nanosheets as Efficient Catalysts for Water Oxidation in Both Alkaline and Neutral Solutions*, Inorg. Chem. Front. **1**, 751 (2014).

[308] C. H. Lee, G. H. Lee, A. M. Van Der Zande, W. Chen, Y. Li, M. Han, X. Cui, G. Arefe, C. Nuckolls, T. F. Heinz, J. Guo, J. Hone, and P. Kim, *Atomically Thin P-n Junctions with van Der Waals Heterointerfaces*, Nat. Nanotechnol. **9**, 676 (2014).

[309] J. Linghu, T. Yang, Y. Luo, M. Yang, J. Zhou, L. Shen, and Y. P. Feng, *High-Throughput Computational Screening of Vertical 2D van Der Waals Heterostructures for High-Efficiency Excitonic Solar Cells*, ACS Appl. Mater. Interfaces **10**, 32142 (2018).

[310] M. M. Furchi, A. Pospischil, F. Libisch, J. Burgdörfer, and T. Mueller, *Photovoltaic Effect in an Electrically Tunable Van Der Waals Heterojunction*, Nano Lett. **14**, 4785 (2014).

[311] M. Bernardi, M. Palummo, and J. C. Grossman, *Extraordinary Sunlight Absorption and One Nanometer Thick Photovoltaics Using Two-Dimensional Monolayer Materials*, Nano Lett. **13**, 3664 (2013).

[312] Q. Zhao, Y. Guo, Y. Zhou, Z. Yao, Z. Ren, J. Bai, and X. Xu, *Band Alignments and Heterostructures of Monolayer Transition Metal Trichalcogenides MX3(M = Zr, Hf; X=S, Se) and Dichalcogenides MX2(M = Tc, Re; X=S, Se) for Solar Applications*, Nanoscale **10**, 3547 (2018).

[313] S. Bhattacharyya and A. K. Singh, *Semiconductor-Metal Transition in Semiconducting Bilayer Sheets of Transition-Metal Dichalcogenides*, Phys. Rev. B - Condens. Matter Mater. Phys. **86**, 075454 (2012).

[314] T. Boeker, R. Severin, A. Mueller, C. Janowitz, R. Manzke, D. Voss, P. Krueger, A. Mazur, and J. Pollmann, *Band Structure of MoS2, MoSe2, and Alpha-MoTe2: Angle-Resolved Photoelectron Spectroscopy and Ab-Initio Calculations*, Phys. Rev. B **64**, 235305 (2001).

[315] V. O. Özçelik, J. G. Azadani, C. Yang, S. J. Koester, and T. Low, *Band Alignment of Two-Dimensional Semiconductors for Designing Heterostructures with Momentum Space Matching*, Phys. Rev. B **94**, 035125 (2016).

[316] S. Fang, R. Kuate Defo, S. N. Shirodkar, S. Lieu, G. A. Tritsaris, and E. Kaxiras, *Ab Initio Tight-Binding Hamiltonian for Transition Metal Dichalcogenides*, Phys. Rev. B - Condens. Matter Mater. Phys. **92**, 205108 (2015).

[317] F. Lévy and H. Berger, *Single Crystals of Transition Metal Trichalcogenides*, J.

Cryst. Growth **61**, 61 (1983).

[318] C. Si, Z. Lin, J. Zhou, and Z. Sun, *Controllable Schottky Barrier in GaSe/Graphene Heterostructure: The Role of Interface Dipole*, 2D Mater. **4**, 015027 (2017).

[319] J. Wang, Z. Guan, J. Huang, Q. Li, and J. Yang, *Enhanced Photocatalytic Mechanism for the Hybrid G-C_3N_4/MoS_2 Nanocomposite*, J. Mater. Chem. A **2**, 7960 (2014).

[320] T. Björkman, A. Gulans, A. V. Krasheninnikov, and R. M. Nieminen, *Van Der Waals Bonding in Layered Compounds from Advanced Density-Functional First-Principles Calculations*, Phys. Rev. Lett. **108**, 235502 (2012).

[321] F. A. Rasmussen and K. S. Thygesen, *Computational 2D Materials Database: Electronic Structure of Transition-Metal Dichalcogenides and Oxides*, J. Phys. Chem. C **119**, 13169 (2015).

[322] M. C. Scharber, D. Mühlbacher, M. Koppe, P. Denk, C. Waldauf, A. J. Heeger, and C. J. Brabec, *Design Rules for Donors in Bulk-Heterojunction Solar Cells - Towards 10 % Energy-Conversion Efficiency*, Adv. Mater. **18**, 789 (2006).

[323] M. Bernardi, M. Palummo, and J. C. Grossman, *Semiconducting Monolayer Materials as a Tunable Platform for Excitonic Solar Cells*, ACS Nano **6**, 10082 (2012).

[324] L. J. Zhou, Y. F. Zhang, and L. M. Wu, *SiC2 Siligraphene and Nanotubes: Novel Donor Materials in Excitonic Solar Cells*, Nano Lett. **13**, 5431 (2013).

[325] Y. Liang, Y. Dai, Y. Ma, L. Ju, W. Wei, and B. Huang, *Novel Titanium Nitride Halide TiNX (X= F, Cl, Br) Monolayers: Potential Materials for Highly Efficient Excitonic Solar Cells*, J. Mater. Chem. A **6**, 2073 (2018).

[326] X. Lv, W. Wei, C. Mu, B. Huang, and Y. Dai, *Two-Dimensional GeSe for High Performance Thin-Film Solar Cells*, J. Mater. Chem. A **6**, 5032 (2018).

[327] J. Dai and X. C. Zeng, *Bilayer Phosphorene: Effect of Stacking Order on Bandgap and Its Potential Applications in Thin-Film Solar Cells*, J. Phys. Chem. Lett. **5**, 1289 (2014).

[328] V. D. Ganesan, J. Linghu, C. Zhang, Y. P. Feng, and L. Shen, *Heterostructures of Phosphorene and Transition Metal Dichalcogenides for Excitonic Solar Cells: A First-Principles Study*, Appl. Phys. Lett. **108**, 122105 (2016).

[329] A. Chernikov, T. C. Berkelbach, H. M. Hill, A. Rigosi, Y. Li, O. B. Aslan, D. R. Reichman, M. S. Hybertsen, and T. F. Heinz, *Exciton Binding Energy and Nonhydrogenic Rydberg Series in Monolayer WS2*, Phys. Rev. Lett. **113**, 76802 (2014).

[330] A. Ramasubramaniam, *Large Excitonic Effects in Monolayers of Molybdenum and Tungsten Dichalcogenides*, Phys. Rev. B **86**, 115409 (2012).

[331] A. R. Klots, A. K. M. Newaz, B. Wang, D. Prasai, H. Krzyzanowska, J. Lin, D. Caudel, N. J. Ghimire, J. Yan, B. L. Ivanov, K. A. Velizhanin, A. Burger, D. G. Mandrus, N. H. Tolk, S. T. Pantelides, and K. I. Bolotin, *Probing Excitonic States in Suspended Two-Dimensional Semiconductors by Photocurrent Spectroscopy*, Sci. Rep. **4**, 6608 (2014).

Appendix

Permissions for content reused

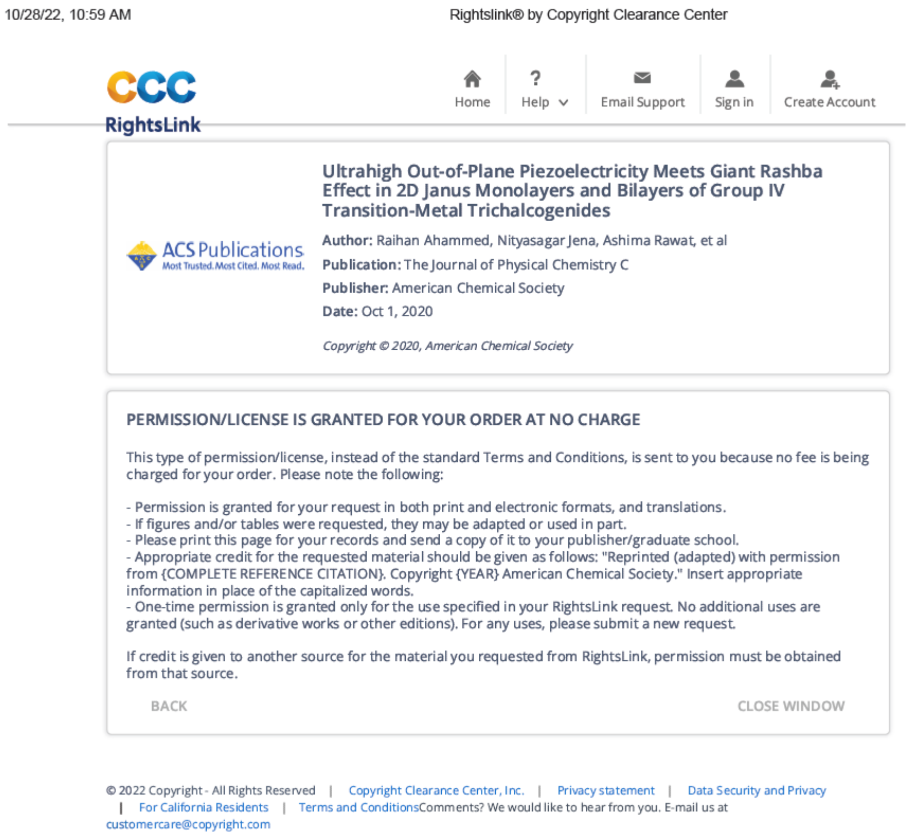

10/28/22, 10:59 AM Rightslink® by Copyright Clearance Center

Ultrahigh Out-of-Plane Piezoelectricity Meets Giant Rashba Effect in 2D Janus Monolayers and Bilayers of Group IV Transition-Metal Trichalcogenides

Author: Raihan Ahammed, Nityasagar Jena, Ashima Rawat, et al

Publication: The Journal of Physical Chemistry C

Publisher: American Chemical Society

Date: Oct 1, 2020

Copyright © 2020, American Chemical Society

PERMISSION/LICENSE IS GRANTED FOR YOUR ORDER AT NO CHARGE

This type of permission/license, instead of the standard Terms and Conditions, is sent to you because no fee is being charged for your order. Please note the following:

- Permission is granted for your request in both print and electronic formats, and translations.
- If figures and/or tables were requested, they may be adapted or used in part.
- Please print this page for your records and send a copy of it to your publisher/graduate school.
- Appropriate credit for the requested material should be given as follows: "Reprinted (adapted) with permission from {COMPLETE REFERENCE CITATION}. Copyright {YEAR} American Chemical Society." Insert appropriate information in place of the capitalized words.
- One-time permission is granted only for the use specified in your RightsLink request. No additional uses are granted (such as derivative works or other editions). For any uses, please submit a new request.

If credit is given to another source for the material you requested from RightsLink, permission must be obtained from that source.

© 2022 Copyright - All Rights Reserved | Copyright Clearance Center, Inc. | Privacy statement | Data Security and Privacy | For California Residents | Terms and ConditionsComments? We would like to hear from you. E-mail us at customercare@copyright.com

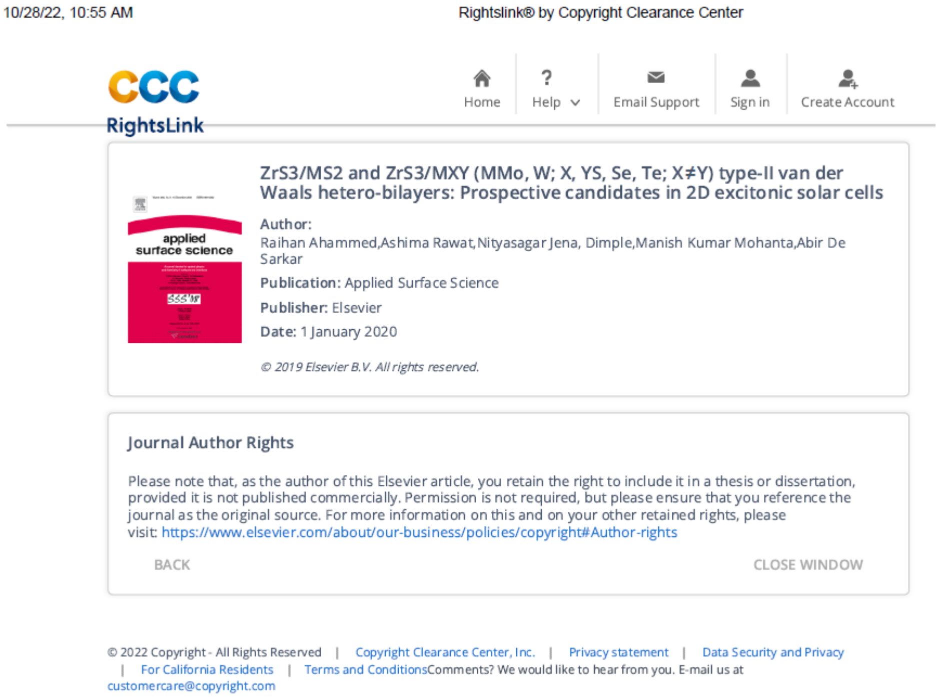

10/28/22, 10:55 AM Rightslink® by Copyright Clearance Center

ZrS3/MS2 and ZrS3/MXY (MMo, W; X, YS, Se, Te; X≠Y) type-II van der Waals hetero-bilayers: Prospective candidates in 2D excitonic solar cells

Author:
Raihan Ahammed,Ashima Rawat,Nityasagar Jena, Dimple,Manish Kumar Mohanta,Abir De Sarkar

Publication: Applied Surface Science

Publisher: Elsevier

Date: 1 January 2020

© 2019 Elsevier B.V. All rights reserved.

Journal Author Rights

Please note that, as the author of this Elsevier article, you retain the right to include it in a thesis or dissertation, provided it is not published commercially. Permission is not required, but please ensure that you reference the journal as the original source. For more information on this and on your other retained rights, please visit: https://www.elsevier.com/about/our-business/policies/copyright#Author-rights

© 2022 Copyright - All Rights Reserved | Copyright Clearance Center, Inc. | Privacy statement | Data Security and Privacy | For California Residents | Terms and ConditionsComments? We would like to hear from you. E-mail us at customercare@copyright.com

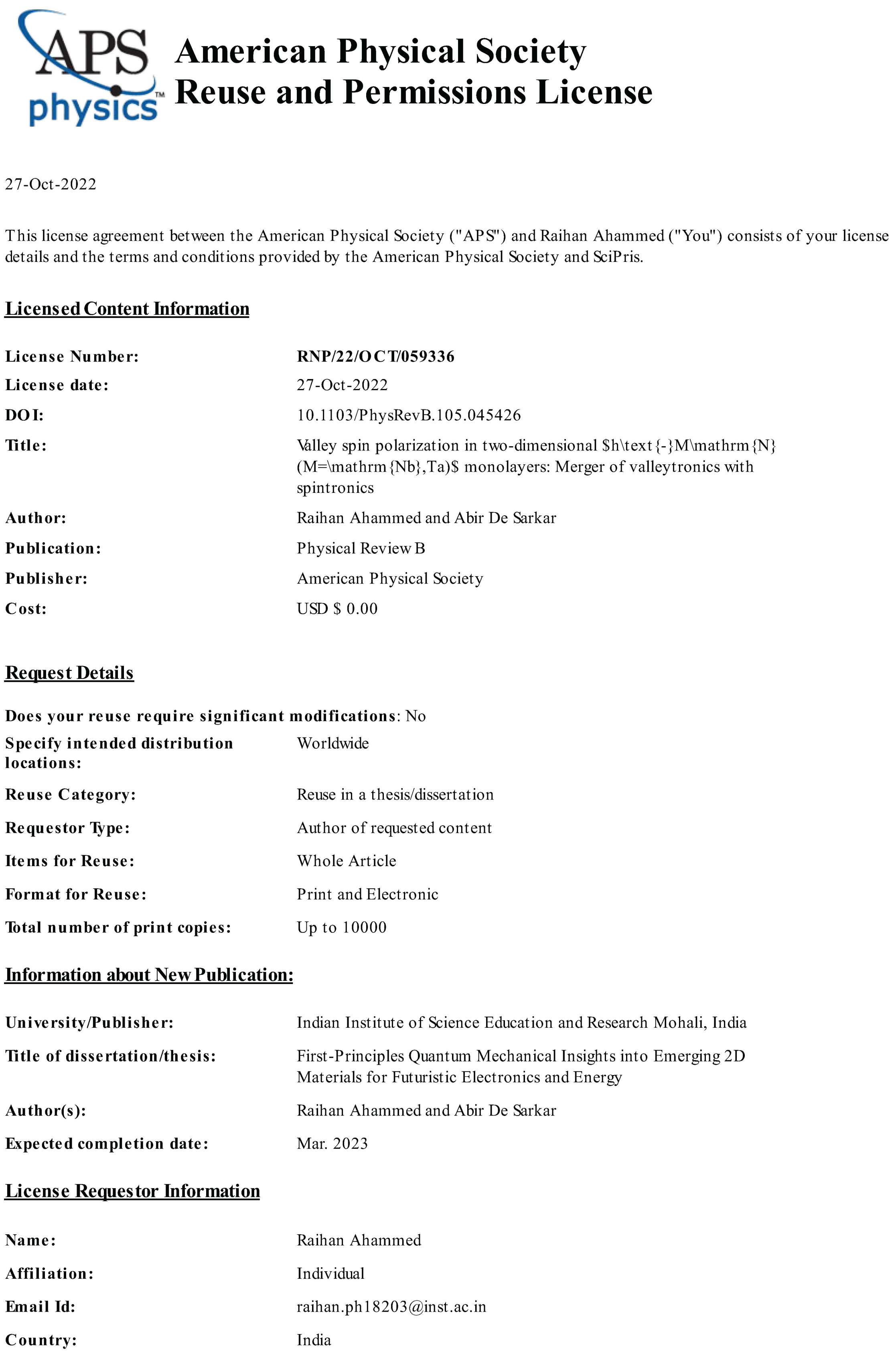

American Physical Society
Reuse and Permissions License

27-Oct-2022

This license agreement between the American Physical Society ("APS") and Raihan Ahammed ("You") consists of your license details and the terms and conditions provided by the American Physical Society and SciPris.

Licensed Content Information

License Number:	**RNP/22/OCT/059336**
License date:	27-Oct-2022
DOI:	10.1103/PhysRevB.105.045426
Title:	Valley spin polarization in two-dimensional $h\text{-}M\mathrm{N} (M=\mathrm{Nb},Ta)$ monolayers: Merger of valleytronics with spintronics
Author:	Raihan Ahammed and Abir De Sarkar
Publication:	Physical Review B
Publisher:	American Physical Society
Cost:	USD $ 0.00

Request Details

Does your reuse require significant modifications: No

Specify intended distribution locations:	Worldwide
Reuse Category:	Reuse in a thesis/dissertation
Requestor Type:	Author of requested content
Items for Reuse:	Whole Article
Format for Reuse:	Print and Electronic
Total number of print copies:	Up to 10000

Information about New Publication:

University/Publisher:	Indian Institute of Science Education and Research Mohali, India
Title of dissertation/thesis:	First-Principles Quantum Mechanical Insights into Emerging 2D Materials for Futuristic Electronics and Energy
Author(s):	Raihan Ahammed and Abir De Sarkar
Expected completion date:	Mar. 2023

License Requestor Information

Name:	Raihan Ahammed
Affiliation:	Individual
Email Id:	raihan.ph18203@inst.ac.in
Country:	India

[Vita]

Mr. Raihan Ahammed received his Bachelor of Science (Hons. in Physics) degree from Ramakrishna Mission Residential College (Autonomous), Narendrapur, Kolkata under the aegis of Calcutta University, Kolkata in 2012 and Master's degree in Applied Physics from the Indian Institute of Technology (IIT) Madras, in 2014. He worked as junior research fellow (JRF) at the Indian Institute of Science ((IISC), Bangalore and the Indian Association for the Cultivation of Science (IACS), Kolkata from 2014 to 2017. He joined the Institute of Nano Science and Technology (INST), Mohali and registered with the Indian Institute of Science Education and Research (IISER), Mohali for the ***Degree of Doctor of Philosophy*** in July 2018. His current research interest is mainly focused on the computational exploration of two-dimensional semiconductors for their advanced applications in energy conversions and futuristic electronic devices.